Safer-by-design emerging nanomaterials : the case of bimetallic gadolinium-cerium oxysulfides

Anh-Minh Nguyen

Sorbonne Université

Ecole doctorale 397 : Physique et Chimie des Matériaux

Laboratoire de Chimie de la Matière Condensée de Paris (LCMCP)

Institut Mondor de Recherche Biomédicale (IMRB)

Safer-by-design emerging nanomaterials: the case of bimetallic gadolinium-cerium oxysulfides

Par M. Anh-Minh Nguyen

Thèse de doctorat de Sorbonne Université

Dirigée par Corinne Chanéac et Sophie Lanone

Présentée et soutenue publiquement le 8 octobre 2019

Devant un jury composé de :

M. Emmanuel Flahaut	Directeur de recherche – Univ. Paul Sabatier	Rapporteur
M. Aurélien Deniaud	Maître de conférences – Univ. Grenoble Alpes	Rapporteur
Mme. Mélanie Auffan	Directrice de recherche – Aix Marseille Univ.	Examinatrice
Mme. Christine Ménager	Professeur – Sorbonne Univ.	Examinatrice
Mme. Corinne Chanéac	Professeur – Sorbonne Univ.	Directrice de thèse
Mme. Sophie Lanone	Directrice de recherche – INSERM	Directrice de thèse
Mme. Sophie Carenco	Chargée de recherche – Sorbonne Univ.	Invitée

Introduction

From the first discovery of controlled use of fire in the Stone Age to nuclear power as one of the technologies of the modern era, countless technologies have been developed to benefit human life. Yet, it is clear nowadays that the major breakthrough brought about by technology depends on its application and use. Nuclear technology led to the development of nuclear weapons with devastating effects on both human and environment. Furthermore, nuclear reactors introduced the issue of global scale accidents and an unresolved waste problem. The most recent accident happened in Fukushima, Japan in 2011, killing over 15,000 people alongside other lasting consequences. The impacts of technology are usually more complex than what they were originally predicted to be. Higher-order effects often emerge when the technology has already settled in society and can be much stronger than the intended first-order effects.

Nanotechnology, as one of the more recently developed technologies, is no exception. Although nanomaterials and nanoparticles have been around for thousands of years, nanotechnology, as a designing tool and set of concepts, was only initiated in the last century. Since then, the potential of this technology has been recognized and it has experienced a boom in the last 20 years. More and more academic research has been dedicated to this field. The number of nanomaterial-containing products on the market has also increased rapidly. They are used in many sectors ranging from energy, electronics, and construction to food, cosmetics and healthcare.

Despite their fascinating properties, nanomaterials carry potential risks towards human health and environment. Similar to chemicals, nanomaterials became regulated. Regulation compliance of used, produced or imported nanomaterials requires precise information on their physicochemical characteristics and potential toxicity. This drives the research and development of nanomaterials towards anticipation of the risk, rather than *a posteriori* determination of them. Hopefully, this approach will prevent us from making the same past chemical-related errors, be it pesticide compounds, fluorochlorohydrocarbons or the over-use of plastics.

In view of anticipation of risks, safer-by-design concept was developed and adopted for nanotechnology in the past 10 years. It consists in integrating knowledge of potential adverse effects into the process of designing nanomaterials, and engineering these undesirable effects out of them. Up until now, this concept was usually employed for existing and already well-known nanomaterials. It responds to toxicity problems detected during formulation or integration of nanomaterials into devices and products. On the other hand, safer-by-design has not yet been applied for research. The novelty of this work is based on the approach followed during this thesis. It consists in following the toxicity of a multifunctional nanomaterial still in the research phase. The synthesis methods and the chemical composition of the material are adjusted to impart targeted properties and applications. The objective is to optimize the performance of the material while minimizing its toxicity. Identification of key parameters that influence these two is particularly crucial. By deploying this approach, we expect developing nanomaterials that meet the safe and performance criteria in close relation with the activity sector and its regulations.

For this work, it is necessary to establish a collaboration between the Laboratory of the Condensed Matter Chemistry of Paris (LCMCP) that possesses the know-how in synthesis and characterization of complex nanostructures, crucial for nanomaterial design, and the Mondor Institute of Biomedical Research (IMRB, INSERM) whose researchers have expertise in evaluation of nanomaterial toxicity. Gadolinium-cerium oxysulfides of compositions $Gd_{2(1-x)}Ce_{2x}O_2S$ have been chosen as emerging nanomaterials for this study since they show potential applications in photocatalysis as well as in biomedical imaging.[1,2] Moreover, because little is known about their toxicity, they are perfect model for developing the safer-by-design approach.

This manuscript is divided to four chapters. The first chapter (Chapter I) provides the context surrounding properties and risks of nanomaterials. Then, from several recent examples in the literature, we redefine the safer-by-design approach for nanomaterials research that serves as blueprint for our study. Chapter II deals with the synthesis and characterization of bimetallic gadolinium-cerium oxysulfide nanoparticles of compositions $Gd_{2(1-x)}Ce_{2x}O_2S$. In Chapter III, the safer-by-design approach is discussed in relation with oxysulfide nanoparticles design for photocatalysis. Alongside the functionality, the toxicity of oxysulfide nanoparticles is assessed by a combination of *in vitro* and *in vivo* experiments. Chapter IV shows preliminary results of oxysulfide nanoparticles developed for fluorescent-magnetic biomedical imaging.

The last part of the manuscript summarizes the results of the three last chapters and proposes perspectives for the safer-by-design approach applied to emerging nanomaterials. Appendices contain an experimental section, a list of articles published and presentations given during the thesis as well as the texts of two articles relevant to the discussion in the manuscript.

References

(1) Larquet, C.; Nguyen, A.-M.; Glais, E.; Paulatto, L.; Sassoye, C.; Selmane, M.; Lecante, P.; Maheu, C.; Geantet, C.; Cardenas, L.; et al. Band Gap Engineering from Cation Balance: The Case of Lanthanide Oxysulfide Nanoparticles. *Chem. Mater.* **2019**, *31* (14), 5014–5023.

(2) Osseni, S. a; Lechevallier, S.; Verelst, M.; Perriat, P.; Dexpert-Ghys, J.; Neumeyer, D.; Garcia, R.; Mayer, F.; Djanashvili, K.; Peters, J. a; et al. Gadolinium Oxysulfide Nanoparticles as Multimodal Imaging Agents for T2-Weighted MR, X-Ray Tomography and Photoluminescence. *Nanoscale* **2014**, *6* (1), 555–564.

Table of Contents

Introduction **1**

Table of Contents **5**

Chapter I – Safer-by-design approach for emerging nanomaterials **7**

Chapter II – Gadolinium and gadolinium-cerium oxysulfide nanoparticles: synthesis and characterization **31**

Chapter III – Towards safer-by-design bimetallic Gd-Ce oxysulfide nanoparticles for photocatalysis **83**

Chapter IV – Potential application of bimetallic Gd-Ce oxysulfide nanoparticles in biomedical imaging **155**

Conclusion and perspectives **179**

Appendix I – Experimental Section **183**

Appendix II – List of publications **195**

Appendix III – Synthesis of Ce_2O_2S and $Gd_{2(1-y)}Ce_{2y}O_2S$ nanoparticles and reactivity from in situ X-ray absorption spectroscopy and X-ray photoelectron spectroscopy **199**

Appendix IV – Thermal stability of oleates-stabilized Gd_2O_2S nanoplates in inert and oxidizing atmospheres **211**

Chapter I

Safer-by-design approach for emerging nanomaterials

Table of contents

I.1. Nanomaterials 9
I.1.1. Emerging nanotechnology 9
I.1.2. Nanomaterials: from properties to applications 10
I.1.3. Potential risks of nanomaterials 13
I.1.4. Regulation of nanomaterials 15
I.2. Safer-by-design nanomaterials 17
I.2.1. Safer-by-design concept 17
I.2.2. Recent examples of safer-by-design approaches 17
I.2.2.1. Modification of inorganic core 17
I.2.2.2. Modification of surface 20
I.2.3. A reviewed vision of safer-by-design approach for nanomaterials 22
I.3. Thesis outline 24
References 25

I.1. Nanomaterials

I.1.1. Emerging nanotechnology

Although nanoparticles and nanomaterials have empirically been used for centuries by in many crafts, nanotechnology, as a designing tool and set of concepts, is one of the more recent technologies in human history of innovation. It involves control and manipulation of matters at the nanometer scale. For comparison, one nanometer is equal to one-billionth of a meter ($1\ nm = 10^{-9}\ m$), i.e. only approximately $1/10{,}000^{th}$ of the thickness of a human hair.

The ideas and concepts behind nanotechnology started with a talk entitled "There's Plenty of Room at the Bottom" by the Nobel laureate Richard Feynman in 1959, in which he said: "*What would the properties of materials be if we could really arrange the atoms the way we want them? … I cannot see exactly what would happen, but I can hardly doubt that when we have some control of the arrangement of things on a small scale, we will get an enormously greater range of possible properties that substances can have, and of different things that we can do*."[1] More than a decade later, in 1974, the term "nanotechnology" was proposed by Norio Taniguchi to describe the processes of creating material structures with nanometer precision.[2] Since then, this modern technology has inflated, along with the miniaturization trend described by Moore's Law. The number of scientific publications in the field has increased rapidly over the years to over 80,000 in 2018 (**Figure I.1**). As the main outcomes of nanotechnology, nanomaterials and nanoparticles have been manufactured and used in many industrial sectors ranging from energy, electronics, construction to food, cosmetics and healthcare (**Figure I.2**).[3] In 2015, the global nanomaterial market value was estimated at between 4.1 and 14.7 billion USD with annual production of millions of tonnes, mainly consisting of historically used carbon black, colloidal silica and titania.[4] It is also worth noting that most of the nanomaterial-containing products come from cosmetics and textile industries. They are products that are used in everyday life.

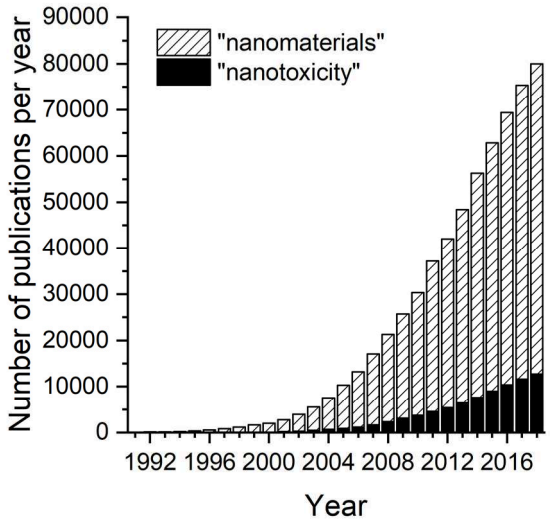

Figure I.1: Number of scientific publications since 1990 containing "nanomaterials" OR "nanoparticles" (white bars with patterns), containing ["nanomaterials" OR "nanoparticles"] AND "toxicity" (black bars) (according to Web of Science accessed on June 12, 2019).

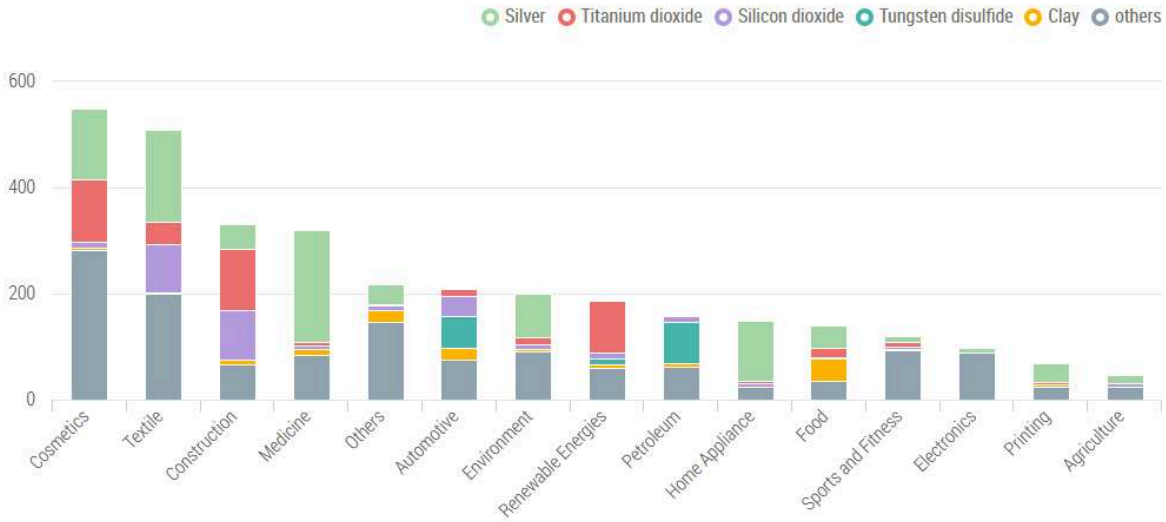

Figure I.2: Number of nanomaterial-containing products in the global market by industry sectors (taken from ref 3).

I.1.2. Nanomaterials: from properties to applications

The strong interest in nanotechnology is due to the wide range of unique properties that nanomaterials exhibit, as Feynman foresaw. At the nanoscale, the material characteristic size becomes comparable to the wavelength of the electrons it carries. In consequence, quantum

confinement effect occurs and gives rise to new properties that do not exist in the macroscopic compound. Typically, semiconductors such as cadmium selenide CdSe are photoluminescent at the nanoscale while they are not as macroscopic solids. Moreover, their emission wavelength depends on the nanoparticle size (**Figure I.3**a).[5,6] The tunable and narrow emission of semiconductor nanoparticles, also known as quantum dots, makes them a competitive choice for the emissive component of light-emitting devices (LEDs), providing a larger color gamut (**Figure I.3**b,c).[7,8] Indeed, Samsung has commercialized a quantum dot-containing TV range, named QLED, since 2017.

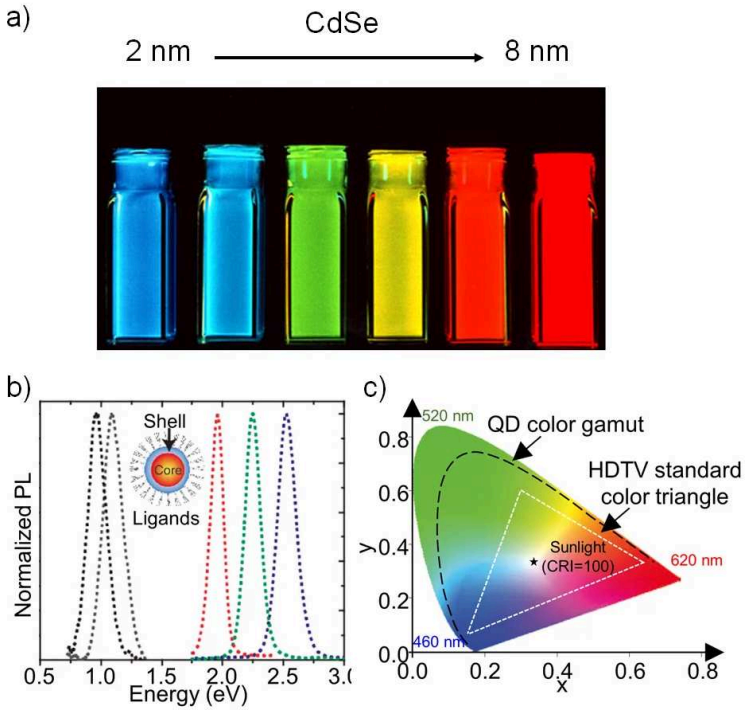

Figure I.3: a) Size-dependent photoluminescence of semiconductor CdSe nanoparticles, also known as quantum dots (image courtesy of Bawendi group at the MIT Department of Chemistry). b) Narrow photoluminescence spectra of quantum dots. c) Chromaticity diagram showing color gamut of quantum dots and of HDTV standard (adapted from ref 7,8).

Smaller nanoparticles exhibit larger specific surface area than large crystals for the same mass of material (**Figure I.4**). As the surface area increases, a larger portion of atoms are exposed to the surrounding environment. Decreasing the nanoparticle size also creates more reactive sites at edges, corners and terraces on the surface. All of these contribute to a higher reactivity of the nanoparticles. As an example, bulk gold is chemically inert and is widely regarded as a poor catalyst. However, when gold is in the form of very small particles with diameters less

than 10 nm, it becomes active for many reactions.[9,10] In particular, gold nanoparticles are used in the industrial scale for the synthesis of methyl methacrylate and vinyl chloride, essential precursors for the production of plastics.[11] Other metallic nanoparticles such as nickel, palladium and platinum are also employed for catalysis.[12]

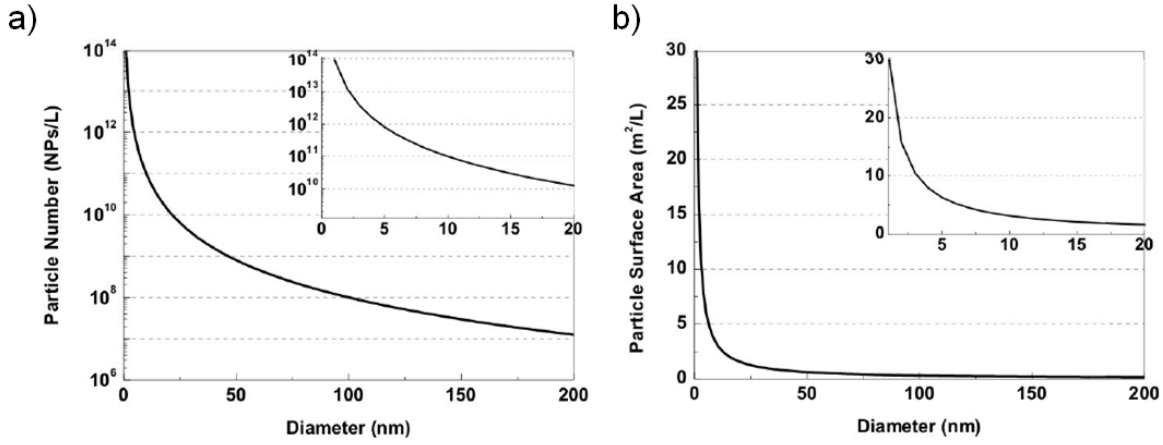

Figure I.4: a) Number of particles and b) surface area of a suspension containing 1 g/L of icosahedral gold nanoparticles crystallized in a face-centered cubic (fcc) phase (adapted from ref 13).

However, the factor that makes nanomaterials the most relevant for industrial applications is a straightforward one: their small physical size. Similar to molecules, small particles can be implemented in most forms of products including fluid and thin layer as additives for additional properties. Moreover, being used as additive, they can become cost-effective.[14] In fact, coating an area of 1 m^2 with nanoparticles of 50 nm as a monolayer only requires 20 – 200 mg of material.

Two key examples are carbon nanoparticles and titanium dioxide TiO_2 nanoparticles or titania. Carbon black particles have been used as additive in car tires to improve the tensile strength and wear resistance since the early 20th century.[14] In the form of nanotube, carbon is also present in Kevlar as filler, enhancing its mechanical properties. As for titania, their rutile form is widely used as white pigment in paint and for food coloring. They are commonly known as titanium white, Pigment White (PW6), E 171 or Cl 77891. In addition, smaller TiO_2 nanoparticles (below 50 nm in diameter) are present in sunscreen as nearly transparent additive and provide UV protection.[14] Small TiO_2 nanoparticles in the anatase form are employed for their photocatalytic properties as well. A prominent example is self-cleaning coating of window glass.[15]

Nanomaterials present many fascinating properties that have made them highly attractive for industry as well as academic research since the last century. Nowadays, efforts continue to be made for development of new nanomaterials to further improve efficiency, reduce cost and search for new properties and functionalities.

I.1.3. Potential risks of nanomaterials

Despite the bright outlooks for the future of nanotechnology, engineered nanomaterials have caused increasing concerns about their safety in recent years. Studies dedicated to assessment of the potential toxicity of nanomaterials emerged in the ’90s and are steadily increasing (**Figure I.1**).

Regarding toxicological impact of nanomaterials, two main exposure contexts can be considered since it may occur during the whole life cycle of nanomaterial-containing products. In the occupational context, workers in production units may be exposed during raw material processing, manufacturing, and final product assembly. In a more general context, the population may be exposed directly during the use of products and indirectly through environmental contamination following the disposal of the products. The respiratory system is the most prominent exposure route for the nanomaterials.[6,16–18] Other exposure routes including skin and gastrointestinal tract are also present for certain industrial sectors, especially during the use of products. Examples such as nanoparticles in cosmetics and food come to mind. Upon penetration to the human body, due to their small size, nanomaterials can translocate from the entry points into the circulatory and lymphatic systems, and ultimately to body tissues and organs.[6,16,18]

The toxicity of nanomaterials seems to be higher than that of their chemically identical bulk counterpart.[17,19–21] The nanometric size makes nanomaterials chemically more reactive, partly due to their large surface to mass ratio. In addition, they may enter the cells and may exert potential damaging actions in sites precluded from larger particles.[22] In fact, it has been demonstrated that nanoscale TiO_2 induces pulmonary inflammation in mouse lung more readily than their bulk counterpart.[19,23,24] Metal and metal oxide nanoparticles such as silver Ag or zinc oxide ZnO frequently induce inflammation and even genotoxicity to cells.[17,21,25,26] Fibrous nanomaterials such as carbon nanotubes induce genotoxicity and have also proven to be carcinogenic for rodents.[17,25,27,28] The toxicity of nanomaterials may also come from the

inherent toxicity of the constituting elements. For example, quantum dots containing cadmium, mercury or lead may release highly toxic Cd^{2+}, Pb^{2+} and Hg^{2+} ions to biological media and causes harmful effects.[6,29] In these cases, a smaller nanoparticle size results in their larger surface contact with the medium, making them more soluble.

In general, the acquired data on toxicity of nanomaterials are not systematic and are scattered. In contrast to molecular compounds which are clearly defined by their atomic constituents, nanomaterials of the same chemical compositions may be described by many other parameters such as their size, shape, crystal structure, surface state, etc. Hence, accurate preparation and characterization of nanomaterials are complex. Moreover, nanomaterials may transform in biological media due to the presence of various biomolecules, e.g. the formation of surface protein corona, aggregation/agglomeration, etc. Considering all of these variations, systematic evaluation of nanomaterial toxicity becomes very challenging. Conclusions have been mainly drawn on a case-by-case basis. Nevertheless, efforts have been made to develop general toxicological paradigms that relate nanomaterial physicochemical characteristics to their toxicity.

One of the most recognized paradigms is the dissolution of nanomaterials in biological media to release toxic heavy metal ions. Prominent examples include Ag, ZnO nanoparticles and Cd-based quantum dots.[6,17,21,25,26] For non-dissolving nanomaterials such as TiO_2, their bandgap and conduction band energy levels have been connected to their potential toxicity through both computational and experimental approaches.[30,31] In fact, the overlap between the conduction band energy of nanomaterials and the redox potential of molecules present in the biological system was the main cause of toxicity.

General mechanisms underlying nanotoxicity have also been intensively sought. Production of reactive oxygen species (ROS) and subsequent generation of oxidative stress were shown to be one of the most important processes.[32,33] In particular, a hierarchical model was developed to explain the role of oxidative stress in cellular response upon exposure to nanomaterials (**Figure I.5**).[33] Low level (Tier 1) of oxidative stress induces protective effects to restore cellular redox homeostasis. If these protective responses fail to provide adequate protection, a further increase in ROS production may result in inflammatory responses (Tier 2), e.g., expression of cytokines and chemokines. At a higher level of oxidative stress (Tier 3), cytotoxic effects involving mitochondria may occur and ultimately lead to cell death.

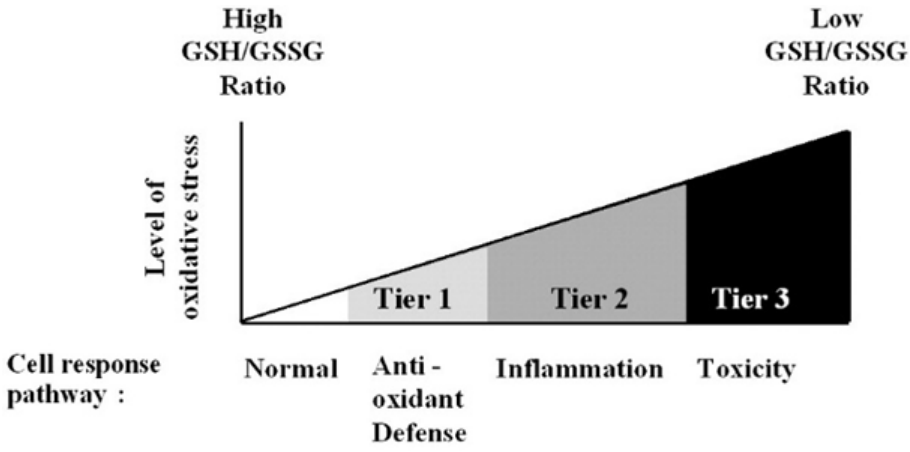

Figure I.5: Hierarchical oxidative stress responses (adapted from ref 33).

I.1.4. Regulation of nanomaterials

Market introduction of chemicals, pharmaceuticals and good components has been regulated since the early 20th century. Nanomaterials are not exceptions. In the European Union, they have been regulated under REACH (Registration, Evaluation, Authorization and Restriction of Chemicals), which are generally applied to chemical substances, since 2006. There was no provision referring explicitly to nanomaterials in the first versions of REACH. However, recent advances in nanotoxicology demonstrated the need and provided important knowledge to complete and clarify the REACH annexes with regard to nanomaterials. In this view, revisions were adopted on December 3, 2018, by the European Commission and the new rules will take effect as of January 1, 2020.

To ensure their safe use and minimize their potential adverse effects on human health and environment, nanomaterials that are manufactured or imported in quantities of more than one tonne per year per company are required to be registered with the European Chemicals Agency (ECHA). The revised REACH annexes stated that manufacturers, importers and downstream users need to systematically characterize the physicochemical properties (particle size, shape, composition, surface properties) of the nanomaterials alongside their hazardous properties. Nanomaterials of similar characteristics and hazard properties also need to be grouped with clear justifications.

Altogether, the revised REACH regulation drives the development of new nanomaterials and nanomaterial-containing products towards an anticipation of the risks, rather than *a posteriori*

determination of them. This leads us to the safer-by-design concept that will be discussed in the next section.

I.2. Safer-by-design nanomaterials

I.2.1. Safer-by-design concept

To address the potential harms of nanomaterials while maintaining their development, safer-by-design concept has been employed recently. First appeared in the literature around 2010, it consists in integrating knowledge of potential adverse effects into the process of designing nanomaterials, and engineering these undesirable effects out of them. For this, both hazard which is the potential of a nanomaterial to cause harmful effect, and exposure which describes a certain dose that human or environment encounter over time, may be considered.[34–36]

Although safer-by-design is relatively new in this field, similar concepts such as green chemistry, quality-by-design, inherent safer design, etc. have been well-established in fields such as chemistry, construction, nuclear technology, aeronautics, water treatment, pharmaceutics, health facilities, etc. since the end of the last century.[34,37–39] In those fields, the concept describes safety measures for the prevention of accidents, illnesses or environmental damage that are applied during the design stage of a facility, process, practice, material or product.

In general, safer-by-design is not new and has been used for years in the industry. Various fields have adopted and developed this concept differently, but the common idea is to design products or processes that possess an intrinsically low risk potential, instead of confining this potential by application of protective systems.[34]

I.2.2. Recent examples of safer-by-design approaches

In the literature, several safer-by-design approaches were reported, mainly to reduce potential hazard of nanomaterials. Most of these studies were based on aforementioned paradigms and focused on modification of either the inorganic core or the surface of the nanomaterials.

I.2.2.1. Modification of inorganic core

One of the first attempts to reduce nanomaterials hazard by a safer-by-design approach was through modification of inorganic core of nanomaterial. In 2011, Xia et al. demonstrated that

the dissolution of zinc oxide ZnO nanoparticles and the Zn^{2+} release, that led to a series of sub-lethal and lethal toxicological responses at the cellular level, could be lessened by iron-doping.[40] ZnO nanoparticles doped with up to 10 at.% of Fe were synthesized by flame spray pyrolysis. They were spherical with size ranging from 8 nm to 20 nm. It was suggested that the presence of iron as dopant reinforced the atom bonding in the particles and decreased the Zn^{2+} dissolution rate, thus the ZnO nanoparticles toxicity. Concrete evidence regarding the bonding reinforcement was however lacking.

Similar to ZnO nanoparticles, copper oxide CuO nanoparticles are known to exhibit toxicity due to the Cu^{2+} dissolution in biological media. Employing the same iron-doping strategy, Naatz et al. showed that the toxicity of CuO nanoparticles could also be reduced.[41] Fe-doped (up to 10 at.%) CuO nanoparticles of size from 10 to 20 nm were synthesized by flame spray pyrolysis. The incorporation of Fe led to distortion of the monoclinic CuO lattice (**Figure I.6**). In fact, CuO has a square planar geometry with each Cu coordinated to four oxygen atoms. By doping with 10% of iron, the Cu-O bond lengths increased from 2.02 to 2.19 Å. The authors hypothesized that this lattice distortion enhanced the material stability. However, further explanation was not provided. Doping above 6 at.% of iron also resulted in the formation of a $CuFe_2O_4$ phase on the surface of the nanoparticles (**Figure I.6**). It was demonstrated that the presence of $CuFe_2O_4$ phase greatly inhibited the dissolution of CuO nanoparticles in various cell culture media. Finally, cytotoxicity of the nanoparticles towards human macrophage-like THP-1 and epithelial BEAS-2B cell lines, as well as their interference with zebrafish hatching were reduced.

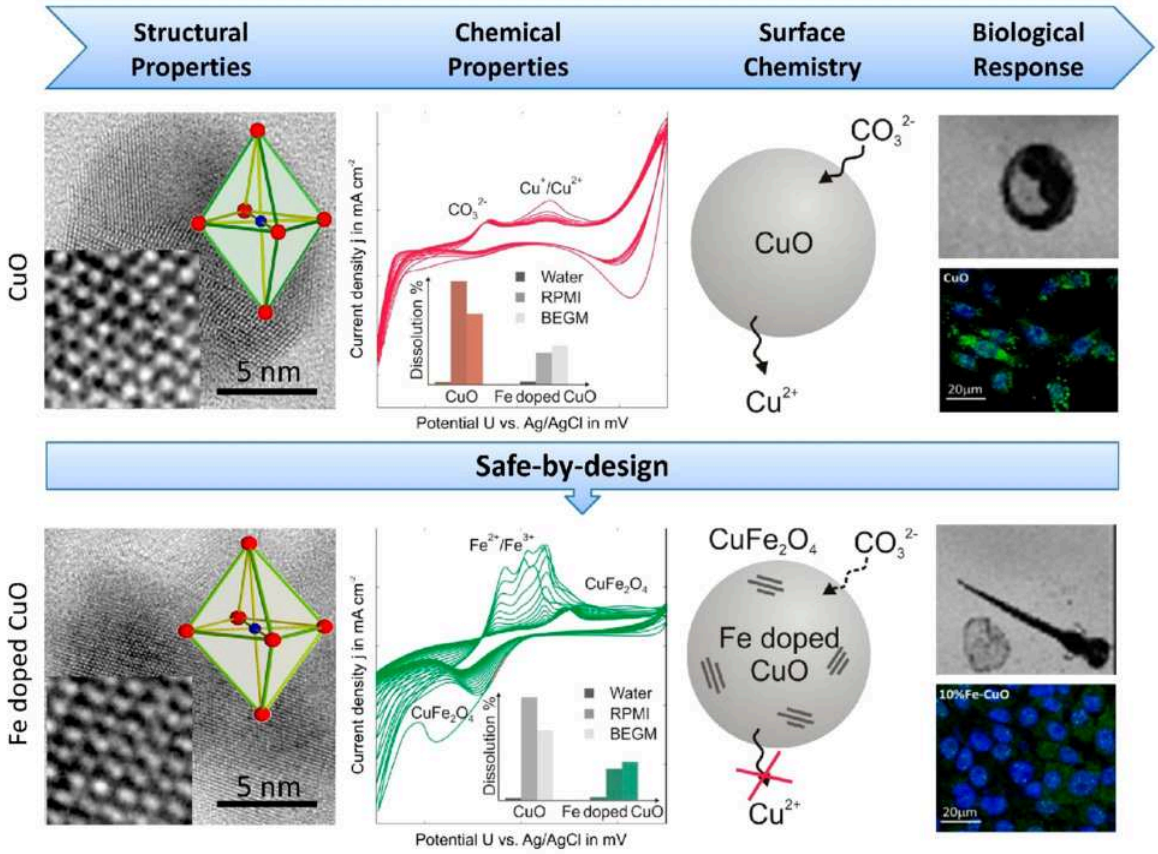

Figure I.6: Structure-activity relationship describing the structural and chemical properties of pristine and iron-doped CuO nanoparticles, and their influence on the biological response assessment (taken from ref 41).

It should be noted that doping is not a universal safer-by-design strategy for all types of nanomaterials. In some cases, doping was shown to enhance toxicity. Indeed, George et al. showed that doping of titanium oxide TiO_2 nanoparticles with Fe^{3+}, using the same flame spray pyrolysis method, reduced their bandgap from 3.3 eV to 2.8 eV (**Figure I.7**a).[42] As a result, their absorption spectrum was shifted towards the visible region, making them more suitable for photocatalysis with visible light. However, the oxidation ability of Fe-doped TiO_2 upon near-visible irradiation (below 3.2 eV) was also found to be superior to that of undoped nanoparticles due to their lower bandgap. Doped TiO_2 nanoparticles induced higher oxidative stress and cell death to macrophages-like RAW 264.7 cells (**Figure I.7**b).

In this example, even though the tailored design strategy led to enhanced functionality of the nanomaterial, it also increased its toxicity. Nevertheless, the acquired knowledge on the potential toxicity of iron-doped TiO_2 nanoparticles remains useful for future development of

novel nanoscale photocatalysts containing TiO_2. Alongside previously discussed examples of safer-by-design ZnO and CuO nanoparticles, this study also highlighted the importance of integrated effort of nanomaterials synthesis and safety assessment in safer-by-design strategies.

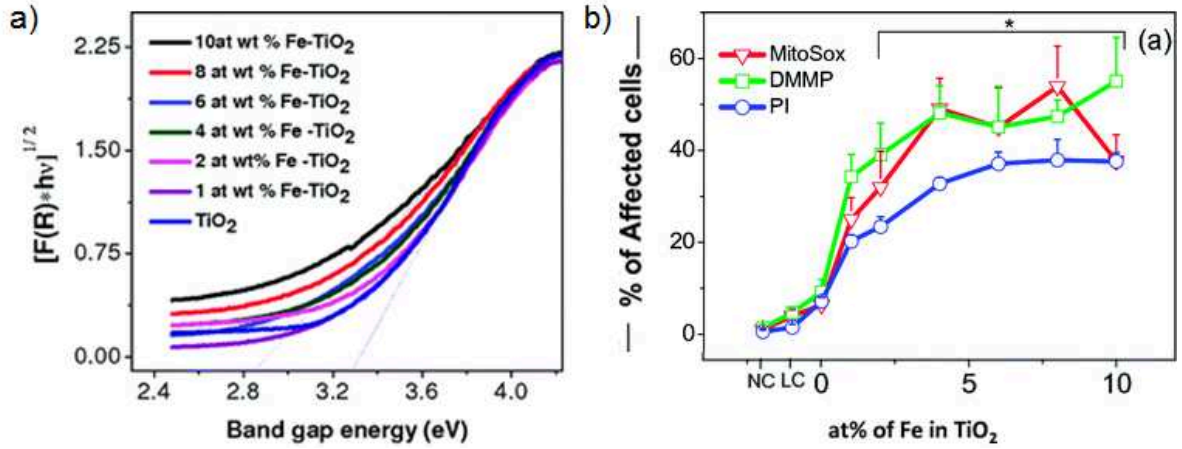

Figure I.7: a) UV-visible absorption of undoped and Fe-doped TiO_2 nanoparticles represented by Kubelka-Munk reflection plot over energy. b) Cytotoxic responses of macrophages-like RAW 264.7 cells exposed to the nanoparticles and near-visible illumination: mitochondrial superoxide generation (MitoSox), decreases in mitochondrial membrane potential (DMMP) and loss of cell viability (PI uptake) (adapted from ref 42).

I.2.2.2. Modification of surface

Beside modification of the inorganic core, surface passivation is another strategy to tackle the dissolution-induced toxicity of nanoparticles such as zinc oxide ZnO. Lewinski et al. recently prepared 5-nm ZnO nanoparticles for photoluminescence properties.[43] They were coated with a densely packed shell of 2-(2-methoxyethoxy)acetate (MEAA) ligands, which acted as polyethylene glycol (PEG) prototype, using an one-pot, self-supporting organometallic procedure (**Figure I.8** Right). This ligand shell passivated the nanoparticles and protected them from subsequent Click Chemistry on their surface, retaining their photoluminescence properties. It was not the case for ZnO nanoparticles prepared by traditional sol-gel methods (**Figure I.8** Left).[44] The authors also showed that the MEAA ligand shell inhibited leaching of Zn^{2+} ions from the inorganic core and generation of free radicals on the surface. It was suggested that the well-passivated ZnO nanoparticles induced negligible oxidative stress and adverse effect on human lung fibroblast MRC-5 and human lung epithelial A549 cells.[43]

Although direct comparison with ZnO nanoparticles prepared by traditional sol-gel route was lacking, this study highlighted the surface passivation strategy to reduce nanomaterial toxicity.

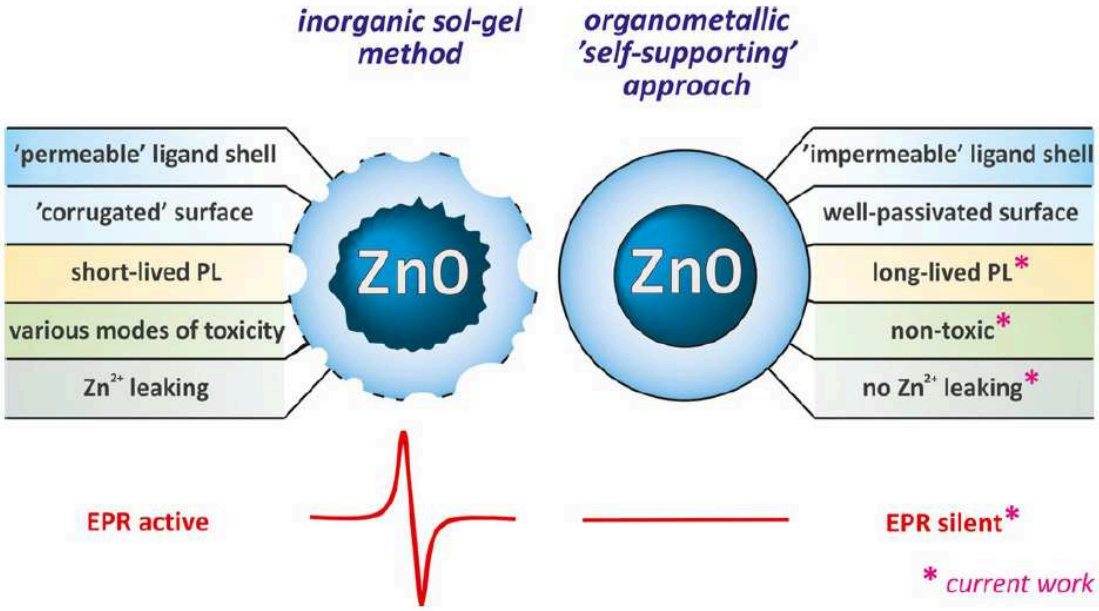

Figure I.8: Comparison of characteristic properties and toxicity of zinc oxide ZnO nanoparticles prepared by traditional sol-gel method and those prepared by novel organometallic self-supporting approach (taken from ref 43).

Another example of a safer-by-design approach relying on surface modification of the nanomaterials is the case of multi-walled carbon nanotubes (MWCNTs). They were shown to cause fibrogenic effects in cells and animal lungs due to their surface hydrophobicity and high aspect ratio.[45] Wang et al. demonstrated that effective surface coating of the nanotubes by biocompatible copolymers such as pluronic F108 (PF108) protected them from damaging the lysosomal membrane and initiating a sequence of cooperative cellular events that play a role in the pathogenesis of pulmonary fibrosis (**Figure I.9**).[46] The author suggested that PF108 coating was a promising approach for designing safer MWCNTs.

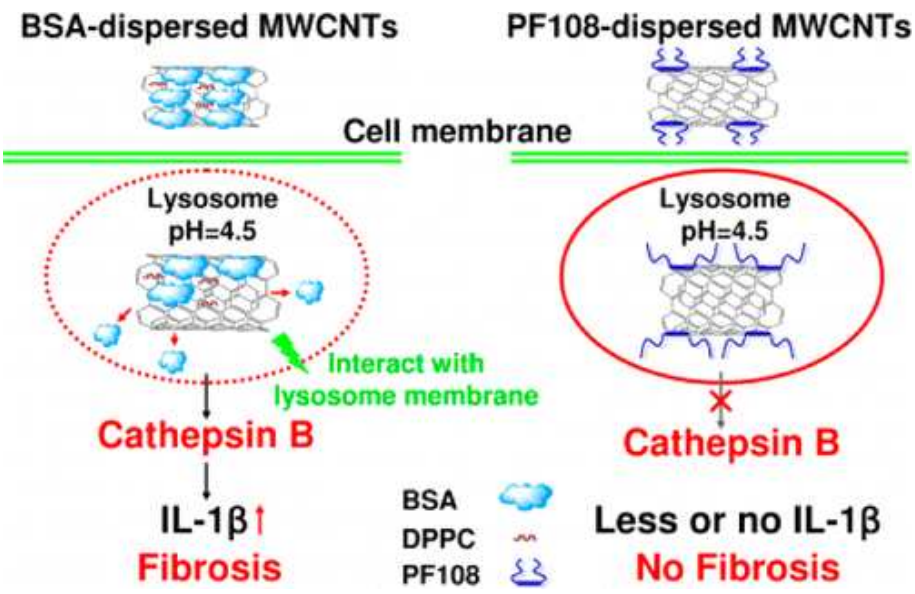

Figure I.9: Comparison between bovine serum albumin (BSA) and pluronic F108 (PF108) as dispersants for multi-walled carbon nanotubes (MWCNTs) in terms of stability, interaction with lysosome membrane as well as pro-fibrogenic effects (taken from ref 46).

I.2.3. A reviewed vision of safer-by-design approach for nanomaterials

In the past ten years, several safer-by-design strategies were successfully implemented to prepare safer metal oxide, carbon-based nanomaterials among others. They mainly consist in modifying either the inorganic core of the nanomaterials or their surface. The examples demonstrated the essence of nanomaterials safer-by-design, i.e. determining the key physicochemical characteristics that contributed to toxicity and how to remediate them by rational design. Nevertheless, it is clear that a gap between materials research and safety assessment still exists. While most of safety studies and safer-by-design approaches have been focused on raw materials, the materials research field has evolved beyond individual nanomaterials to create sophisticated nanostructures and devices. Moreover, these studies mainly targeted well-developed nanomaterials, some of them are already present in commercial products. Current safer-by-design approaches also remain heavy on reducing the potential hazard of nanomaterials. Evaluation of intended functionality after safer-by-design modifications was often neglected. The aforementioned works on safer-by-design copper oxide CuO and zinc oxide ZnO nanoparticles are prominent examples.[40,41] The authors mentioned various functionalities of both nanoparticles such as pigment and UV-absorber. However, these functionalities were not studied after the iron-doping of the nanoparticles to reduce their toxicity.

Taking into account these points, in order to take full advantage of the safer-by-design approach and maximize the potential of nanomaterials, we believe that safer-by-design could be applied in the earliest stage of nanomaterials development, i.e. to novel, emerging nanomaterials that are still in basic research phase. Furthermore, both their toxicity and functionality for a targeted application need to be considered in parallel. For emerging nanomaterials, little is known about their potential risks. Thus, determining the key physicochemical properties that contribute to both the toxicity and the functionality is of particular relevance. Altogether, we propose that the properties, toxicity and functionality of the emerging nanomaterials are to be studied in parallel. These three points can be schematically linked by a feedback loop (**Figure I.10**). By applying this safer-by-design feedback loop over and over, we hope to improve both the functionality and the safety of the nanomaterials by well-designed incremental modifications. As a consequence, it is expected that effects of each modification can also be rationalized.

Lastly, as the nanomaterials evolve through their life cycle, ideally, the safer-by-design concept needs to be applied at every step of nanomaterials development, from basic research to production, uses and end of life to ensure their safety.

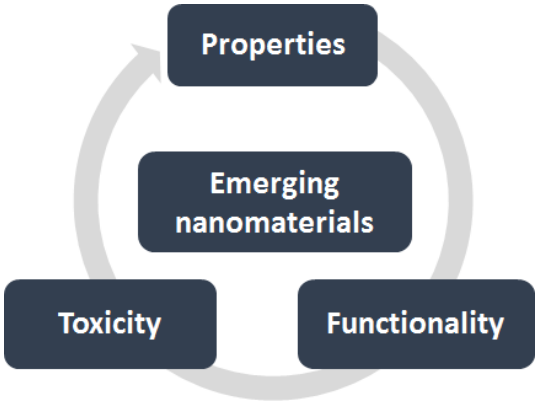

Figure I.10: Schematic representation of safer-by-design approach for emerging nanomaterials.

I.3. Thesis outline

The purpose of this thesis is to apply the reviewed safer-by-design concept discussed above to bimetallic gadolinium-cerium oxysulfide nanoparticles of compositions $Gd_{2(1-x)}Ce_{2x}O_2S$. Despite their promising applications in catalysis and biomedical imaging,[47,48] studies on toxicity of nanoscale oxysulfides remain scarce, making them a perfect model of emerging nanomaterials.

The following chapter (Chapter II) will be dedicated to the synthesis and characterization of bimetallic gadolinium-cerium oxysulfide nanoparticles. The nanoparticles are prepared by colloidal synthesis in organic solvents and their complete description (size, shape, composition, crystalline nature, surface ligand and surface state) is presented. In Chapter III, the safer-by-design approach is discussed in relation with oxysulfide nanoparticles design for photocatalysis. Following attempts to remove surface ligand, the tunable absorption properties of $Gd_{2(1-x)}Ce_{2x}O_2S$ nanoparticles are presented. Their photocatalytic activity under visible light is demonstrated via tests of photodegradation of organic dyes and radical production. Alongside the functionality, the toxicity of oxysulfide nanoparticles is assessed by a combination of *in vitro* (murine macrophage RAW 264.7 cell line) and *in vivo* (C57 black 6 mice) models. Cell viability, oxidative stress and inflammation response are the main discussed endpoints. In order to elucidate the cell-nanoparticle interaction and possible origins of toxicity, cells exposed to nanoparticles are finally mapped by X-ray hyperspectral imaging. Chapter IV shows preliminary results of oxysulfide nanoparticles developed for fluorescent-magnetic biomedical imaging. The photoluminescence of Eu-doped $Gd_{2(1-x)}Ce_{2x}O_2S$ nanoparticles are first discussed. Then, the doped nanoparticles are coated with polyvinylpyrrolidone (PVP) for water-dispersibility. Cytotoxicity of the PVP-coated and Eu-doped is finally characterized. The last part of the manuscript summarizes the results of the three last chapters and proposes perspectives for the safer-by-design approach applied to emerging nanomaterials.

References

(1) Feynman, R. P. There's Plenty of Room at the Bottom. *Eng. Sci.* **1959**, *23* (5), 22–36.

(2) Taniguchi, N. On the Basic Concept of "Nano-Technology." *Proc. Intl. Conf.... Part II, Japan Soc. Precis. Eng.* **1974**, 18–23.

(3) Nanotechnology Products Database https://product.statnano.com/.

(4) Inshakova, E.; Inshakov, O. World Market for Nanomaterials: Structure and Trends. *MATEC Web Conf.* **2017**, *129* (16), 02013.

(5) Alivisatos, A. P. Semiconductor Clusters, Nanocrystals, and Quantum Dots. *Science (80-.).* **1996**, *271* (5251), 933–937.

(6) Reiss, P.; Carrière, M.; Lincheneau, C.; Vaure, L.; Tamang, S. Synthesis of Semiconductor Nanocrystals, Focusing on Nontoxic and Earth-Abundant Materials. *Chem. Rev.* **2016**, *116* (18), 10731–10819.

(7) Wood, V.; Panzer, M.; Sullivan, S. C.; Bulovic, V. Colloidal Quantum Dot Light Emitting Devices. *Colloid. Quantum Dot Optoelectron. Photovoltaics* **2010**, *9780521198* (1), 148–172.

(8) Choi, M. K.; Yang, J.; Hyeon, T.; Kim, D.-H. Flexible Quantum Dot Light-Emitting Diodes for next-Generation Displays. *npj Flex. Electron.* **2018**, *2* (1), 10.

(9) Haruta, M. When Gold Is Not Noble: Catalysis by Nanoparticles. *Chem. Rec.* **2003**, *3* (2), 75–87.

(10) Corma, A.; Garcia, H. Supported Gold Nanoparticles as Catalysts for Organic Reactions. *Chem. Soc. Rev.* **2008**, *37* (9), 2096–2126.

(11) Ciriminna, R.; Falletta, E.; Della Pina, C.; Teles, J. H.; Pagliaro, M. Industrial Applications of Gold Catalysis. *Angew. Chemie - Int. Ed.* **2016**, *55* (46), 14210–14217.

(12) Jia, C. J.; Schüth, F. Colloidal Metal Nanoparticles as a Component of Designed Catalyst. *Phys. Chem. Chem. Phys.* **2011**, *13* (7), 2457–2487.

(13) G., N.; Casals, E.; Ojea, I.; Varon, M.; Puntes, V. The Reactivity of Colloidal Inorganic Nanoparticles. In *The Delivery of Nanoparticles*; InTech, 2012.

(14) Stark, W. J.; Stoessel, P. R.; Wohlleben, W.; Hafner, A. Industrial Applications of Nanoparticles. *Chem. Soc. Rev.* **2015**, *44* (16), 5793–5805.

(15) Troy Darrell, M.; Simon James, H.; Gary Robert, N.; Mathew, W.; Guillermo Benito, G. Antireflective and Self-Cleaning Coatings. WO2013014423A1, July 18, 2012.

(16) Savolainen, K.; Alenius, H.; Norppa, H.; Pylkkänen, L.; Tuomi, T.; Kasper, G. Risk Assessment of Engineered Nanomaterials and Nanotechnologies-A Review. *Toxicology* **2010**, *269* (2–3), 92–104.

(17) Pietroiusti, A.; Stockmann-Juvala, H.; Lucaroni, F.; Savolainen, K. Nanomaterial Exposure, Toxicity, and Impact on Human Health. *Wiley Interdiscip. Rev. Nanomedicine Nanobiotechnology* **2018**, *10* (5), e1513.

(18) Buzea, C.; Pacheco, I. I.; Robbie, K. Nanomaterials and Nanoparticles: Sources and Toxicity. *Biointerphases* **2007**, *2* (4), MR17-R71.

(19) Rossi, E. M.; Pylkkänen, L.; Koivisto, A. J.; Nykäsenoja, H.; Wolff, H.; Savolainen, K.; Alenius, H. Inhalation Exposure to Nanosized and Fine TiO2 Particles Inhibits Features of Allergic Asthma in a Murine Model. *Part. Fibre Toxicol.* **2010**, *7* (1), 35.

(20) Khanna, P.; Ong, C.; Bay, B.; Baeg, G. Nanotoxicity: An Interplay of Oxidative Stress, Inflammation and Cell Death. *Nanomaterials* **2015**, *5* (3), 1163–1180.

(21) Fu, P. P.; Xia, Q.; Hwang, H. M.; Ray, P. C.; Yu, H. Mechanisms of Nanotoxicity: Generation of Reactive Oxygen Species. *J. Food Drug Anal.* **2014**, *22* (1), 64–75.

(22) Pietroiusti, A.; Campagnolo, L.; Fadeel, B. Interactions of Engineered Nanoparticles with Organs Protected by Internal Biological Barriers. *Small* **2013**, *9* (9–10), 1557–1572.

(23) Oberdörster, G.; Ferin, J.; Finkelstein, G.; Wade, P.; Corson, N. Increased Pulmonary Toxicity of Ultrafine Particles? II. Lung Lavage Studies. *J. Aerosol Sci.* **1990**, *21* (3), 384–387.

(24) Ferin, J.; Oberdörster, G.; Penney, D. P.; Soderholm, S. C.; Gelein, R.; Piper, H. C. Increased Pulmonary Toxicity of Ultrafine Particles? I. Particle Clearance, Translocation, Morphology. *J. Aerosol Sci.* **1990**, *21* (3), 381–384.

(25) Lewinski, N.; Colvin, V.; Drezek, R. Cytotoxicity of Nanopartides. *Small* **2008**, *4* (1), 26–49.

(26) Xia, T.; Kovochich, M.; Liong, M.; Mädler, L.; Gilbert, B.; Shi, H.; Yeh, J. I.; Zink, J. I.; Nel, A. E. Comparison of the Mechanism of Toxicity of Zinc Oxide and Cerium Oxide Nanoparticles Based on Dissolution and Oxidative Stress Properties. *ACS*

Nano **2008**, *2* (10), 2121–2134.

(27) Catalán, J.; Siivola, K. M.; Nymark, P.; Lindberg, H.; Suhonen, S.; Järventaus, H.; Koivisto, A. J.; Moreno, C.; Vanhala, E.; Wolff, H.; et al. In Vitro and in Vivo Genotoxic Effects of Straight versus Tangled Multi-Walled Carbon Nanotubes. *Nanotoxicology* **2016**, *10* (6), 794–806.

(28) Kinaret, P.; Ilves, M.; Fortino, V.; Rydman, E.; Karisola, P.; Lähde, A.; Koivisto, J.; Jokiniemi, J.; Wolff, H.; Savolainen, K.; et al. Inhalation and Oropharyngeal Aspiration Exposure to Rod-Like Carbon Nanotubes Induce Similar Airway Inflammation and Biological Responses in Mouse Lungs. *ACS Nano* **2017**, acsnano.6b05652.

(29) Hardman, R. A Toxicologic Review of Quantum Dots: Toxicity Depends on Physicochemical and Environmental Factors. *Environ. Health Perspect.* **2006**, *114* (2), 165–172.

(30) Burello, E.; Worth, A. P. A Theoretical Framework for Predicting the Oxidative Stress Potential of Oxide Nanoparticles. *Nanotoxicology* **2011**, *5* (2), 228–235.

(31) Zhang, H.; Ji, Z.; Xia, T.; Meng, H.; Low-Kam, C.; Liu, R.; Pokhrel, S.; Lin, S.; Wang, X.; Liao, Y. P.; et al. Use of Metal Oxide Nanoparticle Band Gap to Develop a Predictive Paradigm for Oxidative Stress and Acute Pulmonary Inflammation. *ACS Nano* **2012**, *6* (5), 4349–4368.

(32) Fu, P. P.; Xia, Q.; Hwang, H. M.; Ray, P. C.; Yu, H. Mechanisms of Nanotoxicity: Generation of Reactive Oxygen Species. *J. Food Drug Anal.* **2014**, *22* (1), 64–75.

(33) Li, N.; Xia, T.; Nel, A. E. The Role of Oxidative Stress in Ambient Particulate Matter-Induced Lung Diseases and Its Implications in the Toxicity of Engineered Nanoparticles. *Free Radic. Biol. Med.* **2008**, *44* (9), 1689–1699.

(34) Kraegeloh, A.; Suarez-Merino, B.; Sluijters, T.; Micheletti, C. Implementation of Safe-by-Design for Nanomaterial Development and Safe Innovation: Why We Need a Comprehensive Approach. *Nanomaterials* **2018**, *8* (4), 239.

(35) Schwarz-Plaschg, C.; Kallhoff, A.; Eisenberger, I. Making Nanomaterials Safer by Design? *Nanoethics* **2017**, *11* (3), 277–281.

(36) Lin, S.; Yu, T.; Yu, Z.; Hu, X.; Yin, D. Nanomaterials Safer-by-Design: An Environmental Safety Perspective. *Adv. Mater.* **2018**, *30* (17), 1705691.

(37) Yu, L. X. Pharmaceutical Quality by Design: Product and Process Development, Understanding, and Control. *Pharm. Res.* **2008**, *25* (4), 781–791.

(38) Hale, A.; Kirwan, B.; Kjellén, U. Safe by Design: Where Are We Now? *Saf. Sci.* **2007**, *45* (1–2), 305–327.

(39) Kletz, T. A. Inherently Safer Design: The Growth of an Idea. *Process Saf. Prog.* **1996**, *15* (1), 5–8.

(40) Xia, T.; Zhao, Y.; Sager, T.; George, S.; Pokhrel, S.; Li, N.; Schoenfeld, D.; Meng, H.; Lin, S.; Wang, X.; et al. Decreased Dissolution of ZnO by Iron Doping Yields Nanoparticles with Reduced Toxicity in the Rodent Lung and Zebrafish Embryos. *ACS Nano* **2011**, *5* (2), 1223–1235.

(41) Naatz, H.; Lin, S.; Li, R.; Jiang, W.; Ji, Z.; Chang, C. H.; Köser, J.; Thöming, J.; Xia, T.; Nel, A. E.; et al. Safe-by-Design CuO Nanoparticles via Fe-Doping, Cu–O Bond Length Variation, and Biological Assessment in Cells and Zebrafish Embryos. *ACS Nano* **2017**, *11* (1), 501–515.

(42) George, S.; Pokhrel, S.; Ji, Z.; Henderson, B. L.; Xia, T.; Li, L.; Zink, J. I.; Nel, A. E.; Mädler, L. Role of Fe Doping in Tuning the Band Gap of TiO 2 for the Photo-Oxidation-Induced Cytotoxicity Paradigm. *J. Am. Chem. Soc.* **2011**, *133* (29), 11270–11278.

(43) Lewinski, J.; Wolska-Pietkiewicz, M.; Tokarska, K.; Grala, A.; Wojewódzka, A.; Chwojnowska, E.; Grzonka, J.; Cywiński, P.; Kruczała, K.; Sojka, Z.; et al. "Safe-by-Design" Ligand Coated-ZnO Nanocrystals Engineered by an Organometallic Approach: Unique Physicochemical Properties and Low Negative Toxicological Effect toward Lung Cells. *Chem. - A Eur. J.* **2017**.

(44) Grala, A.; Wolska-Pietkiewicz, M.; Danowski, W.; Wróbel, Z.; Grzonka, J.; Lewiński, J. "Clickable" ZnO Nanocrystals: The Superiority of a Novel Organometallic Approach over the Inorganic Sol-Gel Procedure. *Chem. Commun.* **2016**, *52* (46), 7340–7343.

(45) Wang, X.; Xia, T.; Addo Ntim, S.; Ji, Z.; Lin, S.; Meng, H.; Chung, C. H.; George, S.; Zhang, H.; Wang, M.; et al. Dispersal State of Multiwalled Carbon Nanotubes Elicits Profibrogenic Cellular Responses That Correlate with Fibrogenesis Biomarkers and Fibrosis in the Murine Lung. *ACS Nano* **2011**, *5* (12), 9772–9787.

(46) Wang, X.; Xia, T.; Duch, M. C.; Ji, Z.; Zhang, H.; Li, R.; Sun, B.; Lin, S.; Meng, H.; Liao, Y. P.; et al. Pluronic F108 Coating Decreases the Lung Fibrosis Potential of Multiwall Carbon Nanotubes by Reducing Lysosomal Injury. *Nano Lett.* **2012**, *12* (6), 3050–3061.

(47) Larquet, C.; Nguyen, A.-M.; Glais, E.; Paulatto, L.; Sassoye, C.; Selmane, M.; Lecante, P.; Maheu, C.; Geantet, C.; Cardenas, L.; et al. Band Gap Engineering from Cation Balance: The Case of Lanthanide Oxysulfide Nanoparticles. *Chem. Mater.* **2019**, *31* (14), 5014–5023.

(48) Osseni, S. a; Lechevallier, S.; Verelst, M.; Perriat, P.; Dexpert-Ghys, J.; Neumeyer, D.; Garcia, R.; Mayer, F.; Djanashvili, K.; Peters, J. a; et al. Gadolinium Oxysulfide Nanoparticles as Multimodal Imaging Agents for T2-Weighted MR, X-Ray Tomography and Photoluminescence. *Nanoscale* **2014**, *6* (1), 555–564.

Chapter II

Gadolinium and gadolinium-cerium oxysulfide nanoparticles: synthesis and characterization

Table of contents

II.1. Introduction on metal oxysulfide 33
II.1.1. Definition of metal oxysulfide 33
II.1.2. Properties and applications of metal oxysulfides 33
II.1.2.1. Lanthanide oxysulfide 35
II.1.2.2. Transition metal oxysulfide 36
II.1.3. Lanthanide oxysulfide nanomaterials for safer-by-design approach 38
II.2. Synthesis of $Gd_{2(1-x)}Ce_xO_2S$ nanoparticles 40
II.2.1. Colloidal synthesis: a popular approach to explore new nanomaterials 40
II.2.2. Colloidal synthesis of lanthanide oxysulfide nanoparticles 42
II.2.2.1. Synthesis in aqueous medium 42
II.2.2.2. Synthesis in organic medium 43
II.2.3. Synthesis of $Gd_{1-x}Ce_xO_2S$ nanoparticles in organic medium 46
II.2.3.1. Consideration of suitable synthesis method for our study 46
II.2.3.2. Synthesis method 46
II.3. Characterization of $Gd_{2(1-x)}Ce_xO_2S$ nanoplatelets 49
II.3.1. Transition electron microscopy 49
II.3.2. Energy dispersive spectroscopy 50
II.3.3. X-ray absorption 51
II.3.4. X-ray diffraction 52
II.3.5. Infrared spectroscopy 54
II.3.6. Discussion 57
II.3.6.1. Exposed facets and crystallinity 57
II.3.6.2. Tunable cerium content 58
II.3.6.3. Gd_2O_2S-Ce_2O_2S solid solution and oxidation of the nanoparticles in air 59
II.3.6.4. Nanocrystal termination: current hypothesis and perspective 59

II.3.6.5. The presence of sodium 60
II.4. Role of sodium in the synthesis of lanthanide oxysulfide nanoplatelets 61
II.4.1. Influence of sodium stoichiometry 61
II.4.2. Elimination of sodium ions from Gd_2O_2S nanoplatelets 63
II.4.2.1. Washing with organic solvents 64
II.4.2.2. Washing with water 65
II.4.3. Synthesis using other alkali-metal precursors 66
II.4.4. Conclusion and perspective on the role of sodium 71
II.5. Conclusion 74
References 76

II.1. Introduction on metal oxysulfide

II.1.1. Definition of metal oxysulfide

Metal oxysulfides are compounds composing of at least one metal, in addition to oxygen and sulfur both at their reduced state. The generic formula for metal oxysulfides is $M_xO_yS_z$. It should be emphasized that oxygen and sulfur must adopt negative oxidation state (e.g. -I or -II) for the compound to be called "oxysulfide". This is to make a clear distinction with other compounds containing oxygen and sulfur such as metal sulfates $M_x(SO_4)_y$, where the sulfur is oxidized and at positive oxidation state +VI. In the literature, one can find reported oxysulfides under other names such as "thiooxide" and "oxidesulfide".[1–3] However, the term "oxysulfide", proposed by Flahaut et al. in 1958 mostly for Ln_2O_2S (Ln = lanthanide),[4] is now employed in a large majority of the works on compounds containing both reduced oxygen and sulfur.[5]

II.1.2. Properties and applications of metal oxysulfides

Metal oxysulfides are scarcer than their oxide and sulfide counterparts and are mostly artificial. They were often considered undesired byproduct in sulfidation of metal oxides. First discovered in 1827 by Carl Gustaf Mosander in cerium oxysulfide $Ce_xO_xS_z$, other oxysulfides with transition metals, lanthanides and actinides have also been reported in the bulk as well as in the nanoscale.[5] Progression in the field and keystones are shown in **Figure II.1**.

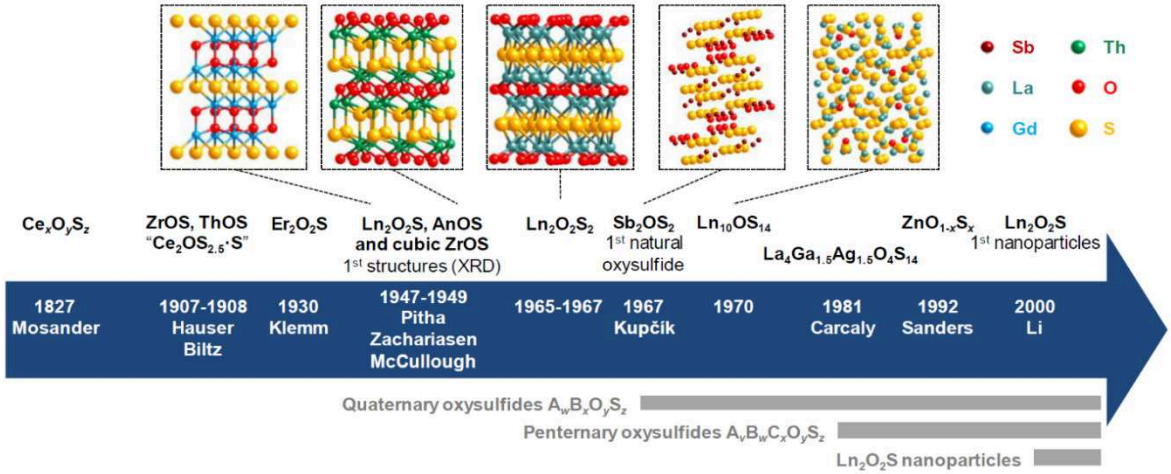

Figure II.1: Key dates and authors of the oxysulfide research with some related structures (taken from ref 5). Ln stands for lanthanide and An for actinide.

One of the reasons for this scarceness is likely because oxysulfides are difficult to obtain. According to their definition, both reduced oxygen and sulfur must be present. However, possessing a large number of oxidation states from -II to +VI, sulfur is easily oxidized in compounds containing both elements. This is why reported structures of metal oxysulfides often show alternate layers of metal-sulfur M-S and metal-oxygen M-O (**Figure II.1**).

The presence of two different types of bonding (M-O and M-S) in metal oxysulfides is an interesting feature. Oxygen and sulfur show a rather large difference in electronegativity: 3.4 and 2.6 respectively by Pauling scale. By consequence, the properties of metal oxide and metal sulfide are quite different. While the M-O bonding in metal oxides has a more ionic character, resulting in them being mostly insulators (e.g. TiO_2, ZnO), the M-S bonding in metal sulfides has a more covalent character, giving rise to their semiconductor properties (e.g. CdS). This also leads to the relatively low solubility in water of metal sulfides compared to metal oxides. If one represents the three main types of chemical bonding by an equilateral triangle scheme, most metal oxysulfides should be close to the center (**Figure II.2**).[6]

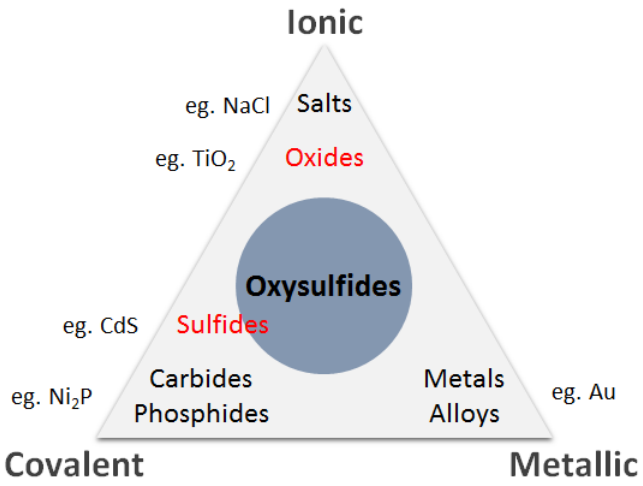

Figure II.2: Van Arkel-Ketelaar triangle representing bonding natures in different families of metal-containing compounds (adapted from ref 6).

Despite being less explored than other families of metal-containing compounds in each corner of the triangle such as the well-known metals and metal oxides or even more exotic compounds such as carbides and phosphides, the position of oxysulfide in this scheme is a privileged one. One could consider studying the effect of the composition (e.g. the S/O ratio) on the properties of the materials or even exploring new properties, especially at the nanoscale.

II.1.2.1. Lanthanide oxysulfide

Among metal oxysulfides, lanthanide oxysulfides with generic formula Ln_2O_2S have been one of the first reported and have been intensely studied up until now. Their applications in the bulk form have been identified since the 1980s as screens and monitors,[7,8] scintillators,[9] lasers,[10,11] etc. For those applications, Y_2O_2S, La_2O_2S and Gd_2O_2S are usually used as matrices and doped with other lanthanides for desired photoluminescence properties.

At the nanoscale, Ln_2O_2S nanoparticles are potential contrast agents for biomedical imaging due to their good chemical and thermal stability. Moreover, similar to their bulk form, they can also host other lanthanides for a variety of photoluminescence properties (**Figure II.3**a).[12,13] In particular, Yb/Er co-doped lanthanide oxysulfide nanoparticles were used for upconversion luminescence imaging[14] while Eu-doped Y_2O_2S nanoparticles were reported for their persistent photoluminescence properties.[15]

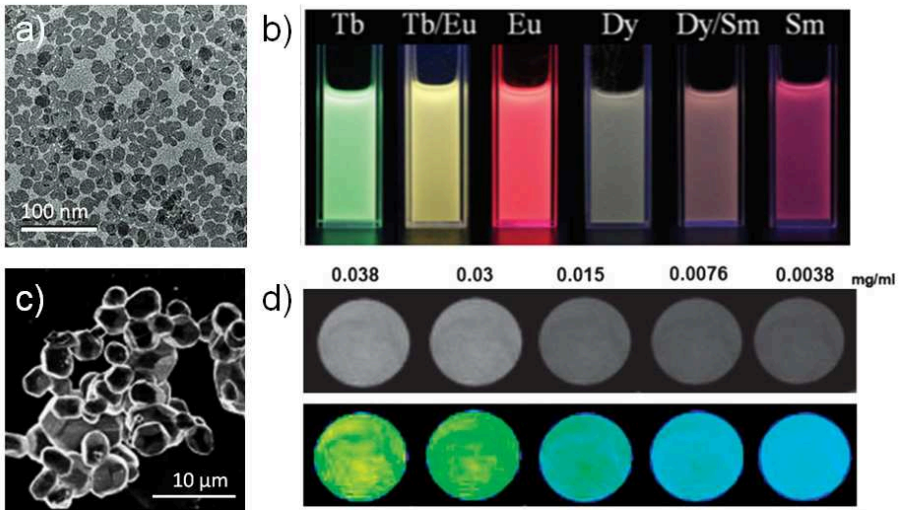

Figure II.3: a) TEM image of lanthanide-doped Gd_2O_2S nanoparticles and b) their photoluminescence under 254 nm excitation (adapted from ref 13). c) SEM image of doped Gd_2O_2S nanoparticles and d) their gray-scaled as well as color-mapped magnetic resonance images at different concentrations (adapted from ref 14).

Lanthanides can also exhibit high magnetic susceptibility, which is of major importance for magnetic imaging techniques such as Magnetic Resonance Imaging (MRI). In fact, Gd_2O_2S nanoparticles have already been reported as potential contrast agents for MRI due to the $4f^7$ electron configuration of Gd^{III} in the structure (**Figure II.3**b).[14,16]

Other than applications in biomedical imaging, catalysis based on redox reactions using Ln_2O_2S has also been explored. Notably, Ce_2O_2S nanoparticles on carbon have been tested for oxygen reduction reaction (ORR)[17] while Eu_2O_2S nanoparticles catalyzed reaction of CO and water to yield CO_2 and H_2.[18]

II.1.2.2. Transition metal oxysulfide

Compared to lanthanide oxysulfides, transition metal oxysulfides are scarcer. Especially ternary metal oxysulfides containing a lone transition metal. Whereas, quaternary oxysulfides containing one transition metal and one lanthanide/rare-earth element are more common.[5]

In the bulk form or as thin films, ternary transition metal oxysulfides have been mostly studied for their electrochemical properties due to the often-large number of oxidation states of the transition metal compared to lanthanides. It is indeed the case for titanium,[19] tungsten[20] or molybdenum oxysulfides.[21,22] These studies focused heavily on the development of new

cathode and anode for lithium-ion batteries. Due to the larger number of phases available, quaternary oxysulfides have also been reported for other applications such as photoconversion,[23] superconductivity[24] and magnetism.[25]

At the nanoscale, very few transition metal-containing oxysulfides were obtained. They were mostly with zinc,[26–28] cobalt[29] and titanium.[30] These nanoparticles were mainly exploited for their high surface-to-volume ratio, as the number of studies on catalysis dominated. Ishikawa et al. showed that $Sm_2Ti_2S_2O_5$ nanoparticles (**Figure II.4**a) exhibited catalytic activity for water oxidation and reduction under visible light ($440\ nm \leq \lambda \leq 650\ nm$).[30] This is particularly interesting because their oxide counterpart $Sm_2Ti_2O_7$ only absorbs UV light ($\lambda \leq 380\ nm$). By partially replacing oxygen by sulfur, the absorption of the materials shifts to the visible region (**Figure II.4**b). A similar absorption change was also found in $ZnO_{1-x}S_x$ nanoparticles (**Figure II.4**c).[26,27] It was shown that the absorption of the material could even be tuned by modifying the S/O ratio (**Figure II.4**d) and these nanoparticles showed catalytic activity in photodegradation of methyl orange.[26] Other than application in photocatalysis, zinc oxysulfide nanoparticles and cobalt oxysulfide nanoparticles are active in hydrogen evolution reaction (HER) as well.[28,29]

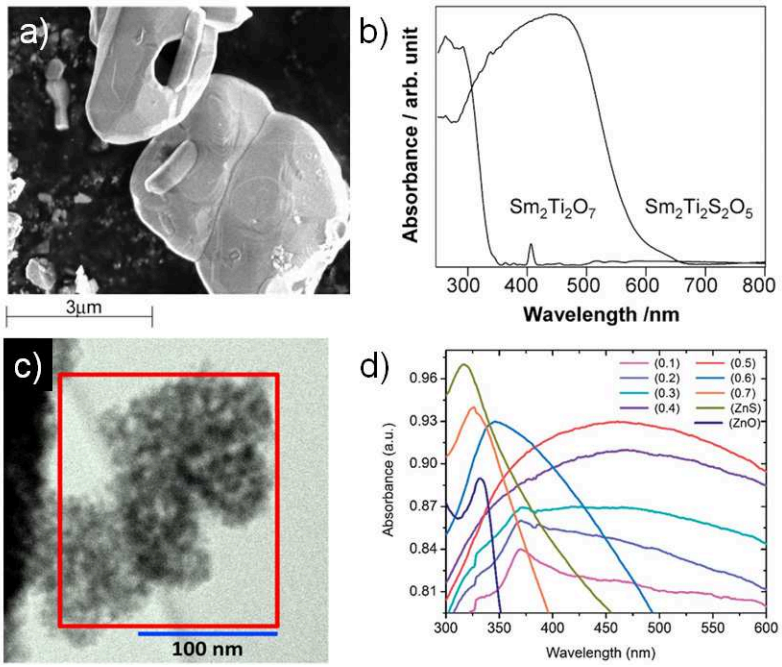

Figure II.4: a) SEM image of $Sm_2Ti_2S_2O_5$ nanoparticles and b) their UV-visible absorption (adapted from ref 30). c) TEM image of $ZnO_{1-x}S_x$ nanoparticles and d) their UV-visible absorption (adapted from ref 26,27).

II.1.3. Lanthanide oxysulfide nanomaterials for safer-by-design approach

As discussed in the first chapter, the essence of the safer-by-design approach is to incrementally modify the material, staying within one family of compound. Two strategies are mainly adopted: modification of the inorganic core and modification of the surface. By changing only one or a few parameters at a time, one can hope to rationalize each modification step. This is of particular importance for fundamental research. Therefore, in order to take full advantage of the safer-by-design approach, it is ideal to work with emerging nanomaterials that are multifunctional and can be easily modified.

In this view, lanthanide oxysulfide Ln_2O_2S nanoparticles seem quite suitable for the safer-by-design approach. In fact, bulk Ln_2O_2S phases have well-known crystalline structure which is advantaging for the rationalization process. The Ln_2O_2S nanoparticles can readily be modified for different properties and applications such as catalysis and biomedical imaging. Moreover, compared to oxide counterparts, the overall bonding in oxysulfide is more covalent. This is expected to result in a lower water solubility of the material, thus potentially a lower toxicity.[31]

As far as multifunctionality goes, gadolinium oxysulfide Gd_2O_2S nanoparticles are promising candidates as they have been used as MRI contrast agent or X-ray absorbing materials. Doped Gd_2O_2S:Ln nanoparticles have been shown to be potential contrast agents for multimodal biomedical imaging.[14,16,32–35]

In our laboratory, we recently succeeded in synthesizing gadolinium-cerium oxysulfide $Gd_{2(1-x)}Ce_xO_2S$ nanoparticles analogous to Gd_2O_2S.[36] The Ce-containing bimetallic nanoparticles are expected to possess even more functions than the monometallic ones due to the distinctive properties of cerium compared to other lanthanides. In contrast to most lanthanides which are trivalent, cerium can be both trivalent Ce^{III} and tetravalent Ce^{IV}. The Ce^{3+}/Ce^{4+} redox couple is responsible for the catalytic and antioxidant properties of cerium(IV) oxide CeO_2 nanoparticles.[37–39] In particular, Gd-doped CeO_2 nanoparticles have been used for therapeutics (antioxidant/MRI) thanks to the antioxidant properties of Ce and the magnetic properties of Gd.[39] Therefore, $Gd_{2(1-x)}Ce_xO_2S$ nanoparticles may be useful for therapeutics as well.

Furthermore, while bulk gadolinium oxysulfide is white and only absorbs UV light, bulk cerium oxysulfide is deep brown and absorbs visible light.[4] We presume that mixed oxysulfide $Gd_{2(1-x)}Ce_xO_2S$ nanoparticles also absorbs in the visible spectrum and the absorption is tunable by the Gd/Ce ratio. It should be noted that tunable absorption in the visible region has already been achieved with $ZnO_{1-x}S_x$ nanoparticles using the S/O ratio (**Figure II.4**d).[26,27] These features would make $Gd_{2(1-x)}Ce_xO_2S$ nanoparticles promising materials for photocatalysis using visible light.

In summary, $Gd_{2(1-x)}Ce_xO_2S$ nanoparticles are versatile nanomaterials due to the potential absorption properties, magnetic properties and catalytic properties (**Figure II.5**). We also assume that they can be doped with other lanthanides for photoluminescent properties similar to analogous Ln_2O_2S. Moreover, the more covalent bonding in oxysulfides may result in lower solubility in aqueous media, and thus lower toxicity compared to metal oxides. Altogether, $Gd_{2(1-x)}Ce_xO_2S$ nanoparticles appear particularly relevant for safer-by-design approach.

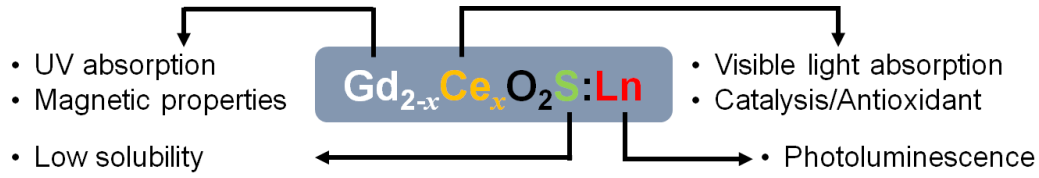

Figure II.5: Design of versatile lanthanide oxysulfide nanomaterials. Ln stands for lanthanide.

II.2. Synthesis of $Gd_{2(1-x)}Ce_xO_2S$ nanoparticles

II.2.1. Colloidal synthesis: a popular approach to explore new nanomaterials

In general, fabrication of nanomaterials and nanoparticles are divided into two major categories: top-down and bottom-up, which refer to how the process of creating these nano-objects is carried out.[40] A top-down approach consists in using physical tools to create nano-objects with desired characteristics, starting from larger dimensions then reduce them (e.g. lithography, mechanical grinding). On the other hand, a bottom-up approach corresponds to using atomic or molecular building blocks to assemble more complex structures at the nanoscale (e.g. sol-gel process). In general, top-down methods such as lithography are highly precise and reliable. However, they are expensive and difficult to scale up. On the other hand, the bottom-up methods are mostly low-cost and easier to scale up. They are also more versatile in terms of product scope as inorganic, organic and hybrid nanomaterials can be fabricated. The main shortcoming is their low precision. The obtained nanomaterials are usually less uniform in size, shape, composition and can present structural defects.

Among bottom-up methods, colloidal synthesis has been employed to explore new nanomaterials due to being relatively simple, low-cost and due to the large catalogue of chemicals available as initial reagents (precursors). In fact, nanoscale lanthanide oxysulfides have been obtained for the first time in 2000 using colloidal synthesis and this method has continued to be used for this type of nanomaterials up until now.[5] Colloidal synthesis consists in heating dissolved precursors in solution to form colloidal suspension of nanoparticles. During the heating, the precursors react to form monomers which are the minimal building units that comprise the final solid (**Figure II.6**). Homogeneous nucleation then occurs and a solid phase spontaneously forms in the solution. These nuclei present stable nucleating surface for other monomers thus heterogeneous nucleation takes place next. This leads to growth of nuclei into nanoparticles.[41–45]

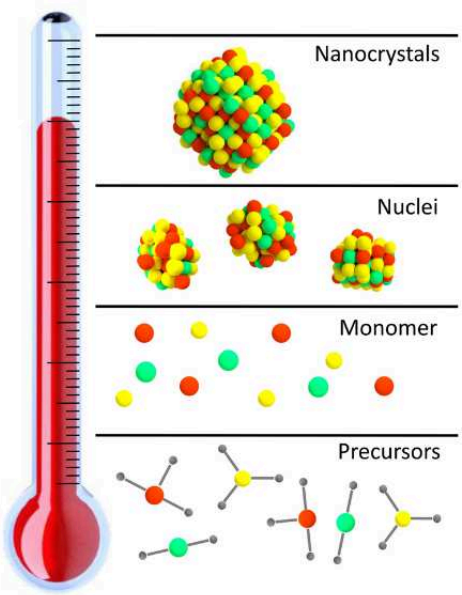

Figure II.6: Colloidal synthesis of nanoparticles by heating dissolved precursors in solution (adapted from ref 41).

Nucleation-growth theory was first introduced by La Mer in the '50s,[46] adapted from a theory developed by Becker and Döring in the 30s.[47] It is a widely-recognized model which is readily used for interpreting experiments.[41–45] The basic idea behind this theory is that a thermodynamic system strives to minimize its energy. The Gibbs free energy of a spherical cluster can be given as:

$$\Delta G = -\frac{4}{3}\pi r^3 |\Delta G_v| + 4\pi r^2 \gamma$$

with the radius *r*, the bulk free energy per unit volume $|\Delta G_v|$ and the surface energy per unit area γ. While the negative term shows that it is favorable to make bonds, the positive term describes how unfavorable it is to create a large surface. As the solution reaches supersaturation in monomers, nucleation occurs and nuclei are formed. However, small nuclei possess extremely large surface which results in important surface energy and makes the system highly unstable. Therefore, they continue to grow in size and the negative term of the equation eventually dominates over the positive one, lowering the overall energy.

In order to lower the energy of the system, nanoparticles also tend to aggregate. Surface ligands are mainly used to avoid this. These molecules have high affinity with the solvent. They bind and cover the surface of the nanoparticles, rendering the latter dispersible. Surface

ligands can play other important roles such as regulation of solubility of precursors and availability of monomers during nucleation and growth of nanoparticles, control the growth process for tunable nanoparticle size and shape by selective binding, or contribution of new functionalities to the nanoparticles.[48]

II.2.2. Colloidal synthesis of lanthanide oxysulfide nanoparticles

Since the first synthesis of lanthanide oxysulfide nanoparticles using lanthanide oxides and elemental sulfur as precursors and ethylenediamine as solvent were reported in 2000 by Li et al.,[2] several other groups have also proposed contributions to the field. Two main categories of colloidal synthesis of lanthanide oxysulfide nanoparticles can be identified depending on the type of solvent used: synthesis in aqueous medium and synthesis in organic medium.

II.2.2.1. Synthesis in aqueous medium

Water has various advantages as solvent. It is abundant and green. The knowledge on formation of inorganic nanoparticles in this medium is substantial.[49] Moreover, synthesized nanoparticles often possess hydrophilic surface or stabilized with hydrophilic ligands. As a result, they can easily be dispersed in water, making them suitable for biomedical applications or catalysis in aqueous media.

One of the main limiting factors of water as a solvent for nanoparticle synthesis is its relatively low boiling point. Thus, to obtain crystalline nanoparticles in aqueous medium is quite challenging and post-synthetic annealing is required. Water also presents an excess amount of dissolved oxygen which is undesirable for oxysulfide synthesis.

Synthesis of lanthanide oxysulfide nanoparticles in water mainly involved metal precursors such as oxides, nitrates and chlorides. Whereas thioacetamide, thiourea and ammonium sulfide or sodium sulfide were employed as sulfur source for the most part. Most reported syntheses resulted first in intermediary phases such as hydroxides $Ln(OH)_3$, hydroxycarbonates $Ln(OH)(CO_3)$ or oxides Ln_2O_3. Only after subsequent sulfidation of the isolated powder at higher temperature from 600 °C to 1200 °C, crystalline Ln_2O_2S nanoparticles were obtained. Nevertheless, the high temperature treatment often resulted in aggregated and sintered nanoparticles.[5]

A demonstrative example is the synthesis of Yb, Er co-doped Y_2O_2S nanoparticles reported by Tian et al. in 2015.[50] Intermediary $Ln(OH)_x(CO_3)_y$ were first obtained and then annealed with or without sulfur vapor at 900 °C to form crystalline nanoparticles of oxysulfide Y_2O_2S:Yb,Er or oxide Y_2O_3:Yb,Er respectively (**Figure II.7**). The obtained Y_2O_2S:Yb,Er nanoparticles are quite aggregated. Even though, individual nanoparticles of size ca. 30 nm can still be distinguished.

In general, the lanthanide oxysulfide nanoparticles prepared by synthesis in aqueous medium and subsequent annealing exhibited size from ca. 30 nm to 1 µm and a wide range of shapes. The nanoparticles were mostly aggregated and irregular in size and shape. These syntheses also mainly focused on doped Gd_2O_2S and Y_2O_2S for uses as phosphors or contrast agents for biomedical imaging.[5]

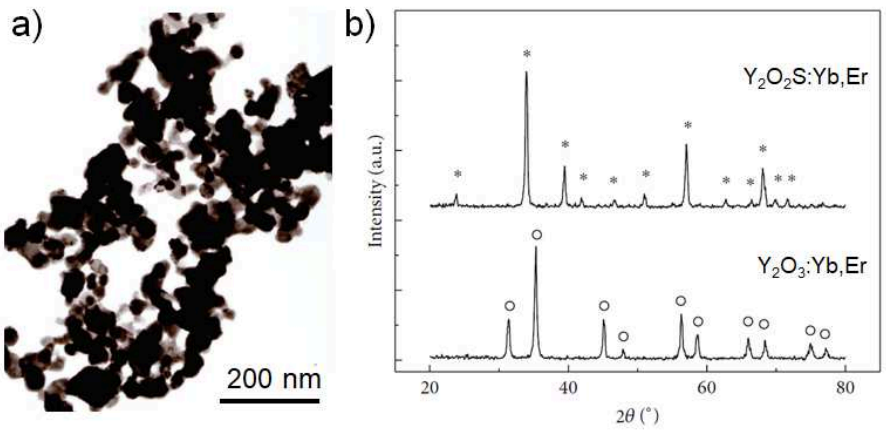

Figure II.7: Synthesis of Y_2O_2S:Yb,Er nanoparticles reported by Tian et al. in 2015. a) TEM images of crystalline Y_2O_2S:Yb,Er nanoparticles. b) XRD patterns of resulted Y_2O_3:Yb,Er nanoparticles after annealing without sulfur at 900 °C and resulted Y_2O_2S:Yb,Er nanoparticles after annealing with sulfur vapor at 900 °C (adapted from ref 50).

II.2.2.2. Synthesis in organic medium

The temperature of reaction medium can reach up to 300 °C with organic solvents, making it easier to obtain crystalline metal oxysulfide nanoparticles in one step. Control of nanoparticles size and shape is also readily achievable thanks to the large catalogue of surface ligands to select from. Moreover, synthesis under inert atmosphere is available using Schlenk techniques. This allows better control of available oxygen in the reaction medium during the synthesis.

Synthesis in organic solvents also enables the use of elemental sulfur in amines as a soluble and stoichiometric sulfur source from the beginning of the reaction. Together with operating under inert atmosphere, this brings forth the possibility to finely control the oxygen and sulfur stoichiometries in the final lanthanide oxysulfide nanoparticles. The S/O ratio is indeed of importance as it can strongly affect the properties of the nanomaterial (see II.1.2.2).

To obtain lanthanide oxysulfide nanoparticles in organic medium, lanthanide complexes such as acetate ($Ln(OAc)_3$) or acetylacetonate ($Ln(acac)_3$) were mainly employed. They were heated in the presence of dissolved elemental sulfur at 280 – 315 °C to form crystalline nanoparticles in one step.[5] Such synthesis was first reported by Ding et al. in 2011 (**Figure II.8**).[12] The authors were able to obtain monodisperse Na-doped La_2O_2S hexagonal nanoplatelets of ca. 2 nm thick and ca. 22 nm wide (**Figure II.8**a-d). The nanoparticles contained sulfur and crystallized in La_2O_2S phase (**Figure II.8**e,f). Oxysulfide nanoplatelets of other lanthanides such as Pr, Nd, Sm, Eu, Gd, Tb were also synthesized using the same method.

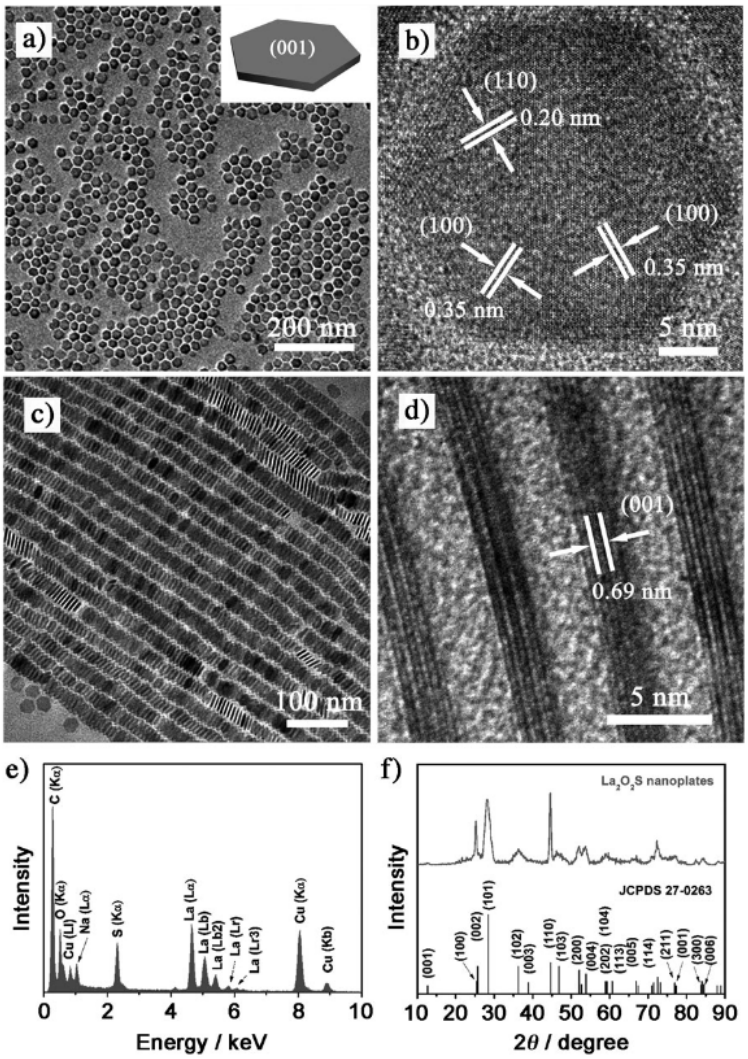

Figure II.8: Synthesis of crystalline La_2O_2S nanoplatelets reported by Ding et al. in 2011. a) TEM and b) HRTEM (taken with [001] incidence) images of Na-doped La_2O_2S nanoplatelets. c) TEM and d) HRTEM (taken with [100] incidence) images of the nanoplatelet superlattice. e) EDS spectrum of the nanoplatelets. f) XRD pattern of the nanoplatelets (taken from ref 12).

Since this synthesis of Ln_2O_2S nanoplatelets reported by Ding et al. in 2011, derivatives syntheses with varied reaction conditions have been carried out by several groups including ours, in order to optimize and rationalize the reaction. In general, this synthetic route stands out because of its versatility. Many Ln_2O_2S (Y, La, Pr, Nd, Sm, Eu, Gd, Tb, Er, Yb) nanoparticles have been indeed obtained this way in the shape of regular nanoplatelets. The nanoplatelets were also monodisperse and of very small size (ca. 1 – 2 nm thick and 1 – 40 nm wide).[5]

Like in aqueous medium, lanthanide oxysulfide synthesized in organic medium could be doped for photoluminescent properties as well. Their applications were again mainly phosphors and contrast agents for biomedical imaging. Nevertheless, synthesis in organic medium resulted in hydrophobic nanoparticles because of the organic surface ligands. Thus, they require post-synthetic surface modification such as ligand removal or ligand exchange in order to be suitable for applications in aqueous medium.

II.2.3. Synthesis of $Gd_{1-x}Ce_xO_2S$ nanoparticles in organic medium

II.2.3.1. Consideration of suitable synthesis method for our study

Either in aqueous medium or in organic medium, each synthetic route towards lanthanide oxysulfide nanoparticles presents its own advantages and limits. Both methods are able to produce Ln_2O_2S nanoparticles. Although, synthesis in organic medium slightly edged over synthesis in aqueous medium when it comes to the number of Ln_2O_2S phases obtained. Ln_2O_2S nanoparticles have been synthesized from almost all lanthanides in organic medium. Yet, cerium is an exception. Prior to our work, Ce_2O_2S nanoparticles had rarely been synthesized. The only example presented was the synthesis of Ce_2O_2S nanoparticles supported on carbon.[17]

In fact, the cerium in Ce_2O_2S phase shows oxidation state III. Hence, one must be extremely careful of the quantity of oxygen available in the reaction medium to avoid oxidation of Ce^{III} to Ce^{IV}. In view of this, synthesis in organic medium seems a more suitable method to acquire cerium-containing oxysulfide nanoparticles. The gadolinium-cerium oxysulfide $Gd_{2(1-x)}Ce_xO_2S$ nanoparticles that we are targeting, are expected to be also sensitive to oxidation.

II.2.3.2. Synthesis method

In order to synthesize $Gd_{2(1-x)}Ce_xO_2S$ nanoparticles, we adapted the synthesis designed for Ln_2O_2S (Y, La, Pr, Nd, Sm, Eu, Gd, Tb, Er, Yb) nanoplatelets reported by Ding et al. in 2011. The results have been published in Larquet et al., *Inorg. Chem.* (2017) and in the Ph.D. thesis of Clément Larquet, defended in September 2018.[5,36] The detailed protocol is described in the experimental section.

This synthesis required gadolinium and cerium acetylacetonates hydrate ($Gd(acac)_3{\cdot}xH_2O$ and $Ce(acac)_3{\cdot}xH_2O$) as metal precursors. The total quantity of metal precursors corresponded to 1 equivalent. The ratio between the two metal precursors could be adjusted for the desired Ce/Gd ratio in the final product. Elemental sulfur (S_8) was employed as sulfur source. S_8 was used with 0.5 equivalents of S vs. the metal cations, corresponding to the final stoichiometry Ln_2O_2S. These three main precursors were added to a mixture of organic compounds containing oleic acid (OA), oleylamine (OAm) and 1-octadecene (ODE) in large excess which played the roles of surface ligands and solvents. Oleylamine also helped to dissolve and activate elemental sulfur.[51] Oxygen could be provided by the acetylacetonate ligands and/or the oleic acid.

Similar to other syntheses in the literature,[12,13,52] an alkali metal source was necessary for the formation of lanthanide oxysulfide nanoplatelets. Its role will be discussed in detail later on. For this synthesis of $Gd_{2(1-x)}Ce_xO_2S$ nanoparticles, 1 equivalent of sodium oleate was used.

The turbid mixture of the seven reagents was first heated to 120 °C under a flow of N_2, resulting in a clear solution. At this temperature, the ketone moiety of acetylacetonate reacted with oleylamine to form water. To remove this excess of water as well as other low-boiling-point impurities, the mixture was degassed *in vacuo* at this temperature for 20 min.

The clear solution was subsequently heated to 310 °C under a flow of N_2. The reaction medium started to become turbid at 280 °C, suggesting the formation of nanoparticles. The turbidity was maximum after 305 °C. The temperature was kept at 310 °C for 30 min. The overall reaction scheme is presented in **Figure II.9** below.

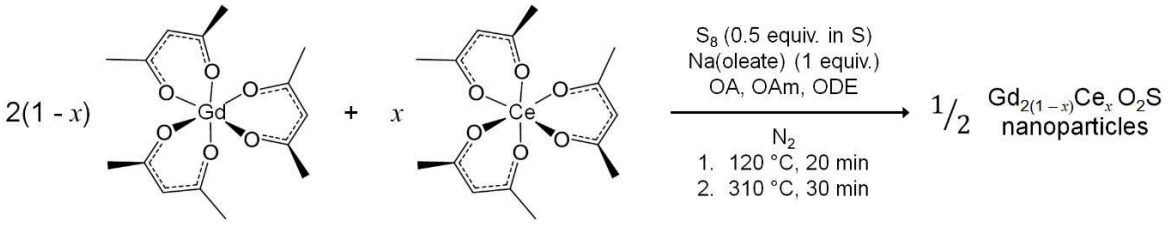

Figure II.9: Reaction scheme of synthesis of $Gd_{2(1-x)}Ce_xO_2S$ nanoparticles.

In order to collect the nanoparticles as a powder, ethanol was added and the reaction medium was centrifuged to yield a sticky solid. This solid was then further washed with a mixture of *n*-hexane and ethanol to remove excess reagents and organic matter. The post-synthetic

treatment was done under air. From 50 mg to 100 mg of product were collected, depending on experiment. These amounts correspond to reaction yields of 50-100% if we assume that the products are the desired $Gd_{2(1-x)}Ce_xO_2S$ nanoparticles and we neglect the weight of remaining organic ligands. Moreover, the yield of the reaction decreased as the cerium fraction increased, in agreement with a previous observation made in the group.[36]

II.3. Characterization of $Gd_{2(1-x)}Ce_xO_2S$ nanoplatelets

In order to study the nanoparticle properties, functionality and toxicity, a complete description of the product is required. Six samples of $Gd_{2(1-x)}Ce_xO_2S$ nanoparticles, with cerium fractions x = 0, 0.01, 0.05, 0.10, 0.20, 0.50, were synthesized. The products were subjected to a number of characterizations to determine their size, shape, chemical composition, crystalline nature and surface state. A description of the synthesized nanoparticles is proposed at the end of this section. The results presented in this section were acquired in collaboration with Clément Larquet as part of his Ph.D. thesis.

II.3.1. Transition electron microscopy

The size and the shape of the Gd_2O_2S (x = 0) and $GdCeO_2S$ (x = 0.5) nanoparticles were characterized by transmission electron microscopy (TEM) (**Figure II.10**). The nanoparticles feature anisotropic 2D morphology and are highly stacked. As a result, precise measurement of the dimension of their basal facets remains desirable. For both Gd_2O_2S and $GdCeO_2S$ nanoparticles, it is roughly estimated to be 20 ± 5 nm. On the other hand, the thickness can be determined thanks to stacked nanoplatelets that expose their side facets. Both nanoplatelets are 2 ± 1 nm thick. The results indicate no significant difference in size and shape between monometallic gadolinium oxysulfide nanoparticles and bimetallic gadolinium-cerium oxysulfide nanoparticles.

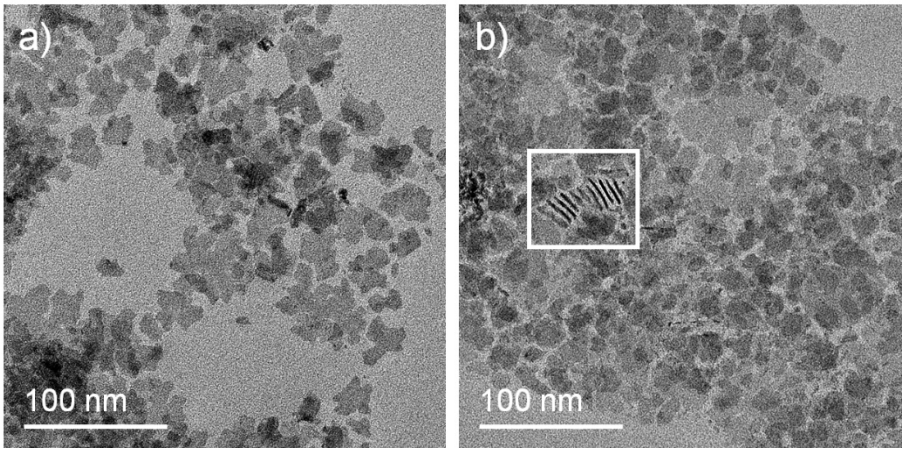

Figure II.10: TEM images of a) Gd_2O_2S and b) $GdCeO_2S$ nanoparticles. The white square indicates the stacked nanoplatelets that expose their side facets.

II.3.2. Energy dispersive spectroscopy

Energy dispersive spectroscopy (EDS) coupled to scanning electron microscopy (SEM) was employed to determine the chemical composition of synthesized $Gd_{2(1-x)}Ce_xO_2S$ nanoplatelets. A typical EDS spectrum is shown in **Figure II.11**.

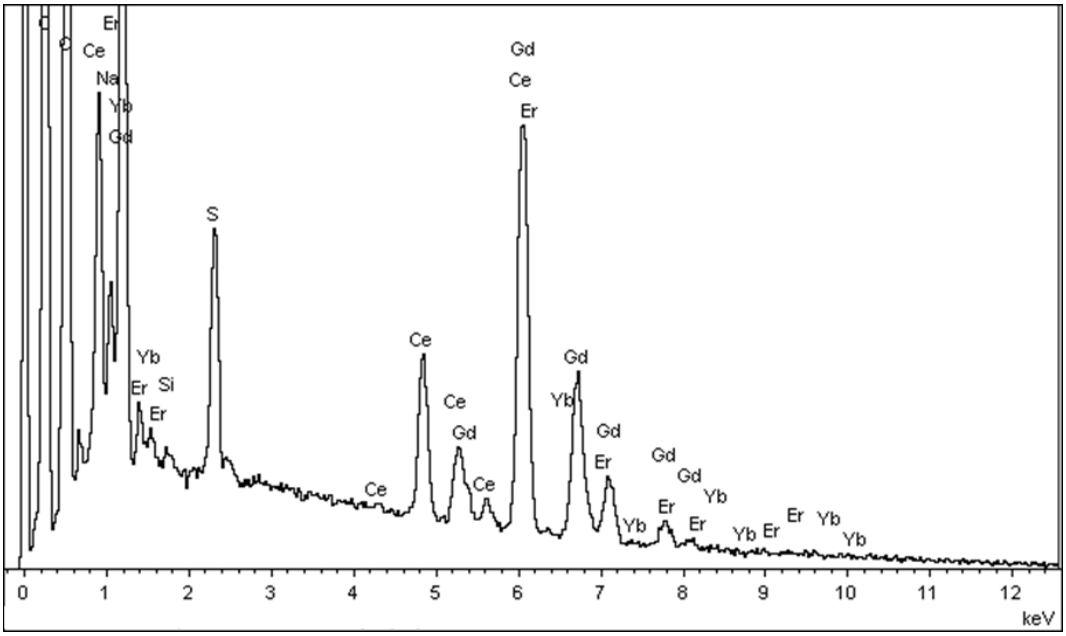

Figure II.11: EDS spectrum of $Gd_{1.6}Ce_{0.4}O_2S$ (x = 0.2) nanoparticles.

Gadolinium and cerium are detected, as expected. Surprisingly, rare-earth impurities are also found. In all of our samples, they are automatically attributed to Er and Yb by the spectrum-analysis software. However, their quantities are negligible (< 1 at.%). Their presence remains questionable since no such impurity was declared in the lanthanide precursors. Alongside the lanthanides, sulfur, oxygen and sodium are also detected. Although, quantification of oxygen is unreliable due to its low atomic number.

Average chemical compositions of the $Gd_{2(1-x)}Ce_xO_2S$ nanoparticles were determined from EDS spectra of at least three different areas of the samples. Cerium contents were calculated as percentages of the total quantity of gadolinium and cerium. Sulfur and sodium contents were presented as equivalents vs. the lanthanides (**Figure II.12**b).

The measured cerium contents in the final products seem to match with the cerium fraction x introduced in the reaction mixture (**Figure II.12**a). The sulfur content varies from 0.18 to 0.23 equivalents vs. lanthanides, much lower than the expected value (0.50) (**Figure II.12**b).

If one takes into account the experimental error of EDS (ca. 5%), this variation between the samples can be considered insignificant. As for the sodium content, the values fluctuate from 0.06 to 0.33 equivalents vs. lanthanides. They are also lower than the quantity of sodium introduced in the reaction mixture. Furthermore, the sodium content of the synthesized $Gd_{2(1-x)}Ce_xO_2S$ nanoparticles seems irreproducible through experiments and through experimentalists.

a)

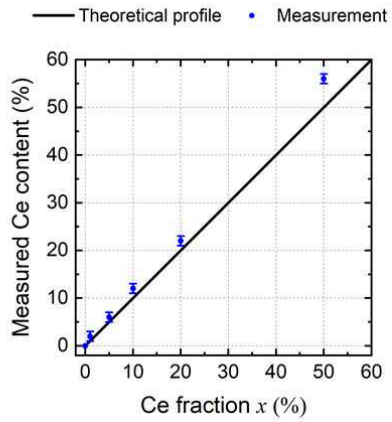

b)

Ce fraction (%)	Ce content (%)	S content (eq.)	Na content (eq.)
0	0	0.19 ± 0.02	0.20 ± 0.03
1	2 ± 1	0.18 ± 0.01	0.22 ± 0.03
5	6 ± 1	0.22 ± 0.01	0.06 ± 0.01
10	12 ± 1	0.18 ± 0.02	0.33 ± 0.04
20	22 ± 1	0.23 ± 0.01	0.10 ± 0.02
50	56 ± 1	0.21 ± 0.03	0.23 ± 0.02

Figure II.12: Chemical compositions of synthesized $Gd_{2(1-x)}Ce_xO_2S$ nanoparticles (x = 0, 0.01, 0.05, 0.10, 0.20, 0.50, are the cerium fraction introduced in the reaction mixture). a) Measured cerium contents (%), calculated as percentages of the total quantity of Gd and Ce, as function of cerium fraction x. The error bars represent the standard deviations of the measurements. b) Measured cerium, sulfur and sodium contents with standard deviations. The sulfur and sodium contents were calculated as equivalents vs. lanthanides.

II.3.3. X-ray absorption

In contrast to gadolinium, cerium can adopt two oxidation states which are Ce^{III} and Ce^{IV}. To determine the oxidation state of cerium in our nanoparticles, we employed X-ray absorption near edge spectroscopy (XANES) at cerium L_{III}-edge (5723 eV). This experiment was done in collaboration with Andrea Zitolo at beamline SAMBA, SOLEIL synchrotron (France).

A series of reference compounds containing cerium(III) and cerium(IV) was measured first. For instance, the XANES spectra of cerium(III) acetylacetonate $Ce(acac)_3$ and cerium(IV) sulfate $Ce(SO_4)_2$ are shown in **Figure II.13**. Cerium(III)-containing compounds exhibit a

characteristic absorption band with maximum of intensity at 5727 eV whereas cerium(IV)-containing compounds feature two maxima at 5731 eV and 5738 eV.

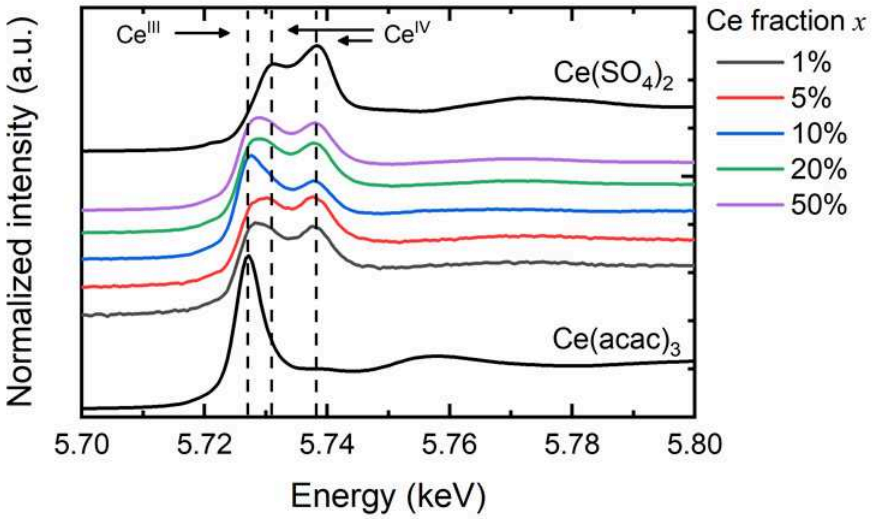

Figure II.13: Normalized XANES spectra at cerium L_{III}-edge of $Gd_{2(1-x)}Ce_xO_2S$ nanoparticles (x = 0, 0.01, 0.05, 0.10, 0.20, 0.50) as well as reference compounds of cerium(III) and cerium(IV): $Ce(acac)_3$ and $Ce(SO_4)_2$ respectively. The dashed lines are a guide to the eye for maxima of absorption intensity of cerium(III) and cerium(IV) containing compounds.

The spectra of $Gd_{2(1-x)}Ce_xO_2S$ nanoparticles were also acquired and compared with those of the reference compounds (**Figure II.13**). In general, both cerium(III) and cerium(IV) are present in our samples. However, the Ce^{III}/Ce^{IV} ratio varies. In particular, compared to the other samples, $Gd_{1.8}Ce_{0.2}O_2S$ (x = 0.1) (blue) shows a more intense absorption maximum at 5727 eV and a less intense one at 5738 eV. Qualitatively, it suggests that this sample possesses more cerium(III) and less cerium(IV) than the others. Using the same arguments, $Gd_{1.9}Ce_{0.1}O_2S$ (x = 0.05) likely presents less cerium(III) than the others. At this stage, no trend can be extracted from the results and the Ce^{III}/Ce^{IV} ratio appears irreproducible through experiments. Confirmation by deconvolution of the absorption spectra to extract contributions of each oxidation state is on-going.

II.3.4. X-ray diffraction

The crystalline nature of the isolated products in powder form was determined by X-ray diffraction (XRD). The diffraction patterns of $Gd_{2(1-x)}Ce_xO_2S$ nanoparticles match that of the

bulk reference Gd_2O_2S (JCPDS 79-5662) (**Figure II.14**a). We thus conclude that the nanoparticles crystallized in a phase isostructural to hexagonal Gd_2O_2S (**Figure II.14**c-e). It is a lamellar structure which can be described as alternating sheets of $[Gd_2O_2]^{2+}$ and S^{2-} (**Figure II.14**c). The gadolinium atom is coordinated to 7 atoms in total, including 4 oxygen atoms and 3 sulfur atoms (**Figure II.14**e). The lattice parameters *a* and *c* of the reference hexagonal Gd_2O_2S phase are 3.85 and 6.66 Å, respectively.

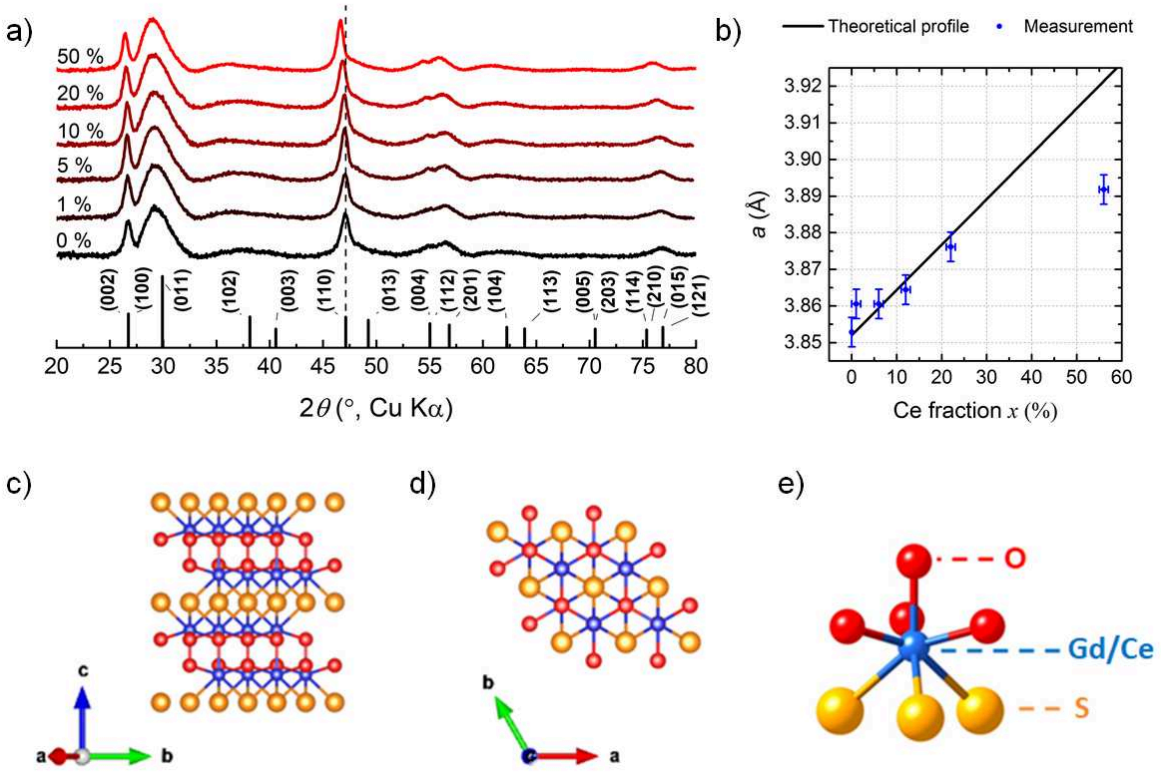

Figure II.14: a) XRD patterns of $Gd_{2(1-x)}Ce_xO_2S$ nanoparticles (x = 0, 0.01, 0.05, 0.10, 0.20, 0.50) with reference pattern of Gd_2O_2S (JCPDS 79-5662). The dashed line is a guide to the eye for the position of the (110) peak of the reference pattern. b) Lattice parameter *a* as function of the cerium fraction *x*. The black line corresponds to the expected values according to Vegard's law. The vertical error bars correspond to the estimated error in position of the diffraction peaks due to the sample holder. The horizontal error bars correspond to the standard deviations of the composition measurements. c) Representation of the lamellar structure of Gd_2O_2S. d) View from the (001) direction of the structure. e) Environment of Gd/Ce in the structure.

Shifts towards smaller angles of some diffraction peaks of the gadolinium-cerium oxysulfide nanoparticles are observed as the cerium content *x* increases (**Figure II.14**a). Lattice parameter $a = 2d_{(110)}$ of the hexagonal structure is plotted as a function of the cerium content

(**Figure II.14**b). Position of the most intense diffraction peak (110) was obtained by fitting it with a pseudo-Voigt function. The shoulder from the (013) peak was also included to improve the precision of the fit. For $x < 0.5$, the lattice parameters a of the $Gd_{2(1-x)}Ce_xO_2S$ nanoparticles seem to follow the linear profile of the Vegard's law, indicating a solid solution of Gd_2O_2S and Ce_2O_2S. It implies statistical substitution of gadolinium atoms in the Gd_2O_2S structure by cerium atoms. This substitution is also favored by the fact that the ionic radii with coordination number VII of cerium(III) and gadolinium(III) are similar (1.14 Å and 1.21 Å respectively). However, for $x = 0.5$, the lattice parameter deviates from the Vegard linear profile, suggesting a different scenario with higher cerium contents.

The diffraction patterns of the $Gd_{2(1-x)}Ce_xO_2S$ nanoparticles also feature peaks of different widths. In particular, we observe that diffraction peaks of (hkl) planes ($l \neq 0$) such as (001) and (102) are broad, while peaks of (hkl) planes ($l = 0$) such as (100) and (110) are narrower.

II.3.5. Infrared spectroscopy

Our synthesis in organic solvent made use of organic ligands (oleic acid/oleates and oleylamine) to produce small and anisotropic $Gd_{2(1-x)}Ce_xO_2S$ nanoparticles as we have shown by means of other characterization techniques. Oleates are good ligands for Ln^{III} species,[53] while oleylamine can also coordinate gadolinium cations via their lone pair (**Figure II.15**a). In order to get insights on these surface ligands, Fourier-transform infrared (FTIR) spectroscopy in attenuated total reflectance (ATR) mode was carried out for $Gd_{2(1-x)}Ce_xO_2S$ nanoparticles (x = 0, 0.01, 0.05, 0.10, 0.20, 0.50) (**Figure II.15**b).

The broad signal at ca. 3300 cm^{-1} can be attributed to either N-H stretching band of oleylamine or O-H stretching band of adsorbed water. Hydrocarbon chains of the organic ligands are observed with the asymmetric and symmetric C-H stretching bands present at ca. 2900 cm^{-1}. The two bands at 1350-1550 cm^{-1} are characteristic of asymmetric and symmetric vibrations of coordinated COO^- groups. Consequently, they are attributed to the coordinated oleates on the surface of the nanoplatelets. The absence of the intense signal of the stretching mode of C=O at 1707 cm^{-1} also suggests that free oleic acid is not present.

There is less evidence of oleylamine coordinated to the surface of the nanoplatelets from the FTIR spectra, since the typical vibration band of NH_2 scissoring mode at 1576 cm^{-1} is masked by the broad signal of the coordinated oleates. Even though, X-ray photoelectron spectroscopy

(XPS) of the N 1s region of the samples confirm the presence of a small amount of nitrogen (< 10% compared to the metals) (data not shown), the quantity of oleylamine bound to the surface of the nanoplatelets is significantly lower than that of oleates. This has been confirmed by thermogravimetric analysis coupled to mass spectroscopy (TGA-MS) (see Appendix IV).[54]

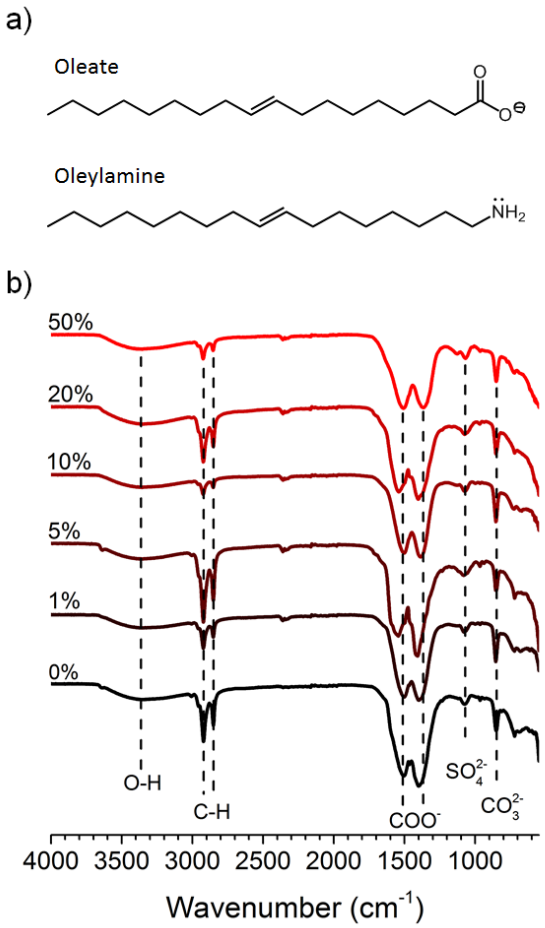

Figure II.15: a) Chemical formulas of oleate and oleylamine. b) ATR-FTIR spectra of $Gd_{2(1-x)}Ce_xO_2S$ nanoparticles (x = 0, 0.01, 0.05, 0.10, 0.20, 0.50).

The vibration bands in the 1050-1200 cm^{-1} are characteristic of S-O stretching in coordinated sulfate SO_4^{2-} group,[55] suggesting that the sulfur is partially oxidized in ambient air. Further proofs of this oxidation were previously acquired by the use of XANES at sulfur K-edge and XPS of the S 2p region.[36]

A rather sharp vibration band at 846 cm^{-1} can be attributed to deformation of CO_3^{2-}, similar to what was observed for $Gd_2(OH)_2CO_3SO_4$ precursor in the synthesis of gadolinium oxysulfates $Gd_2O_2SO_4$.[56] We suspect that this is due to adsorbed CO_2 molecules from ambient air.

At this stage, we can conclude that the surface ligand role was occupied in majority by oleates. In order to shed light onto how the oleates coordinate the surface of the nanoplatelets, we looked into the frequency difference between the asymmetric and symmetric vibrations the COO^- group. Depending on the values of this difference, the coordination mode can be attributed to monodentate, chelating, bridging bidentate and monoatomic bridging (**Figure II.16** I-IV respectively).[57]

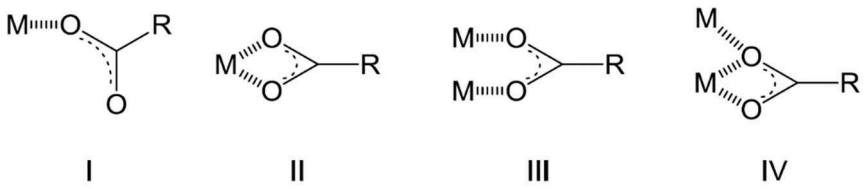

Figure II.16: Coordination modes of carboxylate ligands to metals.

We calculated the frequency difference between the two vibration bands in the $Gd_{2(1-x)}Ce_xO_2S$ nanoparticles and reported the results in **Table II.1**.

Ce fraction *x* (%)	$\nu_{as}(COO^-)$ (cm^{-1})	$\nu_s(COO^-)$ (cm^{-1})	$\nu_{as} - \nu_s$ (cm^{-1})
0	1508	1394	114
1	1508	1398	110
5	1548	1411	137
10	1505	1386	119
20	1548	1406	142
50	1509	1372	137

Table II.1: Positions of asymmetric and symmetric vibration bands of COO^- group of $Gd_{2(1-x)}Ce_xO_2S$ nanoparticles (x = 0, 0.01, 0.05, 0.10, 0.20, 0.50) and their difference in frequency.

All calculated values range from 110 cm^{-1} to 142 cm^{-1} and are all lower than 200 cm^{-1}, suggesting either a chelating or bridging coordination mode and eliminates the possibility of monodentate coordination mode.[57] The absences of the C=O stretching mode discussed

earlier also indicates likewise. We thus conclude that oleates coordinate the $Gd_{2(1-x)}Ce_xO_2S$ nanoplatelets by a mix of chelating and bridging modes. Nevertheless, the exact positions of the two vibration bands and their $\Delta\nu$ varies from sample to sample. They are highly dependent on the washing steps of the synthesis and are irreproducible through experiments.

II.3.6. Discussion

We were able to prepare $Gd_{2(1-x)}Ce_xO_2S$ nanoparticles for the first time using colloidal synthesis in organic solvent. From the results of different characterization techniques, we discuss the composition and structure of the nanoparticles.

II.3.6.1. Exposed facets and crystallinity

The synthesized $Gd_{2(1-x)}Ce_xO_2S$ nanoparticles are anisotropic and has platelet shape. They are ca. 20 nm wide, 2 nm thick and crystallize in a phase isostructural to hexagonal Gd_2O_2S. Their diffraction patterns feature peaks of different widths. In fact, the width of a diffraction peak partly depends on the dimension of its direction. Therefore, this different peak width is consistent with the anisotropic of the $Gd_{2(1-x)}Ce_xO_2S$ nanoparticles. Moreover, broad diffraction peak of a (hkl) plane indicates a small dimension in the [hkl] direction and vice versa. For our nanoparticles, peaks of (hkl) planes with $l \neq 0$ are broad while peaks of (hkl) planes with $l = 0$ are narrow. We thus deduce that the larger basal facets of the nanoplatelets correspond to the (hk0) planes ($l = 0$) (**Figure II.14**d) and the smaller side facets correspond to the (hkl) planes ($l \neq 0$) (**Figure II.14**c). More particularly, by using high-resolution TEM (HRTEM), these facets have been confirmed as (100) and (001), respectively.[5]

To estimate the average crystallite domain size of the nanoparticles, we used the Scherrer equation and the full width at half maximum (FWHM) of the previously fitted (110) peak. The calculated values are reported in **Table II.2**. Crystallite domain sizes remain within the 12-15 nm range in all the samples. No significant change is observed between gadolinium oxysulfide nanoplatelets and gadolinium-cerium oxysulfide nanoplatelets.

x (%)	0	1	5	10	20	50
Crystallite domain size (nm)	12	12	15	13	13	15

Table II.2: Estimated crystallite domain size from the (110) peak by Scherrer equation.

The average crystallite domain sizes of the nanoplatelets are slightly lower than their apparent size measured by TEM (20 ± 5 nm). However, it is worth noting that diffraction peak broadening is not only due to the crystallite size but also the presence of defects and the contribution of the instrument. Therefore, the calculated values of crystallite domain size are likely underestimation of the real ones. If one takes into account other contributions of peak broadening, the crystallite domain size of the $Gd_{2(1-x)}Ce_xO_2S$ nanoplatelets would be closer to their apparent size. Therefore, we speculate that the nanoplatelets are monocrystals. This has been confirmed by complementary HRTEM study.[5]

Overall, a $Gd_{2(1-x)}Ce_xO_2S$ nanocrystal that we obtained can be schematized as in **Figure II.17**. Note that in reality, the shape of nanoplatelets is not perfectly hexagonal (**Figure II.10**).

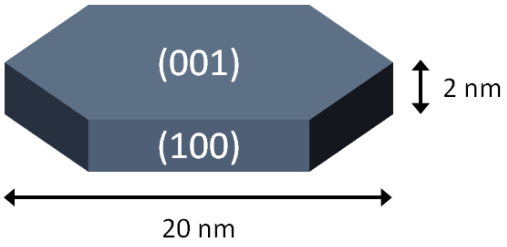

Figure II.17: Schematic representation of a hypothetical $Gd_{2(1-x)}Ce_xO_2S$ hexagonal nanoplatelets.

II.3.6.2. Tunable cerium content

EDS analysis of the synthesized $Gd_{2(1-x)}Ce_xO_2S$ nanoparticles shows that the cerium content in the final products matches with the cerium fraction introduced in the reaction mixture. It indicates that we could effectively tune the cerium content of the nanoplatelets. More importantly, their size, shape and crystal structure remain unchanged. In principle, this will allow us to readily study the effect of cerium content on the properties, functionality and toxicity of the $Gd_{2(1-x)}Ce_xO_2S$ nanoparticles.

II.3.6.3. Gd_2O_2S-Ce_2O_2S solid solution and oxidation of the nanoparticles in air

We demonstrated that synthesized $Gd_{2(1-x)}Ce_xO_2S$ nanoparticles (x = 0, 0.01, 0.05, 0.10, 0.20) were solid solution of Gd_2O_2S and Ce_2O_2S. However, it was not the case for $GdCeO_2S$ (x = 0.5) since the calculated lattice parameter deviated from the Vegard linear profile (**Figure II.14**b). Similar behavior has been previously observed for another series of $Gd_{2(1-x)}Ce_xO_2S$ nanoparticles (see Appendix III).[36] It was demonstrated that these nanoparticles were solid solutions of Gd_2O_2S and Ce_2O_2S for all values of x if they were kept under inert atmosphere after synthesis. In ambient air, nanoparticles containing more than 40% of cerium (x > 0.4) oxidized. Concomitant oxidation of both cerium and sulfur led to the formation of mixed valence phases such as $Ce_2O_{2.5}S$ and subsequently cerium(IV) oxide CeO_2. This is consistent with our observation of both signals of cerium(III) and cerium(IV) in the XANES spectra of the samples, suggesting the beginning of the oxidation process. It is worth noting that the Ce^{III}/Ce^{IV} ratio seemed irreproducible through experiments. This uncontrolled quantity could be a problem for subsequent studies of properties, functionality and toxicity of the $Gd_{2(1-x)}Ce_xO_2S$ nanoparticles.

II.3.6.4. Nanocrystal termination: current hypothesis and perspective

Interestingly, the $(Gd,Ce)_2O_2S$ phase was formed despite the large sulfur defect (only 36 to 46% of the theoretical S content was detected). In fact, the obtained nanoplatelets are very thin (**Figure II.17**). They comprise at maximum three layers of unit cells as the lattice parameter c was reported at 6.66 Å (JCPDS 79-5662). This means that at this scale, the surface can have extreme effect on the overall properties of the nanoparticles. Thus, we propose that the nanoplatelets are terminated by two $[Ln_2O_2]^{2+}$ (Ln = Gd, Ce) layers in their basal facets (**Figure II.18**), resulting in a defect in sulfur content. In this model, the surfaces of the nanoplatelets are positively charged. Thus, surface ligands play a crucial role to compensate these charges. We previously detected oleates as the main ligand present. They may fulfill this role by coordinated the $[Ln_2O_2]^{2+}$ layers in chelating and bridging modes.

The calculated chemical composition of such nanoplatelets of 23 nm wide is $Gd_2O_2S_{0.64}$, already more comparable to that of synthesized nanoplatelets. However, the sulfur content of these $[Ln_2O_2]^{2+}$-terminated $Gd_{2(1-x)}Ce_xO_2S$ nanoplatelets is still superior to that we measured. This likely indicates sulfur vacancies in the internal layers of the nanoplatelets.

In order to substantiate our hypothesis, pair distribution function (PDF) analysis is particularly suitable. The pair distribution function *G*(r) is directly correlated to the probability to find a distance whose length is r between 2 atoms. Thus, this technique does not require an extended crystal analysis and is suitable for amorphous and defective compounds. Preliminary results have been obtained, showing a good agreement between measured PDF and PDF modeled after $[Gd_2O_2]^{2+}$-terminated Gd_2O_2S nanoplatelets.[5]

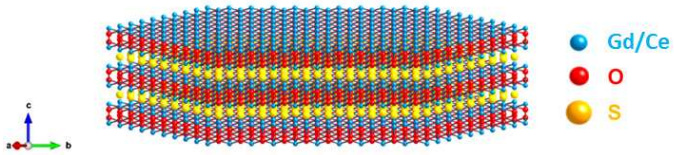

Figure II.18: Schematic representation of $[Ln_2O_2]^{2+}$-terminated $Gd_{2(1-x)}Ce_xO_2S$ nanoplatelets.

Another possibility for this sulfur defect is that as the yield of the reaction is not quantitative, amorphous side-product that do not contain sulfur such as gadolinium or cerium oxide can be present. This is especially probable in nanoparticles that contain more than 40% of cerium. These amorphous side-products can be in the form of very small nanoparticles, thus they are difficult to detect by TEM. However, in-depth analysis of PDF may give us an answer.

II.3.6.5. The presence of sodium

Chemical composition analysis of the $Gd_{2(1-x)}Ce_xO_2S$ nanoplatelets showed that they contain up to 0.33 equivalents of Na vs. lanthanides. While this value is much lower than the quantity of sodium introduced in the reaction mixture, it is way higher than doping levels. Since the nanoplatelets crystallize in phases isostructural to hexagonal Gd_2O_2S and no major change of their crystal structure was observed, it is highly improbable that the total detected quantity of sodium resides in the inorganic core. Moreover, preliminary results of PDF analysis even suggested the absence of sodium there.[5] Together with the fact that the detected sodium quantity in the final product is irreproducible through experiments and experimentalists, we assume that the sodium remains on the surface of the nanoplatelets and can be removed. In the next section, we will attempt to confirm this and to elucidate the role sodium in the synthesis of $Gd_{2(1-x)}Ce_xO_2S$ nanoplatelets.

II.4. Role of sodium in the synthesis of lanthanide oxysulfide nanoplatelets

In order to get insights on the role of sodium in our synthesis of lanthanide oxysulfide nanoplatelets, we considered only the synthesis of Gd_2O_2S nanoparticles to simplify the analysis of results.

II.4.1. Influence of sodium stoichiometry

In the earlier works reporting the synthesis of lanthanide oxysulfide nanoparticles such as one of Ding et al. in 2011,[12] 1 equivalent of the sodium acetylacetonate Na(acac) vs. the lanthanide precursor was systematically added at the beginning of the synthesis. The authors stated that the presence of sodium is crucial for the crystallization of the nanoparticles.

In the syntheses discussed in the previous section, we also employed 1 equivalent of sodium and were able to obtain nanoplatelets of $Gd_{2(1-x)}Ce_xO_2S$ phases. To confirm the statement of Ding et al., we carried out the synthesis of Gd_2O_2S without sodium. The reaction indeed yielded a very small quantity (< 10 mg) of nanoparticles which are amorphous (**Figure II.19**a and f).

We then gradually decreased the quantity of sodium from 1 equivalent to search for the minimum amount necessary for the crystallization of the Gd_2O_2S nanoplatelets. In particular, 0.01, 0.10 and 0.50 equivalents of sodium oleate vs. the gadolinium precursor were added at the beginning of the reaction. The results were reported in **Table II.3** and **Figure II.19** and were compared to those of the synthesis with 1 equivalent of sodium.

Added amount of Na (eq. vs. Gd)	Na content of the product (eq. vs. Gd)	S content of the product (eq. vs. Gd)
0.01	0	0.06 ± 0.01
0.10	0.06 ± 0.02	0.13 ± 0.02
0.50	0.03 ± 0.01	0.22 ± 0.02
1.00	0.20 ± 0.03	0.19 ± 0.02

Table II.3: Sodium and sulfur contents of the products of the syntheses using different quantities of sodium oleate.

With 0.50 equivalents of sodium oleate, the synthesis yielded a reasonable amount of product. Eighty-five milligrams of solid was collected, slightly lower than the obtained amount when 1 equivalent of sodium was used (100 mg). The product is determined to be Gd_2O_2S nanoplatelets (**Figure II.19**f) by XRD. Also, no change in their sulfur content (**Table II.3**), size and shape (**Figure II.19**d) are observed. Their sodium content appears to be lower than what we have obtained with $Gd_{2(1-x)}Ce_xO_2S$ nanoparticles. Nevertheless, if we take into account the experimental error margin of EDS which is ca. 0.05 in this case, this change is not significant.

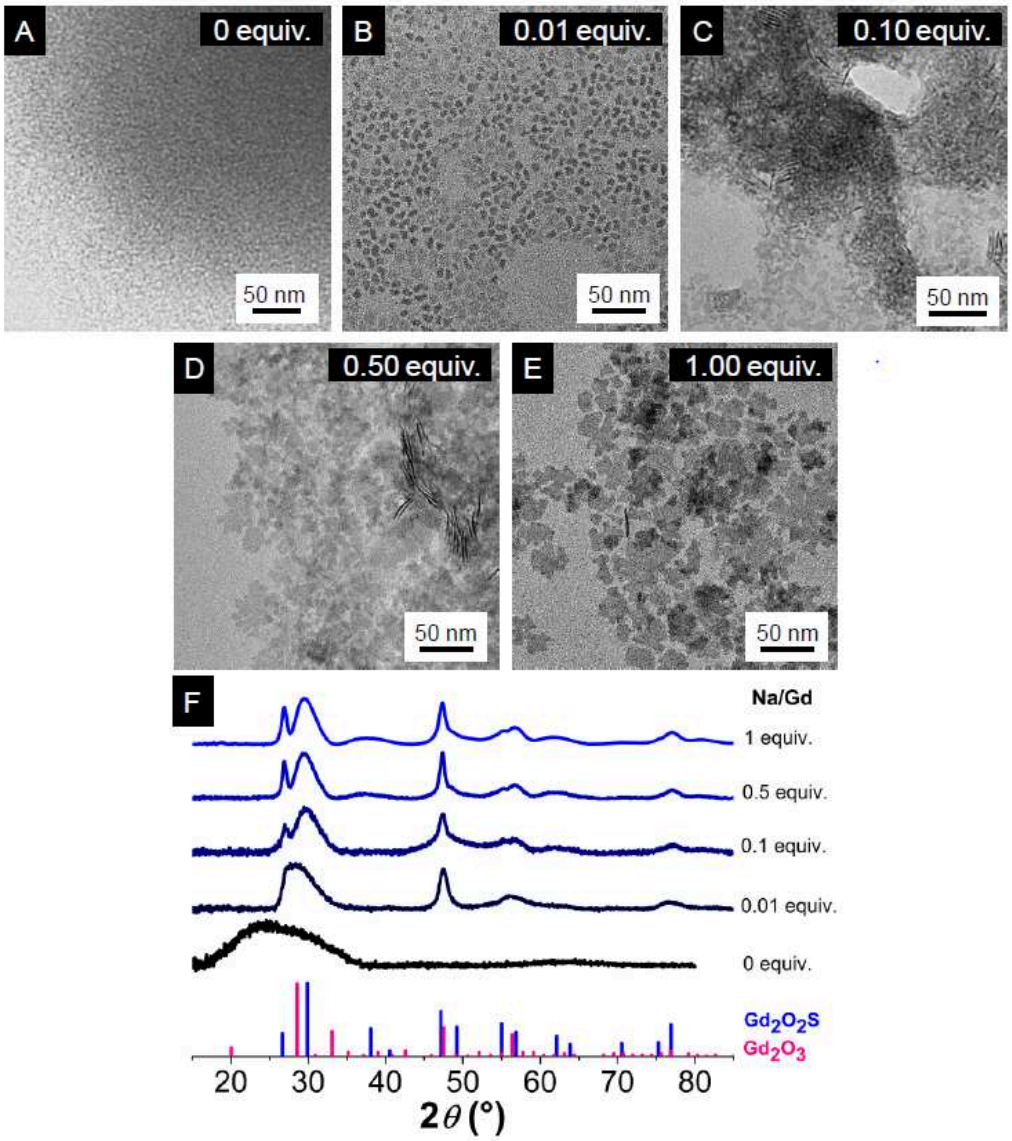

Figure II.19: Influence of added sodium oleate concentration on the size, shape and crystallization of the Gd_2O_2S nanoplatelets. TEM images of the products obtained with (A) 0, (B) 0.01, (C) 0.1, (D) 0.5

and (E) 1 equivalent of added Na(oleate) vs. $Gd(acac)_3$. (F) Corresponding XRD patterns of the products. Figure is taken from ref 5.

With 0.01 equivalents of sodium, we obtained smaller nanoplatelets (ca. 10 nm) (**Figure II.19**c). Remarkably, their XRD pattern still shows crystalline Gd_2O_2S (**Figure II.19**f). The diffraction peaks are broader than those of higher sodium amounts, in agreement with their smaller apparent size. EDS of the product also shows similar results with slightly lower sulfur content.

Lastly, the synthesis with 0.01 equivalents of sodium only yielded 15 mg of product, instead of 100 mg expected for a quantitative reaction. TEM shows even smaller nanoplatelets of ca. 5 nm wide (**Figure II.19**b). Their XRD pattern shows a broad diffraction peak in the range of 25-35 °, probably indicates the presence of an amorphous solid (**Figure II.19**f). The sulfur content is also significantly lower than those of Gd_2O_2S nanoparticles synthesized with higher amounts of sodium oleate. Also, no sodium is present in the final product as expected from the already low quantity added at the beginning of the reaction.

Overall, we concluded that sodium is indeed necessary to obtain crystalline gadolinium oxysulfide nanoplatelets, in agreement with Ding et al.,[12] but not for the reasons proposed in this article, as will be shown below.

II.4.2. Elimination of sodium ions from Gd_2O_2S nanoplatelets

To explain the presence of sodium in the final product as well as its crucial role in the production of crystalline Ln_2O_2S nanoplatelets, Ding et al. employed *ab initio* calculations and proposed that Na^{I} (r(VIII) = 1.26 Å) were inserted in Ln^{III} (r(VIII) = 1.06-1.24 Å) host lattices, creating oxygen vacancies. The latter then favored the formation of oxysulfide phase over its oxide counterpart. They assumed that the synthesized Ln_2O_2S phases were defective and doped with a certain amount of Na, in contrast with our results of PDF analysis which suggest otherwise. The hypothesis of Ding et al. also seems unlikely because we showed that there was no correlation between the quantity of sodium introduced in the reaction mixture, the detected sodium and sulfur contents in the final product as well as the crystallization of Gd_2O_2S. This suggests that the sodium is likely not in the inorganic core of the nanoplatelets but on their surface.

II.4.2.1. Washing with organic solvents

Therefore, in order to acquire hints on the location of sodium, we attempted to remove it from the final product by intensive washes. Typically, the nanoparticles were isolated from the reaction medium by centrifugation with added ethanol. Afterwards, they were washed several times with an *n*-hexane/ethanol mixture (1/3 in volume). The sodium and sulfur contents of the product were measured by EDS at each wash (**Figure II.20**). It is important to note that the sulfur content remains constant during the washes, except for the isolation step where excess sulfur was removed. This likely indicates that the gadolinium oxysulfide nanoparticles are stable during the post-synthetic washes.

After isolating the nanoparticles from the reaction medium by a first centrifugation, 79% of added sodium was already removed. The first wash then removed an additional 8%, resulting in a final sodium content of 0.13 equivalent vs. Gd. The next four washes gradually decreased the sodium content to a final 0.08 equivalents vs. Gd, unable to completely remove all of the sodium at this stage. We assume that only the more labile sodium can be removed by this way.

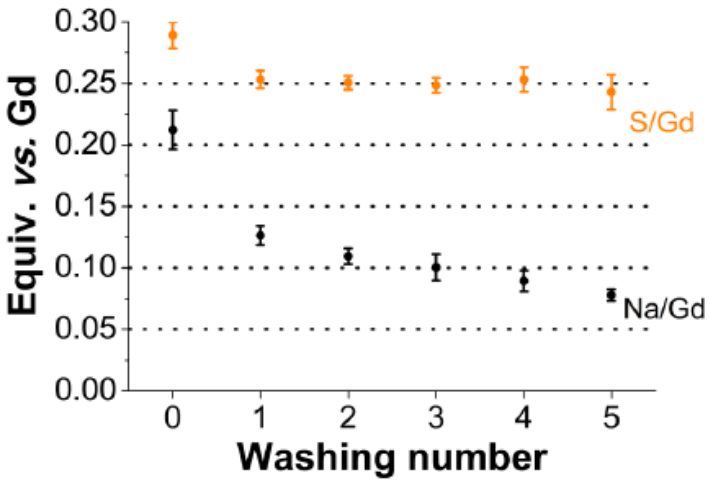

Figure II.20: Evolution of sulfur and sodium contents (eq. vs. Gd) during the washing process of synthesized Gd_2O_2S nanoplatelets (taken from ref 5). Washing number "0" refers to the solid collected from the crude reaction medium by centrifugation with added ethanol.

II.4.2.2. Washing with water

Compared to a mixture of *n*-hexane and ethanol, more soluble species of sodium can form in water. Hence, we suspected that water could help eliminate the remaining sodium from the Gd_2O_2S nanoplatelets. To confirm this, the nanoparticles were dispersed in distilled water and the suspension was left under vigorous stirring for 24 hours. The solid was collected afterwards by simple centrifugation and was characterized by EDS and XRD (**Figure II.21**).

Remarkably, EDS of the solid after washing shows no sodium. The sulfur contents of before and after washing are 17 ± 1% and 15 ± 1% respectively, indicating no loss of sulfur during the washing step. And most importantly, the obtained solid preserves its crystal structure of hexagonal Gd_2O_2S as shown by XRD (**Figure II.21**). Its diffraction pattern is identical to that of initial Gd_2O_2S nanoplatelets.

To recapitulate, we showed that sodium could be completely eliminated from crystalline Gd_2O_2S nanoplatelets without modifying their crystal structure, within the experimental error margin of EDS. More precise chemical composition analysis needs to be done in order to confirm this finding. In particular, it will be done in the future with a newly installed X-ray fluorescence spectrometer in our lab. Nevertheless, this result ensures that the large majority of sodium locates at the surface of gadolinium oxysulfide nanoplatelets.

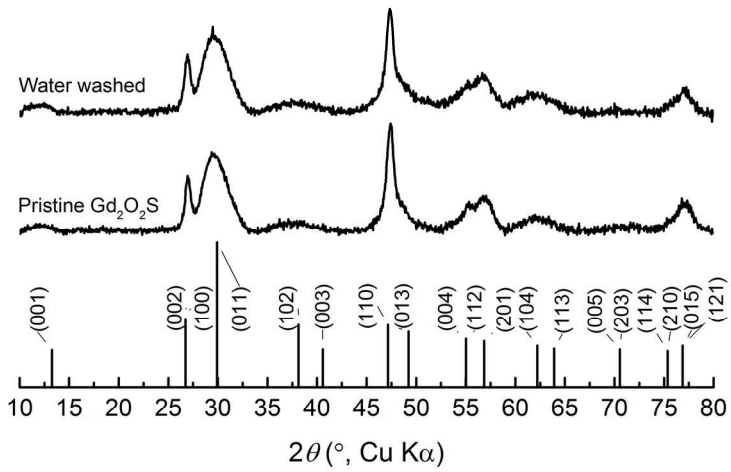

Figure II.21: XRD patterns of pristine Gd_2O_2S nanoplatelets and Gd_2O_2S nanoplatelets washed with water. The reference pattern corresponds to bulk Gd_2O_2S (JCPDS 79-5662).

II.4.3. Synthesis using other alkali-metal precursors

Ding et al. succeeded in synthesizing Ln_2O_2S nanoplatelets using other alkali-metal precursors in 2013.[52] Remarkably, La_2O_2S nanoplatelets were obtained with lithium, sodium and potassium acetylacetonate. Whereas the use of Na(acac) led to formation of 23 nm large nanoplatelets, Li(acac) and K(acac) resulted in 9 nm and 43 nm large nanoplatelets respectively. La_2O_2S nanoplatelets synthesized with lithium and potassium also ended up with lower sulfur content (20% and 19% respectively) than those synthesized with sodium (38%). Interestingly, the nanoplatelets resulted from synthesis with lithium were poorly crystallized compared to the two other cases. The authors finally concluded that the nature of the alkali-metal dopants (lithium, sodium or potassium) could affect the size, shape, crystallinity, composition and phase stability of the nanoplatelets.

First, we questioned the necessity of the alkali-metal for the synthesis of Ln_2O_2S nanoplatelets. Synthesis of Gd_2O_2S nanoplatelets with calcium acetylacetonate $Ca(acac)_2$ was thus carried out. No solid could be collected at the end of the reaction. A monovalent metal ion seems to be required.

Inspired by the experiments of Ding et al., we adapted the synthesis of Gd_2O_2S with different alkali-metal precursors including lithium, sodium and potassium acetylacetonate: Li(acac), Na(acac) and K(acac) respectively. Cesium carbonate $Cs_2(CO_3)$ was also used due to the unavailability of cesium acetylacetonate Cs(acac). It likely reacted with oleic acid and release CO_2 to form Cs(oleate) *in situ*, which then served as the effective cesium precursor in the reaction medium. The results were compared with those of the synthesis of Gd_2O_2S using sodium oleate as alkali precursor (**Table II.4** and **Figure II.22**).

Interestingly, EDS shows comparable sulfur contents in the product of all the syntheses despite the change of alkali-metal (**Table II.4**). The final alkali-metal contents are also similar. Both of these contents are comparable to what we obtained in the synthesis using sodium oleate.

Alkali precursor	S content (eq. vs. Gd)	Alkali-metal content (eq. vs. Gd)
Na(oleate)	0.19 ± 0.01	0.20 ± 0.03
Li(acac)	0.15 ± 0.01	N/A
Na(acac)	0.21 ± 0.01	0.09 ± 0.03
K(acac)	0.19 ± 0.01	0.14 ± 0.01
$Cs_2(CO_3)$	0.16 ± 0.01	0.19 ± 0.01

Table II.4: Sodium and alkali-metal contents of the products of the syntheses using different alkali-metal precursors.

In general, XRD patterns of the products show crystallized hexagonal Gd_2O_2S phase in all the synthesis (**Figure II.22**a). The diffraction peaks are, however, broader in the synthesis using Li(acac). Accordingly, TEM image of the product of this synthesis shows small nanoplatelets of ca. 7 nm (**Figure II.22**b).

For the syntheses with Na(acac), K(acac) and $Cs_2(CO_3)$, unattributed diffraction peaks are observed alongside Gd_2O_2S (**Figure II.22**a). With cesium, these peaks are slightly shifted towards smaller angles (ca. 0.3 °) compared to those obtained with potassium. With sodium, the unattributed phase seems to be present in a smaller amount as its diffraction peaks are barely visible. It is worth noting that these unattributed peaks do not correspond to the reported cubic (JCPDS 012-0797), hexagonal (JCPDS 016-2410) nor monoclinic (JCPDS 042-1465) gadolinium oxides phases. They also do not match with the diffraction patterns of reported phases containing at least two of the following elements: alkali-metal, gadolinium, carbon, nitrogen, oxygen, sulfur, chlorine and hydrogen.

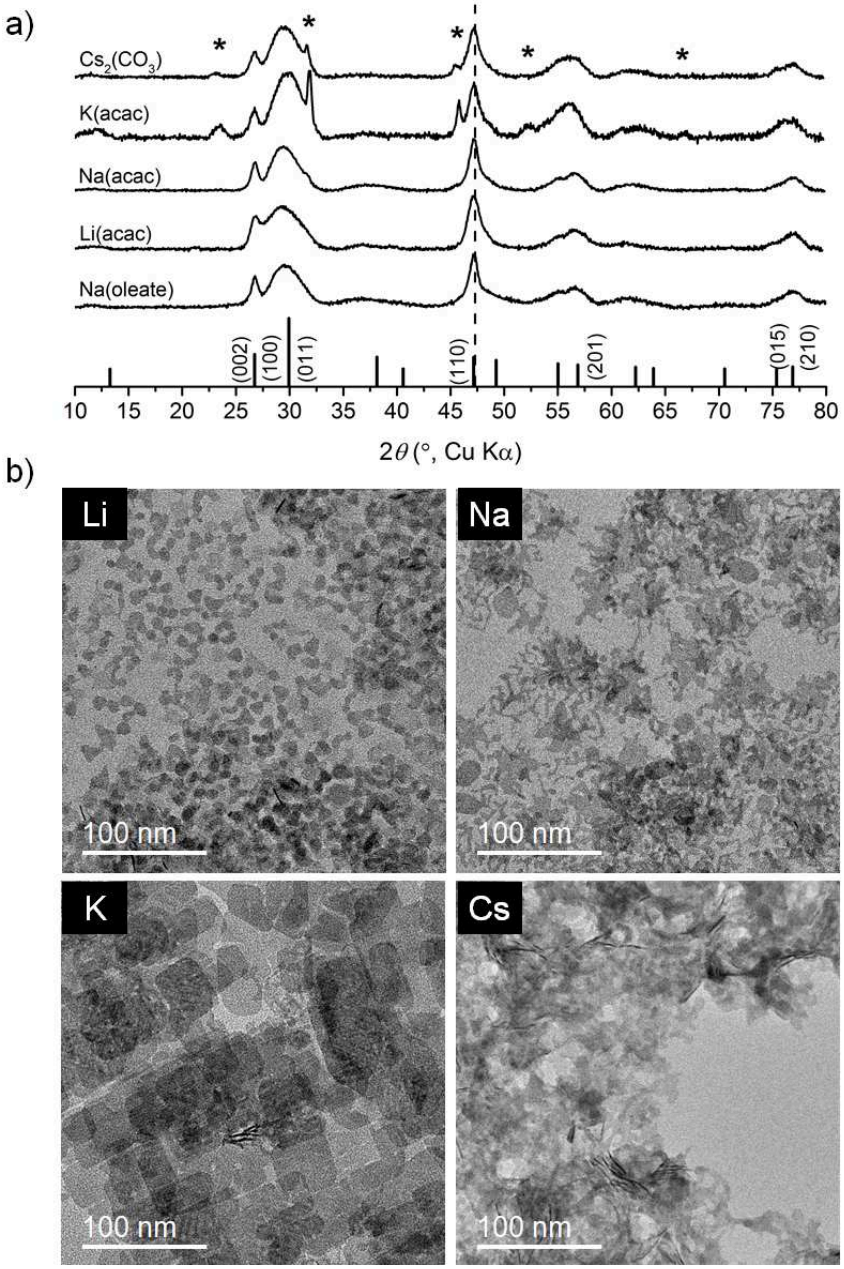

Figure II.22: Synthesis of Gd_2O_2S nanoplatelets with Na(oleate), Li(acac), Na(acac), K(acac) and $Cs_2(CO_3)$. a) XRD patterns of the products as well as the reference pattern of bulk Gd_2O_2S (JCPDS 79-5662). The dashed line is a guide to the eye for the position of the (110) diffraction peak belonging to the reference Gd_2O_2S phase. The asterisks indicate unattributed diffraction peaks. b) Their corresponding TEM images.

TEM images of the products of the syntheses with Na(acac), K(acac) and $Cs_2(CO_3)$ show nanoplatelets of irregular size and shape (**Figure II.22**a). Two categories of nanoplatelets can be distinguished: small nanoplatelets (≤ 20 nm wide) that resemble Gd_2O_2S nanoplatelets obtained with sodium oleate and larger nanoplatelets (≥ 25 nm wide). The latter are especially

large in the synthesis with potassium acetylacetonate. Remarkably, these nanoplatelets are of regular rectangular shape (ca. 30 nm x 100 nm) with round corners. They also appear to be quite thin as the electron beam can pass through.

In order to verify the crystallinity of the large rectangular nanoplatelets in the synthesis with potassium acetylacetonate K(acac) and identify their nature, scanning transmission electron microscopy (STEM) was employed (**Figure II.23**). Lattice fringes were observed, suggesting the crystalline nature of the nanoplatelets (**Figure II.23**c).

Peak n°	**2θ (°)**	**d (Å)**
1	23.4	3.80
2	31.9	2.80
3	45.8	1.98
4	52.4	1.75
5	66.8	1.40

Table II.5: Positions of the unattributed peaks in the diffraction pattern belonging to the product of the synthesis with potassium acetylacetonate K(acac) in **Figure II.22**a.

Fast Fourier Transform (FFT) of a smaller area of the micrograph of nanoplatelets shows a pattern of spots that corresponds to the unidentified phase in their XRD pattern (**Figure II.23**d). Indeed, each marked spot represents a characteristic distance of repetition in the direct space (distance between lattice fringes) and can be attributed to a diffraction peak presented in **Table II.5**. For example, spot n°1 represents a distance of repetition of 3.80 Å, coinciding with the diffraction peak n°1 at 23.4 °. We thus confirmed that the unattributed peaks in the XRD pattern belong to the large rectangular nanoplatelets. However, the corresponding crystal structure remains a mystery.

As of the small nanoplatelets mixed with the large rectangular ones, determining their crystallinity seems to be tricky because they are quite aggregated. Nevertheless, we speculate that they are crystallized in the Gd_2O_2S phase detected by XRD, based on the widths of the diffraction peaks.

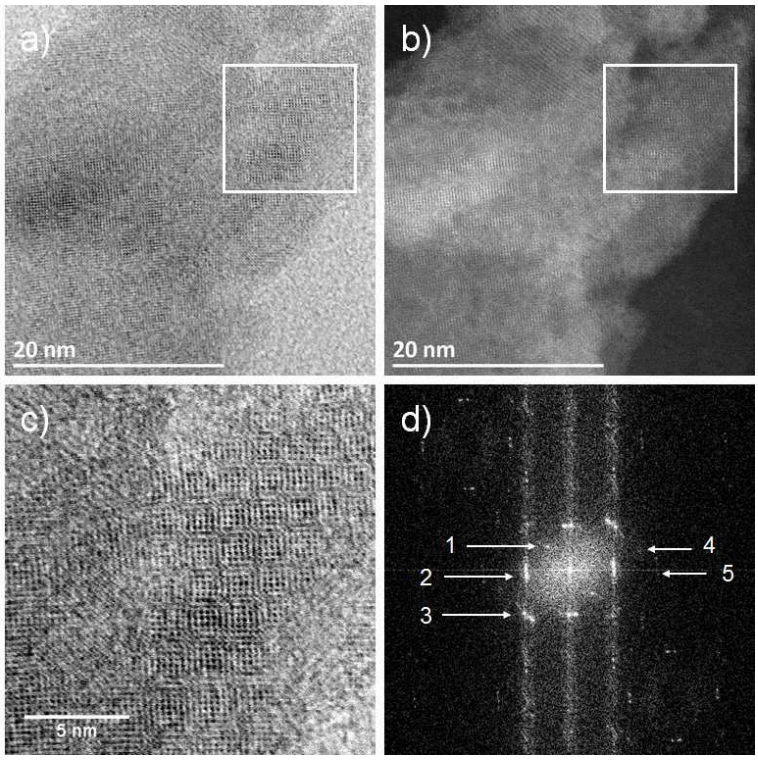

Figure II.23: a) STEM bright field and b) high-angle annular dark-field (HAADF) imaging of the large rectangular nanoplatelets obtained by synthesis with potassium acetylacetonate K(acac). The white square indicates an area where lattice fringes are observed. c) Zoom of the designated white square and its d) FFT.

Overall, we conclude that monovalent metal ions are necessary for the synthesis of Gd_2O_2S nanoplatelets. We were able to synthesized crystallized Gd_2O_2S nanoplatelets of similar sulfur contents using lithium, sodium, potassium and cesium precursors. Surprisingly, the crystallization of Gd_2O_2S was possible even when there is a large difference between the ionic radii of the alkali-metals. No notable contraction or dilation of the unit cell was deduced from the diffraction patterns of the products. This again questions the doping of alkali-metal into the Gd_2O_2S lattices. In fact, while the crystal radius of monovalent sodium in a coordination VII (1.26 Å) is comparable to that of trivalent gadolinium (1.14 Å), those of potassium (1.60 Å) and cesium (1.81 Å and 1.88 Å for coordinations VI and VIII respectively, coordination VII of cesium is not reported) are far larger. In these cases, obtaining an unmodified Gd_2O_2S phase appears improbable if the doping takes place.

II.4.4. Conclusion and perspective on the role of sodium

In this section, we discussed the role of sodium in our colloidal synthesis of Gd_2O_2S nanoplatelets. We confirmed that addition of a sodium precursor at the beginning of the synthesis is necessary for the crystallization of Gd_2O_2S. We showed that only a quantity as low as 0.10 equivalents of sodium oleate vs. gadolinium precursor was needed. Even then, sodium still remained in the final product. Nevertheless, we were able to eliminate all the remaining sodium (within experimental error margin of EDS) by washing the product with water and still preserved the crystal structure of the nanoplatelets. Lastly, we found out that addition of other alkali-metals such as lithium, potassium and cesium could also result in crystallization of Gd_2O_2S of comparable sulfur contents. However, alkaline earth metal such as calcium did not yield any solid.

Altogether, the obtained results in this section support our hypothesis of sodium residing at the surface of the gadolinium oxysulfide nanoplatelets. On the contrary, the sodium doping of Gd_2O_2S seems unlikely. This study was made jointly with small and wide-angle X-ray scattering (SAXS-WAXS) of the reaction medium presented in the Ph.D. thesis of Clément Larquet. A new mechanism of formation of Gd_2O_2S nanoplatelets explaining the role of sodium emerged thanks to these combined results (**Figure II.24**).

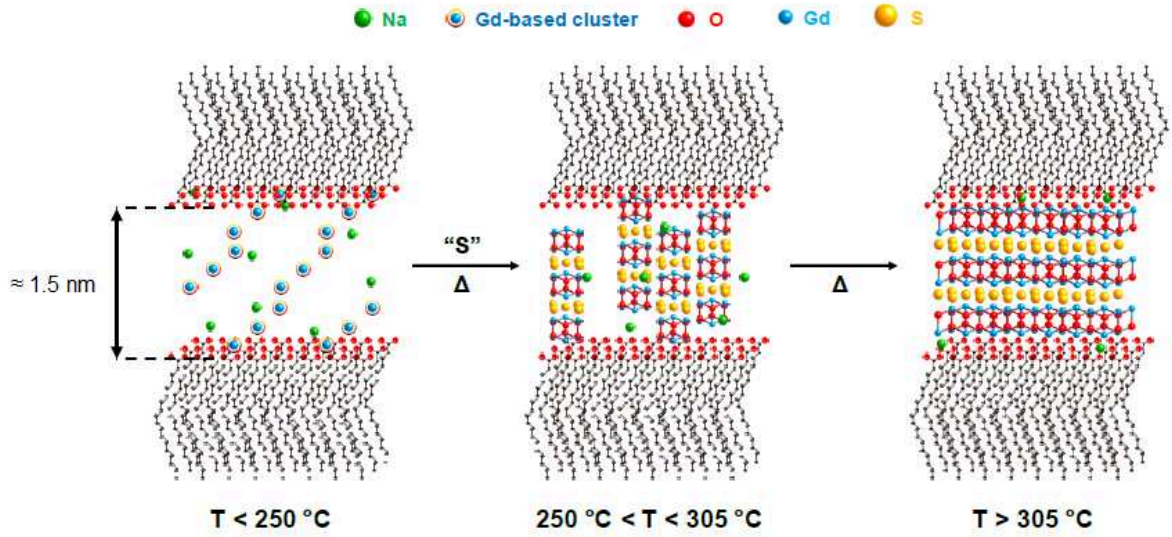

Figure II.24: Proposed mechanism of formation of Gd_2O_2S nanoplatelets from organized clusters (taken from ref 5).

In particular, we proposed that, under our synthetic conditions, a lamellar phase of Na(oleate) exists in the reaction medium, leaving a 1.5 nm thick space in between. This space then served as a template to grow crystalline Gd_2O_2S, resulting in the 2D shape of nanoplatelets. This model also shows that the nanoplatelets need to terminate with positively charged $[Gd_2O_2]^{2+}$ layers to face the oleate ligands. Generally, the proposed mechanism underlines the importance of lamellar phases such as Na(oleate) in the crystallization of nanoscale Gd_2O_2S.

So far, this hypothesis is promising as it fits well with our results. Yet, control syntheses without oleic acid and without both oleic acid and oleate yielded crystalline Gd_2O_2S nanoplatelets even though they are quite aggregated (**Figure II.25**). Thus, this mechanism still needs to be refined.

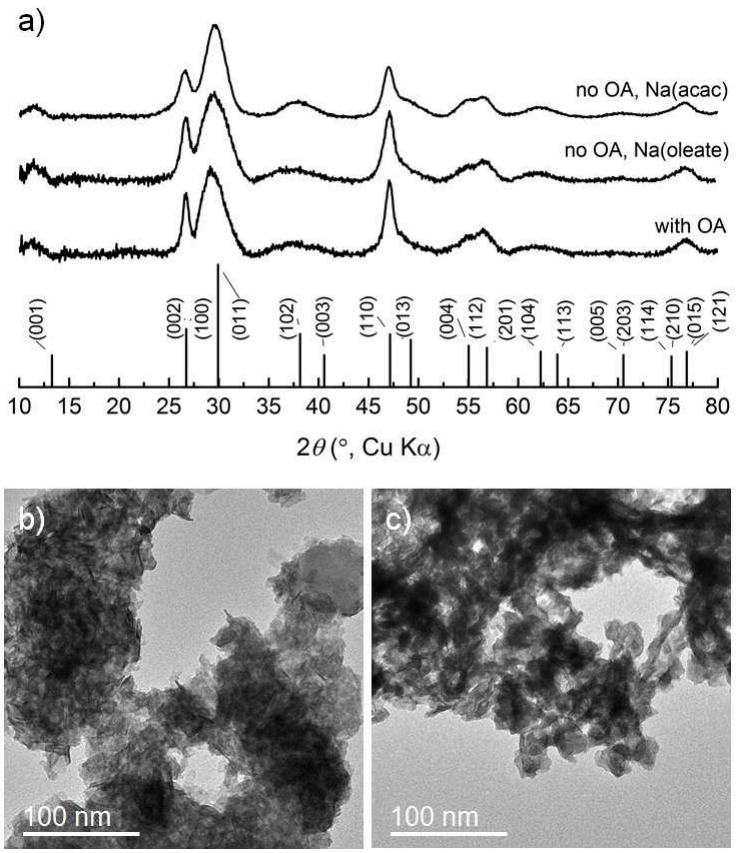

Figure II.25: Synthesis of Gd_2O_2S nanoplatelets without oleic acid and without both oleic acid and oleate. a) XRD patterns of the products as well as the reference pattern of bulk Gd_2O_2S (JCPDS 79-5662). TEM images of the nanoparticles resulted from synthesis a) without oleic acid and c) without both oleic acid and oleate.

The above conclusions were applied for monometallic Gd_2O_2S nanoplatelets. Nevertheless, they are likely applicable for bimetallic $Gd_{2(1-x)}Ce_xO_2S$ nanoplatelets as well. Our preliminary results showed that sodium is also necessary for the synthesis of $Gd_{2(1-x)}Ce_xO_2S$ nanoplatelets and can be completely removed from the final product by the same washing with water (data not shown).

II.5. Conclusion

By employing colloidal synthesis in organic solvent, we were able to synthesized crystalline gadolinium oxysulfide and gadolinium-cerium oxysulfide $Gd_{2(1-x)}Ce_xO_2S$ (x = 0, 0.01, 0.05, 0.10, 0.20, 0.50) nanoplatelets. They are fairly small (2 nm thick and 20 nm wide) and are potential versatile nanomaterials. We expect that they can exhibit interesting absorption, magnetic and catalytic properties. We also assume that they are able to host other lanthanides for tunable photoluminescent property.

Before applying the safer-by-design approach to these promising nanomaterials and studying their properties, functionalities and toxicity, a detailed description of the these $Gd_{2(1-x)}Ce_xO_2S$ nanoplatelets is required. Important hints were deduced from the results of complementary characterization techniques. We summarize our findings in **Figure II.26**.

In particular, the obtained $Gd_{2(1-x)}Ce_xO_2S$ phases are solid solutions of Gd_2O_2S and Ce_2O_2S if kept under inert atmosphere. In ambient air, the nanoparticles start to be oxidized above 40% of Ce. Also, the nanoplatelets terminate by $[Ln_2O_2]^{2+}$ (Ln = Gd, Ce) layers in their basal facets. The resulting charged surfaces are coordinated by oleates, assuring the electrical neutrality.

We showed that sodium in particular, or alkali-metal in general, are necessary for the formation of Gd_2O_2S nanoplatelets. However, they remain in the final product and their quantity (up to 33% vs. lanthanide) is irreproducible through experiments. Yet, we determined that the sodium likely locates at the surface of the nanoplatelets and can be completely eliminated (within the experimental error margin of the chemical composition analysis technique) without modifying the crystal structure of the latter. Thus, we concluded that this uncontrolled quantity is labile enough to be removed, which is good news for the subsequent studies of properties, functionalities and toxicity of the nanoplatelets.

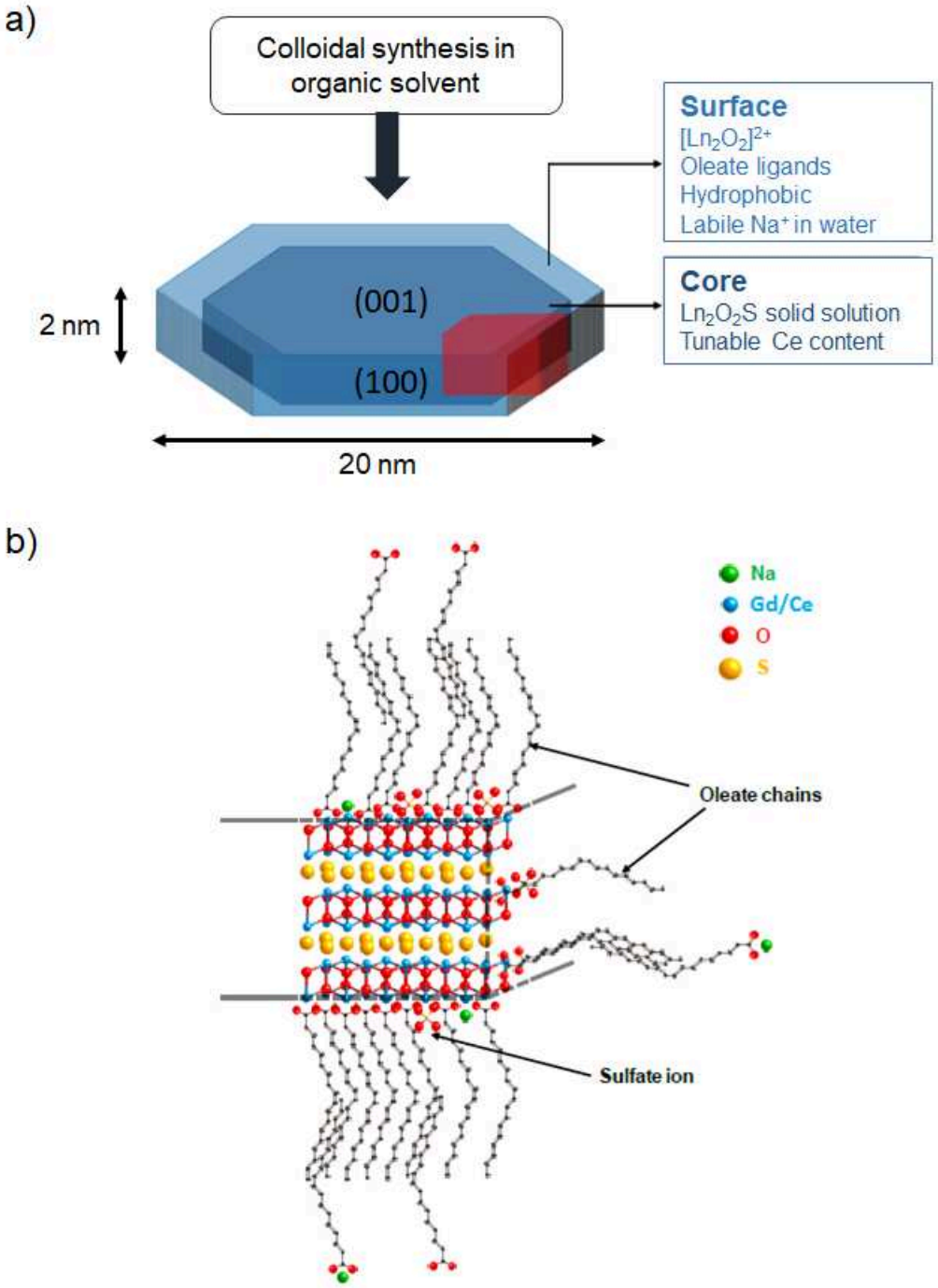

Figure II.26: a) Schematic representation of $Gd_{2(1-x)}Ce_xO_2S$ nanoplatelets and b) zoom in the red area with details of the structure at the interface between the nanocrystal and the ligands (adapted from ref 5). Ln indicates either Gd or Ce.

References

(1) Eick, H. A. The Preparation, Lattice Parameters and Some Chemical Properties of the Rare Earth Mono-Thio Oxides. *J. Am. Chem. Soc.* **1958**, *80* (1), 43–44.

(2) Li, Y.; Huang, Y.; Bai, T.; Li, L. Straightforward Conversion Route to Nanocrystalline Monothiooxides of Rare Earths through a High-Temperature Colloid Technique. *Inorg. Chem.* **2000**, *39* (15), 3418–3420.

(3) Mayer, J. M.; Schneemeyer, L. F.; Siegrist, T.; Waszczak, J. V.; Van Dover, B. New Layered Iron-Lanthanum-Oxide-Sulfide and -Selenide Phases: Fe2La2O3E2(E= S,Se). *Angew. Chemie Int. Ed. English* **1992**, *31* (12), 1645–1647.

(4) Flahaut, J.; Guittard, M.; Patrie, M. Les Oxysulfures Me2O2S Des Éléments Du Groupe Des Terres Rares. *Bull. Soc. Chim. Fr.* 1958, pp 990–994.

(5) Larquet, C. Nanoparticles of Lanthanide and Transition Metal Oxysulfides: From Colloidal Synthesis to Structure, Surface, Optical and Magnetic Properties, 2018.

(6) Larquet, C.; Anh-Minh, N.; Thi Kim-Chi, L.; Ávila-Gutiérrez, M.; Carenco, S. Les Oxysulfures de Lanthanides : Un Terrain de Jeu Pour La Nanochimie. *Actual. Chim.* **2019**, No. 436, 28–31.

(7) Ronda, C. R.; Jüstel, T.; Nikol, H. Rare Earth Phosphors: Fundamentals and Applications. *J. Alloys Compd.* **1998**, *275–277*, 669–676.

(8) Jüstel, T.; Nikol, H.; Ronda, C. New Developments in the Field of Luminescent Materials for Lighting and Displays. *Angew. Chemie - Int. Ed.* **1998**, *37* (22), 3084–3103.

(9) Rossner, W.; Grabmaier, B. C. Phosphors for X-Ray Detectors in Computed Tomography. *J. Lumin.* **1991**, *48–49* (PART 1), 29–36.

(10) Sun, W.; Zhu, K.; Xu, H.; Yang, X.; Yu, M.; Li, X.; Wang, L.; Zhang, Q. Enhanced Absorbing Property of Sm2O2S Laser Absorbent by Doping Er3+/Tm3+. *J. Mater. Sci. Mater. Electron.* **2017**, *28* (1), 697–701.

(11) Iparraguirre, I.; Azkargorta, J.; Merdrignac-Conanec, O.; Al-Saleh, M.; Chlique, C.; Zhang, X.; Balda, R.; Fernández, J. Laser Action in Nd3+-Doped Lanthanum Oxysulfide Powders. *Opt. Express* **2012**, *20* (21), 23690.

(12) Ding, Y.; Gu, J.; Ke, J.; Zhang, Y. W.; Yan, C. H. Sodium Doping Controlled Synthesis of Monodisperse Lanthanide Oxysulfide Ultrathin Nanoplates Guided by Density

Functional Calculations. *Angew. Chemie - Int. Ed.* **2011**, *50* (51), 12330–12334.

(13) Lei, L.; Zhang, S.; Xia, H.; Tian, Y.; Zhang, J. J.; Xu, S. Q. Controlled Synthesis of Lanthanide-Doped Gd2O2S Nanocrystals with a Novel Excitation-Dependent Multicolor Emissions. *Nanoscale* **2017**, *16*, 2102–2105.

(14) Ajithkumar, G.; Yoo, B.; Goral, D. E.; Hornsby, P. J.; Lin, A.-L.; Ladiwala, U.; Dravid, V. P.; Sardar, D. K. Multimodal Bioimaging Using a Rare Earth Doped Gd2O2S:Yb/Er Phosphor with Upconversion Luminescence and Magnetic Resonance Properties. *J. Mater. Chem. B* **2013**, *1* (11), 1561.

(15) Li, W.; Liu, Y.; Ai, P. Synthesis and Luminescence Properties of Red Long-Lasting Phosphor Y2O2S:Eu3+, Mg2+, Ti4+ Nanoparticles. *Mater. Chem. Phys.* **2010**, *119* (1–2), 52–56.

(16) Osseni, S. a; Lechevallier, S.; Verelst, M.; Perriat, P.; Dexpert-Ghys, J.; Neumeyer, D.; Garcia, R.; Mayer, F.; Djanashvili, K.; Peters, J. a; et al. Gadolinium Oxysulfide Nanoparticles as Multimodal Imaging Agents for T2-Weighted MR, X-Ray Tomography and Photoluminescence. *Nanoscale* **2014**, *6* (1), 555–564.

(17) Yang, L.; Cai, Z.; Hao, L.; Xing, Z.; Dai, Y.; Xu, X.; Pan, S.; Duan, Y.; Zou, J. Nano Ce2O2S with Highly Enriched Oxygen-Deficient Ce3+ Sites Supported by N and S Dual-Doped Carbon as an Active Oxygen-Supply Catalyst for the Oxygen Reduction Reaction. *ACS Appl. Mater. Interfaces* **2017**, *9* (27), 22518–22529.

(18) Tan, S.; Paglieri, S. N.; Li, D. Nano-Scale Sulfur-Tolerant Lanthanide Oxysulfide/Oxysulfate Catalysts for Water-Gas-Shift Reaction in a Novel Reactor Configuration. *Catal. Commun.* **2016**, *73*, 16–21.

(19) Martinez, H.; Benayad, A.; Gonbeau, D.; Vinatier, P.; Pecquenard, B.; Levasseur, A. Influence of the Cation Nature of High Sulfur Content Oxysulfide Thin Films MO S (M=W, Ti) Studied by XPS. *Appl. Surf. Sci.* **2004**, *236* (1–4), 377–386.

(20) Martin-Litas, I.; Vinatier, P.; Levasseur, A.; Dupin, J. C.; Gonbeau, D. Electrochemical Properties of Tungsten Oxysulphide Thin Films as Positive Electrodes for Lithium Microbatteries. *Bull. Mater. Sci.* **2003**, *26* (7), 673–681.

(21) Yufit, V.; Nathan, M.; Golodnitsky, D.; Peled, E. Thin-Film Lithium and Lithium-Ion Batteries with Electrochemically Deposited Molybdenum Oxysulfide Cathodes. *J. Power Sources* **2003**, *122* (2), 169–173.

(22) Qiao, Y.; Hu, X.; Liu, Y.; Liang, G.; Croft, M. C.; Huang, Y. Surface Modification of

MoOxSy on Porous TiO2 Nanospheres as an Anode Material with Highly Reversible and Ultra-Fast Lithium Storage Properties. *J. Mater. Chem. A* **2013**, *1* (47), 15128.

(23) Baqais, A.; Curutchet, A.; Ziani, A.; Ait Ahsaine, H.; Sautet, P.; Takanabe, K.; Le Bahers, T. Bismuth Silver Oxysulfide for Photoconversion Applications: Structural and Optoelectronic Properties. *Chem. Mater.* **2017**, *29* (20), 8679–8689.

(24) Ubaldini, A.; Giannini, E.; Senatore, C.; Van Der Marel, D. BiOCuS: A New Superconducting Compound with Oxypnictide-Related Structure. *Phys. C Supercond. its Appl.* **2010**, *470* (SUPPL.1), S356–S357.

(25) Salter, E. J. T.; Blandy, J. N.; Clarke, S. J. Crystal and Magnetic Structures of the Oxide Sulfides CaCoSO and BaCoSO. *Inorg. Chem.* **2016**, *55* (4), 1697–1701.

(26) Pandey, S. K.; Pandey, S.; Pandey, A. C.; Mehrotra, G. K. Zinc Oxysulfide Ternary Alloy Nanocrystals: A Bandgap Modulated Photocatalyst. *Appl. Phys. Lett.* **2013**, *102* (23), 233110.

(27) Pandey, S. K.; Pandey, S.; Parashar, V.; Yadav, R. S.; Mehrotra, G. K.; Pandey, A. C. Bandgap Engineering of Colloidal Zinc Oxysulfide via Lattice Substitution with Sulfur. *Nanoscale* **2014**, *6* (3), 1602–1606.

(28) Abdullah, H.; Kuo, D. H.; Chen, X. High Efficient Noble Metal Free Zn(O,S) Nanoparticles for Hydrogen Evolution. *Int. J. Hydrogen Energy* **2017**, *42* (9), 5638–5648.

(29) Nelson, A.; Fritz, K. E.; Honrao, S.; Hennig, R. G.; Robinson, R. D.; Suntivich, J. Increased Activity in Hydrogen Evolution Electrocatalysis for Partial Anionic Substitution in Cobalt Oxysulfide Nanoparticles. *J. Mater. Chem. A* **2016**, *4* (8), 2842–2848.

(30) Ishikawa, A.; Takata, T.; Kondo, J. N.; Hara, M.; Kobayashi, H.; Domen, K. Oxysulfide Sm2Ti2S2O5 as a Stable Photocatalyst for Water Oxidation and Reduction under Visible Light Irradiation ($\lambda \leq 650$ Nm). *J. Am. Chem. Soc.* **2002**, *124* (45), 13547–13553.

(31) Naatz, H.; Lin, S.; Li, R.; Jiang, W.; Ji, Z.; Chang, C. H.; Köser, J.; Thöming, J.; Xia, T.; Nel, A. E.; et al. Safe-by-Design CuO Nanoparticles via Fe-Doping, Cu–O Bond Length Variation, and Biological Assessment in Cells and Zebrafish Embryos. *ACS Nano* **2017**, *11* (1), 501–515.

(32) Guo, T.; Lin, Y.; Li, Z.; Chen, S.; Huang, G.; Lin, H.; Wang, J.; Liu, G.; Yang, H. H.

Gadolinium Oxysulfide-Coated Gold Nanorods with Improved Stability and Dual-Modal Magnetic Resonance/Photoacoustic Imaging Contrast Enhancement for Cancer Theranostics. *Nanoscale* **2017**, *9* (1), 56–61.

(33) Osseni, S. A.; Lechevallier, S.; Verelst, M.; Dujardin, C.; Dexpert-Ghys, J.; Neumeyer, D.; Leclercq, M.; Baaziz, H.; Cussac, D.; Santran, V.; et al. New Nanoplatform Based on Gd 2 O 2 S: Eu 3+ Core: Synthesis, Characterization and Use for in Vitro Bio-Labelling. *J. Mater. Chem.* **2011**, *21* (45), 18365–18372.

(34) Rosticher, C.; Viana, B.; Fortin, M. A.; Lagueux, J.; Faucher, L.; Chanéac, C. Gadolinium Oxysulfide Nanoprobes with Both Persistent Luminescent and Magnetic Properties for Multimodal Imaging. *RSC Adv.* **2016**, *6* (60), 55472–55478.

(35) Santelli, J.; Lechevallier, S.; Baaziz, H.; Vincent, M.; Martinez, C.; Mauricot, R.; Parini, A.; Verelst, M.; Cussac, D. Multimodal Gadolinium Oxysulfide Nanoparticles: A Versatile Contrast Agent for Mesenchymal Stem Cell Labeling. *Nanoscale* **2018**, *10* (35), 16775–16786.

(36) Larquet, C.; Nguyen, A.-M.; Ávila-Gutiérrez, M.; Tinat, L.; Lassalle-Kaiser, B.; Gallet, J.-J.; Bournel, F.; Gauzzi, A.; Sanchez, C.; Carenco, S. Synthesis of Ce2O2S and Gd2(1–y)Ce2yO2S Nanoparticles and Reactivity from in Situ X-Ray Absorption Spectroscopy and X-Ray Photoelectron Spectroscopy. *Inorg. Chem.* **2017**, *56* (22), 14227–14236.

(37) Trovarelli, A.; De Leitenburg, C.; Boaro, M.; Dolcetti, G. The Utilization of Ceria in Industrial Catalysis. *Catal. Today* **1999**, *50* (2), 353–367.

(38) Walkey, C.; Das, S.; Seal, S.; Erlichman, J.; Heckman, K.; Ghibelli, L.; Traversa, E.; McGinnis, J. F.; Self, W. T. Catalytic Properties and Biomedical Applications of Cerium Oxide Nanoparticles. *Environ. Sci. Nano* **2015**, *2* (1), 33–53.

(39) Eriksson, P.; Tal, A. A.; Skallberg, A.; Brommesson, C.; Hu, Z.; Boyd, R. D.; Olovsson, W.; Fairley, N.; Abrikosov, I. A.; Zhang, X.; et al. Cerium Oxide Nanoparticles with Antioxidant Capabilities and Gadolinium Integration for MRI Contrast Enhancement. *Sci. Rep.* **2018**, *8* (1), 6999.

(40) Biswas, A.; Bayer, I. S.; Biris, A. S.; Wang, T.; Dervishi, E.; Faupel, F. Advances in Top–down and Bottom–up Surface Nanofabrication: Techniques, Applications & Future Prospects. *Adv. Colloid Interface Sci.* **2012**, *170* (1–2), 2–27.

(41) van Embden, J.; Chesman, A. S. R.; Jasieniak, J. J. The Heat-up Synthesis of Colloidal

Nanocrystals. *Chem. Mater.* **2015**, *27* (7), 2246–2285.

(42) Thanh, N. T. K.; Maclean, N.; Mahiddine, S. Mechanisms of Nucleation and Growth of Nanoparticles in Solution. *Chem. Rev.* **2014**, *114* (15), 7610–7630.

(43) Kwon, S. G.; Hyeon, T. Formation Mechanisms of Uniform Nanocrystals via Hot-Injection and Heat-up Methods. *Small* **2011**, *7* (19), 2685–2702.

(44) Chu, D. B. K.; Owen, J. S.; Peters, B. Nucleation and Growth Kinetics from LaMer Burst Data. *J. Phys. Chem. A* **2017**, *121* (40), 7511–7517.

(45) Polte, J. Fundamental Growth Principles of Colloidal Metal Nanoparticles - a New Perspective. *CrystEngComm* **2015**, *17* (36), 6809–6830.

(46) Mer, V. K. La. Nucleation in Phase Transitions. *Ind. Eng. Chem.* **1952**, *44* (6), 1270–1277.

(47) Becker, R.; Döring, W. Kinetische Behandlung Der Keimbildung in Übersättigten Dämpfen. *Ann. Phys.* **1935**, *416* (8), 719–752.

(48) Heuer-Jungemann, A.; Feliu, N.; Bakaimi, I.; Hamaly, M.; Alkilany, A.; Chakraborty, I.; Masood, A.; Casula, M. F.; Kostopoulou, A.; Oh, E.; et al. The Role of Ligands in the Chemical Synthesis and Applications of Inorganic Nanoparticles. *Chem. Rev.* **2019**, *119* (8), acs.chemrev.8b00733.

(49) Jolivet, J. P.; Henry, M.; Livage, J. *Metal Oxide Chemistry and Synthesis: From Solution to Solid State*; John Wiley, 2000.

(50) Tian, Y.; Fu, Y.; Xing, M.; Luo, X. Upconversion Luminescence Properties of Y2O3:Yb,Er and Y2 O2S:Yb,Er Nanoparticles Prepared by Complex Precipitation. *J. Nanomater.* **2015**, *2015*, 1–7.

(51) Thomson, J. W.; Nagashima, K.; MacDonald, P. M.; Ozin, G. A. From Sulfur-Amine Solutions to Metal Sulfide Nanocrystals: Peering into the Oleylamine-Sulfur Black Box. *J. Am. Chem. Soc.* **2011**, *133* (13), 5036–5041.

(52) Zhang, T.; Gu, J.; Ding, Y.; Zhang, Y.-W.; Yan, C.-H. Experimental and Theoretical Studies on the Controlled Synthesis of Alkali-Metal-Doped Rare-Earth Oxysulfide Nanocrystals. *Chempluschem* **2013**, *78* (6), 515–521.

(53) Liu, G.; Conn, C. E.; Drummond, C. J. Lanthanide Oleates: Chelation, Self-Assembly, and Exemplification of Ordered Nanostructured Colloidal Contrast Agents for Medical Imaging. *J. Phys. Chem. B* **2009**, *113* (49), 15949–15959.

(54) Larquet, C.; Hourlier, D.; Nguyen, A.; Torres-Pardo, A.; Gauzzi, A.; Sanchez, C.; Carenco, S. Thermal Stability of Oleate-Stabilized Gd2O2S Nanoplates in Inert and Oxidizing Atmospheres. *ChemNanoMat* **2019**, *5* (4), 539–546.

(55) Hug, S. J. In Situ Fourier Transform Infrared Measurements of Sulfate Adsorption on Hematite in Aqueous Solutions. *J. Colloid Interface Sci.* **1997**, *188* (2), 415–422.

(56) Lian, J.; Liu, F.; Wang, X.; Sun, X. Hydrothermal Synthesis and Photoluminescence Properties of Gd2O2SO4:EU3+ Spherical Phosphor. *Powder Technol.* **2014**, *253*, 187–192.

(57) Deacon, G. B.; Phillips, R. J. Relationships between the Carbon-Oxygen Stretching Frequencies of Carboxylato Complexes and the Type of Carboxylate Coordination. *Coord. Chem. Rev.* **1980**, *33* (3), 227–250.

Chapter III

Towards safer-by-design bimetallic Gd-Ce oxysulfide nanoparticles for photocatalysis

Table of contents

III.1. Photocatalysis 85
III.1.1. Photocatalytic process 85
III.1.2. Photocatalysts 86
III.1.3. Nanoscale photocatalyst: a double-edged sword? 88
III.2. $Gd_{2(1-x)}Ce_{2x}O_2S$ nanoparticles as photocatalysts with visible light 89
III.2.1. Ligand removal 89
III.2.1.1. Washing of nanoparticles 89
2.1.2. Ligand burning 90
2.1.3. Conclusion 92
III.2.2. Tunable absorption 93
III.2.3. Photodegradation of organic dyes 95
III.2.4. Radical production 100
III.2.4.1. Dithiothreitol (DTT) as radical probe 100
III.2.4.2. Validation of the method with commercial TiO_2 P25 nanoparticles 102
III.2.4.3. Bimetallic $Gd_{2(1-x)}Ce_xO_2S$ nanoparticles 104
III.3. Cytotoxicity of $Gd_{2(1-x)}Ce_xO_2S$ nanoparticles 108
III.3.1. Cell line model 108
III.3.2. Cell viability 109
III.3.2.1. Mitochondrial activity 109
III.3.2.2. DNA quantification 112
III.3.2.3. Membrane integrity 113
III.3.3. Sub-lethal effects 115
III.3.3.1. Intracellular ROS activity 116
III.3.3.2. Oxidative stress 118
III.3.3.3. Inflammatory response 119

III.4. Possible origins of cytotoxicity 122
III.4.1. Sodium content 122
III.4.2. Specific surface area 122
III.4.3. Stability of $Gd_{2(1-x)}Ce_{2x}O_2S$ nanoparticles in aqueous media 124
III.4.4. Local characterization of cell-nanoparticle interaction 127
III.4.4.1. XAS-XRF hyperspectral imaging of cells in cryogenic mode 127
III.4.4.2. Imaging cells and nanoparticles composition 128
III.4.4.3. Chemical speciation imaging 134
III.5. *In vivo* toxicity study 137
III.5.1. Non-surgical intratracheal instillation of mice 137
III.5.2. Bronchoalveolar lavage fluid analysis 138
III.5.2.1. Differential cell counts 138
III.5.2.2. Pro-inflammatory cytokine levels 139
III.5.3. Pulmonary toxicity of $Gd_{2(1-x)}Ce_xO_2S$ nanoparticles 140
III.6. Discussion 141
III.6.1. Photocatalytic activity of $Gd_{2(1-x)}Ce_xO_2S$ nanoparticles 141
III.6.2. Toxicity of $Gd_{2(1-x)}Ce_xO_2S$ nanoparticles 142
III.7. Conclusion 146
References 148

III.1. Photocatalysis

Environmental pollution is one of most serious global problem at the moment. It is accompanied by the lack of sufficiently clean energy sources that worsens the situation. In view of this matter, the sun is considered an inexhaustibly abundant, clean and safe energy source. Photocatalysis is one of the most effective strategies to take advantage of this energy. Since its discovery in the early 20th century, it has been regarded as a major advance in solving the global energy problem, due to its applications in environmental cleaning such as self-cleaning glasses, purification of water and air, artificial photosynthesis, etc.[1]

One of the first impacting reports on photocatalysis was that of Fujishima and Honda in 1972.[2] The authors described the electrochemical photolysis of water to produce oxygen and hydrogen on semiconducting TiO_2 electrodes. Since then, immense research efforts were made by the scientific community to understand the fundamental mechanism behind the process and improve its efficiency.[1,3–5]

III.1.1. Photocatalytic process

The photocatalytic process is defined as the acceleration of a reaction with light in the presence of a catalyst, usually a semiconductor. The reaction occurs on its solid surface. The process first involves the transfer and the adsorption of the reactants from the reaction medium to the reaction sites on the surface of the catalyst. This depends on the different properties of the catalyst such as surface area, porosity, charge, hydrophobicity/hydrophilicity, etc. In particular, higher surface area provides more reaction sites for the reactants and increase the reaction yield.

The reaction is initiated by absorption of light with energy equal or greater than the bandgap of the semiconductor. As a result of this irradiation, pairs of electrons and holes are generated in the conduction band (CB) and the valence band (VB) of the solid, respectively (**Figure III.1**). Subsequently, there are two possible scenarios: the electron and hole recombine and generate heat or they are separated and diffuse to the surface of the catalyst, in contact with the reactants. In the second case, the catalyst can then act as electron donor or acceptor towards adsorbed molecules if the redox reaction is thermodynamically allowed.

As an example of this process, photodegradation of organic pollutants in the presence of TiO_2 nanoparticles in water is depicted in **Figure III.1**. Upon bandgap excitation of the material, surface electrons and holes react with oxygen and water molecules to form superoxide radicals $O_2^{\bullet-}$ and hydroxyl radicals $^{\bullet}OH$ respectively. These radicals then react with the organic pollutant to break it down into small molecules such as water and CO_2.

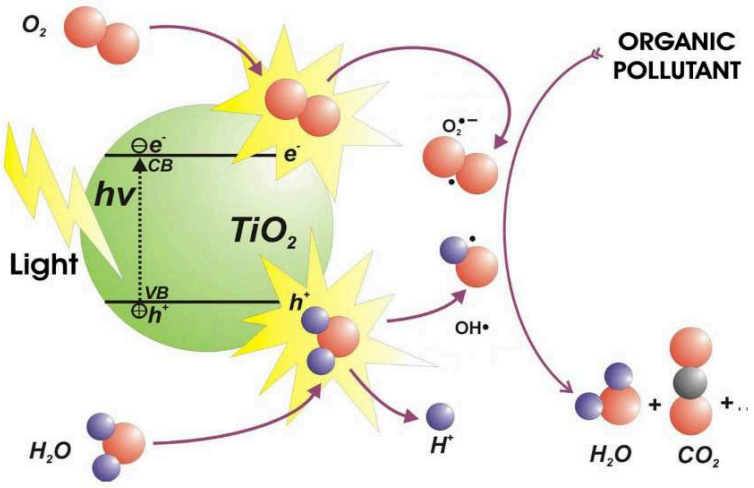

Figure III.1: Schematic representation of photocatalysis process by bandgap illumination of a semiconductor nanoparticle (taken from ref 4). CB and VB stand for conduction band and valence band respectively.

III.1.2. Photocatalysts

Based on the aforementioned principle of the photocatalytic process, several criteria for the design of photocatalyst can be deduced: (i) high surface area to increase the contact with the reactants; (ii) appropriate surface state (porosity, charge, hydrophobicity/hydrophilicity) so that the surface is accessible to the reactants; (iii) suitable bandgap value and position for easier excitation of the catalyst and to trigger redox reactions; (iv) high absorption coefficient to generate more electron-hole pairs; (v) low probability of electron-hole recombination to enhance the efficiency of the process.

The era of photocatalyst development coincides with the boom of nanotechnology. This led to a focus shift in the field towards nanoscale photocatalysts which exhibit extremely high surface-to-volume ratio. Nowadays, titanium dioxide TiO_2 is the most common photocatalyst because it features excellent efficiency and chemical stability.[1] In particular, the commercial TiO_2 P25 powder, containing nanoparticles of anatase and rutile phases, is widely considered

the standard material for photocatalysis.[6] However, TiO_2 P25 nanoparticles exhibit a relatively wide bandgap of ca. 3.1 eV, meaning that they only absorb UV light ($\lambda < 400$ nm). This only represents ca. 7% of the total irradiated solar energy (**Figure III.2**a). Taking into account the limited yield of electron-hole pair generation in the photocatalyst, even less energy eventually serves the catalytic reaction. On the other hand, the visible region of the spectrum represents ca. 44% of the total energy of the sun. Therefore, new photocatalysts operating with visible light are highly sought.

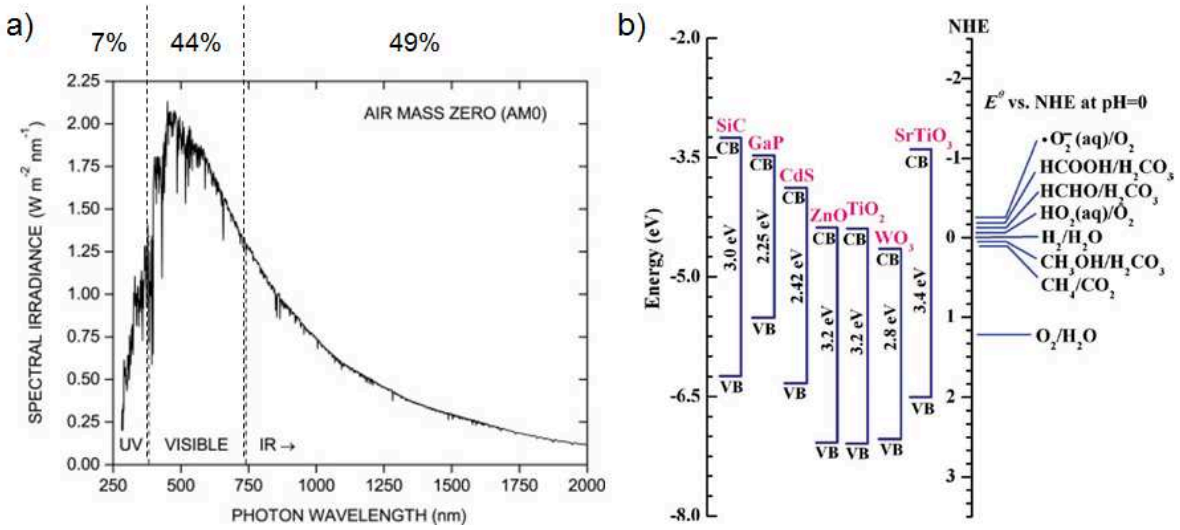

Figure III.2: a) Solar spectrum and energy percentages of UV, visible and infrared lights (adapted from ref 7). b) Positions of conduction and valence bands of several semiconductors relative to the energy levels of various redox couples in water (taken from ref 8).

Several strategies were examined to develop photocatalysts with visible light. These strategies include modification of TiO_2 to tune its bandgap by doping with light elements and d-block metals or by construction of hetero-junctions with metals such as Pt, Pd. Moreover, semiconductors other than TiO_2 such as WO_3, CdS or $BiVO_4$ were also considered.[8–10] The bandgaps of some of those are presented in **Figure III.2**b in comparison with the energy levels of various redox couples in water. Nevertheless, so far, the efficiency of the photocatalysis is still much lower with visible light than UV light. They usually suffer from high recombination rate of electron-hole pairs or low absorption cross section. Efforts still are still needed to develop new efficient photocatalysts with visible light.

III.1.3. Nanoscale photocatalyst: a double-edged sword?

In addition to make efforts to develop new nanoscale photocatalysts with high efficiency, it is also important to consider their potential toxicity. There was first a general consensus in the photocatalysis field that TiO_2 nanoparticles were non-toxic, based on results of their cytotoxicity tests.[1,11,12] Yet, inhalation studies on mice seemed to suggest otherwise.[13–15] Inflammatory responses were prominently shown. In 2017, the European Chemicals Agency even concluded that TiO_2, without further physicochemical description, should be classified as category 2 carcinogen (suspected human carcinogen). There has also been evidence of TiO_2 nanoparticles impacting the ecosystem.[16,17]

This controversy around the safety of TiO_2 nanoparticles, even though mainly present in the sectors of food and cosmetics, still emphasizes the need to develop new photocatalysts. Potential backlash from the society due to the concerns towards nanomaterials in general may hinder their development for photocatalysis. Therefore, we apply the safer-by-design approach (see Chapter I) for $Gd_{2(1-x)}Ce_xO_2S$ nanoparticles to evaluate their potential as photocatalysts with visible light (**Figure III.3**). In particular, their absorption properties, performance in photocatalysis tests and preliminary toxicity will be discussed next in this chapter.

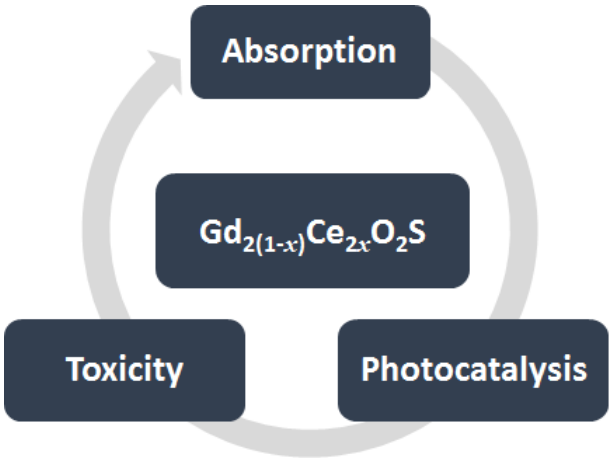

Figure III.3: Safer-by-design approach for $Gd_{2(1-x)}Ce_xO_2S$ as potential photocatalysts with visible light.

III.2. $Gd_{2(1-x)}Ce_{2x}O_2S$ nanoparticles as photocatalysts with visible light

III.2.1. Ligand removal

In the previous chapter, we showed that oleates were the main ligands at the surface of as prepared $Gd_{2(1-x)}Ce_xO_2S$ nanoplatelets. For photocatalytic reactions, however, the surface of the catalyst needs to be accessible to water molecules for radical production. Consequently, the hydrophobic carbon chains are an obstacle for photodegradation process of organic pollutants. We thus attempted to remove these organic ligands.

III.2.1.1. Washing of nanoparticles

The simplest way to remove the organic ligands is washing the nanoparticles with solvents. We thus increased the number of washes after the synthesis. The nanoparticles isolated from the reaction medium were washed up to 7 times with mixture of *n*-hexane and ethanol (1:3 in volume, 40 mL in total). After each wash, a comparable amount of product (ca. 2 mg) was analyzed by Fourier Transform Infrared spectroscopy (FTIR) in ATR mode. The spectra of washed Gd_2O_2S nanoparticles are shown in **Figure III.4**. Characteristic vibration bands of the ligands such as the asymmetric and symmetric C-H stretching bands at ca. 2900 cm^{-1} and the two bands of coordinated COO^- groups at 1350-1550 cm^{-1} are analyzed.

After the first wash, we clearly observe C-H vibration bands whereas those of the coordinated COO^- groups are faint. This suggests the presence of uncoordinated molecules such as oleylamine, octadecene or oleic acid, trapped in the product. The signals of these molecules mask those of coordinated oleates ligands. Accordingly, the obtained product was also very viscous.

As expected, a sole wash is not enough to remove excess organic molecules from the product. In the previously described synthesis of $Gd_{2(1-x)}Ce_xO_2S$ nanoplatelets (see Chapter II), the nanoparticles were washed three times. After three washes, the COO^- vibration bands appear more pronounced. We thus conclude that the majority of excess uncoordinated ligands was removed. The product was a dry powder at this stage.

Starting from the 4th wash, the FTIR spectra show insignificant decrease of the intensities of both C-H and COO^- vibration bands. Even after seven washes in total, these bands are still

present. Washing the nanoparticles with a mixture of *n*-hexane and ethanol does not seem to be the most efficient method to remove ligands.

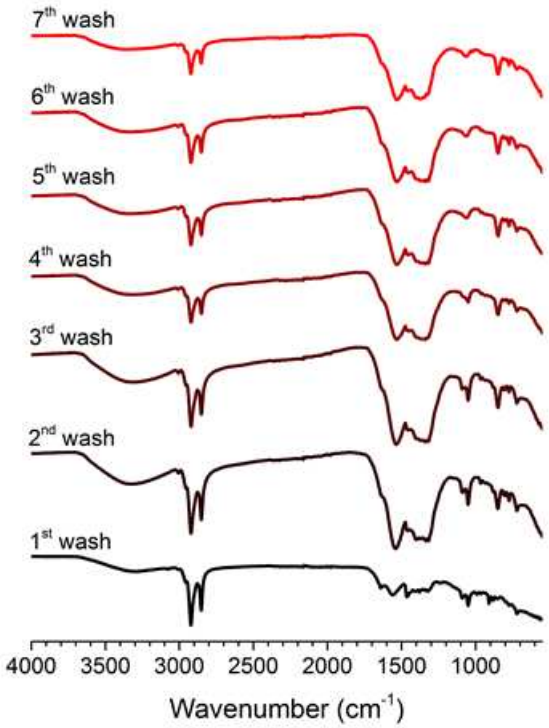

Figure III.4: FTIR spectra of Gd_2O_2S nanoparticles after different numbers of wash.

2.1.2. Ligand burning

We turned to another ligand removal method which is heating the product at high temperatures. In fact, the organic compounds have lower thermal stability than the inorganic core. Taking advantage of this, we heated the synthesized Gd_2O_2S nanoparticles at 500 °C during 2 hours. The thermal treatment was carried out under inert atmosphere (argon) in order to avoid the oxidation of oxysulfide phase.

The product was first analyzed by FTIR (**Figure III.5**). Strikingly, the asymmetric and symmetric C-H stretching bands at ca. 2900 cm^{-1} disappear after the thermal treatment. This suggests decomposition of the carbon chains, resulting in free carbon. We still observe the vibrations bands of coordinated COO^- groups. They probably remain to compensate the positively charged surface of the nanoparticles even though their carbon chain is decomposed. We speculate that these COO^- groups belong to short chain oleates such as acetates. These

results have later been confirmed in the lab with in-depth Thermogravimetric Analysis (TGA) (see Appendix IV).[18] Besides carboxylate groups, sulfates and carbonates are still present in the product after ligand burning.

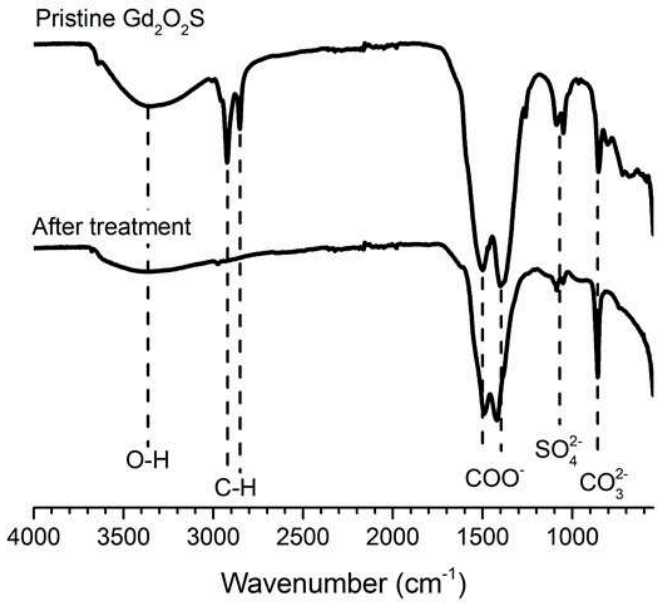

Figure III.5: FTIR spectra of Gd_2O_2S nanoparticles before and after thermal treatment at 500 °C under inert atmosphere (argon).

TEM image of the product shows aggregates of nanoplatelets of size comparable to the pristine Gd_2O_2S (**Figure III.6**a and b). After the treatment, Gd_2O_2S is still the main crystalline phase, as shown by XRD (**Figure III.6**c). However, other narrow diffraction peaks are also detected. They may be attributed to oxides such as cubic Gd_2O_3, $NaGdO_2$ and gadolinium oxysulfate $Gd_2O_2SO_4$. The narrow peaks probably correspond to large nanoparticles present in the product but could not be observed by TEM. It should be reminded that our oxysulfide nanoparticles present sulfur defects. The formation of large oxysulfide crystals is thus prohibited and the oxygen-rich phases are favored.

We showed that the carbon chain of surface-coordinated oleates could be decomposed by thermal treatment of the nanoparticles during 2 hours at 500 °C under argon. The nanoplatelets were aggregated and large crystallites of oxides and oxysulfate were detected by XRD. We conclude that ligand burning can be an efficient method to remove organic ligands from the oxysulfide nanoparticles. Nevertheless, optimization of the treatment conditions needs to be done to avoid formation of oxygen-rich phases. Complementary results

have shown that a thermal treatment at 350 °C during 20 min under oxidizing atmosphere (O_2/He) could decompose the organic ligands while preserving the oxysulfide crystalline structure of the nanoparticles (see Appendix IV).[18] These results pave the way for future studies of properties of $Gd_{2(1-x)}Ce_xO_2S$ nanoparticles in the cases where the organic ligands are undesirable.

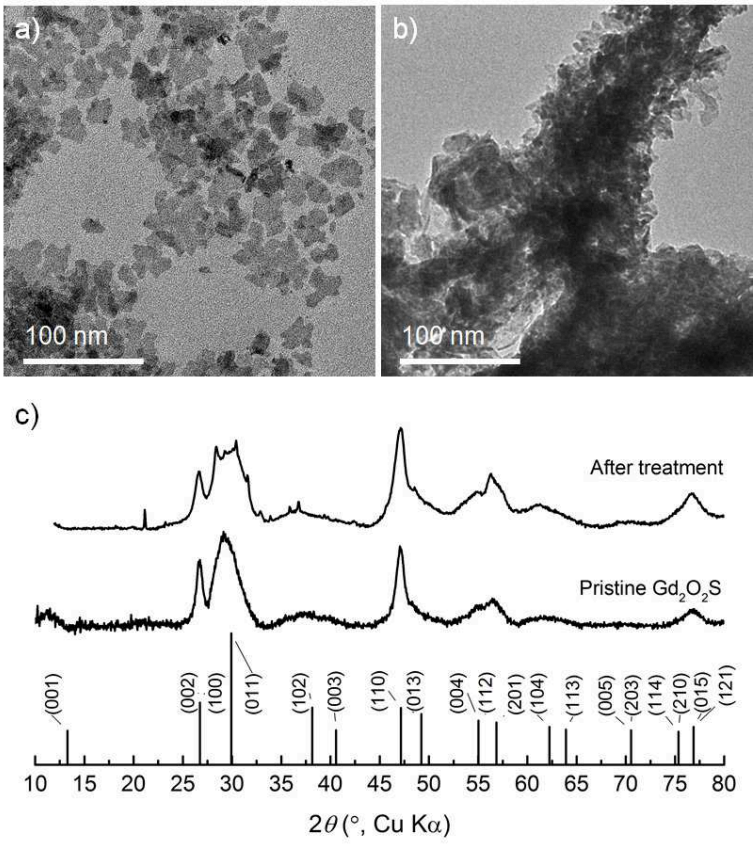

Figure III.6: Thermal treatment of Gd_2O_2S nanoparticles. TEM images of the nanoparticles a) before and b) after the treatment. c) XRD patterns of pristine nanoparticles and the product after the treatment. The reference pattern corresponds to bulk hexagonal Gd_2O_2S (JCPDS 79-5662).

2.1.3. Conclusion

In this section, we discussed the possibility of removing hydrophobic ligands from the synthesized Gd_2O_2S nanoparticles for catalytic reactions in aqueous media. The simple method of washing could only eliminate the excess uncoordinated ligands. On the other hand, thermal treatment at 500 °C could completely burn the carbon chains of the ligands, leaving short chain carboxylates on the surface of the nanoparticles. Nevertheless, oxides and oxysulfate phases were formed. Besides those two methods, we also attempted to displace the

oleates by smaller surface ligands such as BF_4^- at room temperature. However, after the treatment, oleates still remained and the nanoparticles were oxidized (data not shown).

These results emphasize the important role of oleates as surface ligand to ensure the charge balance and compensate the lack of sulfur of the oxysulfide nanoplatelets. Because the nanoplatelets are very thin (2 nm), complete removal of the ligands in solution may result in drastic modification of the overall object. Yet, ligand burning with optimized conditions can represent a smooth way to remove the ligands for future studies. In the present study, however, we use $Gd_{2(1-x)}Ce_xO_2S$ nanoparticles washed three times with mixture of *n*-hexane and ethanol.

III.2.2. Tunable absorption

In 1958, Flahaut et al. synthesized a series of bulk Ln_2O_2S (Ln = lanthanide) and reported their physical properties.[19] The authors stated that Gd_2O_2S was white while Ce_2O_2S was deep brown. Inspired by these results, we synthesized bimetallic $Gd_{2(1-x)}Ce_xO_2S$ nanoparticles with the hope to tune the absorption properties of the material by adjusting its cerium content.

At the nanoscale, the colors of the gadolinium and cerium oxysulfides seem to be similar to those of their bulk phase. Dry powder of synthesized Gd_2O_2S nanoparticles appears white (**Figure III.7**). As for Ce_2O_2S nanoparticles, their powder is deep brown but they are easily oxidized in air to give a green powder instead.[20] Colors of powders of bimetallic $Gd_{2(1-x)}Ce_xO_2S$ nanoparticles are between white and brown. The color gradually becomes darker as the cerium content increases (**Figure III.7**). This is probably due to the substitution of Gd^{III} for Ce^{III} in the Gd_2O_2S phase that we discussed in the previous chapter.

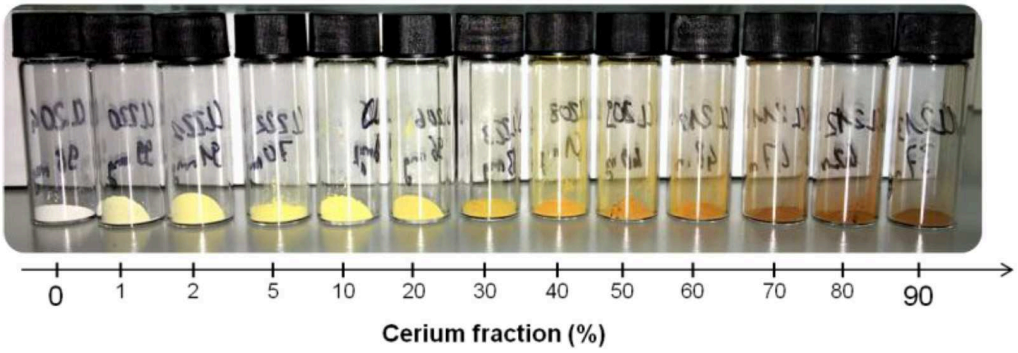

Figure III.7: Change of powder color of $Gd_{2(1-x)}Ce_{2x}O_2S$ nanoparticles (x from 0 to 90%) due to Gd^{III}/Ce^{III} substitution (taken from ref [21]).

To characterize the absorption of the synthesized $Gd_{2(1-x)}Ce_xO_2S$ (x = 0, 1, 5, 10, 20, 50%) powders, we employed UV-visible diffuse reflectance spectroscopy (**Figure III.8**). The Kubelka-Munk function of reflectance F(R) was calculated from obtained apparent absorbance. This function is directly proportional to the extinction coefficient of the material, thus to its absorption properties.

The Ce/Gd substitution strongly affects the absorption of the nanomaterials, in accordance to their color. In fact, spectrum of the synthesized Gd_2O_2S nanoparticles indicates absorption in the UV region with a threshold around 270 nm. The bandgap of the material was previously estimated at ca. 4.7 eV using Tauc plot.[21] This value is greater than that of TiO_2 P25 nanoparticles (ca. 3.1 eV). Whereas, spectra of synthesized $Gd_{2(1-x)}Ce_xO_2S$ nanoparticles shows gradual shifts of absorption threshold towards the visible region. At the extreme of cerium content in this series of samples, $GdCeO_2S$ (x = 50%) nanoparticles feature an absorption threshold over 530 nm, corresponding to an estimated bandgap of 2.3 eV.[21] The bandgap of $GdCeO_2S$ nanoparticles is thus smaller than that of TiO_2 P25 nanoparticles. It is also in the low side when compared to discovered photocatalysts with visible light such as WO_3 (**Figure III.2**b).

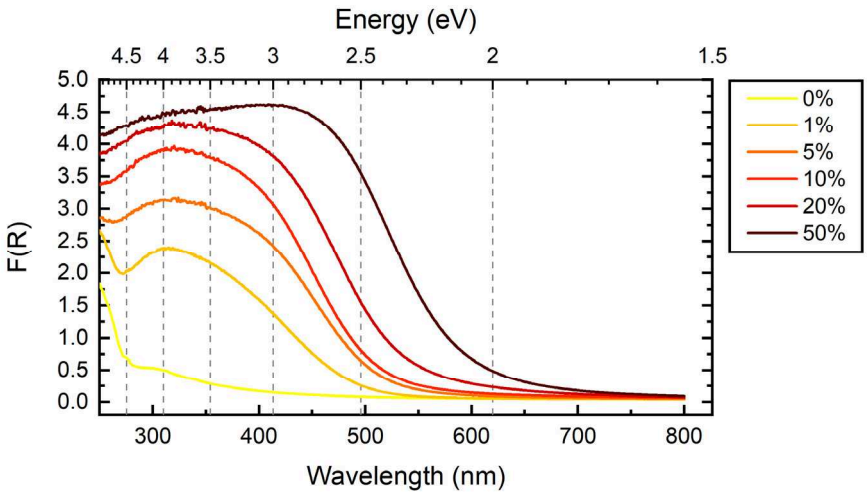

Figure III.8: UV-visible diffuse reflectance spectra of $Gd_{2(1-x)}Ce_{2x}O_2S$ nanoparticles (x from 0 to 50%). The Y-axis is expressed as the Kubelka-Munk function F(R) calculated from obtained apparent absorbance.

The obtained results confirm that the absorption of the bimetallic $Gd_{2(1-x)}Ce_{2x}O_2S$ nanoparticles can be tuned within a wide wavelength range (250 – 550 nm) by adjusting the Gd/Ce ratio. Moreover, in the last chapter, we have already shown that this ratio was controllable by our synthesis. The tunable absorption in the visible region makes $Gd_{2(1-x)}Ce_xO_2S$ nanoparticles particularly interesting for visible-light photocatalysis (visible-blind ultraviolet photodetectors, multiple bandgap solar cell).

III.2.3. Photodegradation of organic dyes

In order to probe the photocatalytic activity of the $Gd_{2(1-x)}Ce_xO_2S$ nanoparticles, we studied the photodegradation of organic dyes such as rhodamine B (RhB) or methylene blue (MB) (**Figure III.9**), commonly used in the literature as a model for the photocatalytic depollution process.[22,23] These dyes exhibit intense absorption in the visible spectrum (λ_{max}(RhB) = 554 and λ_{max}(MB) = 665 nm). Consequently, their degradation can be readily monitored by UV-visible absorption spectroscopy.

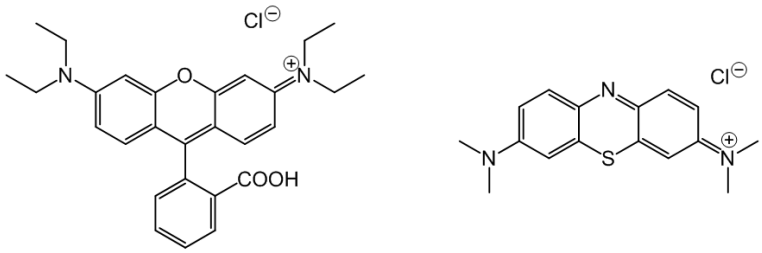

Rhodamine B
λ_{max} = 554 nm

Methylene Blue
λ_{max} = 665 nm

Figure III.9: Chemical formulas of commonly used organic dyes to probe photocatalytic activity.

Our photocatalysis setup is home-built as presented in **Figure III.10**. The light source is a square plate holder containing nine LEDs. They exhibit monochromatic emission centered at 501 nm with a full width at half maximum (FWHM) of ca. 30nm. Photocatalytic tests using the same light source have already been reported by our colleagues in the lab.[10,24]

Figure III.10: Homebuilt photocatalysis setup using cyan light (λ = 501 nm) produced by nine LEDs. The irradiated vials contain suspensions of $Gd_{2(1-x)}Ce_{2x}O_2S$ nanoparticles in aqueous rhodamine B solutions. During the reaction, the setup was kept in the dark.

Light excitation at 501 nm corresponds to an energy of 2.5 eV. Hence, this cyan light can excite the bandgap of $GdCeO_2S$ (x = 50%) nanoparticles (2.3 eV) to create pairs of electron and hole. Whereas, its energy is not sufficient to excite the wide bandgap of Gd_2O_2S (x = 0%) nanoparticles (4.7 eV). We thus expected a big difference of photocatalytic activity between the two nanoparticles.

In typical experiments, aqueous rhodamine B solutions with initial absorbance of 0.8 were prepared. Gd_2O_2S and $GdCeO_2S$ nanoparticles were dispersed in the solutions for a final concentration of 1 mg/mL, similar to what was reported in the literature for other photocatalysts with visible light such as $BiVO_4$ or Bi_2WO_6.[10,24] The suspensions were first kept in the dark under stirring for 1 h to reach the adsorption/desorption equilibrium of the dye. During the irradiation, aliquots were taken at regular time point and were centrifuged to remove the nanoparticles. The filtrates were then analyzed by UV-visible absorption spectroscopy. The obtained results are presented in **Figure III.11**.

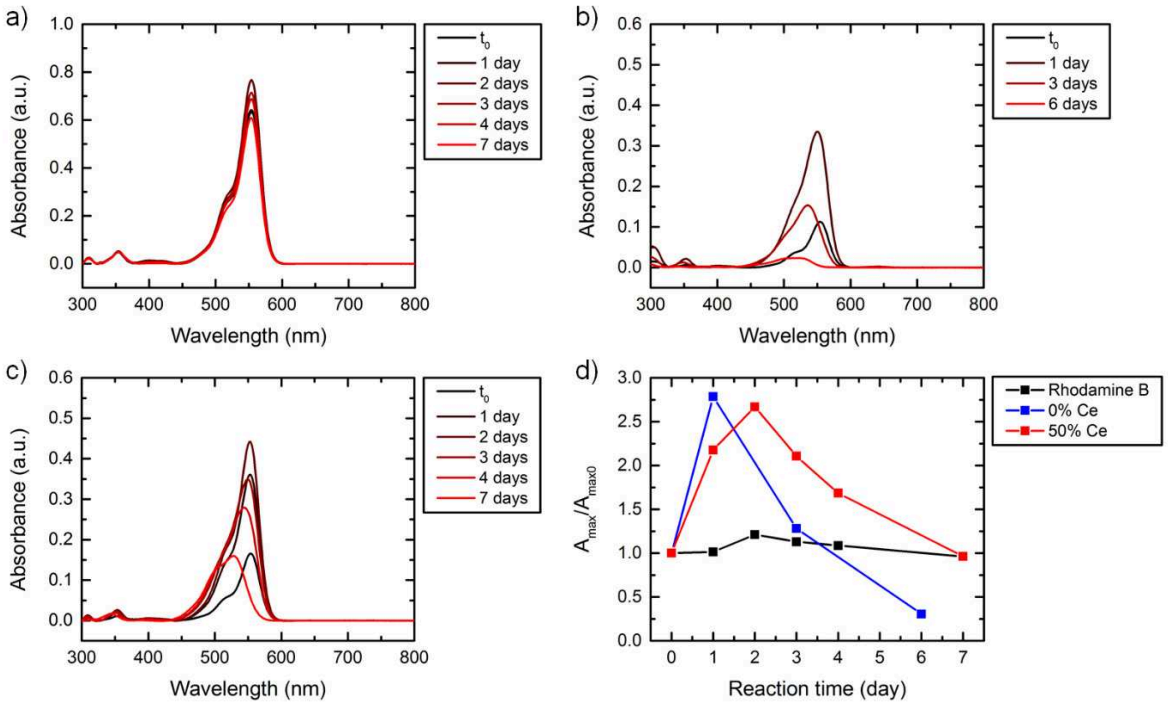

Figure III.11: Photodegradation of rhodamine B under irradiation with 501 nm light, in the presence of $Gd_{2(1-x)}Ce_{2x}O_2S$ ($x = 0$, 50%) nanoparticles. UV-visible absorption spectra over time of a) RhB without nanoparticles, b) RhB in presence of Gd_2O_2S ($x = 0\%$), c) RhB in presence of $GdCeO_2S$ ($x = 50\%$). t_0 corresponds to the start of irradiation. d) Corresponding evolutions of normalized maximum absorbance over time.

Initial test in the absence of the nanoparticles shows no significant change of absorption of RhB even after 7 days (**Figure III.11**a and d). The slight fluctuation of intensity is within the experimental error margin (ca. 0.2 of A_{max}/A_{max0}). Thus, catalyst is necessary for the photodegradation of Rh B.

For both Gd_2O_2S and $GdCeO_2S$ nanoparticles, the maximum absorbance at t_0 is much lower than that of the control experiment (0.10 and 0.15 vs. 0.78) (**Figure III.11**a-c). This is due to the adsorption of RhB on the nanoparticles. In particular, dye adsorption on Gd_2O_2S seems slightly more efficient than on $GdCeO_2S$ as less RhB is detected in the filtrate (0.10 vs. 0.15), suggesting a difference in specific surface area of the two samples. After the first 1 – 2 days, the maximum absorbance increases significantly (**Figure III.11**d), likely because of desorption of the dye from the nanoparticles. This desorption can be explained by the heating accompanied the irradiation.

Afterwards, maximum absorbance decreases in the presence of both Gd_2O_2S and $GdCeO_2S$ nanoparticles (**Figure III.11**b-d). Surprisingly, both nanoparticles photodecompose RhB with excitation at 501 nm. However, the reaction takes place during at least 6 days and is quite slow. Besides the decrease of maximum absorbance, we also notice that the absorption spectra shift towards the blue over time. These shifts are characteristic of degradation of RhB via *N*-deethylation in a stepwise process (four *N*-ethyl groups).[25] The final maximum absorbances in the case of Gd_2O_2S and $GdCeO_2S$ are 509 and 525 nm, respectively. The former corresponds to the thrice *N*-deethylated product while the latter corresponds to the twice *N*-deethylated product. Interestingly, the reaction appears slightly faster with Gd_2O_2S nanoparticles.

The photodegradation of RhB via *N*-deethylation are assigned to a photosensitized process where the excited dye molecule transfers its electron to the conduction band of the nanoparticle (**Figure III.12**a).[23,25,26] This electron then reduce O_2 in water to form superoxide anion radical $O_2^{\bullet-}$. The latter eventually reacts with the dye molecules, resulting in the *N*-deethylation reaction. It should be noted that this process is only feasible if the relative energy levels are appropriate. In fact, the excited state of the dye D*, the conduction band (CB) of the catalyst and the redox couples $O_2/O_2^{\bullet-}$ need to be in an increasing order (top to bottom) of energy as in **Figure III.12**a. It is also crucial that the dye can absorb excitation light which is our case (i.e. RhB absorbs 501 nm light).

This photosensitized process explains why Gd_2O_2S nanoparticles are active in the photodegradation of RhB even though their bandgap is too wide to be excited by a 501 nm light. On the other hand, the bandgap of $GdCeO_2S$ nanoparticles can be excited by this excitation light. Hence, they likely photodegrade RhB via two reaction pathways:

photosensitization and photocatalysis.[4,23,26] The former is similar to that of Gd_2O_2S nanoparticles (**Figure III.12**a) while the latter is depicted in **Figure III.12**b.

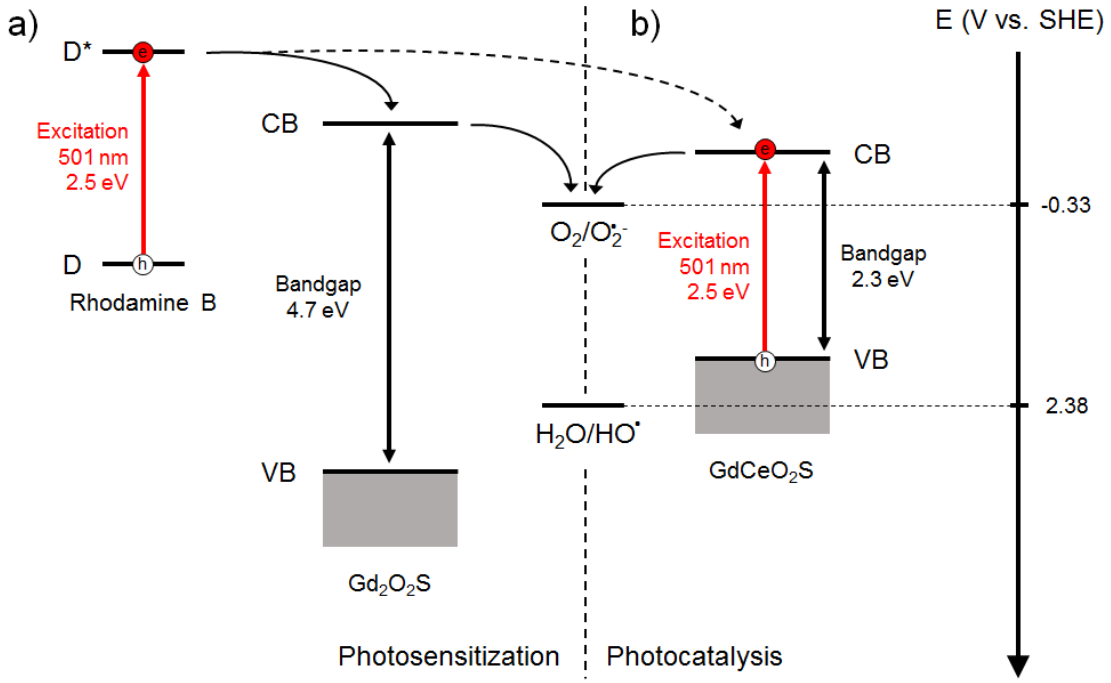

Figure III.12: Simplified schematic representation of a) photosensitization and b) photocatalysis processes upon excitation of wide bandgap Gd_2O_2S ($x = 0\%$) nanoparticles and small bandgap $GdCeO_2S$ ($x = 50\%$) nanoparticles. Note that the positions of covalence and conduction bands are hypothetical. VB and CB stand for valence band and conduction band. D and D* denote ground state and excited state of the dye respectively. "h" and "e" indicate hole and electron.

In the photocatalytic process, the excited pair of electron and hole can directly react with oxygen or water molecules to form $O_2^{\bullet-}$ or $^{\bullet}OH$ radicals, respectively. This again depends on the relative positions of the energy levels. In order to produce both radicals, the potentials of redox couples $O_2/O_2^{\bullet-}$ and $^{\bullet}OH/H_2O$ (E vs. SHE = -0.33 and 2.38 V respectively)[27,28] needs to be in between the bandgap of the catalyst. Thus, only materials with bandgap superior to 2.71 eV are suitable.

$GdCeO_2S$ nanoparticles with a bandgap of 2.3 eV cannot directly generate both $O_2^{\bullet-}$ and $^{\bullet}OH$ radicals by photocatalysis using 501 nm light. Furthermore, we have already shown that they photodegrade RhB via *N*-deethylation reaction, hence photosensitization of the dye. In order for this process to be possible, the energy of the conduction band of the $GdCeO_2S$

nanoparticles needs to be lower than that of the redox couples $O_2/O_2^{\bullet-}$. We thus propose an energy diagram explaining the photocatalysis by the $GdCeO_2S$ nanoparticles in **Figure III.12**b. Consequently, the cerium-containing nanoparticles only directly generate superoxide radical $O_2^{\bullet-}$. However, it should be noted that this simplified model does not take into account curvature of the band at the interface with the reaction medium. Hence, this diagram can only be applied to the surface of the nanoparticles and not the inner core.

Overall, both Gd_2O_2S ($x = 0\%$) nanoparticles and $GdCeO_2S$ ($x = 50\%$) nanoparticles photodegrade RhB with visible light at 501 nm. Although, the reaction is quite slow, probably due to the large quantity of organic ligands on the surface of the nanoparticles that creates a hydrophobic layer. In the case of Gd_2O_2S nanoparticles, the dye was degraded *via* a photosensitized pathway while it can be both photosensitization and photocatalysis for $GdCeO_2S$ nanoparticles. In the reaction with both nanoparticles, superoxide radicals $O_2^{\bullet-}$ likely forms first. They can, however, subsequently transform into $^{\bullet}OH$ in water. Electronic paramagnetic resonance (EPR) spectroscopy will be employed to confirm the nature of formed radicals.

The photodegradation of RhB appears slightly faster in the case of Gd_2O_2S nanoparticles. This can be explained by the difference in kinetics of photosensitized and photocatalytic processes as well as the potential difference of specific surface area of the two samples.

Lastly, we also carried out the photodegradation of methylene blue (MB) with our nanoparticles. However, preliminary results indicated that MB degraded in the absence of nanoparticles under experiment conditions (data not shown).

III.2.4. Radical production

In the last section, we showed that Gd_2O_2S ($x = 0\%$) nanoparticles and $GdCeO_2S$ ($x = 50\%$) nanoparticles likely produced superoxide radical $O_2^{\bullet-}$ under irradiation and photodegraded rhodamine B. Thus, in order to evaluate the photocatalytic activity of $Gd_{2(1-x)}Ce_xO_2S$ nanoparticles, we studied their ability to produce radicals.

III.2.4.1. Dithiothreitol (DTT) as radical probe

Detection of radicals such as hydroxyl radical $^{\bullet}OH$ and superoxide radical $O_2^{\bullet-}$ under photocatalytic conditions has been carried out by a wide range of methods including

spectroscopy, colorimetry, fluorescence, etc.[27] Standing out is EPR spin trapping method. It consists in trapping the radicals which have short lifetime in solution with molecules such as 5,5-dimethyl-1pyrroline *N*-oxide (DMPO). The formed adduct DMPO-R$^{\bullet}$ has a longer lifetime and can be detected by EPR spectroscopy. This method was developed for selective and efficient detection of photogenerated radicals even at low concentrations.[29] Nevertheless, EPR spectroscopy requires specific and expensive equipment. Hence, alternative methods are also developed. Colorimetry and fluorescence using selective radical probes are the most commonly used. For example, tetrazolium (XTT) (colorimetry) is used for detection of $O_2^{\bullet-}$ while terephthalic acid (fluorescence) and p-nitrosodimethylaniline (RNO) (colorimetry) are used for $^{\bullet}$OH.[27]

In the lab, we have experiences in employing dithiothreitol (DTT) as molecular probe to evaluate production of reactive oxygen species (ROS) in a cellular media. This was proved to be an efficient method to study latent ability of particles to generate oxidative stress.[30–32] Although the DTT assay appears less attractive in a photocatalytic context because of the low sensitivity and selectivity for different types of radicals, it can still be very useful for screening radical production under irradiation. Thus, we adapted an experimental protocol for 96-well plate to screen the photocatalytic activities of $Gd_{2(1-x)}Ce_{2x}O_2S$ nanoparticles.

In principle, DTT molecules can react with 5,5'-dithiobis-(2-nitrobenzoic acid) (DTNB or Ellman's reagent), cleaving the disulfide bond to form 2-nitro-5-thiobenzoic acid (TNB). This reaction between the two colorless compounds results in a product with intense yellow color (λ_{max} = 405 nm) (**Figure III.13**-1). Thus, the quantity of present DTT can be measured using UV-visible absorption spectroscopy.

Semiconductor nanoparticles generate radicals in water under irradiation. In particular, we showed that $Gd_{2(1-x)}Ce_{2x}O_2S$ nanoparticles exposed to 501 nm light likely produced superoxide radical $O_2^{\bullet-}$. In the presence of ROS, DTT molecule transforms into its radical form DTT-S$^{\bullet}$ and ultimately results in disulfide molecules ox-DTT (**Figure III.13**-2). However, colorless ox-DTT does not react with DTNB to form detectable TNB. Hence, this method can be used to indirectly evaluate radical production. High number of produced radicals results in small quantity of TNB detected and vice versa.

Typically, aqueous DTT solution and suspension of nanoparticles in water are added in each well of a 96-well plate in duplicate. One plate is irradiated by light from LEDs during 4 hours while the other is left in the dark during the same amount of time. The $Gd_{2(1-x)}Ce_{2x}O_2S$ nanoparticles containing cerium ($x > 0\%$) absorb at the wavelength used to detect TNB (405 nm). Thus, the plates are centrifuged and only the supernatant is taken and transferred to new plates. Excess DTNB is then added to the supernatant to form TNB in a quantitative reaction. The absorbance at 405 nm is finally measured for each well, thanks to a microplate reader.

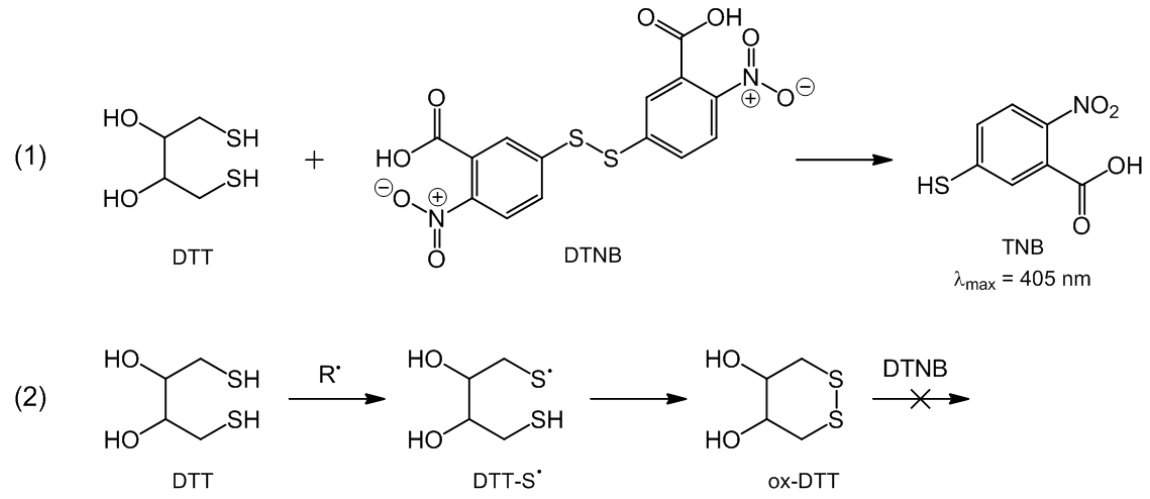

Figure III.13: DTT as radical probe. Reaction scheme of (1) DTT with DTNB to form an intense yellow product, detectable by UV-visible absorption spectroscopy and (2) DTT with radicals in solution to form disulfide ox-DTT that does not react with DTNB.

III.2.4.2. Validation of the method with commercial TiO_2 P25 nanoparticles

In order to confirm that the DTT assay can effectively evaluate radical production under irradiation, we first carried out the experiment with commercial TiO_2 P25 nanoparticles. These nanoparticles are well known for their high photocatalytic activity with UV light and they can generate both $O_2^{\bullet-}$ or $^{\bullet}OH$ radicals.[1] For this experiment, we use nine LEDs whose emission is centered at 391 nm and FWHM of ca. 15 nm as light source (**Figure III.14**a).

Control test of DTT in the absence of nanoparticles gave similar final absorbance values in the dark and under irradiation: 1.46 ± 0.01 and 1.44 ± 0.03 respectively. DTT molecules are thus stable under our experimental conditions.

Experiments with increasing concentration of TiO_2 nanoparticles (50, 100, 500 and 1000 µg/mL) were carried out. Detected quantities of DTT are normalized with that of the control experiment without nanoparticles (**Figure III.14**b, dots). Radical production of the nanoparticles is evaluated by calculating the difference between the normalized DTT quantities in the dark and under irradiation (**Figure III.14**b, bars).

In the dark, DTT quantity remains unchanged when the nanoparticle concentration increases (**Figure III.14**b, black dots). Their normalized values are slightly above 1, likely due to absorption of a small fraction of TiO_2 nanoparticles that we were unable to remove by centrifugation. This result indicates that no radical is formed without irradiation of the photocatalysts.

Under irradiation with 391 nm light on the other hand, the normalized DTT quantity linearly decreases when the nanoparticle concentration increases (**Figure III.14**b, purple dots). At the lowest tested concentration of nanoparticles (50 µg/mL), the radical production is ca. 0.6. Whereas at 1000 µg/mL of nanoparticles, it reaches 0.9, indicating that the photogenerated radicals already reacted with almost all of DTT molecules.

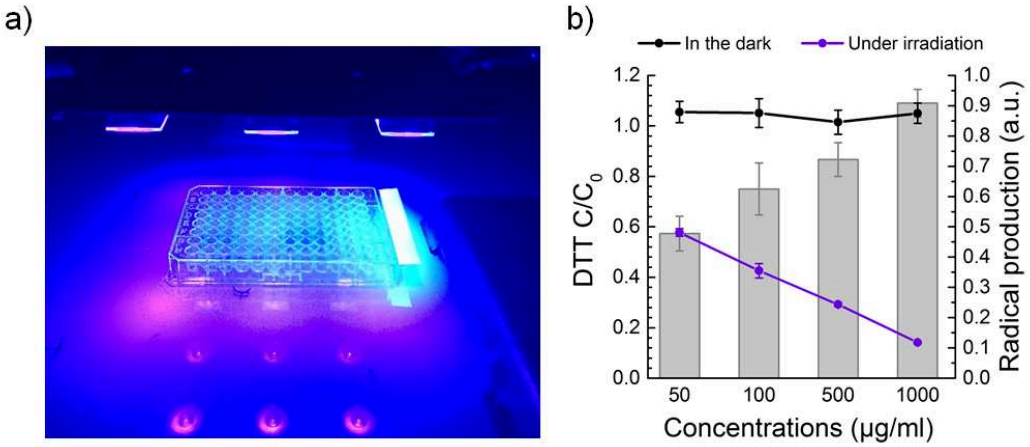

Figure III.14: a) Experimental setup for evaluation of radical production under irradiation of 391 nm UV light produced from nine LEDs. b) Normalized quantities of DTT after 4 h in the dark and under irradiation (dots), in the presence of different concentrations of TiO_2 P25 (left y-axis). Radical productions under irradiation calculated as difference between the normalized DTT quantities in the dark and under irradiation is presented as bar graph (right y-axis).

Overall, we confirmed the photocatalytic activity of TiO_2 P25 nanoparticles by evaluating their ability to produce radical under UV irradiation. Hence, DTT assay can be used to screen the activity of gadolinium-cerium oxysulfide $Gd_{2(1-x)}Ce_xO_2S$ nanoparticles.

III.2.4.3. Bimetallic $Gd_{2(1-x)}Ce_xO_2S$ nanoparticles

For the radical production evaluation of $Gd_{2(1-x)}Ce_xO_2S$ nanoparticles, we used the same visible light source (emission centered at 501 nm) as in the previously discussed photodegradation of rhodamine B (**Figure III.15**a). We again expect better activity from the nanoparticles with higher cerium content because they absorb more efficiently in the visible region. Moreover, photosensitization cannot occur under the conditions of this experiment because DTT molecules only absorb in the UV region.

We first carried out the control test in the absence of nanoparticles. The obtained absorbance values in the dark and under irradiation are comparable: 1.48 ± 0.01 and 1.44 ± 0.03 respectively. We confirm that DTT remains stable under a less energetic irradiation with 501 nm light.

In order to evaluate the photocatalytic activity of $Gd_{2(1-x)}Ce_xO_2S$ nanoparticles, a reference photocatalyst is necessary for comparison. As discussed in the previous section, TiO_2 P25 nanoparticles are efficient photocatalysts. However, they are only active under UV light. We then turned to $BiVO_4$ nanoparticles previously synthesized in our lab by Dr. Tamar Saison.[10] They were reported to exhibit a small bandgap of 2.5 eV and could be excited by 501 nm, similar to our $GdCeO_2S$ nanoparticles (band gap 2.3 eV). They also likely generate radicals under irradiation and efficiently degrade rhodamine B via both photosensitization and photocatalysis. Thus, $BiVO_4$ nanoparticles seem suitable to be a reference.

Like TiO_2 P25 nanoparticles, $BiVO_4$ nanoparticles do not produce radicals in the dark (**Figure III.15**b, black dots). Less DTT is observed under irradiation at higher concentrations of nanoparticles (500 – 1000 µg/mL) (**Figure III.15**b, cyan dots). In particular, radical production of $BiVO_4$ nanoparticles at 1000 µg/mL reaches 0.2 (**Figure III.15**b, grey bars).

With increasing concentrations of Gd_2O_2S (0% Ce) nanoparticles and $GdCeO_2S$ (50% Ce) nanoparticles, surprisingly, the normalized DTT quantity decreases in the dark to below 1 (**Figure III.15**c and d respectively, black dots). Under irradiation, it decreases even further,

indicating radical production with visible light (cyan points). At the highest nanoparticle concentration (1000 µg/mL), the radical productions are evaluated at 0.1 and 0.2 for Gd_2O_2S and $GdCeO_2S$ respectively (grey bars). However, the high uncertainty of the value in the case of Gd_2O_2S nanoparticles makes it difficult to confirm whether they can photogenerate radicals. In contrast, $GdCeO_2S$ nanoparticles seem to produce radicals under irradiation with 501 nm light.

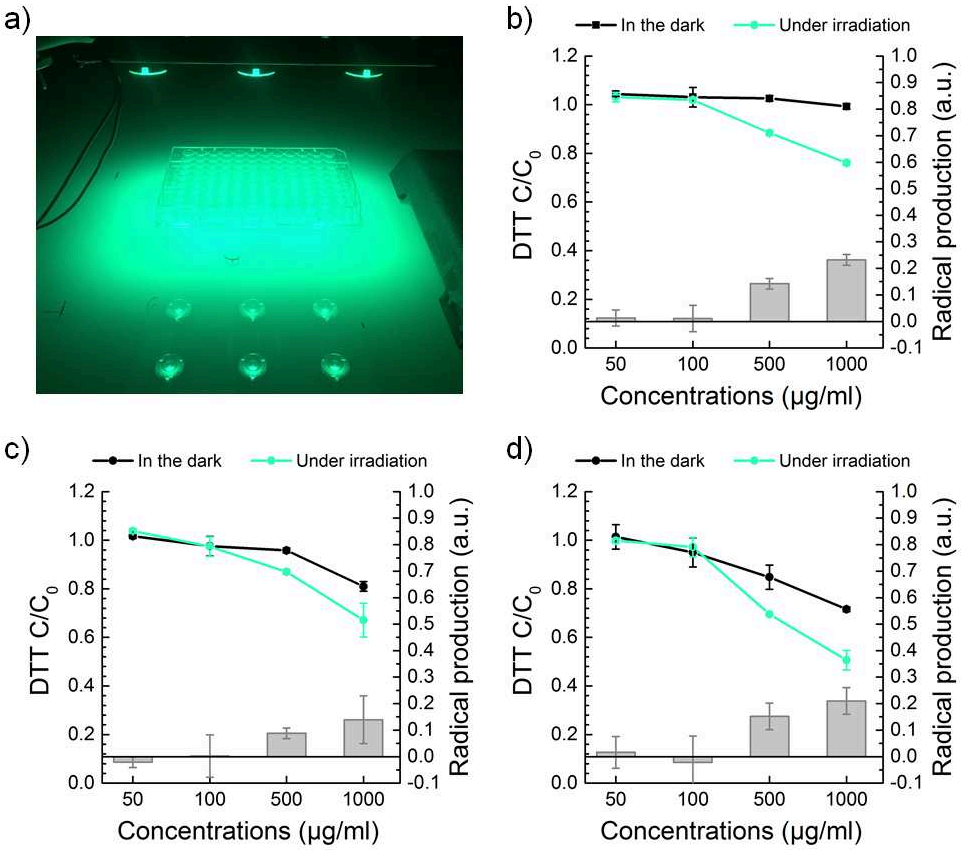

Figure III.15: a) Experimental setup for evaluation of radical production under irradiation of 501 nm visible light produced from nine LEDs. Radical production under irradiation of 501 nm visible light of b) $BiVO_4$ nanoparticles, c) Gd_2O_2S ($x = 0\%$) nanoparticles and d) $GdCeO_2S$ ($x = 50\%$) nanoparticles at different concentrations of photocatalysts.

Altogether, we conclude that both $BiVO_4$ and $GdCeO_2S$ nanoparticles produce radical under irradiation with 501 nm light. Their activities also appear to be similar but far below that of TiO_2 P25 nanoparticles with UV light (0.2 vs. 0.9). As for Gd_2O_2S nanoparticles, however, we cannot confirm their activity because of the high uncertainty of the result. Surprisingly, we observed a decrease of DTT quantities at higher concentration of oxysulfide nanoparticles

in the dark. This suggests either radical production in the absence of light or adsorption of DTT molecules on the $GdCeO_2S$ nanoparticles. In fact, adsorbed DTT would be eliminated with the nanoparticles during the centrifugation step, giving rise to a bias in our evaluation of photocatalytic activity.

The same experiment was carried out for $Gd_{2(1-x)}Ce_xO_2S$ nanoparticles with intermediate cerium contents (1, 5, 10, 20%). The results at 1000 µg/mL of catalyst are summarized in **Figure III.16**. We indeed observe fluctuations of the normalized DTT quantities across the samples in the dark as well as under irradiation (from 0.4 to 1.0). We thus speculate that these samples do not possess the same specific surface area. This affects their ability to adsorb DTT molecules of the nanoparticles, hence the large differences between the measured DTT quantities. Nevertheless, it is worth noting that radical production is observed for cerium containing $Gd_{2(1-x)}Ce_xO_2S$ nanoparticles, especially at cerium content higher than 5%.

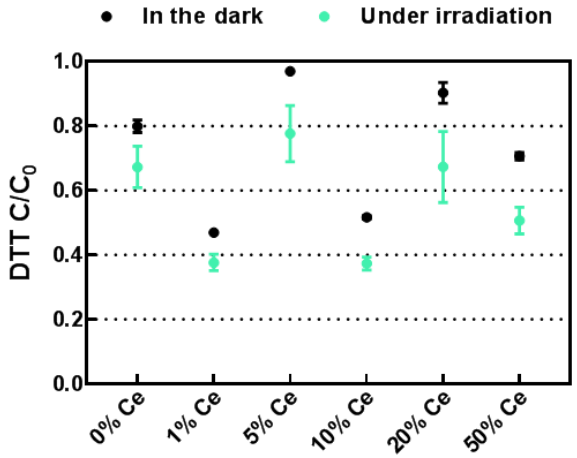

Figure III.16: Normalized DTT quantities measured after 4 h in the dark and under irradiation with 1000 µg/mL of $Gd_{2(1-x)}Ce_xO_2S$ nanoparticles (x from 0 to 50%).

In conclusion, with the DTT assay, we showed that cerium-containing $Gd_{2(1-x)}Ce_xO_2S$ nanoparticles photogenerate radicals with visible light, especially at higher cerium contents and nanoparticle concentrations. However, this observed activity is likely mediated by adsorption of DTT on the nanoparticles, giving rise to a bias in the analysis of results. Comparison between different samples is thus difficult. We can only conclude whether the photocatalyst produces radical. Moreover, radicals are detected indirectly using DTT. The

results must be confirmed by another technique. In the next step of the study, evaluation of radical production using EPR spectroscopy would be ideal.

III.3. Cytotoxicity of $Gd_{2(1-x)}Ce_xO_2S$ nanoparticles

In this section, we discuss the potential toxicity of $Gd_{2(1-x)}Ce_xO_2S$ nanoparticles, as part of the safer-by-design approach. Compared to animal studies, cell-line studies are less ethically questionable, easier to control, reproduce and less expensive. Thus, in this section, we will present *in vitro* studies using the developed nanoparticles as a first step towards understanding their toxicity.

III.3.1. Cell line model

When foreign matters such as microorganisms and nanoparticles come in contact with the body of humans or animals, they get countered by the innate defense mechanisms of the host. The epithelial surface provides a physical barrier between the inside and the outside of the body. Epithelial cells can also produce chemical substances that hinder the invasion of the foreign matters. Besides, the body can also react with immune responses. Macrophages are likely the first cells of the immune system that the foreign matters encounter. They are capable of recognizing, ingesting by phagocytosis and clearing foreign matters. Hence, understanding how epithelial cells and macrophages react to exposure to the foreign matters can give insights on the toxicity of this latter.

Immortalized RAW 264.7 cells (**Figure III.17**) are commonly used in our group as well as in other groups as an *in vitro* model of macrophages to assess the cytotoxicity of different nanoparticles.[11,33–35] The RAW 264.7 are macrophage-like cells, originating from Albelson leukemia virus transformed cell line derived from BALB/c mice. These cells have been used in laboratories for more than 40 years and are described as an appropriate model of macrophages.[36] They are capable of phagocytosis and are also reported to be stable for long-term growth (up to 30 passages) in cell culture. Hence, we employed this cell-line to evaluate the cytotoxicity of $Gd_{2(1-x)}Ce_xO_2S$ nanoparticles.

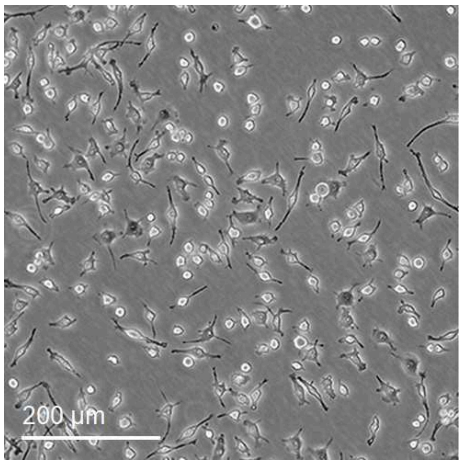

Figure III.17: Optical microscope image of murine macrophage RAW 264.7 cell line provided by American Type Culture Collection (ATCC® TIB-71™).

III.3.2. Cell viability

The cytotoxicity of $Gd_{2(1-x)}Ce_xO_2S$ nanoparticles was first assessed. Exposure of the cells to cytotoxic agents can affect different parameters of the cells such as their metabolic activity, membrane permeability, DNA content, etc. Thus, we performed various assays to evaluate each of these endpoints.

Following exposure of RAW 264.7 cells to selected nanoparticles at different concentrations (1, 10, 50, 100 µg/mL) during 24 h, WST-1, Hoechst and LDH assays were performed to characterize mitochondrial activity, cellular DNA content and membrane integrity of the macrophages, respectively.

III.3.2.1. Mitochondrial activity

WST-1 assay is a colorimetric method to characterize mitochondrial activity of the cells. This method is based on the cleavage of the colorless tetrazolium salt WST-1 to formazan by mitochondrial reductase, which exists in the mitochondrial respiratory chain and is only active in viable cells (**Figure III.18**). An increase of the mitochondrial activity leads to an increase of the production of formazan dye and vice versa. Formazan exhibits a dark yellow color and thus, the mitochondrial activity can be assessed using UV-visible absorption spectroscopy.

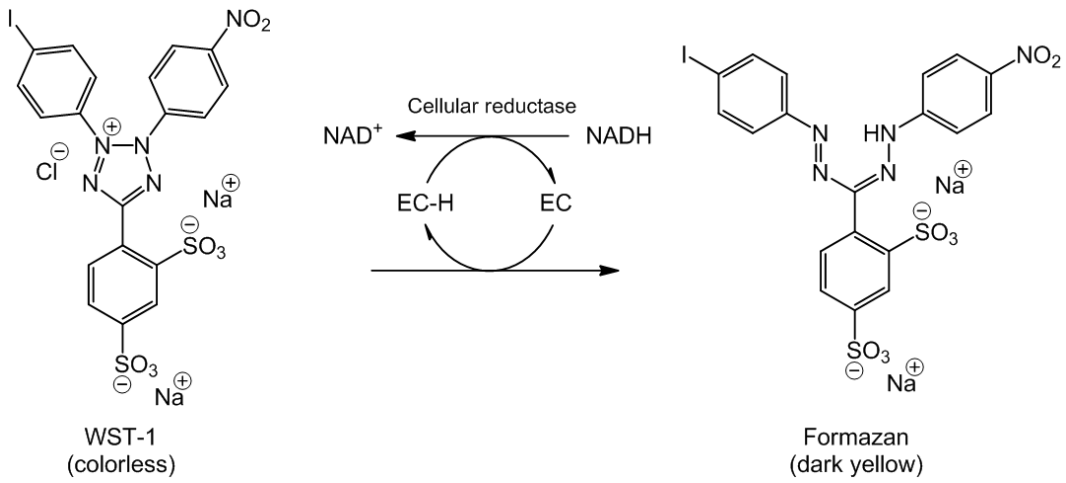

Figure III.18: Cleavage of tetrazolium salt WST-1 to formazan by mitochondrial dehydrogenase. EC stands for electron coupling reagent.

In this experiment, RAW 264.7 cells were exposed to nanoparticles for 24 h. The exposed-cells were then incubated with WST-1 solution for 3 h. The absorption of resulting media is measured by a microplate reader at 450 nm and the relative mitochondrial activity is calculated by normalizing the obtained absorbance values to that of unexposed cells.

The experiment was carried out for $Gd_{2(1-x)}Ce_xO_2S$ nanoparticles with 0%, 10%, 50% of cerium as well as commercial TiO_2 P25 nanoparticles as control (**Figure III.19**a). The mitochondrial activity of the RAW 264.7 macrophages remains constant around 100% compared to unexposed cells upon exposure up to 100 µg/mL of TiO_2 nanoparticles. With Gd_2O_2S (0% Ce) nanoparticles, the mitochondrial activity rises slightly above 100% at lower concentrations then decreases when the concentration increases. It stops at ca. 75% at the highest tested concentration of nanoparticles (100µg/mL). As for cerium-containing $Gd_{2(1-x)}Ce_xO_2S$ nanoparticles, the measured mitochondrial activity remains around 100% of that observed for unexposed cells after exposure to 1 or 10 µg/mL of nanoparticles. However, exposure to higher concentration of nanoparticles (50 and 100 µg/mL) significantly decreases the mitochondrial activity of the cells to close to 0% of that of unexposed cells.

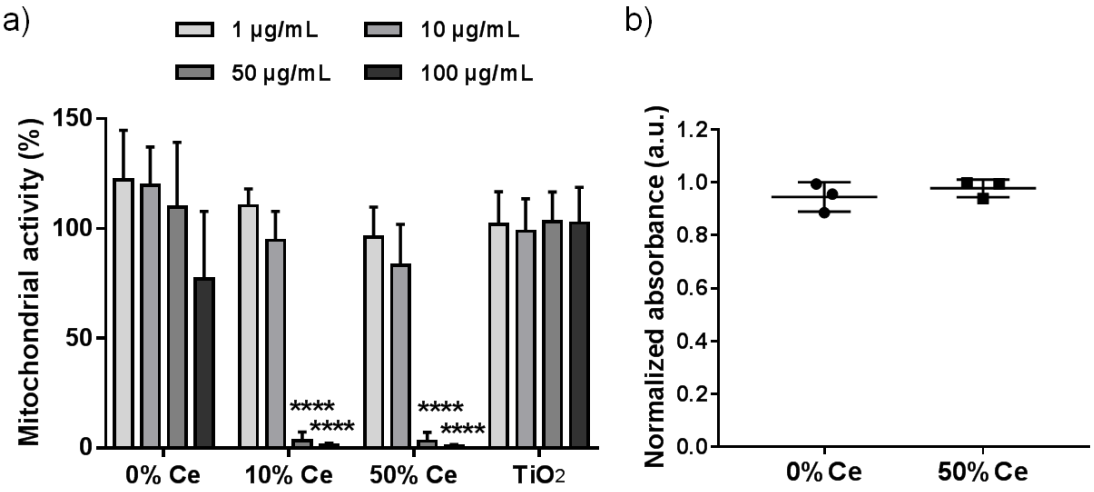

Figure III.19: a) WST-1 assay of RAW 264.7 macrophages exposed to $Gd_{2(1-x)}Ce_xO_2S$ and TiO_2 P25 nanoparticles at different concentrations during 24 h. The mitochondrial activities were reported as percentages of that of unexposed cells. The experiments were repeated at least three times. **** signifies a p-value inferior to 0.0001. b) Assay interference test: incubation of formazan dye with 100 µg/mL of $Gd_{2(1-x)}Ce_xO_2S$ nanoparticles. Resulting absorbance is normalized by that of formazan dye.

The decrease of the mitochondrial activity of the cells can be due to adsorption of formazan dye to the nanoparticles. In order to verify this, culture medium of RAW 264.7 cells incubated with WST-1 solution for 3 h was taken and mixed with either distilled water as control experiment, or suspensions of nanoparticles for another 3 h. The absorbance at 450 nm was then measured and normalized with that of the control experiment. The results of Gd_2O_2S (0% Ce) and $GdCeO_2S$ (50% Ce) are presented in **Figure III.19**b. The normalized absorbance values for both nanoparticle samples (with and without cerium) fluctuate around 1. This indicates that the nanoparticles do not significantly adsorb formazan dye.

The results from the interference test rule out the effect of adsorption of formazan dye by the nanoparticles on our observations. WST-1 assay shows that TiO_2 nanoparticles do not have any effect on the mitochondrial activity of the macrophages. Gd_2O_2S nanoparticles without Ce induce changes at the highest concentration even though not significant. Their impact on the metabolic activity of the cell seems therefore limited. However, oxysulfide nanoparticles containing 10% Ce and 50% Ce inhibit mitochondrial activity of the cells at 50 and 100 µg/mL. This indicates cytotoxic effect of these cerium-containing nanoparticles.

III.3.2.2. DNA quantification

Fluorometry is a highly sensitive and simple method to quantify DNA. The principle of this method is essentially based on the binding of fluorescent compounds to nucleic acids by intercalation. One of the most commonly used fluorescent dyes is Hoechst 33258 (**Figure III.20**). When excited at 360 nm, the fluorescence emission at 460 nm of the dye increases significantly in the presence of DNA. This method is capable of detecting nanograms of DNA and can be used to determine cellular DNA content.

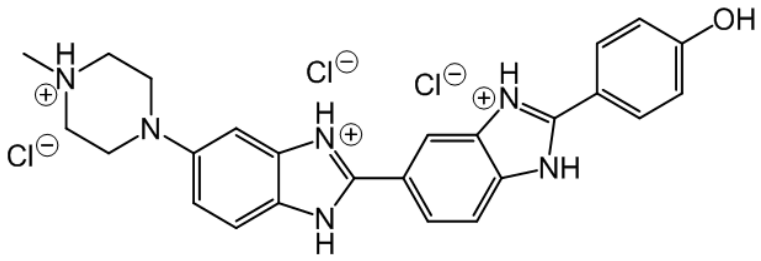

Figure III.20: Chemical formula of Hoechst 33258 molecule.

RAW 264.7 macrophages that were exposed to nanoparticles in microplates were incubated with water for 30 min. This cytolysis step is necessary to release intracellular DNA in the culture medium. Then, solution of Hoechst dye was added and fluorescence intensity was measured in each well with a microplate reader.

The assay was performed with $Gd_{2(1-x)}Ce_xO_2S$ and TiO_2 P25 nanoparticles at different concentrations from 1 to 100 µg/mL (**Figure III.21**). The obtained fluorescence intensity was normalized to that of unexposed cells. Interestingly, for all nanoparticles and at all concentrations, no significant change in cellular DNA content is observed. The DNA contents remain at 100% compared to unexposed cells.

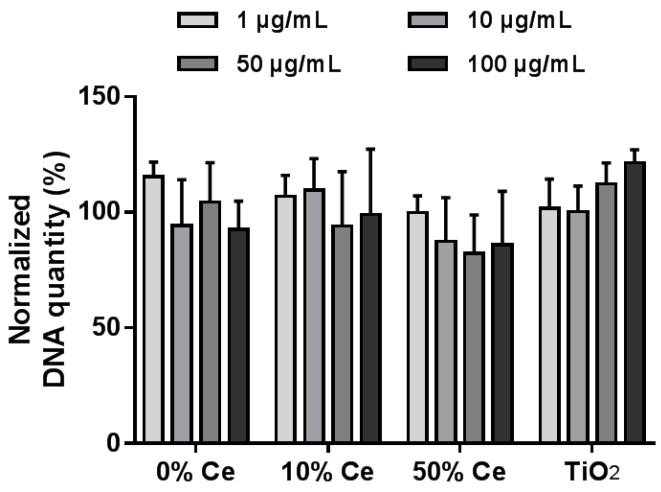

Figure III.21: Cellular DNA quantification of RAW 264.7 macrophages exposed to $Gd_{2(1-x)}Ce_xO_2S$ and TiO_2 P25 nanoparticles at different concentrations during 24 h. The cellular DNA contents were reported as percentages of that of unexposed cells. The experiments were repeated at least three times.

III.3.2.3. Membrane integrity

Exposure of cells to cytotoxic agents can also compromise the cell membrane integrity, then allowing cellular contents to leak outside the cell. Viability assays based on this principle include monitoring the release of lactate dehydrogenase (LDH), which is a stable cytoplasmic enzyme present in all cells. This method relies on measuring the activity of LDH in catalyzing the redox reaction between NAD^+ and lactate to form NADH and pyruvate (**Figure III.22**). Then, NADH can react with tetrazolium salts in the presence of a catalyst to form formazan in a cleavage reaction similar to that of WST-1 assay. The quantity of formed formazan is related to the quantity of LDH released and can be measured by UV-visible absorption spectroscopy. A higher LDH quantity detected indicates that the membrane integrity is more compromised and vice versa.

Typically, the media of RAW 264.7 cells exposed to nanoparticles were taken and incubated with a mixture of tetrazolium salt and catalyst for the cleavage reaction during 30 min. The reaction was then stopped by addition of HCl solution and the absorbance at 490 nm was measured by a microplate reader.

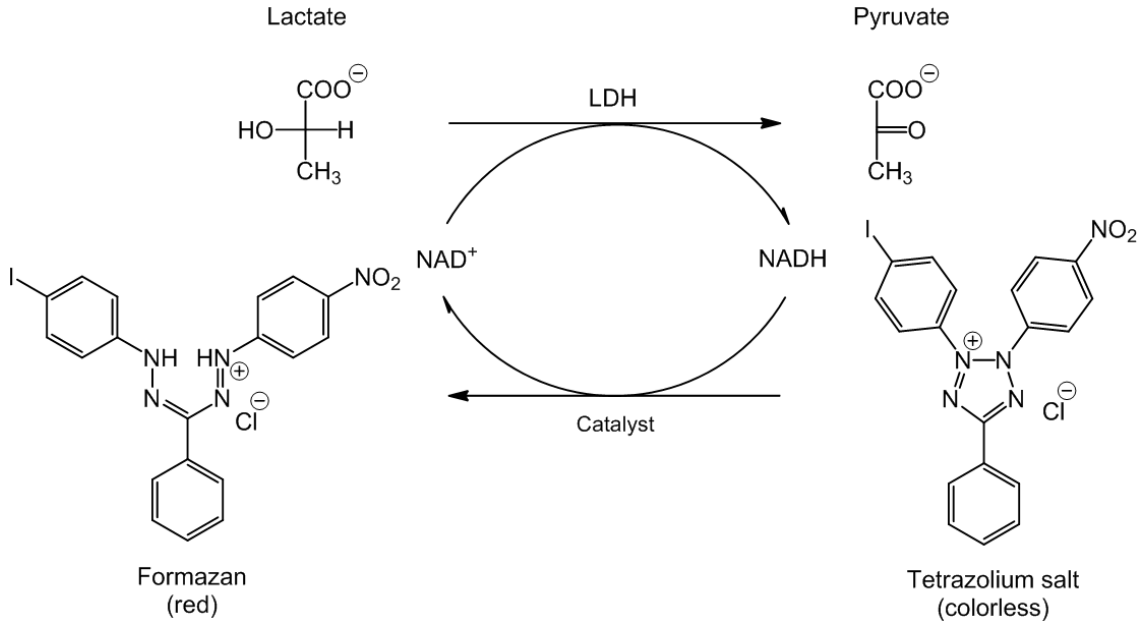

Figure III.22: Released lactate dehydrogenase reduces NAD^+ to NADH and results in cleavage of tetrazolium salt to formazan.

The released LDH quantity was measured for the cells exposed to $Gd_{2(1-x)}Ce_xO_2S$ and TiO_2 P25 nanoparticles as well as solution of Triton X-100 (diluted at 2%) (**Figure III.23**). The latter serves as a positive control for the experiments as it can lyse the cells, resulting in maximum amount of released LDH. The obtained values were normalized with that of unexposed cells.

As expected, upon exposure to Triton X-100 solution, RAW 264.7 cells show an increase of detected LDH compared to that of unexposed cells (**Figure III.23**). The normalized LDH quantity is measured at ca. 200%. Cells exposed to TiO_2 nanoparticles shows unchanged LDH quantity released in the medium compared to unexposed cell, at all tested concentrations of nanoparticles. With Gd_2O_2S nanoparticles, the normalized quantity of LDH is slightly below 100% at 1 µg/mL. However, it rises significantly to ca. 145% at 100 µg/mL of nanoparticles. As for the cerium-containing nanoparticles, the measured LDH quantity remains around 100% at 1 and 10 µg/mL of nanoparticles. Surprisingly, at higher concentrations of nanoparticles, the values decrease significantly to below 50% compared to that of unexposed cells. This decrease can be observed from 50 µg/mL for nanoparticles with 10% of cerium and from 100 µg/mL for nanoparticles with 50% of cerium.

This decrease of LDH quantity upon exposure to nanoparticles compared to unexposed cells has already been observed by Han et al. in 2011 for copper and silver nanoparticles.[37] The inactivation of LDH molecules non-specifically in solution can be explained either by their adsorption on the nanoparticles, their oxidation catalyzed by metallic nanoparticles or generation of free radicals caused by the nanoparticles. We have previously shown that $Gd_{2(1-x)}Ce_xO_2S$ nanoparticles are capable of adsorbing molecules such as DTT. They can also generate radicals under 500 nm visible light. Yet, the LDH assay uses 490 nm light to measure the LDH quantity. Thus, it is highly likely that these properties of $Gd_{2(1-x)}Ce_xO_2S$ nanoparticles interfere with the assay and inactivate LDH molecules. We conclude that the LDH assay is unsuitable to assess the cytotoxicity of our $Gd_{2(1-x)}Ce_xO_2S$ nanoparticles. Other assays such as Neutral red, Trypan blue or calcein acetoxymethyl (calcein AM) are available to assess the membrane integrity of the cells and could be employed instead.

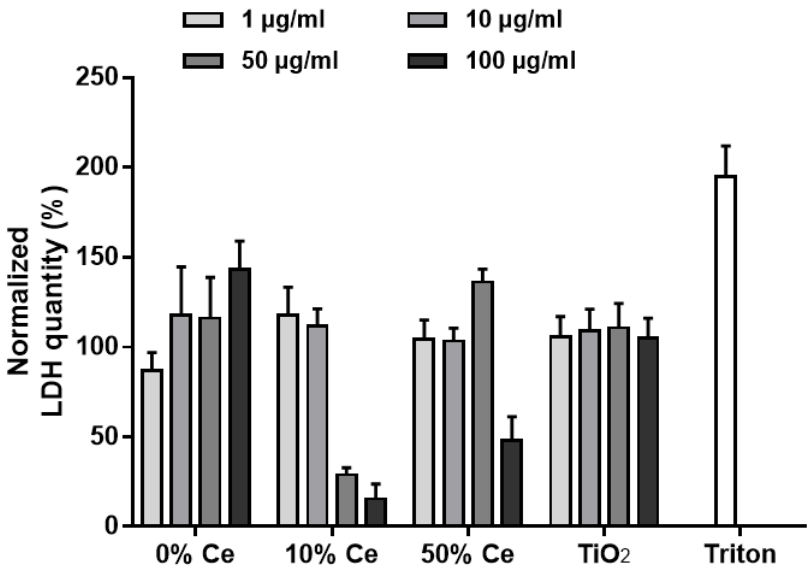

Figure III.23: Monitor of release of lactate dehydrogenase (LDH) of RAW 264.7 macrophages exposed to $Gd_{2(1-x)}Ce_xO_2S$ and TiO_2 P25 nanoparticles at different concentrations during 24 h. Triton was employed as positive control of the experiment. The LDH quantities were reported as percentages of that of unexposed cells. The experiments were repeated at least three times.

III.3.3. Sub-lethal effects

Not all deleterious effects of the nanoparticles towards the cell result in membrane or metabolic function defects. Detecting cellular responses upon exposure to sub-lethal doses of

nanoparticles is of particular importance to gather insights on the mechanisms that lead to cell death at higher concentrations of nanoparticles.

We have shown in the last section that severe damages to the cell were detected after 24 h from 50 µg/mL of cerium-containing nanoparticles. However, at 10 µg/mL, the nanoparticles had no visible effect on the viability of the macrophages. Thus, this concentration of nanoparticles is suitable for sub-lethal effect studies. Shorter duration of nanoparticles exposure (below 24 h) may also be relevant.

III.3.3.1. Intracellular ROS activity

First, we looked into the intracellular production of reactive oxygen species (ROS) of the RAW 264.7 macrophages in response to the exposure to oxysulfide nanoparticles. For this purpose, we employed the H_2DCF-DA assay. This fluorometric assay makes use of an originally non-fluorescent derivative of fluorescein diacetate H_2DCF-DA (**Figure III.24**). This lipophilic molecule can pass through the plasma membrane of the cells and then is de-esterified by non-specific cellular esterase to form non-fluorescent dialcohol H_2DCF. This dialcohol molecule is hydrophilic. Thus, it stays inside the cell and can be eventually oxidized by intracellular ROS to form DCF which is fluorescent. Taking advantage of this process, intracellular ROS production can be measured by simple fluorescence spectroscopy.

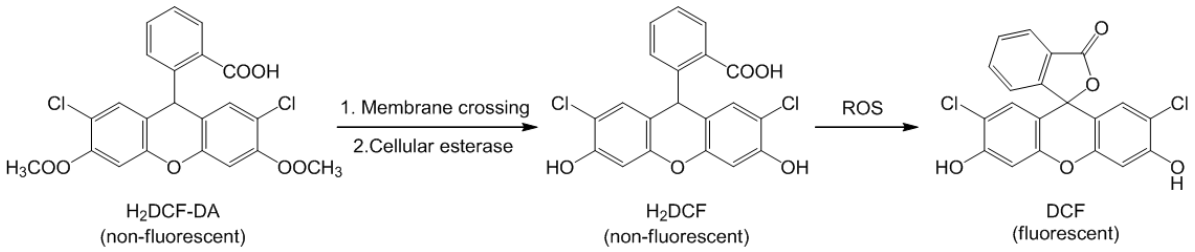

Figure III.24: Measuring intracellular ROS activity by H_2DCF-DA assay.

In practice, RAW 264.7 macrophages were incubated with H_2DCF-DA solution for 1 hour so that the latter can diffuse into the cells. The cells were then washed several times with fresh culture medium to eliminate the H_2DCF-DA molecules that remain in the extracellular medium. This step is necessary to remove unwanted signals that come from extracellular sources of ROS such as nanoparticles. Subsequently, the cells containing H_2DCF are exposed

to the nanoparticles and the fluorescence intensity of DCF is measured at different exposure times.

RAW 264.7 cells exposed to Gd_2O_2S nanoparticles as well as previously proved cytotoxic $Gd_{2(1-x)}Ce_xO_2S$ nanoparticles (10 and 50% of cerium) were subjected to the H_2DCF-DA assay. The measured fluorescence intensities after 15 and 45 min were normalized to that of unexposed cells. The results are presented in **Figure III.25**.

Following exposure to 10 µg/mL of $Gd_{2(1-x)}Ce_xO_2S$ nanoparticles during 15 min, the normalized fluorescence intensity remains at ca. 1 for all tested nanoparticles (**Figure III.25**, light gray bars). After 45 min, oxysulfide nanoparticles containing 10% Ce increase the fluorescence intensity slightly above 1 but not significantly. For Gd_2O_2S (0% Ce) and $GdCeO_2S$ (50% Ce) nanoparticles, the intensity stays at ca. 1.

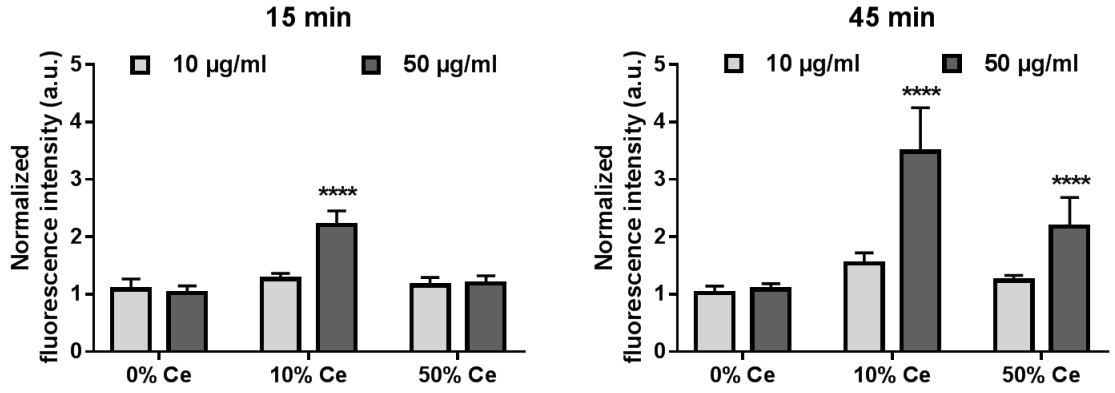

Figure III.25: Intracellular ROS activity of RAW 264.7 cells upon exposure to 10 and 50 µg/mL of $Gd_{2(1-x)}Ce_xO_2S$ nanoparticles (0, 10 and 50% Ce) after 15 min and 45 min. The ROS activities were normalized to that of unexposed cells. The experiments were repeated three times. **** indicates a p-value inferior to 0.0001.

Exposure to 50 µg/mL of nanoparticles, however, results in changes of the fluorescence intensity of DCF compared to that of unexposed cells (**Figure III.25**, light grey). After 15 min of exposure, cells exposed to Gd_2O_2S (0% Ce) and $GdCeO_2S$ (50% Ce) nanoparticles show normalized fluorescence intensities around 1. Yet, cells exposed to $Gd_{1.8}Ce_{0.2}O_2S$ (10% Ce) nanoparticles increase significantly to ca. 2. After 45 min of exposure, Gd_2O_2S (0% Ce) nanoparticles induce no change in the DCF fluorescence intensity compared to that at 15 min. Nevertheless, the normalized fluorescence intensity increases to above 3 following exposure

of cells to $Gd_{1.8}Ce_{0.2}O_2S$ (10% Ce) nanoparticles and to above 2 in the case of $GdCeO_2S$ (50% Ce) nanoparticles.

The results of the H_2DCF-DA assay suggest that, at 50 µg/mL, the cerium-containing nanoparticles induce an increase of intracellular ROS production as soon as 15 min after exposure. This ROS activity increases even further after 45 min of exposure. In contrast, no change of ROS activity is detected after exposure to Gd_2O_2S nanoparticles in the same conditions, compared to unexposed cells.

Consequently, we speculate that oxidative stress is likely one of the pathways that lead to death of RAW 264.7 macrophages upon exposure to cerium-containing $Gd_{2(1-x)}Ce_xO_2S$ nanoparticles. Hence, we investigated the expression of specific protein in response to oxidative stress.

III.3.3.2. Oxidative stress

Heme oxygenase-1 (HO-1) is an enzyme that catabolizes heme to obtain biliverdin, acting as anti-oxidants.[38] HO-1 is induced in response to oxidative stress and inflammatory stimuli. It provides protective effects against a variety of cellular stresses. Thus, expression of HO-1 is a relevant parameter to study oxidative stress.

Similar to previously described cell viability assays, we exposed RAW 264.7 macrophages to 10 µg/mL of Gd_2O_2S (0% Ce) nanoparticles or $GdCeO_2S$ (50% Ce) nanoparticles for 24 hours. The cells were then lysed and the amount of expressed HO-1 was studied by western blot. As a positive control, the cells were treated with 10 µg/mL of lipopolysaccharide (LPS), an endotoxin.

Western blot analysis shows the presence of HO-1 by fluorescence bands at ca. 32 kDa for untreated as well as treated cells (**Figure III.26**a). Bands of β-actin are also detected at ca. 47 kDa. They are of similar intensity, indicating comparable expression of this housekeeping gene. Comparison between the fluorescence intensities of HO-1 band is thus straightforward. The results suggest higher expression of HO-1 in the cells treated with LPS than in untreated cells. Nevertheless, HO-1 expression levels of cells treated with nanoparticles are comparable to the control. By quantifying the intensities of fluorescence bands of three repeated experiments, we demonstrated that there is indeed no significant difference between the two

(**Figure III.26**b). Hence, at this stage, it is not clear that lanthanide oxysulfide nanoparticles induce oxidative stress in RAW 264.7 cells.

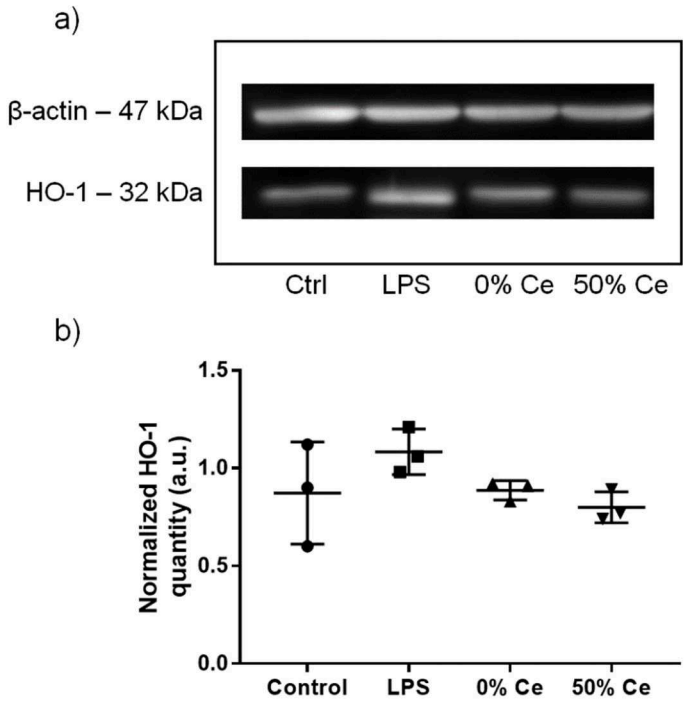

Figure III.26: HO-1 expression of RAW 264.7 cells after 24 h of exposure to 10 µg/mL of Gd_2O_2S (0% Ce) nanoparticles and $GdCeO_2S$ (50% Ce) nanoparticles. Cell treatment with 10 µg/mL of LPS was used as positive control. a) Results from western blot analysis of HO-1 and β-actin. b) Deduced average quantities of HO-1 from the intensity of the fluorescent bands of three repeated western blot analyses. They are normalized with the corresponding β-actin quantity.

III.3.3.3. Inflammatory response

Besides oxidative stress, inflammation is also a relevant cellular response to exposure to nanoparticles. In order to study the inflammatory response of the cell upon exposure to $Gd_{2(1-x)}Ce_xO_2S$ nanoparticles, we measured the pro-inflammatory cytokine levels. In particular, interleukin 6 (IL-6), interleukin 1beta (IL- 1β) and tumor necrosis factor alpha (TNF-α) are important inflammation markers and were chosen to be studied in a preliminary study.

We treated RAW 264.7 cells in a similar fashion to oxidative stress study, i.e. nanoparticles at10 µg/mL during 24 hours. LPS was employed as positive control. After the exposure, the

cells were taken and centrifuged to remove remaining cells and nanoparticles. The levels of selected cytokines in the cell supernatant were then evaluated by ELISA microassay analysis. The results are presented in **Figure III.27**.

The quantities of secreted IL- 6 and IL- 1β in untreated cells are below the detection limit of the ELISA kit. Whereas, around 250 pg/mL of TNF-α was detected in the same sample. As expected, treatment with LPS increases all three IL-6, IL- 1β and TNF-α cytokine levels significantly compared to untreated cells. The exact quantity of secreted TNF-α is, however, undetermined due to saturation of measured absorbance in ELISA microassay analysis. Cells exposed to Gd_2O_2S (0% Ce) nanoparticles and $GdCeO_2S$ (50% Ce) show no IL- 6 and IL- 1β secretion, as for untreated cells. Compared to the control, the level of TNF-α is higher in cells exposed to $GdCeO_2S$ (50% Ce) nanoparticles while that with Gd_2O_2S (0% Ce) nanoparticles is unchanged. However, given the high variability between the three independent experiments, we could not conclude on the significance of this secretion.

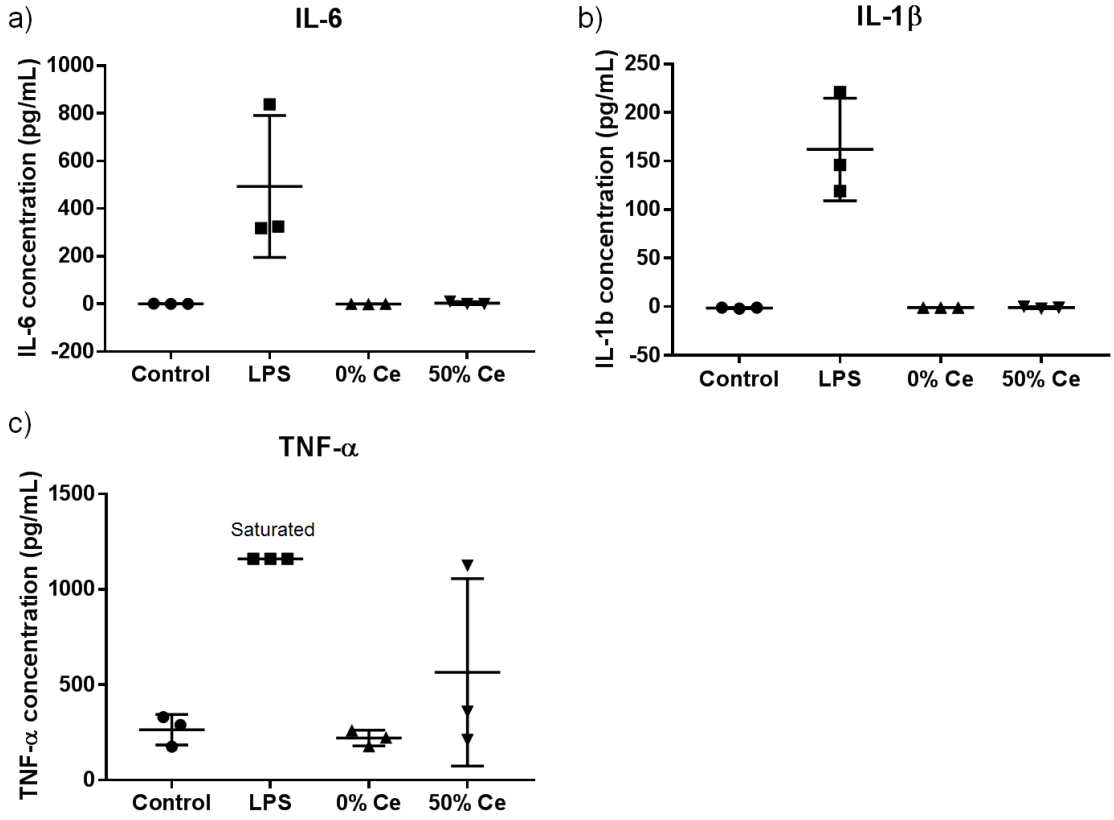

Figure III.27: a-c) Pro-inflammatory cytokines IL- 6, IL- 1β and TNF-α secretion levels of RAW 264.7 cells treated with 10 µg/mL of Gd_2O_2S (0% Ce) nanoparticles and $GdCeO_2S$ (50% Ce) nanoparticles during 24 h. Cell treatment with 10 µg/mL of LPS was used as positive control.

The detected levels of inflammation markers IL- 6, IL- 1β and TNF-α in LPS-stimulated RAW 264.7 cells are comparable to that found in the literature, validating our experiment.[39] Nevertheless, there is no evidence of inflammation from the cells after 24 hours of exposure to 10 µg/mL of $Gd_{2(1-x)}Ce_xO_2S$ nanoparticles.

III.4. Possible origins of cytotoxicity

In the previous section, we showed that cerium-containing $Gd_{2(1-x)}Ce_xO_2S$ nanoparticles were significantly more cytotoxic than Gd_2O_2S nanoparticles. Although we could not clearly determine the cellular mechanisms that led to this cytotoxicity, signs of ROS activity were detected. In this section, instead of focusing on the cell response, we will investigate the nanoparticles and why they could be cytotoxic.

III.4.1. Sodium content

As previously discussed, the sodium content of synthesized $Gd_{2(1-x)}Ce_xO_2S$ nanoparticles is non-consistent through samples (see Chapter II). Furthermore, the sodium can be released in the medium when the nanoparticles are suspended in water. Therefore, when cells are exposed to the nanoparticles, they are treated with an additional amount of sodium as well.

In particular, previously studied $Gd_{2(1-x)}Ce_xO_2S$ nanoparticles features sodium contents from 0.20 to 0.33 equivalents vs. lanthanide (**Table III.1**). Among those, $Gd_{1.8}Ce_{0.2}O_2S$ (10% Ce) nanoparticles contain the maximum quantity of sodium: 0.33 equivalent vs. lanthanides. Accordingly, cells exposed to 100 µg/mL of this nanoparticle are treated with ca. 0.1 mM of sodium. This amount is negligible compared to extracellular sodium concentration at equilibrium which is in the range of 137-155 mM.[40] Hence, it is highly unlikely that the released sodium is the source of the cytotoxicity of the $Gd_{2(1-x)}Ce_xO_2S$ nanoparticles.

III.4.2. Specific surface area

Another suspected parameter is the specific surface area of the nanoparticles. A larger surface area may result in higher activity of the nanoparticles. It may cause harmful effects to the cells.[41] Smaller nanoparticles or aggregates of nanoparticles, which exhibit large specific surface area, also occupy less volume and represent a higher number of units for the same massive concentration. This may as well lead to increased oxidative stress, ROS generation, mitochondrial perturbation, etc.

It seemed that synthesized $Gd_{2(1-x)}Ce_xO_2S$ nanoparticles do not possess the same capability to adsorb molecules (see III.2.4.3). Moreover, we observe that the suspension stability of the nanoparticles in water varies between samples, suggesting different aggregation states.

Hence, we investigate the specific surface area of previously studied $Gd_{2(1-x)}Ce_xO_2S$ nanoparticles containing 0, 10 and 50% of cerium. Due to the small quantity of sample available, only ca. 10 mg of powder of the nanoparticles was analyzed by adsorption isotherm. The corresponding surface area was deduced using the Brunauer-Emmett-Teller (BET) model.

Sample	Na content (eq. vs. lanthanides)	$a_{s,BET}$ ($m^2.g^{-1}$)
0% Ce	0.20 ± 0.03	55
10% Ce	0.33 ± 0.04	81
50% Ce	0.23 ± 0.02	70

Table III.1: Sodium contents measured by SEM-EDS and specific surface areas measured by adsorption isotherm of $Gd_{2(1-x)}Ce_xO_2S$ nanoparticles with 0, 10 and 50% of cerium. The surface area values were extracted using the Brunauer-Emmett-Teller (BET) theory.

The $Gd_{2(1-x)}Ce_xO_2S$ nanoparticles feature specific surface area from 55 to 70 $m^2.g^{-1}$ (**Table III.1**). If we consider the intrinsic experimental error of the adsorption isotherm technique (10 $m^2.g^{-1}$) and potential error from the small amount of analyzed powder, there is no clear difference between the samples containing cerium and those that do not. Thus, it is unlikely that this is the origin of the cytotoxicity of the cerium-containing nanoparticles. In order to confirm this, we selected a different $GdCeO_2S$ (50% Ce) sample with lower specific surface area (32 $m^2.g^{-1}$) and evaluated its cytotoxicity by WST-1 assay. The nanoparticles were prepared using the same colloidal synthesis in organic solvent as described in Chapter II, but with only 0.5 equivalents of sodium precursor vs. lanthanide precursor introduced.

RAW 264.7 macrophages exposed to this new $GdCeO_2S$ nanoparticle sample show no significant difference of mitochondrial activity compared to those exposed to the nanoparticles with higher specific surface area (**Figure III.28**). Thus, the cytotoxicity of the $Gd_{2(1-x)}Ce_xO_2S$ nanoparticles is not only related to the surface exposure.

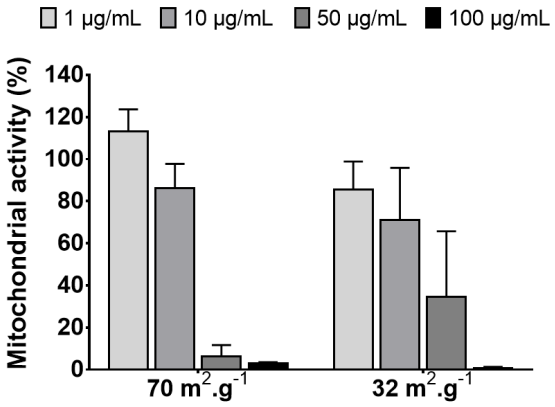

Figure III.28: Mitochondrial activities of RAW 264.7 cells exposed to $GdCeO_2S$ (50% Ce) nanoparticles with different specific surface areas: 70 and 32 $m^2.g^{-1}$. The mitochondrial activities were reported as percentages of that of unexposed cells. The experiments were repeated three times. Statistical analysis revealed no significant difference between the two groups of nanoparticles at comparable concentration.

III.4.3. Stability of $Gd_{2(1-x)}Ce_{2x}O_2S$ nanoparticles in aqueous media

When the nanoparticles are dispersed in cellular medium, they may evolve and interact differently with the cells. It can either lead to biocompatible or bioadverse outcomes. For example, it is well known that the dissolution of zinc oxide (ZnO) and copper oxide (CuO) nanoparticles in aqueous media results in their cytotoxicity.[33,42] Therefore, to acquire insights on the evolution of the $Gd_{2(1-x)}Ce_xO_2S$ nanoparticles in aqueous media, we dispersed them in distilled water and re-characterized them afterwards.

Suspensions in water of the $Gd_{2(1-x)}Ce_xO_2S$ nanoparticles (0% and 50% Ce) at 100 µg/mL were left under vigorous stirring for 24 hours. The nanoparticles were then collected by centrifugation and their size, shape, composition, crystal structure and surface ligand were characterized.

In general, the nanoparticles are more aggregated after treatment with distilled water, as shown by TEM (**Figure III.29**). Aggregates of size up to ca. 5 µm could be observed at higher magnification (data not shown). Interestingly, while $GdCeO_2S$ (50%) nanoparticles preserve their shape (**Figure III.29**d), Gd_2O_2S (0% Ce) nanoparticles have considerably evolved in solution (**Figure III.29**c). The loss of sharp edges may suggest significant change of the platelets at a local level.

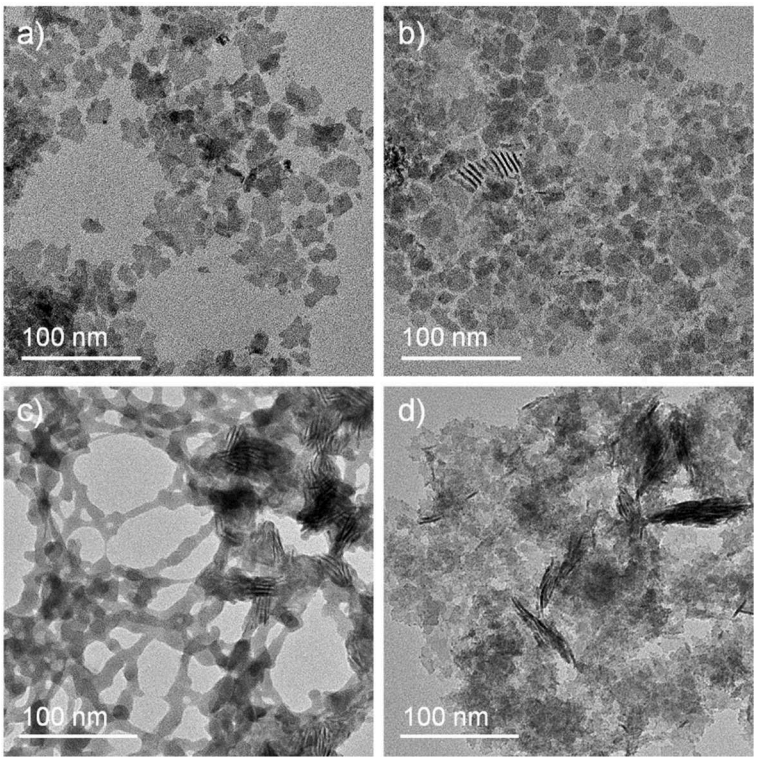

Figure III.29: a, b) TEM images of pristine Gd_2O_2S (0% Ce) and $GdCeO_2S$ (50% Ce) nanoparticles and c, d) their corresponding TEM images after treatment with distilled water.

XRD patterns of the products show unchanged crystal structures for both Gd_2O_2S (0% Ce) and $GdCeO_2S$ (50% Ce) nanoparticles after the water treatment (**Figure III.30**a). The composition of the nanoparticles remains the same as well. In fact, for Gd_2O_2S nanoparticles, the sulfur contents before and after treatment are measured at 0.17 ± 0.01 and 0.15 ± 0.01 equivalents vs. lanthanide by SEM-EDS, respectively. In the case of $GdCeO_2S$ nanoparticles, they are determined at 0.20 ± 0.01 and 0.19 ± 0.01, respectively. The cerium content of the pristine $GdCeO_2S$ nanoparticles is 0.48 ± 0.01 and that of treated nanoparticles is 0.49 ± 0.01. FTIR spectra of both nanoparticles before and after the water treatment are also identical.

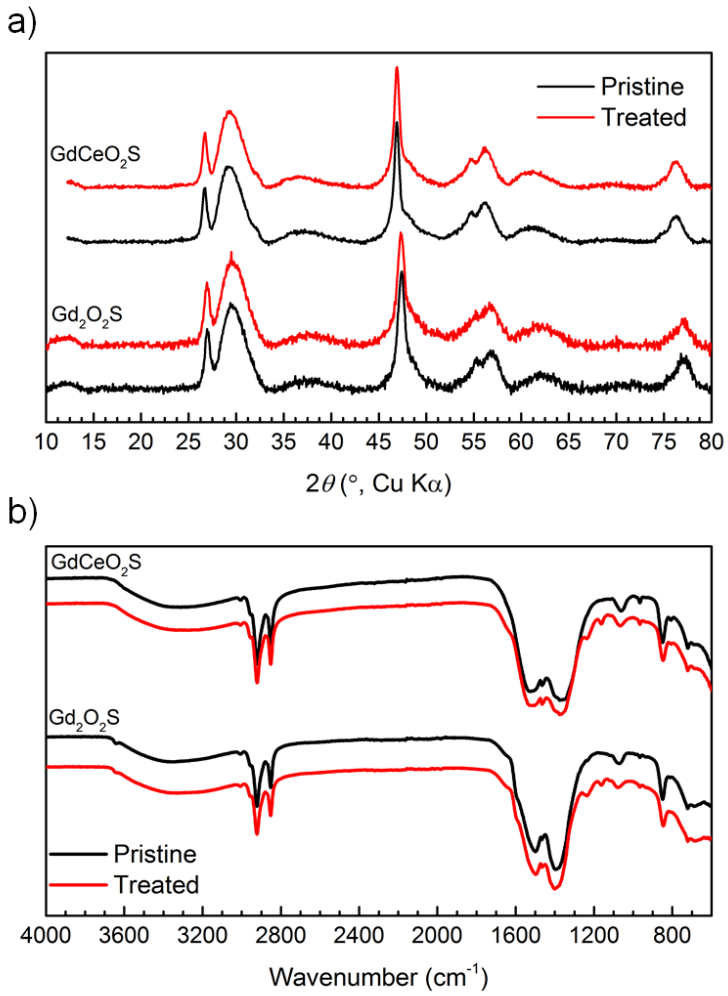

Figure III.30: a) XRD patterns of pristine and treated Gd_2O_2S (0% Ce) and $GdCeO_2S$ (50% Ce) nanoparticles. b) Their corresponding FTIR spectra.

Overall, from ensemble characterization techniques, there was no detectable change of the chemical composition, crystal structure and surface ligand of the $Gd_{2(1-x)}Ce_xO_2S$ (0 and 50% Ce) nanoparticles after their treatment with distilled water during 24 hours. Yet, by TEM, we observed modification of the morphology of Gd_2O_2S nanoparticles to rod-like objects while $GdCeO_2S$ nanoparticles remain platelets. Whether this new morphology of Gd_2O_2S nanoparticles is related to their lower cytotoxicity towards RAW 264.7 cells it is still to be investigated. Nevertheless, this result proves that the nanoparticles can be modified locally in water. It also emphasizes the need of local characterization techniques to elucidate the origin of the cytotoxicity of the cerium-containing oxysulfide nanoparticles.

III.4.4. Local characterization of cell-nanoparticle interaction

Cryo-TEM is a powerful technique that allows characterization of individual nanoparticles in cells. Coupled with EDS or Electron Energy Loss Spectroscopy (EELS), this technique can also give information on chemical composition and speciation of the nanoparticles. However, efforts are still needed to develop cryo-TEM into a reliable tool to investigate cell-nanoparticle interaction. On the other hand, synchrotron-based X-ray hyperspectral imaging is well-known for characterizing both the cell and the nanoparticle at a mesoscopic scale. Reports in the literature have shown intracellular fate of nanoparticles using this technique.[43,44] In particular, Ferraro et al. have demonstrated that the oxidation state of cerium in cerium(IV) oxide CeO_2 nanoparticles could be modified upon incubation with the cells.[43] Therefore, it is fitting to employ the same technique to characterize the interaction between RAW 264.7 macrophages and $Gd_{2(1-x)}Ce_xO_2S$ nanoparticles, also containing cerium.

III.4.4.1. XAS-XRF hyperspectral imaging of cells in cryogenic mode

The X-ray hyperspectral imaging experiments were carried out at beamline ID21 of the European Synchrotron Radiation Facility (ESRF) in Grenoble (France) with the help of Dr. Ana Elena Pradas del Real, Dr. Hiram Castillo and Dr. Murielle Salomé.

For this experiment, we exposed RAW 264.7 cells to 10 µg/mL of $Gd_{2(1-x)}Ce_xO_2S$ (0, 10 and 50% Ce) nanoparticles, similar to the previous sub-lethal effect studies. The cells were then cryo-preserved by snap-freezing. This technique preserves better the cell morphology and structure than other fixation methods such as freeze-drying, presenting a major advantage over the latter. Typically, the snap-freezing was carried out with liquid nitrogen-cooled isopentane at ca. -150 °C. Isopentane acted as a better thermal conductor than liquid nitrogen, thus avoiding uneven freezing and cracking of the cells. Snap-frozen cells were preserved at -80 °C before being transferred to a vacuum chamber cooled at ca. -130 °C at the beamline ID21 for the measurements.

The beamline ID21 is equipped with a focused X-ray beam, allowing acquisition of X-ray fluorescence (XRF) and X-ray absorption (XAS) spectra of an area as small as 0.5 μm^2. XRF addresses the chemical composition of the sample while XAS provides its chemical speciation. Therefore, using the focused beam to scan, both chemical composition and speciation distributions of the sample can be recorded.

III.4.4.2. Imaging cells and nanoparticles composition

We analyzed the composition distribution of the samples containing RAW 264.7 cells exposed to $Gd_{2(1-x)}Ce_xO_2S$ nanoparticles first. This also provided better visualization of the cells as well as the nanoparticles in the samples. For the XRF experiment, the photon energy of the beam was fixed at 7.4 keV so that we could record fluorescence signal of gadolinium (Lα-line at 6.06 keV). The Lα-line of cerium is at lower energy, 4.84 keV. A typical cumulated XRF spectrum recorded in a 100 µm^2 area of cells exposed to $GdCeO_2S$ (50% Ce) nanoparticles is presented in **Figure III.31**.

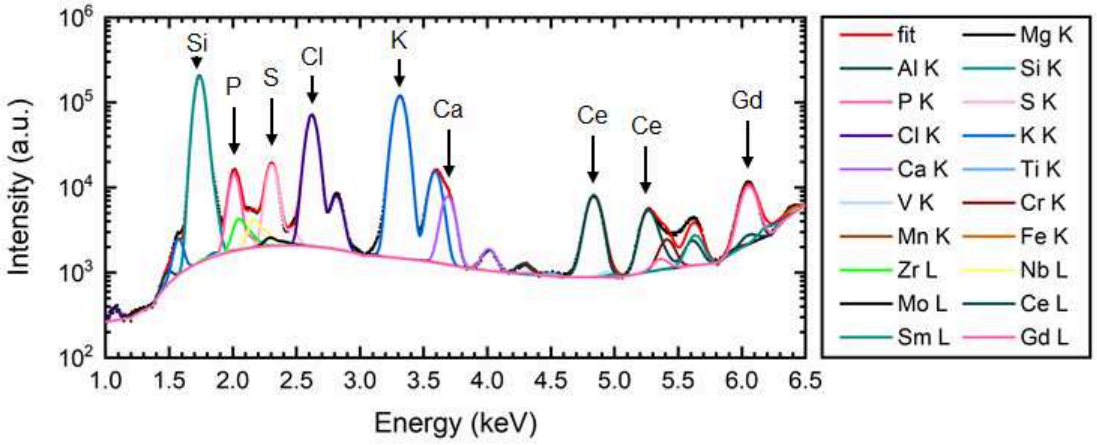

Figure III.31: Black dotted line: cumulated spectrum of a 100 µm^2 X-ray fluorescence map of cells exposed to $GdCeO_2S$ (50% Ce) nanoparticles. Color lines: fit of peaks from elements with color legend on the right. The arrows indicate several elements that are relevant for the cells, the nanoparticles and the experimental setup.

The spectrum can be deconvoluted into peaks corresponding to fluorescence lines of different elements. Those that are usually found in cell medium such as S, P, K, Cl, Ca, Mg or Fe are all present. Ce and Gd are also detected as expected of $GdCeO_2S$ nanoparticles. The signal of other elements (Al, Si, Ti, Cr, etc.) comes from the experimental setup.

For quantification, a thin-film XRF reference sample was measured. This sample contains several elements homogeneously deposited in 1 – 3 atomic layers. Their absolute contents are known. The absolute composition of the samples can thus be deduced in ppm or mM (**Table III.2**). However, the values extracted by this method are approximate because of the difference of matrix between our samples and the reference sample. Consequently, analysis

of absolute concentrations of elements between the samples is semi-quantitative. On the other hand, analysis of relative concentrations between elements in one sample is reliable.

Element	Line	Concentration (mM)
Mg	K	69.9
Al	K	96.0
Si	K	13850
P	K	290.1
S	K	165.1
Cl	K	365.7
K	K	238.4
Ca	K	9.3
Ti	K	0.0
V	K	0.1
Cr	K	0.6
Mn	K	0.0
Fe	K	0.2
Zr	L	31.3
Nb	L	20.1
Mo	L	3.5
Ce	L	3.6
Sm	L	0.6
Gd	L	2.8

Table III.2: Quantification of detected elements of cumulated X-ray fluorescence spectrum of cells exposed to $GdCeO_2S$ (50% Ce) nanoparticles.

Elemental maps describing the distribution of K, P, S and Ca of unexposed cells are presented in **Figure III.32**. The cells are visualized in areas of high concentrations of K, P or S. Although the maximum detected concentration of potassium is comparable to those of phosphorus and sulfur (0.05 vs. 0.10 and 0.07 mM, respectively), it is distributed more homogeneously inside the cells. Therefore, cells can be more readily visualized using distribution of K. This is in agreement with a previous report at the same beamline.[43] The

macrophages have round shape of ca. 20 µm. Some of them are elongated. Their geometries are consistent with those observed by optical microscopy in culture (**Figure III.17**).

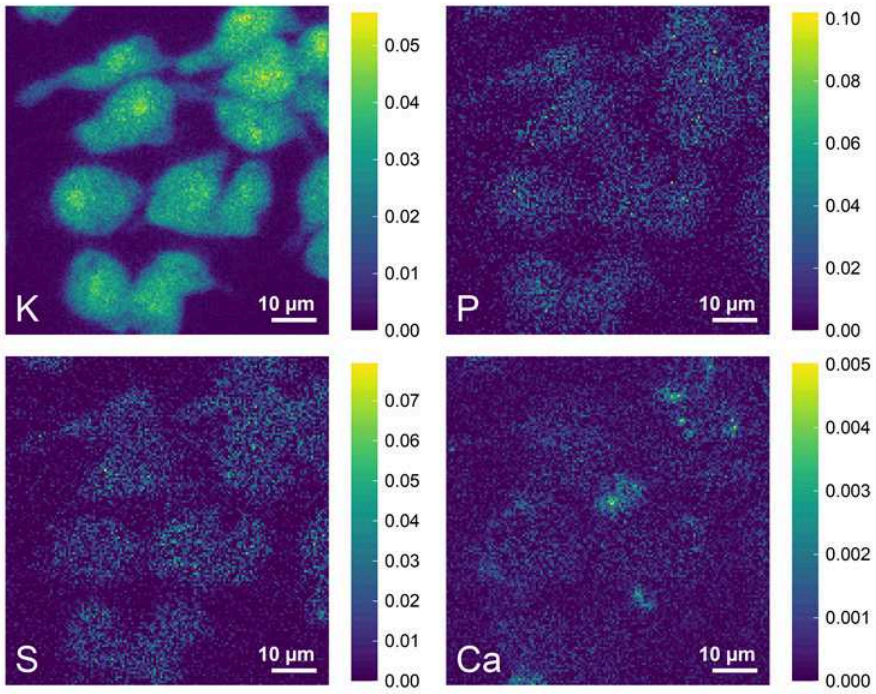

Figure III.32: Single-element XRF maps (72 µm × 73 µm) of non-exposed cells showing distribution of K, P, S and Ca. The images are displayed using a linear scale. The values in the color bars represent the concentration of elements in mM. The XRF maps were acquired at 7.4 keV.

Calcium is also detected but in lower quantities (maximum concentration of 0.005 mM). Its distribution does not clearly correlate to those of the other three cell-marker elements. Even so, Ca plays an important role in cell signaling and is involved in inflammatory mechanisms.[45,46] Thus, it is necessary to monitor the Ca distribution in the cells exposed to nanoparticles.

Cells exposed Gd_2O_2S (0% Ce), $Gd_{1.8}Ce_{0.2}O_2S$ (10% Ce) and $GdCeO_2S$ (50% Ce) nanoparticles were analyzed in the same fashion as unexposed cells. Their respective single-element maps are presented in **Figure III.33**, **Figure III.34** and **Figure III.35**. The K maps show no change of morphology of the cells after exposure to the nanoparticles. The concentration of potassium remains comparable in all samples as well, with a maximum varying from 0.05 to 0.15 mM.

The $Gd_{2(1-x)}Ce_xO_2S$ nanoparticles are localized using Gd maps. Aggregates of size ranging from 0.5 to 5 µm are observed. Larger aggregates locate mainly outside of the cells. As expected, cerium is not detected in the sample of Gd_2O_2S (0% Ce) nanoparticles. Whereas, in those of gadolinium-cerium nanoparticles, cerium is indeed measured and co-localized with gadolinium.

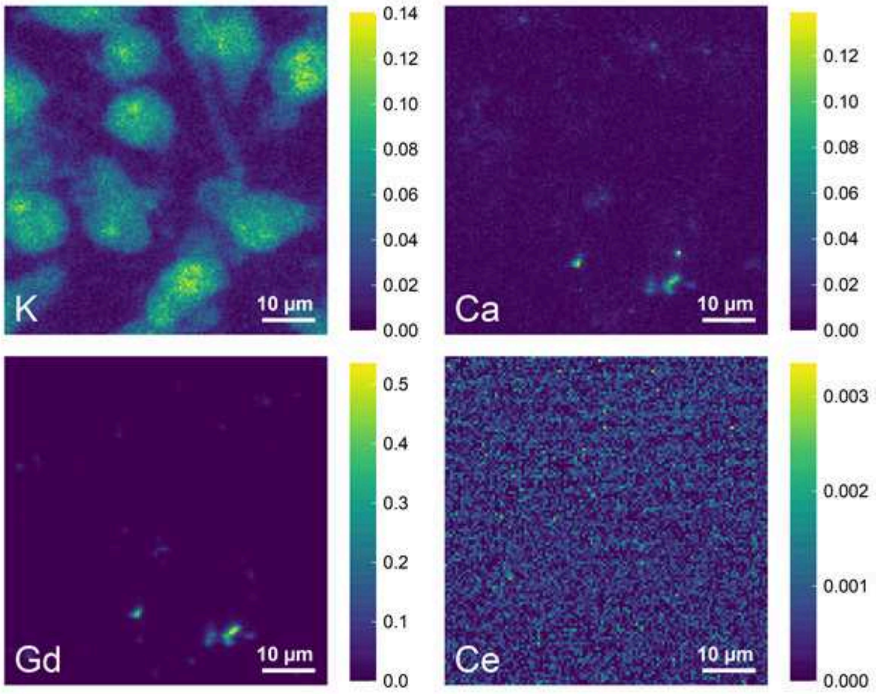

Figure III.33: Single-element XRF maps (61 µm × 61 µm) of cells exposed to Gd_2O_2S (0% Ce) nanoparticles showing distribution of K, Ca, Gd and Ce. The images are displayed using a linear scale. The values in the color bars represent the concentration of elements in mM. The XRF maps were acquired at 7.4 keV.

Interestingly, the calcium maps indicate increases of Ca concentration compared to unexposed cells. The maximum concentrations of calcium detected in cells exposed to nanoparticles are in the range of 0.04 – 0.16 mM, ca. 10 to 30-fold of that detected in unexposed cells. Moreover, co-localization of calcium and gadolinium is observed.

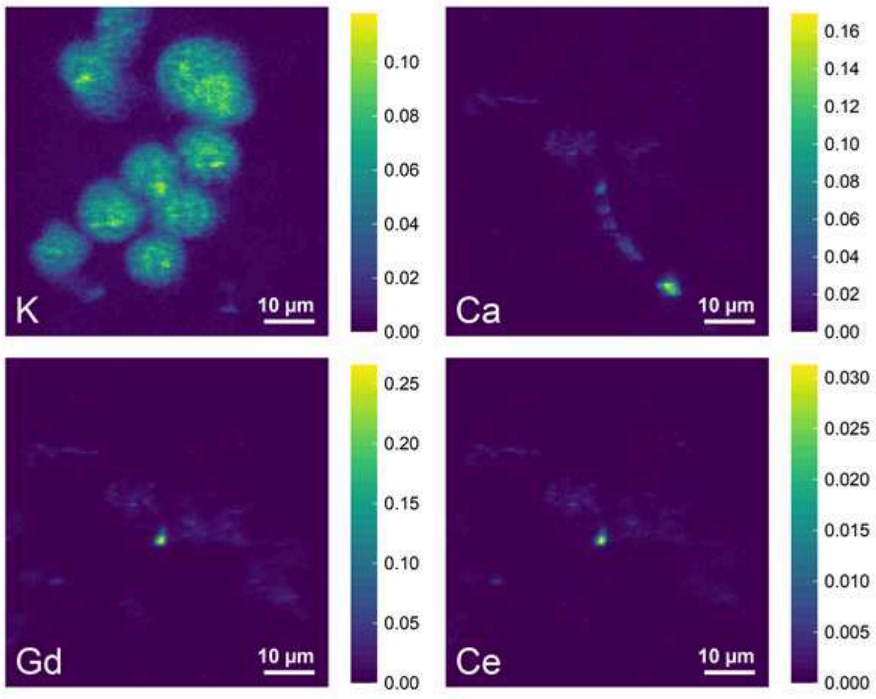

Figure III.34: Single-element XRF maps (64 µm × 69 µm) of cells exposed to $Gd_{1.8}Ce_{0.2}O_2S$ (10% Ce) nanoparticles showing distribution of K, Ca, Gd and Ce. The images are displayed using a linear scale. The values in the color bars represent the concentration of elements in mM. The XRF maps were acquired at 7.4 keV.

In order to evaluate the Ce/Gd ratio throughout the maps of the $Gd_{1.8}Ce_{0.2}O_2S$ (10% Ce) and $GdCeO_2S$ (50% Ce) samples, we plotted the concentration of Ce as function of the concentration of Gd at each pixel (**Figure III.36**). A linear profile is present in both cases, confirming the visually observed co-localization between Gd and Ce. The slope of the profile indicates the average Ce/Gd ratio in the whole map. Compared to the values obtained by EDS for pristine nanoparticles (0.14 ± 0.01 for $Gd_{1.8}Ce_{0.2}O_2S$ and 1.25 ± 0.05 for $GdCeO_2S$), the ratio is lower for the nanoparticles incubated with the cells. This suggests a loss of cerium during the cell treatment. The loss of cerium is clear in the $Gd_{1.8}Ce_{0.2}O_2S$ (10% Ce) samples (**Figure III.36**a). In contrast, this loss is very subtle in the $GdCeO_2S$ (50% Ce) samples since the slope of the linear profile is only slightly lower than that of pristine nanoparticles (**Figure III.36**b). Nevertheless, groups of points that deviate from the average linear profile are detected, featuring nanoparticles with lower cerium contents. This loss of cerium remains to be confirmed by measuring the Ce/Gd ratio of pristine nanoparticles using XRF in the same experimental conditions.

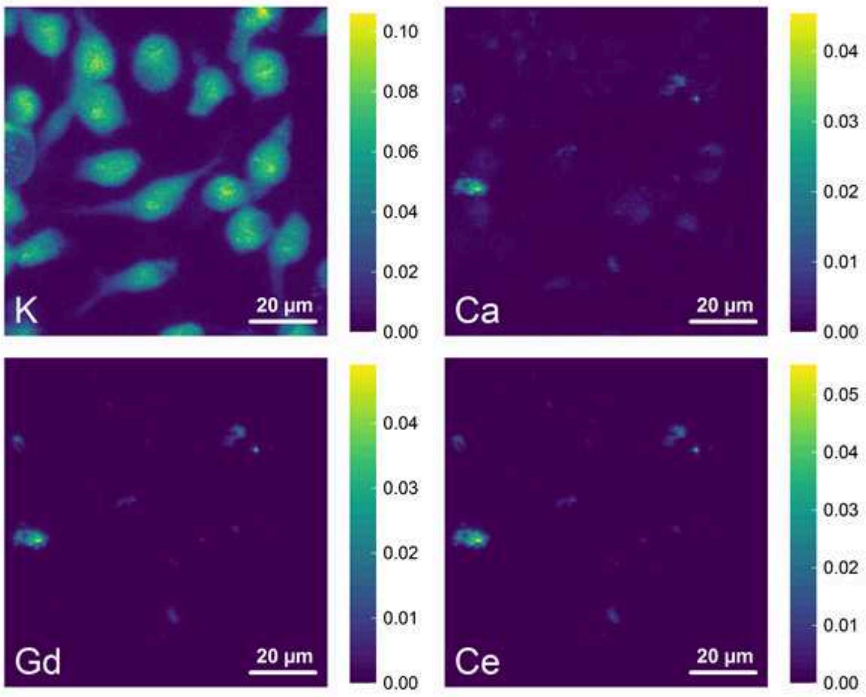

Figure III.35: Single-element XRF maps (100 µm × 100 µm) of cells exposed to $GdCeO_2S$ (50% Ce) nanoparticles showing distribution of K, Ca, Gd and Ce. The images are displayed using a linear scale. The values in the color bars represent the concentration of elements in mM. The XRF maps were acquired at 7.4 keV.

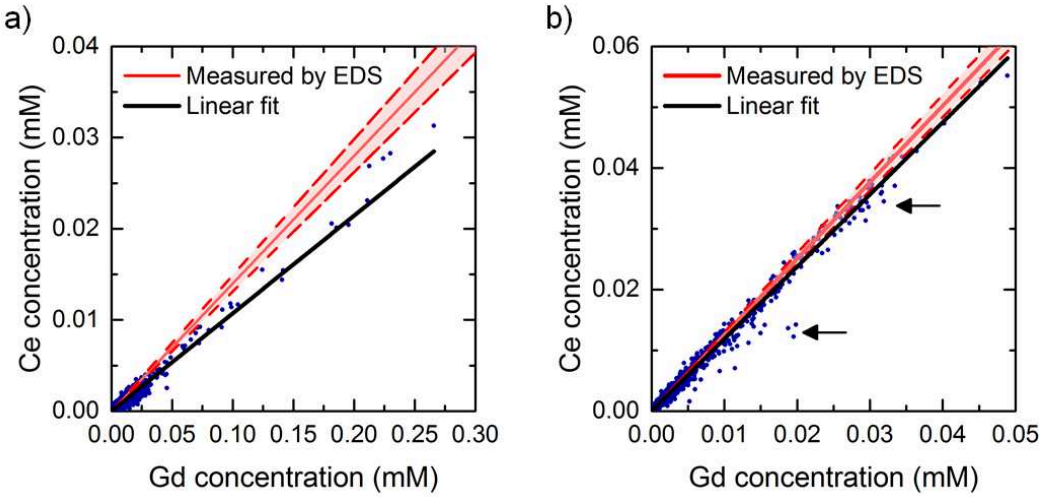

Figure III.36: Scatter plot of concentration profile of Ce over Gd in XRF maps of cells exposed to nanoparticles containing a) 10% and b) 50% of cerium. The red zones describe the standard deviation of the EDS measurement. The arrows indicate the groups of points that deviate from the linear concentration profile.

III.4.4.3. Chemical speciation imaging

In order to gather information on the chemical speciation of the nanoparticles, we performed XAS on selected samples. For this, the photon energy of the X-ray beam was set to 5.8 keV, at the Ce L_3-edge. Similar to the chemical composition imaging, XRF maps were acquired. At this energy, fluorescence of gadolinium does not occur. Thus, the nanoparticles were visualized using the cerium distribution. The cells were still visualized using the K maps. Small areas containing both nanoparticles and cells were selected and hyperspectral images were recorded using the focused X-ray beam.

Typically, XRF spectra and X-ray absorption intensity were first recorded at a given photon energy. The photon energy of the beam was then modified and the process was repeated. Eventually, we acquired hyperspectral maps where a XAS spectrum is associated with each pixel of an XRF map. We were interested in the oxidation state of cerium so only the near edge region (XANES) was measured (from 5.68 to 5.78 keV).

Potassium and cerium merged XRF map of an individual cell incubated with $Gd_{1.8}Ce_{0.2}O_2S$ (10% Ce) nanoparticles is presented in **Figure III.37** Left. XANES spectra of reference compounds of cerium(III), cerium(IV), pristine oxysulfide nanoparticles and two nanoparticle-containing zones inside the cell are also presented in **Figure III.37** Right. Cerium in the pristine nanoparticles is both Ce^{III} and Ce^{IV}, consistent with the previous obtained results at SAMBA beamline of SOLEIL synchrotron (see Chapter II). The two analyzed zones of the XRF map present different absorption intensities at 5723 eV, characteristic of Ce^{III}. While Zone 1 shows higher intensity than that of pristine nanoparticles, Zone 2 shows similar intensity. At 5736 eV, characteristic of Ce^{IV}, the absorption intensities of the two zones are the same as that of the pristine nanoparticles.

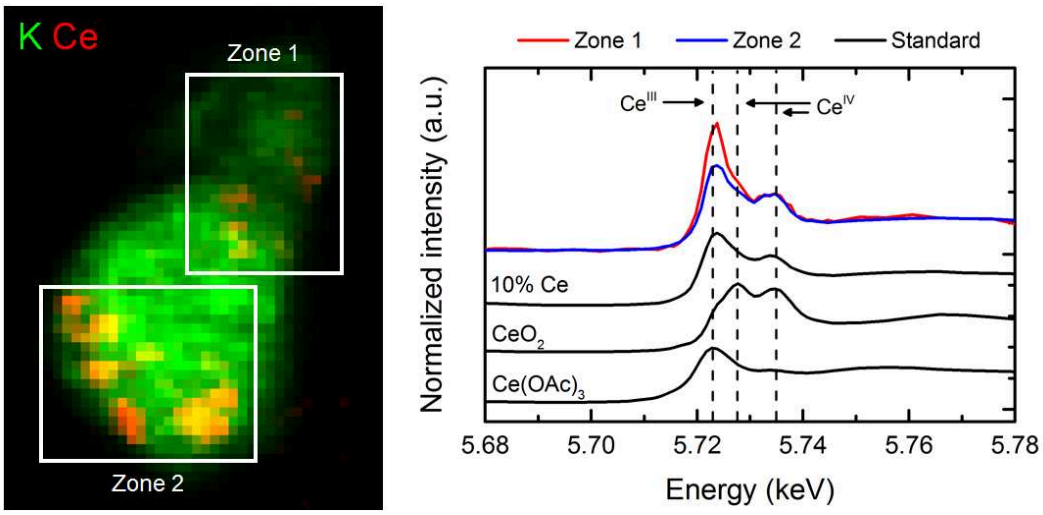

Figure III.37: Left: Merged XRF map of $Gd_{1.8}Ce_{0.2}O_2S$ (10% Ce) acquired at 5.8 keV showing distributions of K and Ce. Right: Normalized XANES spectra of reference compounds and zones indicated in the map.

As for $GdCeO_2S$ (50% Ce) nanoparticles, a small group of cells with nanoparticles nearby was selected for the experiment (**Figure III.38** Left). Several nanoparticle-containing zones were analyzed by XANES and compared to the pristine nanoparticles (**Figure III.38** Right). Similar to the $Gd_{1.8}Ce_{0.2}O_2S$ (10% Ce) nanoparticles, the cerium in $GdCeO_2S$ (50% Ce) nanoparticles shows mixed valence III/IV. XANES spectra of analyzed zones are identical to that of the pristine nanoparticles, in contrast with the previous case.

We detected change of absorption intensity at 5723 eV between two different groups of $Gd_{1.8}Ce_{0.2}O_2S$ (10% Ce) nanoparticles inside a RAW 264.7 cell. This likely indicates a modification of the oxidation state of cerium. Nanoparticles in Zone 1 present more Ce^{III} than those in Zone 2 and the pristine nanoparticles.

Similar change of oxidation state of cerium was reported for cerium oxide CeO_2 nanoparticles incubated with human HeLa cells.[43] We speculate that the nanoparticles in these two zones may have different biological environments. Thus, they interact with intracellular ROS differently. The increase Ce^{III} quantity in Zone 1 is probably due to the reduction of Ce^{IV} by superoxide radicals $O_2^{\bullet-}$. The presence of such mechanism was already proposed by Celardo et al. to explain the antioxidant activity of CeO_2 nanoparticles.[47]

Surprisingly, no change of oxidation state of cerium was detected for $GdCeO_2S$ (50% Ce) nanoparticles incubated with RAW 264.7 cells. It may be related to the fact that the $GdCeO_2S$ (50% Ce) nanoparticles induce less intracellular ROS production than $Gd_{1.8}Ce_{0.2}O_2S$ (10% Ce) nanoparticles (**Figure III.25**). Moreover, it is coherent with the observed difference of cerium loss between these two nanoparticles. Nevertheless, analyses on a larger number of areas need to be done to substantiate our hypotheses.

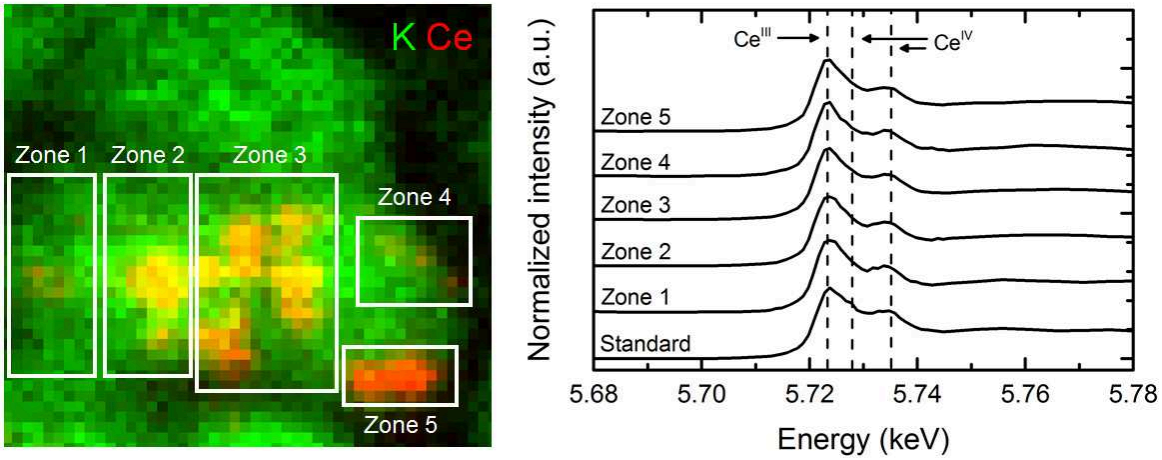

Figure III.38: Left: Merged map of $GdCeO_2S$ (50% Ce) acquired at 5.8 keV showing distributions of K and Ce. Right: Normalized XANES spectra of standards and zones indicated in the map.

III.5. *In vivo* toxicity study

Although we have shown the cytotoxicity of gadolinium-cerium nanoparticles using cell-line studies, the ultimate goal is to determine whether the $Gd_{2(1-x)}Ce_xO_2S$ nanoparticles are harmful for human health. Thus, it is necessary to carry out *in vivo* experiments on animals next.

Human skin, lungs and gastrointestinal tract are in constant contact with environment. In particular, the lungs and gastrointestinal tract are the most likely points of entry for nanoparticles.[48] The nanoparticles can be inhaled into the body from air via the upper respiratory tract. The lung is then the first line of contact for the nanoparticles that gain entry to the body. It is the most likely organ for long-term exposure.[49] Therefore, the pulmonary toxicity of nanoparticles requires consideration. In this section, we will discuss the potential acute *in vivo* toxicity of the $Gd_{2(1-x)}Ce_xO_2S$ nanoparticles based on results on mice.

III.5.1. Non-surgical intratracheal instillation of mice

Fifteen C57BL/6 mice of 12 weeks old were divided into three groups of five individuals. One group was subjected to non-surgical intratracheal instillation of 15 µL of distilled water and served as control group. The two others were instilled with 50 µg of either Gd_2O_2S (0% Ce) and $GdCeO_2S$ (50% Ce) nanoparticles in 15 µL of distilled water. The mice were sacrificed after 24 hours and bronchoalveolar lavage (BAL) fluid was collected for differential cell counts as well as measuring cytokines level.

The exposure dose of nanoparticles was estimated in the context of professional activities, based on the occupational exposure limit value of particulate matters in the French work regulations which is 5 $mg.m^{-3}.h^{-1}$. We considered that 48 $L.min^{-1}$ of air may be inhaled during a moderate physical effort.[50] For a working period of 8 hours, the resulting dose is thus 0.1152 g of nanoparticles. If this dose is for a 70 kg person, the corresponding dose for a 30 g mouse would be 50 µg.

III.5.2. Bronchoalveolar lavage fluid analysis

III.5.2.1. Differential cell counts

Cells in the BAL fluids of the three groups of mice were stained with Diff-Quick (Dade Behring, La Défense, France) and were observed with optical microscope. Representative images of each group are presented in **Figure III.39**a-c. In general, alveolar macrophages are observed. No sign of nanoparticles is seen in almost all of the samples except for one mouse of the Gd_2O_2S (0% Ce) group (**Figure III.39**b). Aggregates of nanoparticles are detected. They are internalized by the macrophages.

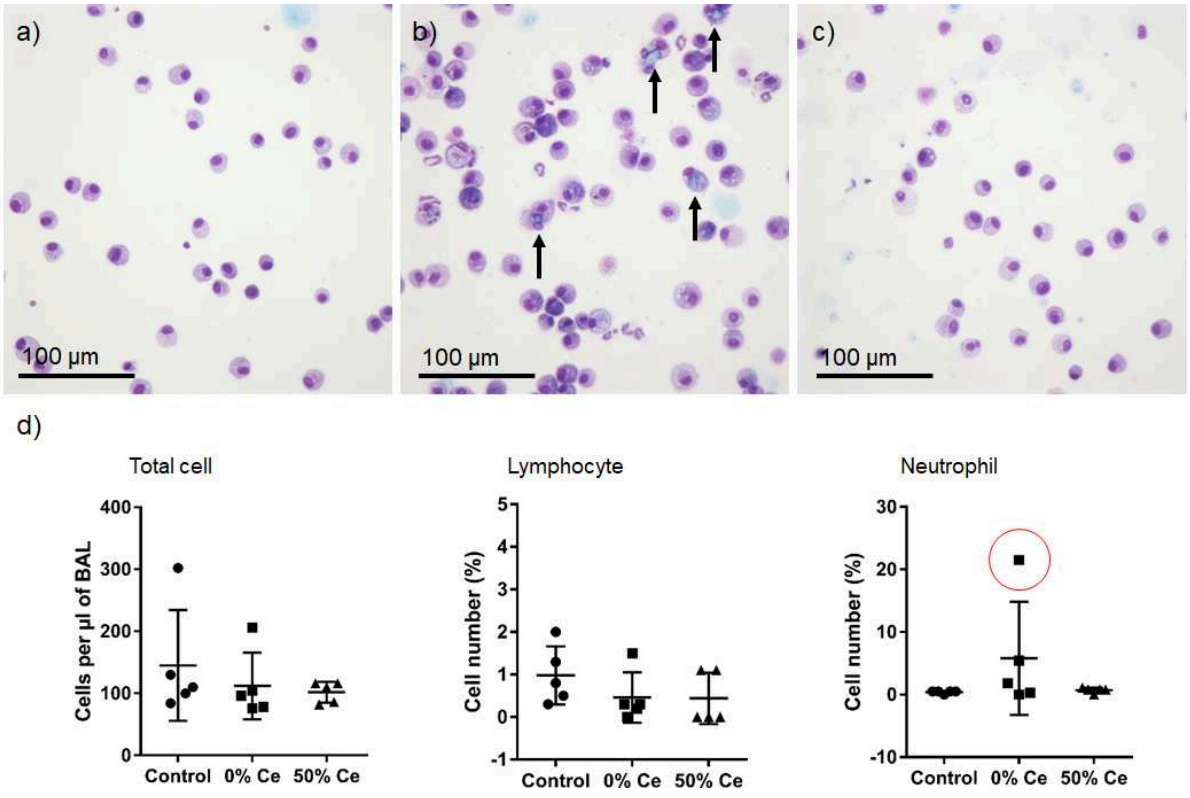

Figure III.39: Optical microscopy images of stained cells in BAL fluid collected from mice instilled with a) distilled water, b) Gd_2O_2S (0% Ce) nanoparticles and c) $GdCeO_2S$ (50% Ce) nanoparticles. The arrows indicate aggregates of nanoparticles. d) Total concentration of cells, cell counts of lymphocyte and neutrophil in BAL fluids of each group of mice. The cell counts of lymphocyte and neutrophil were reported as percentages of the total number of cells. The red circle indicates the high cell count of neutrophil.

The total cell counts show no significant trend between the control group, Gd_2O_2S (0% Ce) and $GdCeO_2S$ (50% Ce) (**Figure III.39**d). It is also the case for the lymphocyte and neutrophil

cell counts. The average lymphocyte and neutrophil cell counts of all three groups are close to zero. However, the BAL fluid collected from one particular mouse instilled with Gd_2O_2S (0% Ce) shows remarkably higher neutrophil cell count (21 cells) than that of all other mice. It is in the same BAL fluid that we noted the presence of nanoparticles.

III.5.2.2. Pro-inflammatory cytokine levels

Similar to the cell-line studies, the levels of pro-inflammatory cytokines IL- 6, IL- 1β and TNF-α in the collected BAL fluids were measured using ELISA microassay analysis. The results are presented in **Figure III.40**. Average concentrations of the three cytokines are all below 2 pg/mL, well below the detection limit of the ELISA kits. This may suggest that the proteins are too diluted in the BAL fluids for detection.

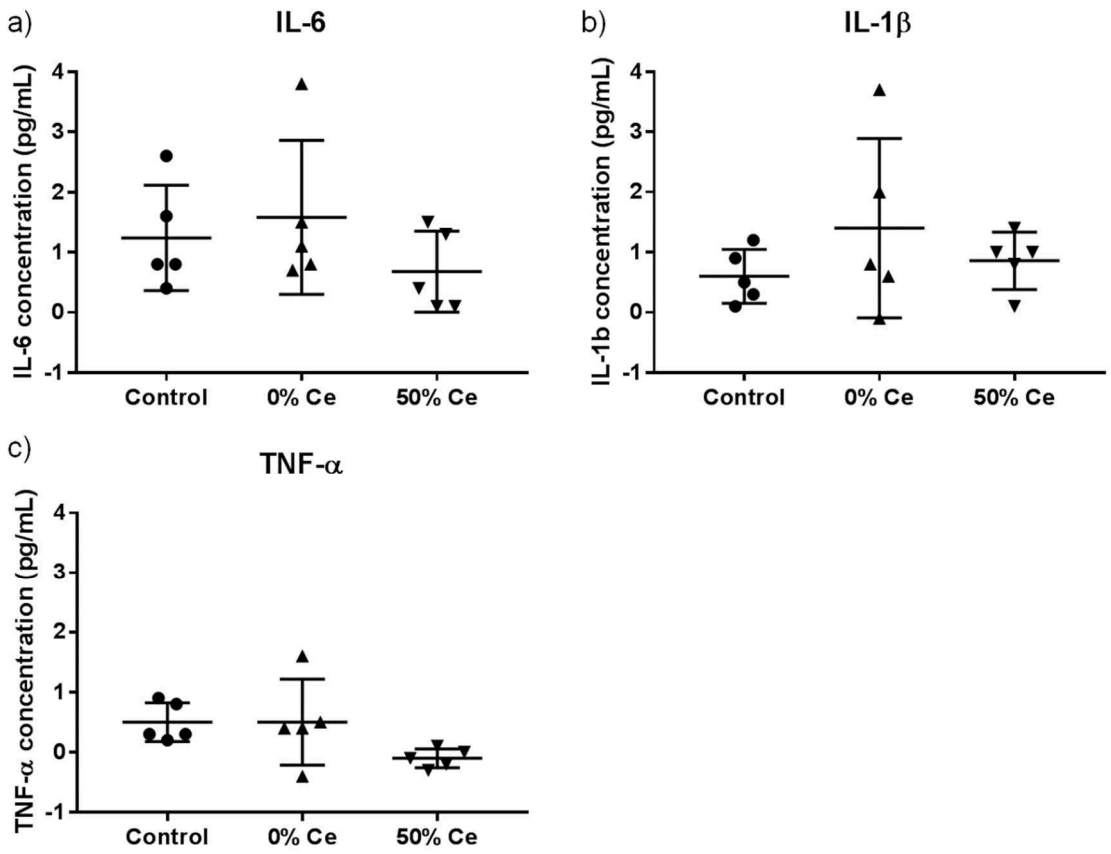

Figure III.40: Pro-inflammatory cytokines a) IL- 6, b) IL-1β and c) TNF-α levels in BAL fluids collected from mice instilled with distilled water, Gd_2O_2S (0% Ce) nanoparticles and $GdCeO_2S$ (50% Ce) nanoparticles. The negative values are due to the error of the measurement. They indicate that the corresponding cytokines levels are undetectable.

III.5.3. Pulmonary toxicity of $Gd_{2(1-x)}Ce_xO_2S$ nanoparticles

We attempted to compare acute pulmonary toxicities of Gd_2O_2S (0% Ce) and $GdCeO_2S$ (50% Ce) by non-surgical intratracheal instillation to mice. The pro-inflammatory cytokine levels and the cell count of neutrophil, which is a marker of inflammation, in the BAL fluids were negligible. This may suggest an absence of inflammatory response of the lung 24 hours after the instillation. Even though, the peak of the inflammatory response can still take place before or after the 24-hour mark. Yet, the nanoparticles were nowhere to be seen in the BAL fluids, except for that of one mouse. Due to the hydrophobic character of the oxysulfide nanoparticles, they are easily aggregated in water. Therefore, we speculate that formed aggregates could not be effectively instilled to the lung of the mice and were stuck either in the catheter used for instillation or the tracheal of the mice. At this stage, conclusion of the pulmonary toxicity of $Gd_{2(1-x)}Ce_xO_2S$ nanoparticles cannot be drawn. Improvement of the experimental protocol may be required. Repeated instillation experiments are also important to determine the chronic toxicity of $Gd_{2(1-x)}Ce_xO_2S$ nanoparticles.

III.6. Discussion

III.6.1. Photocatalytic activity of $Gd_{2(1-x)}Ce_xO_2S$ nanoparticles

In this chapter, we evaluated the potential of $Gd_{2(1-x)}Ce_xO_2S$ nanoplatelets prepared by colloidal synthesis in organic solvent as photocatalysts with visible light. We showed that cerium plays an important role in bandgap and absorption tuning of the $Gd_{2(1-x)}Ce_xO_2S$ nanomaterials. Higher cerium contents resulted in smaller bandgap and gave rise to absorption in the visible region of the electromagnetic spectrum. Cerium-containing nanoparticles exhibited photocatalytic activities under 501 nm irradiation. In particular, $GdCeO_2S$ (50% Ce) nanoparticles could degrade rhodamine B with visible light *via* both photosensitization and photocatalysis. DTT assay also indicated that they photogenerated radicals in water. However, this radical production needs to be confirmed by EPR spectroscopy or other colorimetric and fluorescent methods using selective radical probes.[27] The determination of radical nature would also give insights on the relative positions of conduction and valence bands of the nanoparticles compared to the redox couples $O_2/O_2^{\bullet-}$ and $^{\bullet}OH/H_2O$.

$GdCeO_2S$ (50% Ce) nanoparticles showed more potential for photocatalysis with visible light than Gd_2O_2S (0% Ce) nanoparticles because of their lower bandgap energy (2.3 eV vs. 4.7 eV, respectively) and absorption in the visible region (absorption threshold at ca. 530 mn). The bandgap of $GdCeO_2S$ nanoparticles is lower than that of TiO_2 P25 nanoparticles (ca. 3.1 eV) and also in the low side compared to previously reported photocatalysts with visible light such as WO_3, $BiVO_4$ or Bi_2WO_6.[8,10,24] Furthermore, synthesized $GdCeO_2S$ nanoplatelets exhibited larger specific surface area (70 $m^2.g^{-1}$) compared to previously reported TiO_2 P25, $BiVO_4$ or Bi_2WO_6 nanoparticles (below 50 $m^2.g^{-1}$) in similar studies.[10,24] Altogether, they seem to be very promising photocatalysts. Yet, photodegradation of rhodamine B in the presence of $GdCeO_2S$ nanoplatelets was incomplete even after one week of continuous irradiation at 501 nm. In contrast, TiO_2 P25, $BiVO_4$ and Bi_2WO_6 nanoparticles at comparable concentrations took only hours to complete the reaction.[10,24] The difference of light sources between the studies certainly plays a part in this and $GdCeO_2S$ nanoplatelets could also possess low absorption cross section or high electron-hole pair recombination rate. Further analysis is required to confirm. At this stage, we speculate that the main reason for the low photocatalytic activity of oxysulfide nanoplatelets is their hydrophobic surface. In fact, even after intensive washing, organic ligands remained on the surface of the nanoparticles. They

ensured the charge balance of the latter. However, this hydrophobic layer likely hindered the access of water molecules to the surface of the catalysts, resulting in a slow photodegradation of RhB. To improve the kinetics of the reaction, the ligands must be removed. Thermal treatment with optimized conditions seems a promising method (see Appendix IV).[18]

III.6.2. Toxicity of $Gd_{2(1-x)}Ce_xO_2S$ nanoparticles

In parallel to the study of photocatalytic activity of $Gd_{2(1-x)}Ce_xO_2S$ nanoparticles, we evaluated their potential toxicity by carrying out several *in vitro* and *in vivo* experiments. The cytotoxicity of $Gd_{2(1-x)}Ce_xO_2S$ nanoplatelets prepared by colloidal synthesis in organic solvent was assessed for the first time using murine macrophage-like cells RAW 264.7. Up to 100 µg/mL of nanoparticles were tested. Cytotoxicity assessments of nanoparticles are widely carried out in this range of concentration and it is where their adverse effect is often detected.[51,52] Using the same range of concentration for our study allows comparison between our results and those previously reported. It is also worth noting that these concentrations are much lower than that used in photocatalytic tests of $Gd_{2(1-x)}Ce_xO_2S$ nanoparticles (1 mg/mL). Thus, the adverse effect of the nanoparticles in photocatalytic context would be even more important than what is determined in toxicity assays.

The results of cell viability assays showed that $Gd_{2(1-x)}Ce_xO_2S$ nanoparticles were more cytotoxic than TiO_2 P25 nanoparticles which are the most commonly used photocatalysts. In the literature regarding nanoparticle toxicity, only a few studies reported the potential toxicity of oxysulfide nanoparticles. These studies focus mainly on doped Gd_2O_2S nanoparticles for biomedical imaging.[53–57] In general, they have negligible cytotoxic effect. However, these nanoparticles are coated with polymers such as polyvinylpyrrolidone (PVP) or polyethylene glycol (PEG) to assure their dispersion in water. Therefore, their surface state is completely different from that of our nanoparticles making comparison between the two difficult. Besides oxysulfide nanoparticles, lanthanide oxide nanoparticles such as Gd_2O_3 and CeO_2 are the most similar to our nanoparticles when it comes to chemical composition. Studies on their toxicity using the same RAW 264.7 cell line revealed that most lanthanide oxide nanoparticles, including Gd_2O_3, are cytotoxic except for CeO_2.[33,51] The origin of the toxicity seemed to be the release of lanthanide ions from the particle surface. This led to complexation and capture of biological phosphates from cellular membranes and proteins, triggering the lysosomal damage.[51] However, in our case, Gd_2O_2S nanoparticles showed negligible cytotoxicity. It

should be noted that the more covalent bonding in oxysulfides is expected to lower their solubility in aqueous media. Moreover, the surface of our nanoparticles is coordinated by hydrophobic molecules. Therefore, they tend to aggregate in biological medial. This may lower their exposed surface, limiting the release of ions.

Overall, due to the difference of various physicochemical parameters between our nanoparticles and those reported in the literature, comparison of their toxicity is challenging. However, since our $Gd_{2(1-x)}Ce_xO_2S$ nanoplatelets were synthesized using the same method, they possess similar physicochemical characteristics (see Chapter II). Therefore, the results of their cytotoxicity can be readily discussed together. We showed that while the cytotoxic of Gd_2O_2S nanoparticles was negligible, cerium-containing $Gd_{2(1-x)}Ce_xO_2S$ nanoparticles (10% and 50% Ce) were significantly more cytotoxic. The effect of different sodium contents and specific surface areas between samples did not seem to be significant. Upon dispersion in water, although slight change of morphology of Gd_2O_2S nanoparticles was detected, the overall chemical composition, crystal structure and surface ligand of the $Gd_{2(1-x)}Ce_xO_2S$ nanoparticles were preserved. Therefore, the presence of cerium is likely responsible for the detected cytotoxicity. At this stage, no correlation was found between the cerium content and the adverse effect of the nanoparticles. Synchrotron-based X-ray hyperspectral imaging showed that nanoparticles incubated with the cells seemed to possess lower cerium content than that of pristine nanoparticles, suggesting a release of cerium to the medium. Interestingly, in contrast, ceria nanoparticles (CeO_2) showed negligible dissolution in biological media.[58,59] The contribution of the released cerium to the observed cytotoxicity could be evaluated by carrying out exposure of cells to sources of cerium ions of comparable quantities. Besides the release of cerium, modification of the oxidation state of cerium in a group of nanoparticles containing 10% Ce compared to the pristine nanoparticles was observed as well. Similar change of oxidation state of cerium was reported for cerium oxide CeO_2 nanoparticles incubated with human HeLa cells.[43] It suggested an interaction of the cerium-containing nanoparticles with intracellular ROS. To support this hypothesis, we already showed that the gadolinium-cerium oxysulfide nanoparticles induced significantly more intracellular ROS production than gadolinium oxysulfide nanoparticles after only 15 min of exposure. Both the release of cerium and its change of oxidation state could be at the origin of the observed cytotoxicity. Nevertheless, further confirmations are required. In particular, results of a larger dataset are needed. In view of this, post-mortem characterization of cell pellets after exposure

to nanoparticles would be relevant. The determination of the key parameters that lead to the cytotoxicity of $Gd_{2(1-x)}Ce_xO_2S$ nanoparticles is crucial to deploy strategies to alleviate it.

In order to confirm our findings on the cytotoxicity of $Gd_{2(1-x)}Ce_xO_2S$ nanoparticles, it would be relevant to compare the results between different cell lines. We believe that human epithelial cells such as BEAS-2B or human macrophages THP-1 that are widely used should be studied next since we seek to evaluate the effect of nanoparticles on human health. Evaluation of genotoxicity of the nanoparticles is also of importance. In addition, responses of the cells upon exposure to nanoparticles as well as mechanisms underlying cell death should be explored to elucidate the nanoparticles toxicity. For example, aforementioned gadolinium oxide nanoparticles triggered lysosomal damage in cells that led to pyroptosis of the cells.[51] Autophagy and apoptosis are also common cellular mechanisms that respond to nanoparticle exposure.[33,42] In this work, we only attempted to evaluate oxidative stress and inflammatory response of the cells upon exposure to $Gd_{2(1-x)}Ce_xO_2S$ nanoparticles. There was no evidence of both of these responses after 24 hours of exposure at a sub-lethal dose. We speculate that either the concentration of nanoparticles is too low for detectable responses of the cells or the peak of the responses take place earlier or later than 24 h. Additional experiments at different exposure durations are required.

Calcium release is also a major oxidative stress response that may lead to mitochondrial perturbation and cell death.[60] Using XRF imaging, we detected increases of the concentration of calcium in the samples containing cells exposed to nanoparticles compared to that of unexposed cells. Moreover, co-localization between Ca and Gd, thus the nanoparticles, was observed. Two explanations can be provided: adsorption of calcium species from the cell culture or extracellular flux of calcium generated by the cell. The latter was observed for carbon nanotubes in an unpublished work in our lab, indicating cell response upon exposure. In our case, however, this calcium flux is highly improbable because of the 10 to 30-fold increase of calcium concentration. We thus speculate that the observed co-localization between Ca and Gd is due to the adsorption of calcium on the nanoparticles.

Phagocytosis is the main response of macrophages upon exposure to foreign matters. Therefore, internalization of nanoparticles by the cells needs to be characterized. In aqueous media, $Gd_{2(1-x)}Ce_xO_2S$ nanoparticles aggregate due to their hydrophobic surface. The size of the aggregates could not be measured by Dynamic Light Scattering (DLS) because of the low

stability of the suspensions. However, XRF imaging of cells exposed to the nanoparticles revealed aggregates of size ranging from 0.5 to 5 µm, consistent with TEM observation of the same nanoparticles in water. Larger aggregates located outside of the cells while smaller ones were either on top of the cells or inside them. Optical microscopy failed to provide information on the location of smaller aggregates due to its limit of resolution. To determine whether aggregates of $Gd_{2(1-x)}Ce_xO_2S$ nanoparticles were internalized by the macrophages or not, chemical analysis such as Inductively Coupled Plasma Optical Emission Spectrometry (ICP-OES) of the cellular content might be carried out. TEM of sections of fixed cells exposed to nanoparticles would also confirm this.[61]

To acquire more insights on the effect of $Gd_{2(1-x)}Ce_xO_2S$ nanoparticles towards the cells, Fourier transform infrared microspectroscopy of single cells exposed to the nanoparticles was carried out at SMIS beamline, SOLEIL synchrotron. Alterations in protein structure, cell membrane alteration and changes in energy metabolism of the cells may be monitored using this technique. Data treatment and analysis will be performed using multivariate statistical analysis in the next coming weeks.

III.7. Conclusion

In this chapter, we discussed the safer-by-design approach in relation with the $Gd_{2(1-x)}Ce_{2x}O_2S$ nanoparticles design for photocatalysis. First, the oxysulfide nanoplatelets synthesized in organic medium were intensively washed to remove the hydrophobic surface ligands that potentially hinder their surface reactivity in water. Then their absorption properties were characterized. We demonstrated that the bandgap of the oxysulfide nanoparticles and their absorption were tunable with the cerium content. Higher cerium content led to smaller bandgap and absorption in the visible region of the spectrum (**Figure III.41**).

The visible absorption of cerium-containing nanoparticles gave rise to their photocatalytic activities with 501 nm light. They were able to photogenerated radicals in water and photodegrade rhodamine B. Nevertheless, their efficiency was lower than that of reference TiO_2 P25 nanoparticles, possibly due to remaining organic ligands on the surface of the nanoparticles. To improve the performance of $Gd_{2(1-x)}Ce_{2x}O_2S$ nanoplatelets, the ligands need to be further removed by thermal treatment.

The cerium made $Gd_{2(1-x)}Ce_{2x}O_2S$ nanoparticles a potential candidate for photocatalyst with visible light. However, cerium-containing nanoparticles were proved to be more cytotoxic than those that do not. This was likely due to a loss of cerium during the cell treatment and its reactivity towards intracellular ROS.

Overall, we highlighted the crucial role of cerium on the functionality and the toxicity of $Gd_{2(1-x)}Ce_{2x}O_2S$ nanoparticles. It was originally included in view of design of new photocatalyst with visible light. While the cerium indeed had positive effects on the functionality of the nanoparticles, it was also proved to increase their cytotoxicity. According to our view on the safer-by-design approach, further improvements are desired and the feedback loop needs to be applied again (**Figure III.41**). A compromise on the cerium content of the $Gd_{2(1-x)}Ce_{2x}O_2S$ nanoparticles might be necessary in the future for both functional and safe gadolinium-cerium oxysulfide nanomaterials. In particular, a low cerium content at doping regime (< 5% Ce) would be promising as it may reduce the toxicity while preserving absorption in the visible region (absorption threshold at ca. 450 nm).

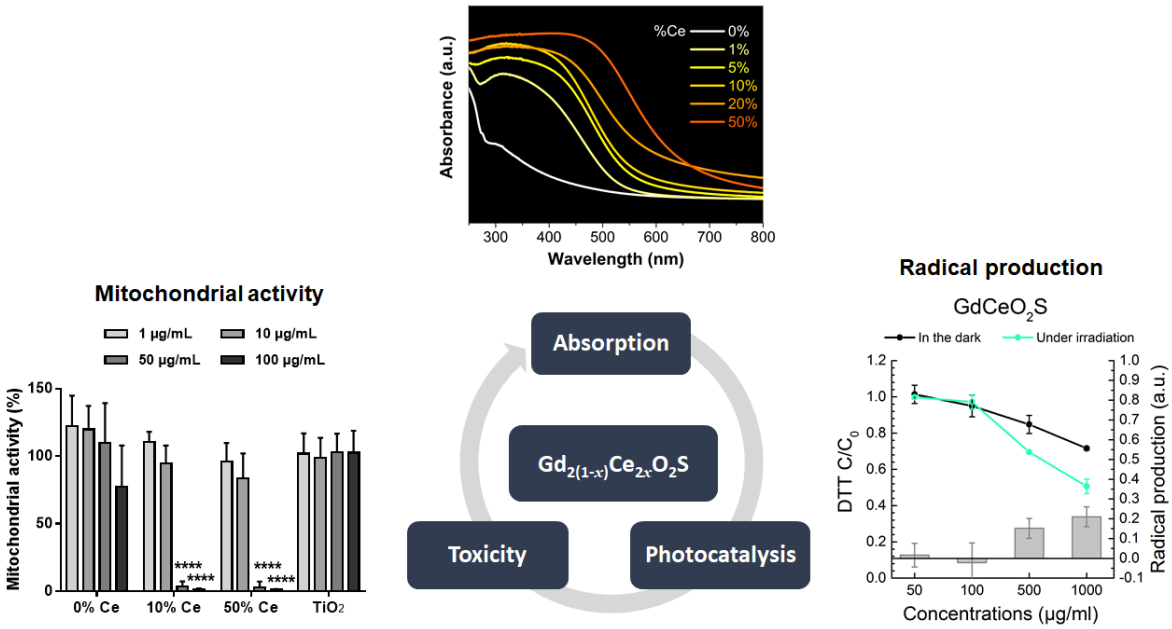

Figure III.41: Main results acquired on the property, functionality and toxicity of $Gd_{2(1-x)}Ce_{2x}O_2S$ nanoparticles.

References

(1) Schneider, J.; Matsuoka, M.; Takeuchi, M.; Zhang, J.; Horiuchi, Y.; Anpo, M.; Bahnemann, D. W. Understanding TiO2 Photocatalysis: Mechanisms and Materials. *Chem. Rev.* **2014**, *114* (19), 9919–9986.

(2) Fujishima, A.; Honda, K. Electrochemical Photolysis of Water at a Semiconductor Electrode. *Nature* **1972**, *238* (5358), 37–38.

(3) Fujishima, A.; Zhang, X.; Tryk, D. A. TiO2 Photocatalysis and Related Surface Phenomena. *Surf. Sci. Rep.* **2008**, *63* (12), 515–582.

(4) Ibhadon, A.; Fitzpatrick, P. Heterogeneous Photocatalysis: Recent Advances and Applications. *Catalysts* **2013**, *3* (1), 189–218.

(5) Linsebigler, A. L.; Lu, G.; Yates, J. T. Photocatalysis on TiO2 Surfaces: Principles, Mechanisms, and Selected Results. *Chem. Rev.* **1995**, *95* (3), 735–758.

(6) Ohno, T.; Sarukawa, K.; Tokieda, K.; Matsumura, M. Morphology of a TiO2 Photocatalyst (Degussa, P-25) Consisting of Anatase and Rutile Crystalline Phases. *J. Catal.* **2001**, *203* (1), 82–86.

(7) Kirk, A. P. *Solar Photovoltaic Cells: Photons to Electricity*; 2014.

(8) Tong, H.; Ouyang, S.; Bi, Y.; Umezawa, N.; Oshikiri, M.; Ye, J. Nano-Photocatalytic Materials: Possibilities and Challenges. *Adv. Mater.* **2012**, *24* (2), 229–251.

(9) Dong, P.; Xi, X.; Hou, G. Typical Non–TiO2-Based Visible-Light Photocatalysts. In *Semiconductor Photocatalysis - Materials, Mechanisms and Applications*; InTech, 2016.

(10) Saison, T.; Chemin, N.; Chanéac, C.; Durupthy, O.; Mariey, L.; Maugé, F.; Brezová, V.; Jolivet, J.-P. New Insights Into BiVO4 Properties as Visible Light Photocatalyst. *J. Phys. Chem. C* **2015**, *119* (23), 12967–12977.

(11) Zhang, H.; Ji, Z.; Xia, T.; Meng, H.; Low-Kam, C.; Liu, R.; Pokhrel, S.; Lin, S.; Wang, X.; Liao, Y. P.; et al. Use of Metal Oxide Nanoparticle Band Gap to Develop a Predictive Paradigm for Oxidative Stress and Acute Pulmonary Inflammation. *ACS Nano* **2012**, *6* (5), 4349–4368.

(12) Hussain, S. M.; Hess, K. L.; Gearhart, J. M.; Geiss, K. T.; Schlager, J. J. In Vitro Toxicity of Nanoparticles in BRL 3A Rat Liver Cells. *Toxicol. Vitr.* **2005**, *19* (7), 975–

983.

(13) Warheit, D. B.; Webb, T. R.; Reed, K. L.; Frerichs, S.; Sayes, C. M. Pulmonary Toxicity Study in Rats with Three Forms of Ultrafine-TiO2 Particles: Differential Responses Related to Surface Properties. *Toxicology* **2007**, *230* (1), 90–104.

(14) Shi, H.; Magaye, R.; Castranova, V.; Zhao, J. Titanium Dioxide Nanoparticles: A Review of Current Toxicological Data. *Part. Fibre Toxicol.* **2013**, *10* (1), 15.

(15) Anses. *Collective Expert Appraisal Report: Establishment of Chronic Reference Value by Inhalation for Titanium Dioxide under Nanoform*; 2019.

(16) Simonin, M.; Richaume, A.; Guyonnet, J. P.; Dubost, A.; Martins, J. M. F.; Pommier, T. Titanium Dioxide Nanoparticles Strongly Impact Soil Microbial Function by Affecting Archaeal Nitrifiers. *Sci. Rep.* **2016**, *6* (1), 33643.

(17) Roy, B.; Chandrasekaran, H.; Palamadai Krishnan, S.; Chandrasekaran, N.; Mukherjee, A. UVA Pre-Irradiation to P25 Titanium Dioxide Nanoparticles Enhanced Its Toxicity towards Freshwater Algae Scenedesmus Obliquus. *Environ. Sci. Pollut. Res.* **2018**, *25* (17), 16729–16742.

(18) Larquet, C.; Hourlier, D.; Nguyen, A.; Torres-Pardo, A.; Gauzzi, A.; Sanchez, C.; Carenco, S. Thermal Stability of Oleate-Stabilized Gd2O2S Nanoplates in Inert and Oxidizing Atmospheres. *ChemNanoMat* **2019**, *5* (4), 539–546.

(19) Flahaut, J.; Guittard, M.; Patrie, M. Les Oxysulfures Me2O2S Des Éléments Du Groupe Des Terres Rares. *Bull. Soc. Chim. Fr.* 1958, pp 990–994.

(20) Larquet, C.; Nguyen, A.-M.; Ávila-Gutiérrez, M.; Tinat, L.; Lassalle-Kaiser, B.; Gallet, J.-J.; Bournel, F.; Gauzzi, A.; Sanchez, C.; Carenco, S. Synthesis of Ce2O2S and Gd2(1–y)Ce2yO2S Nanoparticles and Reactivity from in Situ X-Ray Absorption Spectroscopy and X-Ray Photoelectron Spectroscopy. *Inorg. Chem.* **2017**, *56* (22), 14227–14236.

(21) Larquet, C. Nanoparticles of Lanthanide and Transition Metal Oxysulfides: From Colloidal Synthesis to Structure, Surface, Optical and Magnetic Properties, 2018.

(22) Chen, C.; Ma, W.; Zhao, J. Semiconductor-Mediated Photodegradation of Pollutants under Visible-Light Irradiation. *Chem. Soc. Rev.* **2010**, *39* (11), 4206–4219.

(23) Rochkind, M.; Pasternak, S.; Paz, Y. Using Dyes for Evaluating Photocatalytic

Properties: A Critical Review. *Molecules* **2015**, *20* (1), 88–110.

(24) Saison, T.; Gras, P.; Chemin, N.; Chanéac, C.; Durupthy, O.; Brezová, V.; Colbeau-Justin, C.; Jolivet, J. P. New Insights into Bi2WO6 Properties as a Visible-Light Photocatalyst. *J. Phys. Chem. C* **2013**, *117* (44), 22656–22666.

(25) Watanabe, T.; Takizawa, T.; Honda, K. Photocatalysis through Excitation of Adsorbates. 1. Highly Efficient N-Deethylation of Rhodamine B Adsorbed to Cadmium Sulfide. *J. Phys. Chem.* **1977**, *81* (19), 1845–1851.

(26) Wu, T.; Liu, G.; Zhao, J.; Hidaka, H.; Serpone, N. Photoassisted Degradation of Dye Pollutants. V. Self-Photosensitized Oxidative Transformation of Rhodamine B under Visible Light Irradiation in Aqueous TiO 2 Dispersions. *J. Phys. Chem. B* **2002**, *102* (30), 5845–5851.

(27) Nosaka, Y.; Nosaka, A. Y. Generation and Detection of Reactive Oxygen Species in Photocatalysis. *Chem. Rev.* **2017**, *117* (17), 11302–11336.

(28) Wardman, P. Reduction Potentials of One Electron Couples Involving Free Radicals in Aqueous Solution. *J. Phys. Chem. Ref. Data* **1989**, *18* (4), 1637–1755.

(29) Perkins, M. J. Spin Trapping. *Adv. Phys. Org. Chem.* **1980**, *17* (C), 1–64.

(30) Sauvain, J. J.; Rossi, M. J.; Riediker, M. Comparison of Three Acellular Tests for Assessing the Oxidation Potential of Nanomaterials. *Aerosol Sci. Technol.* **2013**, *47* (2), 218–227.

(31) Li, N.; Sioutas, C.; Cho, A.; Schmitz, D.; Misra, C.; Sempf, J.; Wang, M.; Oberley, T.; Froines, J.; Nel, A. Ultrafine Particulate Pollutants Induce Oxidative Stress and Mitochondrial Damage. *Environ. Health Perspect.* **2003**, *111* (4), 455–460.

(32) Sauvain, J. J.; Deslarzes, S.; Riediker, M. Nanoparticle Reactivity toward Dithiothreitol. *Nanotoxicology* **2008**, *2* (3), 121–129.

(33) Xia, T.; Kovochich, M.; Liong, M.; Mädler, L.; Gilbert, B.; Shi, H.; Yeh, J. I.; Zink, J. I.; Nel, A. E. Comparison of the Mechanism of Toxicity of Zinc Oxide and Cerium Oxide Nanoparticles Based on Dissolution and Oxidative Stress Properties. *ACS Nano* **2008**, *2* (10), 2121–2134.

(34) Cohignac, V.; Landry, M. J.; Ridoux, A.; Pinault, M.; Annangi, B.; Gerdil, A.; Herlin-Boime, N.; Mayne, M.; Haruta, M.; Codogno, P.; et al. Carbon Nanotubes, but Not Spherical Nanoparticles, Block Autophagy by a Shape-Related Targeting of

Lysosomes in Murine Macrophages. *Autophagy* **2018**, *14* (8), 1323–1334.

(35) Park, M. V. D. Z.; Neigh, A. M.; Vermeulen, J. P.; de la Fonteyne, L. J. J.; Verharen, H. W.; Briedé, J. J.; van Loveren, H.; de Jong, W. H. The Effect of Particle Size on the Cytotoxicity, Inflammation, Developmental Toxicity and Genotoxicity of Silver Nanoparticles. *Biomaterials* **2011**, *32* (36), 9810–9817.

(36) Taciak, B.; Białasek, M.; Braniewska, A.; Sas, Z.; Sawicka, P.; Kiraga, Ł.; Rygiel, T.; Król, M. Evaluation of Phenotypic and Functional Stability of RAW 264.7 Cell Line through Serial Passages. *PLoS One* **2018**, *13* (6), e0198943.

(37) Han, X.; Gelein, R.; Corson, N.; Wade-Mercer, P.; Jiang, J.; Biswas, P.; Finkelstein, J. N.; Elder, A.; Oberdörster, G. Validation of an LDH Assay for Assessing Nanoparticle Toxicity. *Toxicology* **2011**, *287* (1–3), 99–104.

(38) Choi, A. M. K.; Alam, J. Heme Oxygenase-1: Function, Regulation, and Implication of a Novel Stress-Inducible Protein in Oxidant-Induced Lung Injury. *Am. J. Respir. Cell Mol. Biol.* **1996**, *15* (1), 9–19.

(39) Muniandy, K.; Gothai, S.; Badran, K. M. H.; Suresh Kumar, S.; Esa, N. M.; Arulselvan, P. Suppression of Proinflammatory Cytokines and Mediators in LPS-Induced RAW 264.7 Macrophages by Stem Extract of Alternanthera Sessilis via the Inhibition of the NF- κ B Pathway. *J. Immunol. Res.* **2018**, *2018*, 1–12.

(40) Ackerman, G. L. *Serum Sodium*; Butterworths, 1990.

(41) Shin, S.; Song, I.; Um, S. Role of Physicochemical Properties in Nanoparticle Toxicity. *Nanomaterials* **2015**, *5* (3), 1351–1365.

(42) Naatz, H.; Lin, S.; Li, R.; Jiang, W.; Ji, Z.; Chang, C. H.; Köser, J.; Thöming, J.; Xia, T.; Nel, A. E.; et al. Safe-by-Design CuO Nanoparticles via Fe-Doping, Cu–O Bond Length Variation, and Biological Assessment in Cells and Zebrafish Embryos. *ACS Nano* **2017**, *11* (1), 501–515.

(43) Ferraro, D.; Tredici, I. G.; Ghigna, P.; Castillio-Michel, H.; Falqui, A.; Benedetto, C. Di; Alberti, G.; Ricci, V.; Anselmi-Tamburini, U.; Sommi, P. Dependence of the Ce(III)/Ce(IV) Ratio on Intracellular Localization in Ceria Nanoparticles Internalized by Human Cells. *Nanoscale* **2017**.

(44) Bussy, C.; Paineau, E.; Cambedouzou, J.; Brun, N.; Mory, C.; Fayard, B.; Salomé, M.; Pinault, M.; Huard, M.; Belade, E.; et al. Intracellular Fate of Carbon Nanotubes inside

Murine Macrophages: PH-Dependent Detachment of Iron Catalyst Nanoparticles. *Part. Fibre Toxicol.* **2013**, *10* (1), 24.

(45) Liu, X.; Wang, N.; Zhu, Y.; Yang, Y.; Chen, X.; Fan, S.; Chen, Q.; Zhou, H.; Zheng, J. Inhibition of Extracellular Calcium Influx Results in Enhanced IL-12 Production in LPS-Treated Murine Macrophages by Downregulation of the CaMKK β -AMPK-SIRT1 Signaling Pathway. *Mediators Inflamm.* **2016**, *2016*, 1–15.

(46) Maurya, M. R.; Subramaniam, S. A Kinetic Model for Calcium Dynamics in RAW 264.7 Cells: 1. Mechanisms, Parameters, and Subpopulational Variability. *Biophys. J.* **2007**, *93* (3), 709–728.

(47) Celardo, I.; Pedersen, J. Z.; Traversa, E.; Ghibelli, L. Pharmacological Potential of Cerium Oxide Nanoparticles. *Nanoscale* **2011**, *3* (4), 1411–1420.

(48) Buzea, C.; Pacheco, I. I.; Robbie, K. Nanomaterials and Nanoparticles: Sources and Toxicity. *Biointerphases* **2007**, *2* (4), MR17-R71.

(49) Li, J. J. en; Muralikrishnan, S.; Ng, C. T.; Yung, L. Y. L.; Bay, B. H. Nanoparticle-Induced Pulmonary Toxicity. *Exp. Biol. Med.* **2010**, *235* (9), 1025–1033.

(50) Int Panis, L.; de Geus, B.; Vandenbulcke, G.; Willems, H.; Degraeuwe, B.; Bleux, N.; Mishra, V.; Thomas, I.; Meeusen, R. Exposure to Particulate Matter in Traffic: A Comparison of Cyclists and Car Passengers. *Atmos. Environ.* **2010**, *44* (19), 2263–2270.

(51) Mirshafiee, V.; Sun, B.; Chang, C. H.; Liao, Y. P.; Jiang, W.; Jiang, J.; Liu, X.; Wang, X.; Xia, T.; Nel, A. E. Toxicological Profiling of Metal Oxide Nanoparticles in Liver Context Reveals Pyroptosis in Kupffer Cells and Macrophages versus Apoptosis in Hepatocytes. *ACS Nano* **2018**, *12* (4), 3836–3852.

(52) Lewinski, N.; Colvin, V.; Drezek, R. Cytotoxicity of Nanopartides. *Small* **2008**, *4* (1), 26–49.

(53) Ajithkumar, G.; Yoo, B.; Goral, D. E.; Hornsby, P. J.; Lin, A.-L.; Ladiwala, U.; Dravid, V. P.; Sardar, D. K. Multimodal Bioimaging Using a Rare Earth Doped Gd2O2S:Yb/Er Phosphor with Upconversion Luminescence and Magnetic Resonance Properties. *J. Mater. Chem. B* **2013**, *1* (11), 1561.

(54) Guo, T.; Lin, Y.; Li, Z.; Chen, S.; Huang, G.; Lin, H.; Wang, J.; Liu, G.; Yang, H. H. Gadolinium Oxysulfide-Coated Gold Nanorods with Improved Stability and Dual-

Modal Magnetic Resonance/Photoacoustic Imaging Contrast Enhancement for Cancer Theranostics. *Nanoscale* **2017**, *9* (1), 56–61.

(55) Osseni, S. A.; Lechevallier, S.; Verelst, M.; Dujardin, C.; Dexpert-Ghys, J.; Neumeyer, D.; Leclercq, M.; Baaziz, H.; Cussac, D.; Santran, V.; et al. New Nanoplatform Based on Gd 2 O 2 S: Eu 3+ Core: Synthesis, Characterization and Use for in Vitro Bio-Labelling. *J. Mater. Chem.* **2011**, *21* (45), 18365–18372.

(56) Osseni, S. a; Lechevallier, S.; Verelst, M.; Perriat, P.; Dexpert-Ghys, J.; Neumeyer, D.; Garcia, R.; Mayer, F.; Djanashvili, K.; Peters, J. a; et al. Gadolinium Oxysulfide Nanoparticles as Multimodal Imaging Agents for T2-Weighted MR, X-Ray Tomography and Photoluminescence. *Nanoscale* **2014**, *6* (1), 555–564.

(57) Santelli, J.; Lechevallier, S.; Baaziz, H.; Vincent, M.; Martinez, C.; Mauricot, R.; Parini, A.; Verelst, M.; Cussac, D. Multimodal Gadolinium Oxysulfide Nanoparticles: A Versatile Contrast Agent for Mesenchymal Stem Cell Labeling. *Nanoscale* **2018**, *10* (35), 16775–16786.

(58) Pulido-Reyes, G.; Rodea-Palomares, I.; Das, S.; Sakthivel, T. S.; Leganes, F.; Rosal, R.; Seal, S.; Fernández-Pinãs, F. Untangling the Biological Effects of Cerium Oxide Nanoparticles: The Role of Surface Valence States. *Sci. Rep.* **2015**, *5* (1), 15613.

(59) Brunner, T. J.; Wick, P.; Manser, P.; Spohn, P.; Grass, R. N.; Limbach, L. K.; Bruinink, A.; Stark, W. J. In Vitro Cytotoxicity of Oxide Nanoparticles: Comparison to Asbestos, Silica, and the Effect of Particle Solubility. *Environ. Sci. Technol.* **2006**, *40* (14), 4374–4381.

(60) Cho, A. K.; Sioutas, C.; Miguel, A. H.; Kumagai, Y.; Schmitz, D. A.; Singh, M.; Eiguren-Fernandez, A.; Froines, J. R. Redox Activity of Airborne Particulate Matter at Different Sites in the Los Angeles Basin. *Environ. Res.* **2005**, *99* (1), 40–47.

(61) Shi, Y.; Hélary, C.; Haye, B.; Coradin, T. Extracellular versus Intracellular Degradation of Nanostructured Silica Particles. *Langmuir* **2018**, *34* (1), 406–415.

Chapter IV

Potential application of bimetallic Gd-Ce oxysulfide nanoparticles in biomedical imaging

Table of contents

IV.1. Doped $Gd_{2(1-x)}Ce_{2x}O_2S$ nanoparticles as potential contrast agents 157
IV.1.1. Examples of oxysulfide nanoparticles for multimodal biomedical imaging. 158
IV.1.2. Design $Gd_{2(1-x)}Ce_{2x}O_2S$ nanoplatelets for biomedical imaging 159
IV.2. PVP-coated Eu-doped $Gd_{2(1-x)}Ce_{2x}O_2S$ nanoparticles..... 161
IV.2.1. Eu-doped $Gd_{2(1-x)}Ce_{2x}O_2S$ nanoparticles 161
IV.2.2. Optical properties of pristine Eu-doped $Gd_{2(1-x)}Ce_{2x}O_2S$ nanoparticles 164
IV.2.2.1. Effect of dopant level..... 164
IV.2.2.2. Photoluminescence quenching by cerium..... 165
IV.2.3. PVP-coating of $Gd_{2(1-x)}Ce_{2x}O_2S$ nanoparticles 166
IV.2.3.1. PVP-coating and characterization of products..... 166
IV.2.3.2. Reducing PVP content in the final product..... 169
IV.2.4. Optical properties of PVP-coated Gd_2O_2S:Eu nanoparticles 170
IV.2.5. Cytotoxicity of PVP-coated gadolinium oxysulfide nanoparticles 171
IV.3. Discussion..... 173
IV.4. Conclusion 175
References 176

IV.1. Doped $Gd_{2(1-x)}Ce_{2x}O_2S$ nanoparticles as potential contrast agents

In the last chapter, we showed that $Gd_{2(1-x)}Ce_{2x}O_2S$ nanoplatelets prepared by colloidal synthesis in organic solvent were potential candidate for photocatalyst with visible light. However, these nanoparticles may also find applications in multimodal biomedical imaging as previously discussed in Chapter II. In fact, examples in the literature show that lanthanide oxysulfide nanoplatelets can be doped with other lanthanides for a variety of photoluminescence properties (**Figure IV.1**).[1,2] Gadolinium oxysulfide Gd_2O_2S nanoparticles also exhibit high magnetic susceptibility which makes them relevant for magnetic imaging (see Chapter II, Figure 3b).[3–8] Moreover, it was recently demonstrated in our lab that the $Gd_{2(1-x)}Ce_{2x}O_2S$ nanoplatelets were paramagnetic and their magnetic properties could be tuned with the cerium content.[9,10]

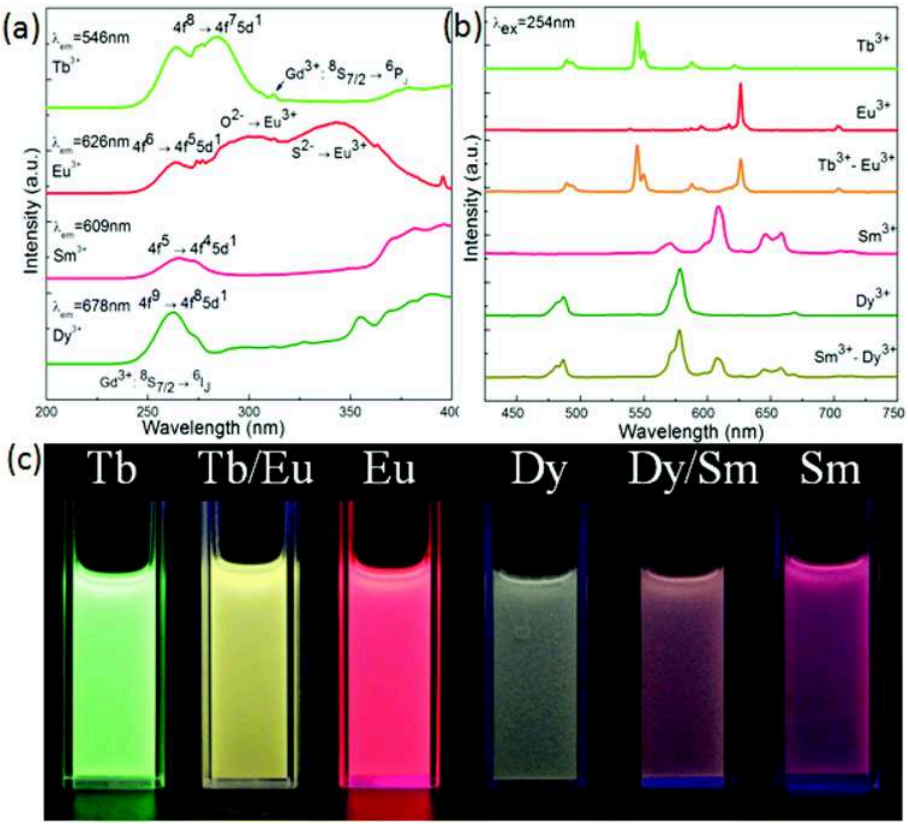

Figure IV.1: (a) Photoluminescence excitation spectra of $Gd_2O_2S:Tb^{3+}$ (or Eu^{3+}, Sm^{3+}, and Dy^{3+}). (b) Photoluminescence spectra of $Gd_2O_2S:RE^{3+}$ (RE^{3+} = Tb^{3+}, Tb^{3+}/Eu^{3+}, Eu^{3+}, Sm^{3+}, Sm^{3+}/Dy^{3+}, Dy^{3+}) nanoplatelets in cyclohexane solution (2 $mg.mL^{-1}$) under 264 nm excitation; (c) are the corresponding images of (b) under 254 nm excitation (taken from ref [1]).

IV.1.1. Examples of oxysulfide nanoparticles for multimodal biomedical imaging

Osseni et al. reported for the first time in 2011 that oxysulfide nanoparticles could potentially be employed for biomedical imaging.[6] They prepared 100 nm Eu-doped Gd_2O_2S nanoparticles which strongly absorb X-ray or near UV (363 nm) and re-emit a red light at 624 nm. These nanoparticles were coated with a 10 nm layer of amino-silica shell, giving opportunities to graft biomolecules for potential drug delivery application. It was shown that coated Gd_2O_2S:Eu nanoparticles easily internalized NIH3T3 mouse living cells and could be imaged by epifluorescence microscopy. The nanoparticles were not cytotoxic up to 1 mg/mL, based on evaluation of cell proliferation.

The same group later reported in 2014 that aforementioned Gd_2O_2S:Eu nanoparticles without the silica coating were also water-dispersible (**Figure IV.2**a). They could be employed not only for photoluminescence imaging but also for T_2-weighted magnetic resonance imaging and X-ray tomography (**Figure IV.2**c-d).[8] The relaxation rate r_2 of the Gd_2O_2S:Eu nanoparticles was determined to be 114 $s^{-1}.mM^{-1}$ at B = 7 T, comparable to commercial contrast agents based on iron oxide nanoparticles such as Endorem and Resovist. However, they slightly inhibited proliferation of MDA-MB231 cancer cells above 100 µg/mL (**Figure IV.2**b).

More recently, it was reported that these Gd_2O_2S:Eu nanoparticles could also be PEGylated.[3] PEGylated nanoparticles showed slightly higher relaxation rate r_2 = 123 $s^{-1}.mM^{-1}$ than that of uncoated Gd_2O_2S:Eu nanoparticles. Furthermore, whole body *in vivo* distribution, elimination and toxicity evaluation revealed a high tolerance of the PEGylated nanoparticles with slow clearance.

Rosticher et al. also demonstrated the usability of Gd_2O_2S nanoparticles doped with Eu^{3+}, Ti^{4+} and Mg^{2+} for persistent luminescence imaging.[5] The nanoparticles were polydisperse with diameters ranging from 20 to 100 nm. They emitted red light at ca. 620 nm which persisted after 2 min of excitation at 365 nm. Their relaxation rates for magnetic imaging r_1 and r_2 were determined to be 6.7 and 8.8 $s^{-1}.mM^{-1}$ at B = 1 T, respectively. No information on the potential toxicity of these nanoparticles was provided.

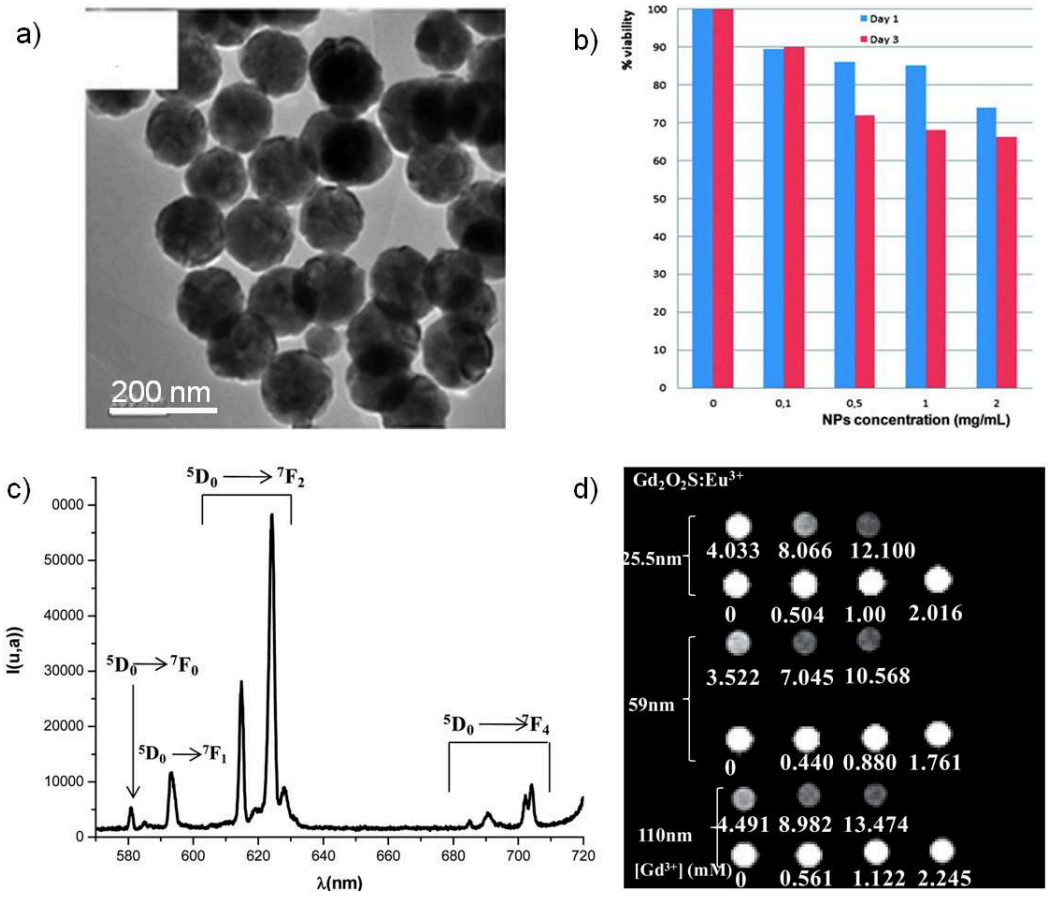

Figure IV.2: a) TEM image of Gd_2O_2S:Eu nanoparticles. b) Proliferation of MDA-MB231 cancer cells exposed to the nanoparticles. c) Photoluminescence spectrum of the Gd_2O_2S:Eu nanoparticles recorded with 363 nm excitation light source. d) T_2-weighted magnetic resonance images of Gd_2O_2S:Eu nanoparticles (adapted from ref [8]).

IV.1.2. Design $Gd_{2(1-x)}Ce_{2x}O_2S$ nanoplatelets for biomedical imaging

The previous examples showcased the potential of lanthanide-doped gadolinium oxysulfide nanoparticles for multimodal biomedical imaging. Yet, there is no related study on the smaller oxysulfide nanoplatelets obtained from colloidal synthesis in organic solvent. It is due to the limited number of studies on these nanoplatelets in overall, but also possibly due to their hydrophobic nature, making them incompatible with most biomedical applications. Despite this drawback, these nanoplatelets likely possess larger apparent surface area than previously mentioned nanoparticles. Therefore, they could potentially exhibit higher contrast for Magnetic Resonance Imaging (MRI) since only the Gd^{3+} ions close to the surface contribute to the contrast effect.[11–13] We thus attempted to design a prototype of contrast agent for magnetic and photoluminescence imaging based on our $Gd_{2(1-x)}Ce_{2x}O_2S$ nanoplatelets.

Considering the variety of previously reported photoluminescence properties of doped lanthanide oxysulfide nanoplatelets (**Figure IV.1**a), we believe that europium, which generates a sharp and intense emission at ca. 624 nm, is a relevant dopant for photoluminescence imaging. In fact, the penetration in biological tissue at this wavelength is inherently better than at lower wavelengths.[14] Hence, we first synthesized Eu-doped $Gd_{2(1-x)}Ce_{2x}O_2S$ nanoplatelets. Then, in order to make the nanoplatelets water-dispersible, we coated them with polyvinyl pyrrolidone (PVP) which is a biocompatible polymer for biomedical imaging.[15,16]

IV.2. PVP-coated Eu-doped $Gd_{2(1-x)}Ce_{2x}O_2S$ nanoparticles

IV.2.1. Eu-doped $Gd_{2(1-x)}Ce_{2x}O_2S$ nanoparticles

To synthesize europium-doped gadolinium-cerium oxysulfide nanoplatelets, we adapted the synthesis protocol employed for undoped $Gd_{2(1-x)}Ce_{2x}O_2S$ nanoplatelets described in Chapter II. First, gadolinium oxysulfide Gd_2O_2S nanoplatelets doped with different quantities of Eu (0.5, 1, 2 and 4 at.% of Eu vs. the total quantity of lanthanide) were prepared. Then, gadolinium-cerium $Gd_{2(1-x)}Ce_{2x}O_2S$ oxysulfide nanoplatelets (x = 0.02, 0.10, 0.20) doped with 2% of Eu were also synthesized. The products were characterized by powder XRD and TEM.

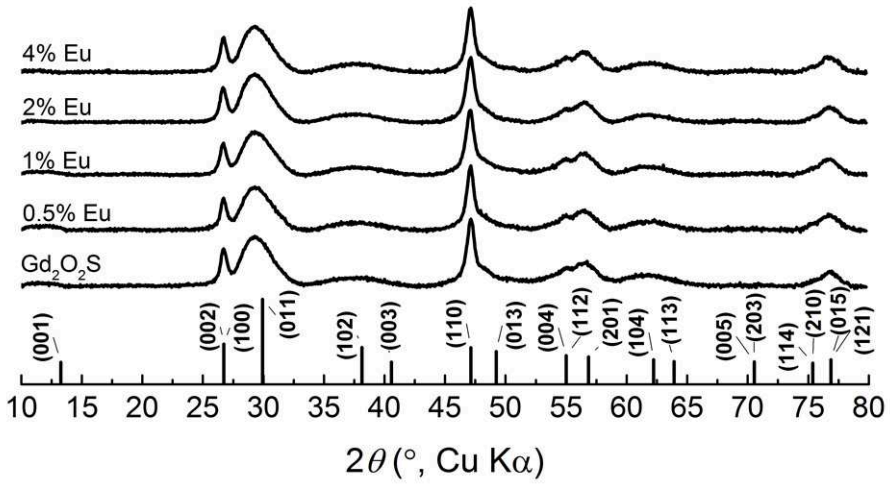

Figure IV.3: XRD patterns of Eu-doped Gd_2O_2S nanoparticles (0.5, 1, 2, 4 at.% Eu vs. total quantity of lanthanide) with reference pattern of bulk hexagonal Gd_2O_2S (JCPDS 79-5662).

Eu-doped Gd_2O_2S nanoparticles show identical XRD patterns to undoped Gd_2O_2S nanoplatelets (**Figure IV.3**). They all match with that of the bulk hexagonal Gd_2O_2S (JCPDS 79-5662). Consequently, inclusion of up to 4 at.% of europium in the Gd_2O_2S lattice does not seem to induce significant strain.

The Eu-doped gadolinium oxysulfides are nanoplatelets, as shown by TEM (**Figure IV.4**a-d). They seem to be of similar size (ca. 20 nm) and shape to undoped Gd_2O_2S nanoplatelets (**Figure IV.4**e).

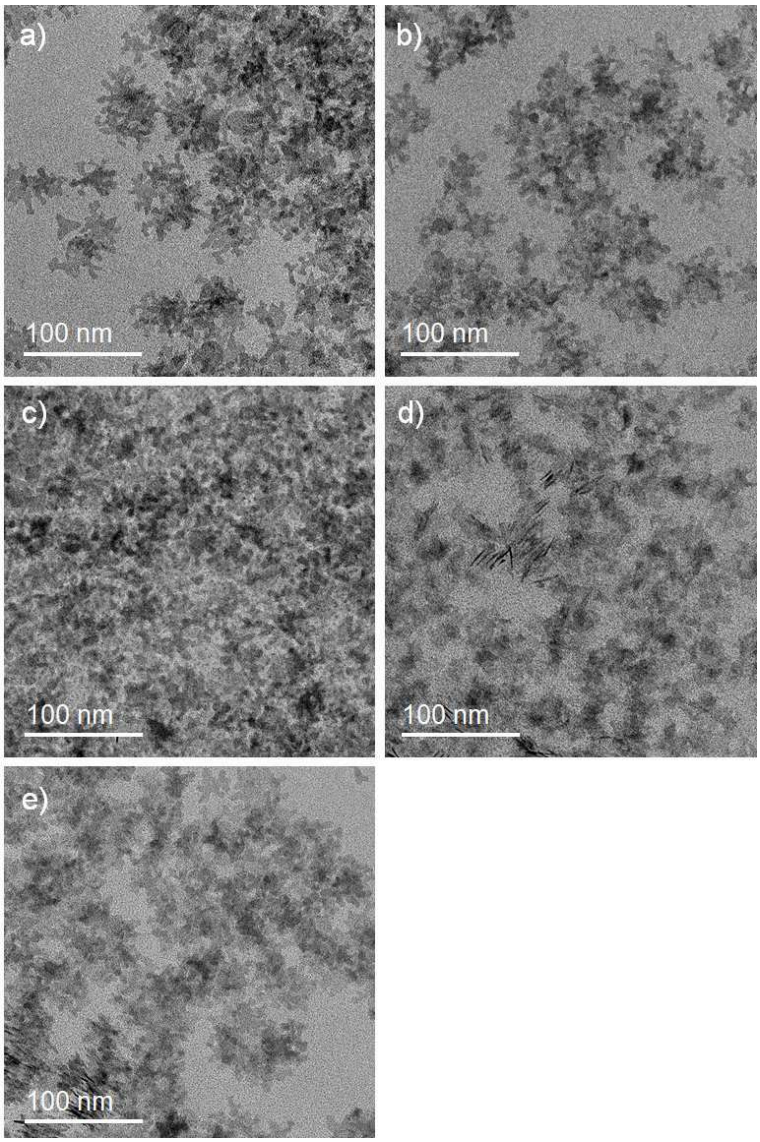

Figure IV.4: a-d) TEM images of Gd_2O_2S nanoparticles doped with 0.5, 1, 2, 4 at.% Eu vs. total quantity of lanthanides, respectively. e) TEM image of undoped Gd_2O_2S nanoparticles.

Doped gadolinium-cerium oxysulfide nanoplatelets show shifts of diffraction peaks compared to those of the reference bulk Gd_2O_2S (**Figure IV.5**a). Lattice parameters $a = 2d_{(110)}$ of the hexagonal structures are deduced from the positions of the (110) diffraction peak. They follow the Vegard's law that describes solid solutions of gadolinium and cerium oxysulfide phases (**Figure IV.5**b). The results are in accordance with those of undoped $Gd_{2(1-x)}Ce_{2x}O_2S$ nanoplatelets (see Chapter II).

TEM images of the Eu-doped $Gd_{2(1-x)}Ce_{2x}O_2S$ nanoplatelets (**Figure IV.6**) again indicate no change of size and shape compared to undoped Gd_2O_2S nanoplatelets (**Figure IV.4**e).

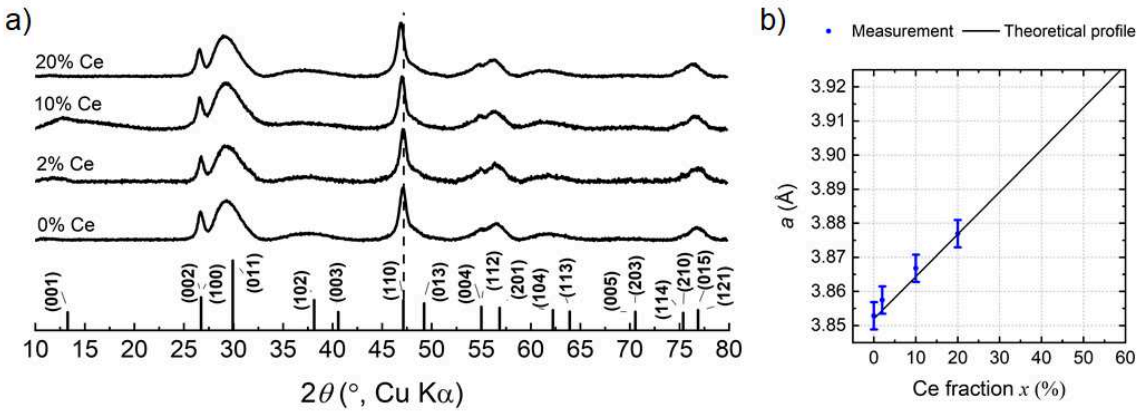

Figure IV.5: a) XRD patterns of Eu-doped (2 at.% vs. total quantity of lanthanide) $Gd_{2(1-x)}Ce_{2x}O_2S$ nanoparticles (x = 0, 0.02, 0.10, 0.20) with reference pattern of bulk hexagonal Gd_2O_2S (JCPDS 79-5662). The dashed line is a guide to the eye for the position of the (110) peak of the reference pattern. b) Lattice parameter a as function of the cerium fraction x. The black line corresponds to the expected values according to Vegard's law. The vertical error bars correspond to the estimated error in position of the diffraction peaks due to the sample holder.

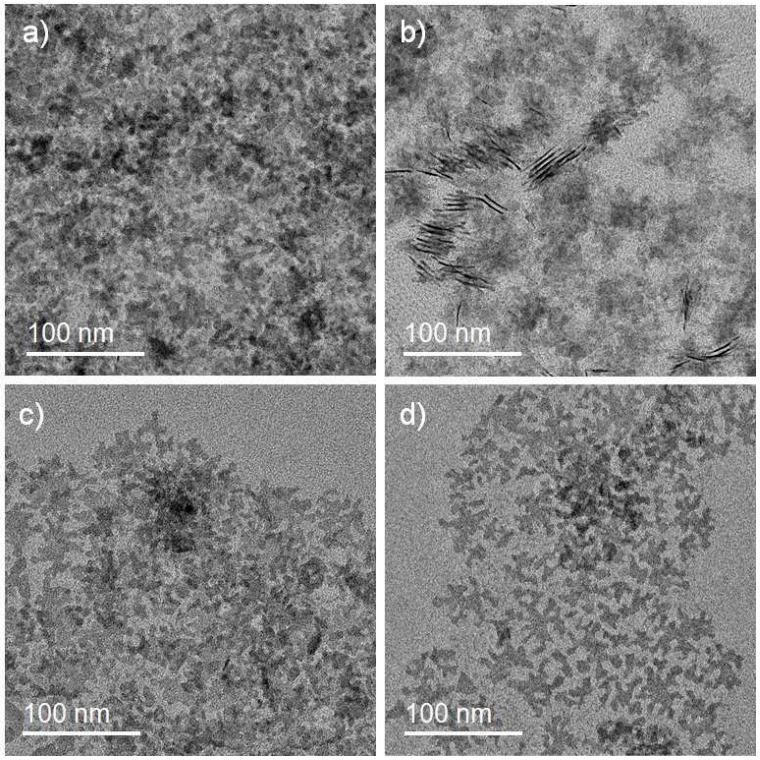

Figure IV.6: a-d) TEM images of Eu-doped (2 at.% vs. total quantity of lanthanide) $Gd_{2(1-x)}Ce_{2x}O_2S$ nanoparticles (x = 0, 0.02, 0.10, 0.20) respectively.

We demonstrated that Eu-doped $Gd_{2(1-x)}Ce_{2x}O_2S$ nanoplatelets could be prepared in the same fashion as for undoped nanoplatelets. Doping with up to 4 at.% of Eu induced no significant

change in size, shape as well as crystal structure of the oxysulfide nanoplatelets. In the next section, we will discuss the optical properties of doped nanoplatelets.

IV.2.2. Optical properties of pristine Eu-doped $Gd_{2(1-x)}Ce_{2x}O_2S$ nanoparticles

Photoluminescence properties of pristine Eu-doped $Gd_{2(1-x)}Ce_{2x}O_2S$ nanoplatelets dispersed in *n*-hexane was characterized. For this, the crude product (after synthesis) was washed three times with a mixture of *n*-hexane and ethanol to remove excess reagents and organic matters. However, the suspensions in *n*-hexane obtained this way were turbid, suggesting strong light scattering. The nanoplatelets were likely aggregated and this might alter their optical properties in suspension.

In order to prevent aggregation of the nanoplatelets, 1 equivalent (vs. total quantity of lanthanides) of oleic acid as stabilizing agent was added after the first wash. At the end of the post-synthetic treatment, the solid was dispersed in *n*-hexane. This suspension was diluted to a final concentration of ca. 1 mM of lanthanides. It was then sonicated for 5 min at room temperature to give a clear suspension of Eu-doped $Gd_{2(1-x)}Ce_{2x}O_2S$ nanoplatelets. The optical properties of obtained nanoparticle suspensions were characterized by UV-visible absorption and photoluminescence spectroscopies.

IV.2.2.1. Effect of dopant level

Gd_2O_2S nanoparticles doped with 0.5, 1, 2 and 4 at.% of Eu vs. the total quantity of lanthanide show similar absorption spectra (**Figure IV.7**a). However, their total absorbance varies, indicating different concentrations of nanoparticles between suspensions.

Photoluminescence spectra of the Eu-doped $Gd_{2(1-x)}Ce_{2x}O_2S$ suspensions were recorded using an excitation light at 250 nm (**Figure IV.7**b). To compensate the difference of concentration between the suspensions, the spectra were normalized with the absorbance at 300 nm. All samples show a typical emission of Eu^{3+} at 624 nm.[1,2] This emission corresponds to the $^5D_0 \rightarrow {}^7F_2$ transition of Eu^{3+}. It seems to be the most intense at 1% of Eu. Its intensity decreases at higher concentrations of dopant (2% and 4%), likely due to the concentration quenching effect.[6,17]

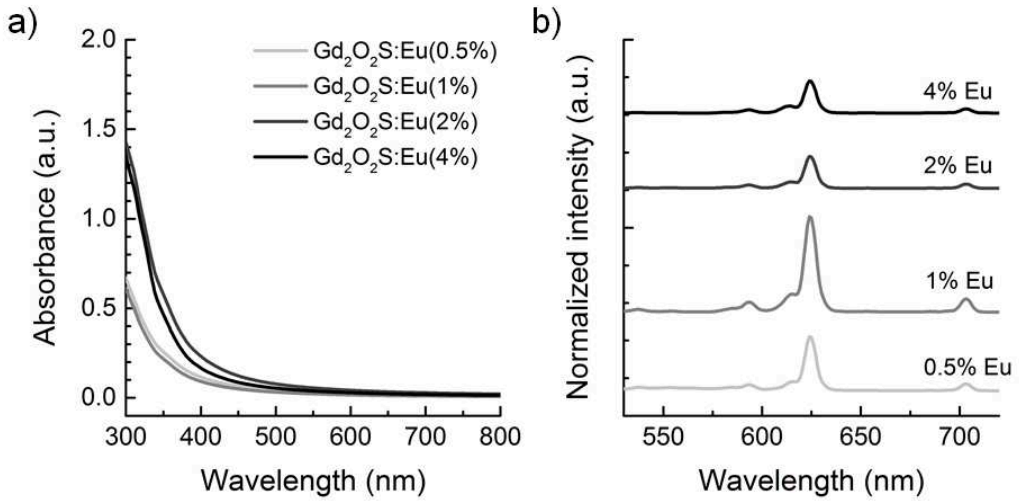

Figure IV.7: a) UV-visible absorption spectra of suspensions in *n*-hexane of Gd_2O_2S nanoparticles doped with 0.5, 1, 2, 4 at.% Eu vs. total quantity of lanthanides and b) their respective normalized photoluminescence spectra recorded with excitation at 250 nm.

The observed optimal dopant level is lower than that reported by Lei et al. (1% vs. 4% respectively).[1] However, the photoluminescence intensity depends on the distribution of the Eu^{3+} emitters in the Gd_2O_2S matrix. For example, aggregated Eu^{3+} or those located near the surface of the nanoplatelets are more susceptible to quenching.[17] In order to get insights on the distribution of Eu^{3+} in the oxysulfide nanoplatelets, more in-depth analyses such as photoluminescence decay and excitation spectroscopy are required.

IV.2.2.2. Photoluminescence quenching by cerium

Suspensions of Eu-doped $Gd_{2(1-x)}Ce_{2x}O_2S$ nanoplatelets exhibit different absorption properties depending on the cerium content. The absorption threshold shifts towards the visible region of the spectrum as the cerium content increases (**Figure IV.8**a). This is in agreement with the results of undoped nanoparticles (see Chapter III). However, it prevents us from using the absorbance values to normalize the photoluminescence spectra.

The photoluminescence spectra of Eu-doped $Gd_{2(1-x)}Ce_{2x}O_2S$ nanoparticles suspensions are presented in **Figure IV.8**b. For all samples, an intense peak corresponding to the 2nd order of Rayleigh scattering at 500 nm is detected. A less intense one at 750 nm can be attributed to the 3rd order of the light scattering. Since the intensity of scattered light depends on the

concentration of particles, we normalized the photoluminescence spectra using the intensity of the 2nd order peak at 500 nm.

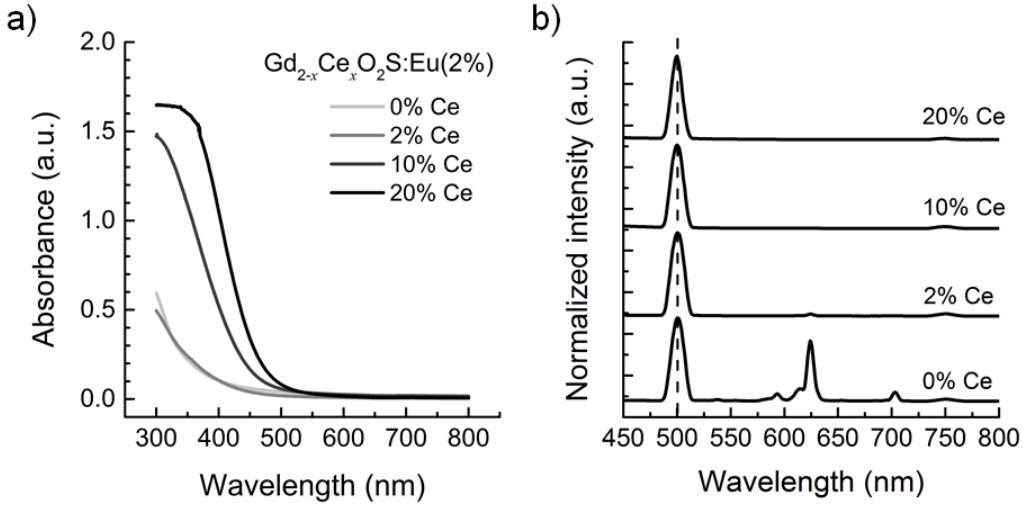

Figure IV.8: a) UV-visible absorption spectra of suspensions in *n*-hexane of Eu-doped (2 at.% vs. total quantity of lanthanide) $Gd_{2(1-x)}Ce_{2x}O_2S$ nanoparticles (x = 0, 0.02, 0.10, 0.20) and b) their respective normalized photoluminescence spectra recorded with 250 nm excitation light.

Although the characteristic emission of Eu^{3+} at 624 nm is observed at 2% of cerium, it is a lot less intense than that of Gd_2O_2S:Eu nanoparticles. At higher cerium-content (10% and 20%), it completely disappears. This may suggest photoluminescence quenching of europium due to the presence of cerium.

IV.2.3. PVP-coating of $Gd_{2(1-x)}Ce_{2x}O_2S$ nanoparticles

IV.2.3.1. PVP-coating and characterization of products

For biomedical applications, the nanoparticles need to be dispersed in aqueous media. However, we proved that the surface of $Gd_{2(1-x)}Ce_{2x}O_2S$ nanoplatelets synthesized in organic solvent was mainly occupied by oleates (see Chapter II and Chapter III). These nanoparticles are highly hydrophobic and cannot be dispersed in water. Thus, it is difficult to employ them per se as contrast agents. In order to make Eu-doped $Gd_{2(1-x)}Ce_{2x}O_2S$ nanoplatelets water-dispersible, we coated them with polyvinyl pyrrolidone (PVP). For this, we adapted a method reported by Fang et al. in 2014 for 3-nm gadolinium oxide Gd_2O_3 nanoparticles.[13]

As prepared Eu-doped $Gd_{2(1-x)}Ce_{2x}O_2S$ nanoparticles were dispersed in *n*-hexane. The final clear suspension was mixed with dichloromethane and a solution of PVP (MW = 55000) in dimethylformamide (DMF) with 1:1:2 volume ratios, respectively. The mixture was then heated at reflux at 90 °C for 16 hours. The product was recovered by adding diethyl ether to the reaction medium and subsequent centrifugation.

This coating process was first carried out for Gd_2O_2S:Eu(2%) nanoparticles with 0.08 equivalents of PVP under ambient air and nitrogen as well as with 0.018 equivalents of PVP under nitrogen. The products were characterized by powder XRD (**Figure IV.9**). They all mainly crystallized in hexagonal Gd_2O_2S phase as expected. XRD patterns of the products obtained with 0.08 eq. of PVP in ambient air and with 0.018 eq. of PVP under nitrogen feature additional diffraction peaks at 31.9 ° and 45.6 °. These peaks are more intense in the product obtained in ambient air. They do not correspond to the reported cubic (JCPDS 012-0797), hexagonal (JCPDS 016-2410) nor monoclinic (JCPDS 042-1465) gadolinium oxides Gd_2O_3 phases. Nevertheless, their positions seem to be close to those of the side-product of the synthesis of Gd_2O_2S nanoparticles using K(acac) as alternative alkali metal precursor (see Chapter II, Figure 22).

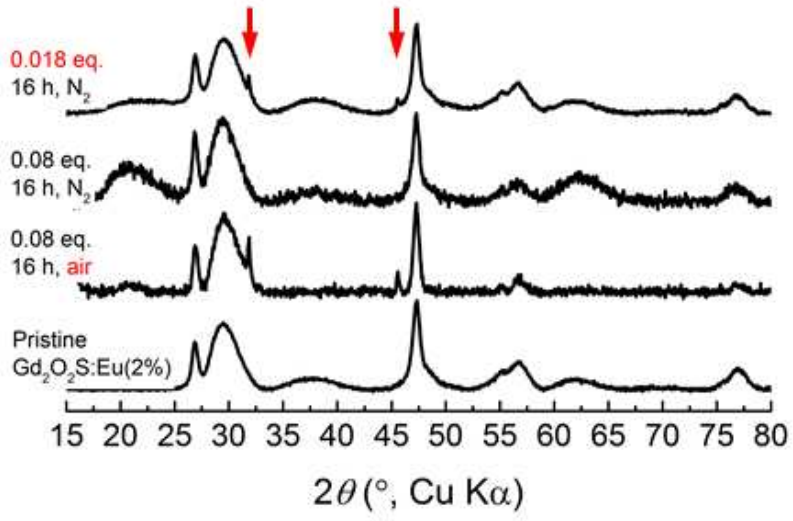

Figure IV.9: XRD pattern of pristine Gd_2O_2S:Eu(2%) nanoparticles and those of obtained product after PVP-coating with different experimental conditions. The red arrows indicate the positions of unattributed diffraction peaks.

PVP-coated Gd_2O_2S:Eu(2%) nanoparticles obtained with both quantities of PVP could be readily dispersed in water to form a clear suspension. Despite the low quality of images due to the presence of the polymer, TEM show nanoplatelets of same characteristics as pristine Gd_2O_2S (**Figure IV.10**a).

Thermogravimetric analysis of the products obtained with 0.018 and 0.08 eq. of PVP under nitrogen was carried out with the help of Benoit Fleury at the IPCM lab at Sorbonne Université. The results first show a loss of adsorbed water around 100 °C (**Figure IV.10**b). It presents ca. 11 wt.% of the total mass. From ca. 300 °C, PVP and organic ligands remained from the synthesis starts to degrade. Above 500 °C, the mass of the sample remains constant, suggesting a total degradation of the organics.

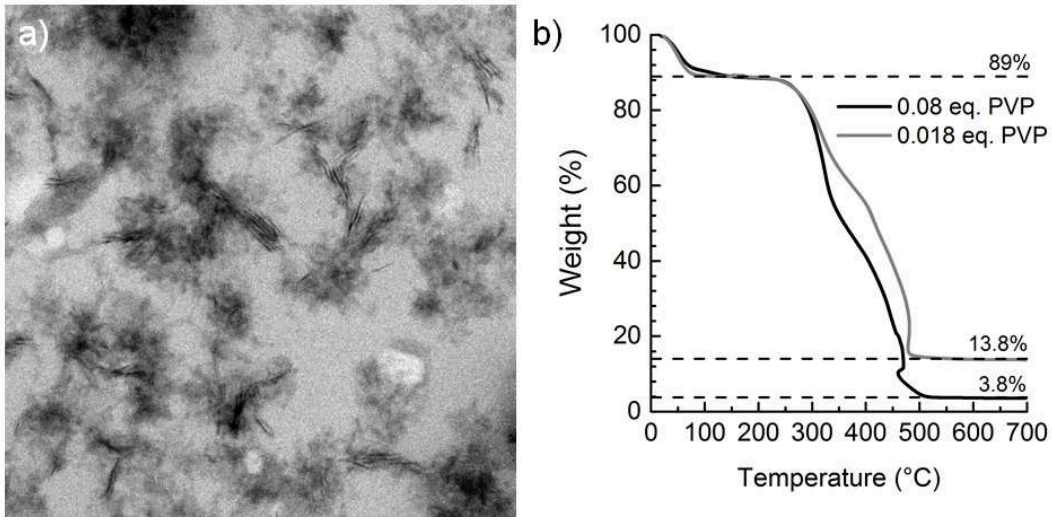

Figure IV.10: a) TEM image of PVP-coated Gd_2O_2S:Eu(2%) nanoparticles and b) their thermogravimetric analysis.

The organics content of coated nanoparticles can be determined by measuring the weight loss between 300 and 500 °C. We have previously shown that pristine $Gd_{2(1-x)}Ce_{2x}O_2S$ nanoparticles contained around 30 wt.% of organic ligands (see Appendix IV).[18] If we assume that the same quantity of organic ligands remained in our coated nanoparticles, we can deduce the PVP-content of the latter. The results are reported in **Table IV.1**. In both cases, the measured PVP content appears slightly higher than the expected value. It may suggest a small loss of nanoparticles during the coating process, in agreement with its non-quantitative yield (estimated from 50 to 70%).

Eq. of PVP vs. Gd	Expected PVP content (wt.%)	Measured organics content (wt.%)	Estimated PVP content (wt.%)
0.018	71	82	74
0.08	92	96	94

Table IV.1: Expected and measured PVP contents of PVP-coated Gd_2O_2S:Eu(2%) nanoparticles.

In general, we demonstrated that Eu-doped Gd_2O_2S nanoparticles could be coated by PVP using a previously published protocol by Fang et al.[13] Despite the presence of a crystalline side-product, by using 0.08 eq. of PVP and heating under inert atmosphere for 16 hours, its quantity could be minimized. However, the final PVP content in the product was determined to be 96 wt.%. Resulting small quantity of nanoparticles present may imply larger amount of product needed for desired performance in biomedical imaging. Therefore, we tried to reduce the quantity of PVP in the final product.

IV.2.3.2. Reducing PVP content in the final product

In the last section, we assumed that the side-product could be formed by heating the oxysulfide nanoparticles under air and 0.018 eq. of PVP vs. Gd was likely insufficient to prevent its formation upon heating for 16 hours even under nitrogen. Therefore, we reduced the heating time to 4 hours and doubled the quantity of PVP to 0.036 eq. vs. Gd. The XRD patterns of PVP-coated undoped and Eu-doped Gd_2O_2S nanoparticles are presented in **Figure IV.11**. They are identical to that of the pristine nanoparticles. Previously observed diffraction peaks at 31.9 ° and 45.6 ° attributed to the unidentified side-product are absent.

We showed that PVP-coated oxysulfide nanoparticles crystallized in pure hexagonal Gd_2O_2S phase could be obtained with as little as 0.036 eq. of PVP vs. Gd. The coating process could also be extended to cerium-containing oxysulfide nanoparticles (data not shown). The final PVP contents in the products are still needed to be confirmed. TGA of the products is planned to be performed in the coming weeks. Further optimization of the coating process is still likely possible. Nevertheless, at the moment, we consider these PVP-coated nanoparticles prototypes of water-dispersible $Gd_{2(1-x)}Ce_{2x}O_2S$ nanoplatelets.

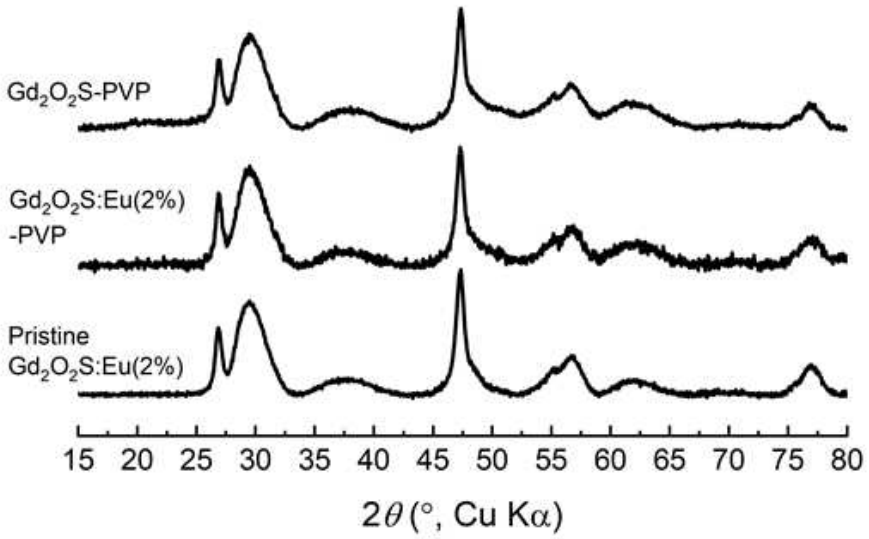

Figure IV.11: XRD pattern of pristine Gd_2O_2S, PVP-coated Gd_2O_2S and Gd_2O_2S:Eu(2%) nanoparticles obtained with 0.036 equivalents of PVP vs. Gd, heating under nitrogen for 4 h.

IV.2.4. Optical properties of PVP-coated Gd_2O_2S:Eu nanoparticles

PVP-coated Gd_2O_2S:Eu(1%) nanoparticles prepared from 0.036 eq. of PVP vs. Gd were dispersed in water for a final concentration of 100 mg/mL to give a clear suspension. The latter was then characterized by UV-visible absorption and photoluminescence spectroscopies. The results were compared with those of suspension of pristine Gd_2O_2S:Eu(1%) nanoparticles in water (**Figure IV.12**).

The absorption spectrum of PVP-coated nanoparticles is slightly deformed compared to that of pristine nanoparticles (**Figure IV.12**a). This is likely due to the more important light scattering of the suspension containing PVP-coated nanoparticles that interferes with its absorption. In fact, the Rayleigh scattering strongly depends on the wavelength ($\sim \lambda^{-4}$). Hence, the change in absorbance is not homogeneous throughout the spectrum.

The photoluminescence spectra of pristine and coated nanoparticles were normalized by their maximum emission intensity. PVP-coated Gd_2O_2S:Eu(1%) nanoparticles exhibit identical emission profile compared to that of pristine nanoparticles (**Figure IV.12**b). The PVP-coating preserves the photoluminescence properties of the Eu-doped Gd_2O_2S:Eu nanoplatelets. Therefore, these water-dispersible nanoparticles can potentially be used as contrast agents for

photoluminescence imaging. Observation by epifluorescence in living cells needs to be done to confirm their performance.

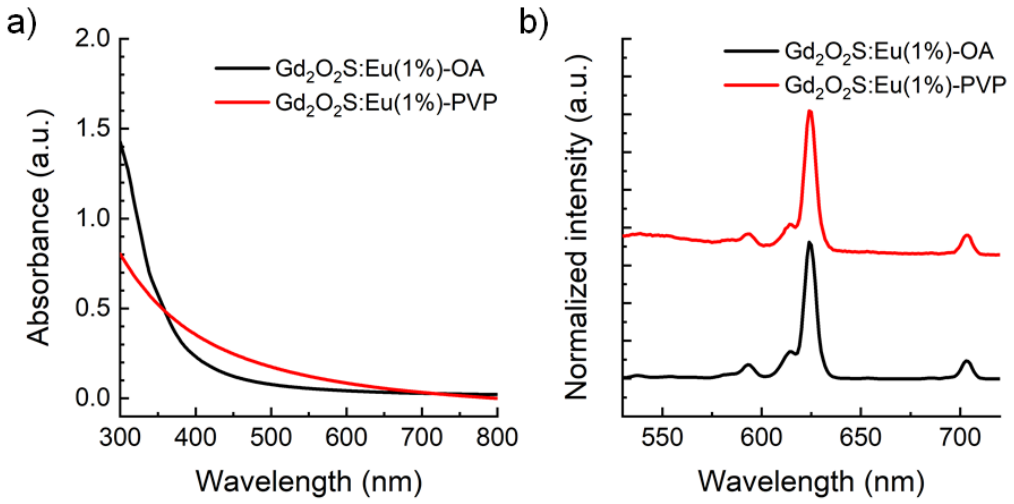

Figure IV.12: a) UV-visible absorption spectra of pristine Gd_2O_2S:Eu(1%) nanoparticles in *n*-hexane (black) and of PVP-coated Gd_2O_2S:Eu(1%) nanoparticles in water (red). b) Their respective normalized photoluminescence spectra recorded with 250 nm excitation light.

IV.2.5. Cytotoxicity of PVP-coated gadolinium oxysulfide nanoparticles

In order to evaluate the potential cytotoxicity of the PVP-coated oxysulfide nanoplatelets, we employed WST-1 assay and measured the mitochondrial activity of treated RAW 264.7 cells. The experiment was carried out in the same fashion as for pristine $Gd_{2(1-x)}Ce_{2x}O_2S$ nanoparticles (see Chapter III). The macrophages were exposed to different concentrations (1, 10, 50 and 100 µg/mL) of PVP-coated Gd_2O_2S and PVP-coated Gd_2O_2S:Eu(1%) nanoparticles during 24 h and their mitochondrial activity was compared to that of unexposed cells (**Figure IV.13**).

At all concentrations of both doped and undoped nanoparticles, the mitochondrial activities of the cells remain above 100% compared to that of unexposed ones. The results are not significantly different than that of titanium dioxide nanoparticles. This suggests negligible adverse effect of PVP-coated gadolinium oxysulfide nanoparticles on RAW 264.7 cells. It should be noted that the real nanoparticle contents of these PVP-coated nanoparticles are much lower than 100%. In fact, they are only about 15% in mass if we consider a quantitative coating process using 0.036 eq. of PVP vs. Gd. This needs to be taken into consideration when

comparing cytotoxicity of nanoparticles discussed in other chapters of this manuscript. So far, the nanoparticle content of reported contrast agents based on Gd_2O_2S nanoparticles was often not provided, making comparison of toxicity very challenging.

Although PVP-coated Gd_2O_2S and PVP-coated Gd_2O_2S:Eu(1%) nanoparticles did not show any adverse effect towards the mitochondrial activity of RAW 264.7 cells, other endpoints of cytotoxicity (cellular DNA content, membrane integrity, inflammation response, oxidative stress, etc.) still need to be characterized to confirm their absence of cytotoxicity (see Chapter III).

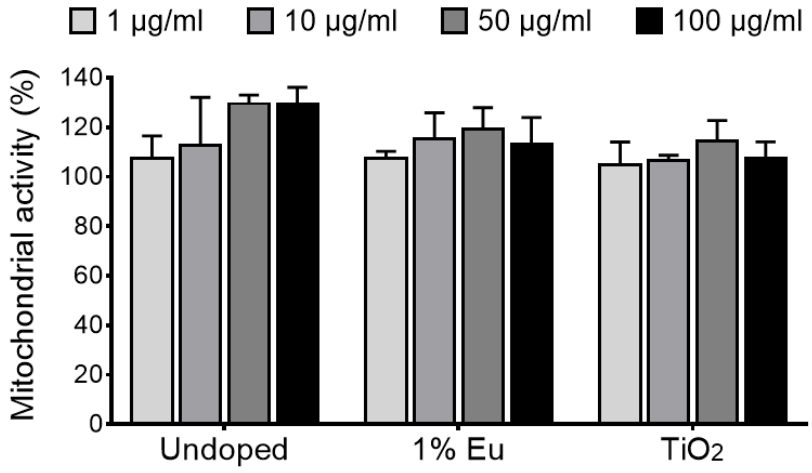

Figure IV.13: WST-1 assay of RAW 264.7 macrophages exposed to PVP-coated Gd_2O_2S, PVP-coated Gd_2O_2S:Eu(1%) and TiO_2 P25 nanoparticles at different concentrations during 24 h. The experiments were repeated three times.

IV.3. Discussion

Eu-doped $Gd_{2(1-x)}Ce_{2x}O_2S$ nanoplatelets were prepared using colloidal synthesis in organic solvent as described in previous chapters. Doping preserved all physicochemical characteristics such as size, shape, crystal structure, etc. of the host. To the best of our knowledge, this is the first time doped bimetallic oxysulfide nanoparticles were reported. It paves the way for the synthesis of trimetallic lanthanide oxysulfide nanoparticles which may feature novel properties and more possibilities to tune their properties.

The Eu-doped $Gd_{2(1-x)}Ce_{2x}O_2S$ nanoplatelets with low cerium content (≤ 2% Ce) exhibit characteristic photoluminescence of Eu^{3+} at ca. 624 nm. This photoluminescence is consistent to that of previously reported Eu-doped Gd_2O_2S nanoparticles for bimodal biomedical imaging.[3–8] At higher cerium contents (≥ 10% Ce) however, the emission at ca. 624 nm was inhibited. Overall, the presence of cerium seemed to quench the photoluminescence of Eu^{3+}, in disagreement with previous studies on Ce^{3+} and Eu^{3+} co-doped compounds such as $YAlO_3$ or YVO_4.[19,20] In those studies, the photoluminescence intensity at 624 nm of co-doped compounds was shown to be higher than that of compounds doped with only Eu. It was suggested that this was due to the energy transfer of Ce^{3+} to Eu^{3+}. We have previously shown that synthesized $Gd_{2(1-x)}Ce_{2x}O_2S$ nanoplatelets were partially oxidized in ambient air (see Chapter II). Increasing the cerium content of the nanoplatelets may lead to the creation of more defects such as surface Ce^{IV}, hence decrease the emission intensity.[21,22] In-depth analysis including photoluminescence lifetime and excitation spectroscopy in solid-state of both cerium and europium centers are needed to confirm. The photoluminescence quenching by cerium make cerium-containing Eu-doped $Gd_{2(1-x)}Ce_{2x}O_2S$ nanoparticles less relevant for bimodal fluorescent-magnetic biomedical imaging than Eu-doped Gd_2O_2S nanoparticles.

We were able to coat the Eu-doped $Gd_{2(1-x)}Ce_{2x}O_2S$ nanoplatelets by PVP (MW = 55000) and dispersed them in water for the first time. Although optimization of the process is still needed, this result highlights the potential of these small nanoparticles as contrast agents for biomedical imaging. A coating protocol similar to that reported by Fang et al. for 3-nm gadolinium oxide Gd_2O_3 nanoparticles was employed.[13] In the article, the author claimed that the PVP displaced the oleic acid on the surface of initial Gd_2O_3 nanoparticles in a ligand exchange reaction. However, no evidence was provided to support this statement. The excess quantity of PVP in the final product also makes characterization of oleic acid by FTIR

difficult. In our case, the $[Ln_2O_2]^{2+}$-terminated surface of the $Gd_{2(1-x)}Ce_{2x}O_2S$ nanoplatelets is coordinated by oleates to ensure the charge balance (see Chapter II). Together with the small thickness of the nanoplatelets (ca. 2 nm), it appears unlikely that oleates are displaced in the reaction with PVP. Therefore, we speculate that PVP simply coated oleates-capped $Gd_{2(1-x)}Ce_{2x}O_2S$ nanoplatelets, making them water-dispersible.

The coating process preserved the size, shape, crystal structure and photoluminescent properties of the nanoparticles. Dynamic Light Scattering (DLS) experiment needs to be done to determinate the hydrodynamic size of the coated nanoparticles. Coating with PVP of different molar mass or with other biocompatible polymers such as polyethylene glycol (PEG) seems a nice way to tune the dispersion properties which could be important for the biodistribution and toxicity of the nanoparticles. Post-functionalization of the polymer is also relevant for targeting.

Results of WST-1 assay of macrophages exposed to PVP-coated nanoparticles showed an absence of adverse effect up to 100 µg/mL. This concentration is comparable to what commonly used for cell labeling using fluorescent microscopy.[3,8] For magnetic imaging, around 100 µM of gadolinium-based contrast agents are usually used.[4,23,24] This concentration corresponds to ca. 100 mg/mL of coated-Gd_2O_2S nanoparticles (85 wt.% of PVP), comparable to our study as well. In addition to carrying out complementary toxicity assays to confirm this, investigating the effect of the coating on the cytotoxicity of the $Gd_{2(1-x)}Ce_{2x}O_2S$ nanoparticles also is of relevance. The polymer shell might prevent the release of cerium to the medium as well as the ROS production of cerium-containing oxysulfide nanoparticles (see Chapter III), thus lower their cytotoxicity. For this, toxicity assays need to be carried out for both PVP-coated nanoparticles and physical mixture of PVP with the nanoparticles of the same ratio between the two.

IV.4. Conclusion

We demonstrated that Eu-doped $Gd_{2(1-x)}Ce_xO_2S$ oxysulfide nanoplatelets prepared by colloidal synthesis in organic solvents could be transferred to aqueous media *via* PVP-coating. PVP-coated Gd_2O_2S:Eu nanoparticles exhibited red emission at ca. 624 nm, showing potential for photoluminescent imaging. Previous results in our lab showed that synthesized $Gd_{2(1-x)}Ce_xO_2S$ nanoplatelets were paramagnetic. Hence, similar to examples of Gd_2O_2S nanoparticles in the literature, they could also be employed for MRI. Preliminary results on mitochondrial activity of macrophages exposed to PVP-coated nanoparticles showed an absence of adverse effect. Altogether, we showed the potential of PVP-coated Gd_2O_2S:Eu nanoparticles for bimodal, fluorescent and magnetic imaging. However, their performance and toxicity are still to be determined in view of developing safer-by-design contrast agents for multimodal imaging based on oxysulfide nanoplatelets.

We also showed that cerium quenched the photoluminescence of europium in nanoplatelets containing both elements. Although Ce played an important role in the tunable optical and magnetic properties of $Gd_{2(1-x)}Ce_xO_2S$ nanoplatelets, its presence seemed to make these nanoparticles less relevant for applications in biomedical imaging. Its potential antioxidant effect for theranostics is also likely inhibited by the polymer coating. Overall, gadolinium oxysulfide Gd_2O_2S nanoparticles may be a better candidate for biomedical applications.

References

(1) Lei, L.; Zhang, S.; Xia, H.; Tian, Y.; Zhang, J. J.; Xu, S. Q. Controlled Synthesis of Lanthanide-Doped Gd2O2S Nanocrystals with a Novel Excitation-Dependent Multicolor Emissions. *Nanoscale* **2017**, *16*, 2102–2105.

(2) Ding, Y.; Gu, J.; Ke, J.; Zhang, Y. W.; Yan, C. H. Sodium Doping Controlled Synthesis of Monodisperse Lanthanide Oxysulfide Ultrathin Nanoplates Guided by Density Functional Calculations. *Angew. Chemie - Int. Ed.* **2011**, *50* (51), 12330–12334.

(3) Santelli, J.; Lechevallier, S.; Baaziz, H.; Vincent, M.; Martinez, C.; Mauricot, R.; Parini, A.; Verelst, M.; Cussac, D. Multimodal Gadolinium Oxysulfide Nanoparticles: A Versatile Contrast Agent for Mesenchymal Stem Cell Labeling. *Nanoscale* **2018**, *10* (35), 16775–16786.

(4) Guo, T.; Lin, Y.; Li, Z.; Chen, S.; Huang, G.; Lin, H.; Wang, J.; Liu, G.; Yang, H. H. Gadolinium Oxysulfide-Coated Gold Nanorods with Improved Stability and Dual-Modal Magnetic Resonance/Photoacoustic Imaging Contrast Enhancement for Cancer Theranostics. *Nanoscale* **2017**, *9* (1), 56–61.

(5) Rosticher, C.; Viana, B.; Fortin, M. A.; Lagueux, J.; Faucher, L.; Chanéac, C. Gadolinium Oxysulfide Nanoprobes with Both Persistent Luminescent and Magnetic Properties for Multimodal Imaging. *RSC Adv.* **2016**, *6* (60), 55472–55478.

(6) Osseni, S. A.; Lechevallier, S.; Verelst, M.; Dujardin, C.; Dexpert-Ghys, J.; Neumeyer, D.; Leclercq, M.; Baaziz, H.; Cussac, D.; Santran, V.; et al. New Nanoplatform Based on Gd 2 O 2 S: Eu 3+ Core: Synthesis, Characterization and Use for in Vitro Bio-Labelling. *J. Mater. Chem.* **2011**, *21* (45), 18365–18372.

(7) Ajithkumar, G.; Yoo, B.; Goral, D. E.; Hornsby, P. J.; Lin, A.-L.; Ladiwala, U.; Dravid, V. P.; Sardar, D. K. Multimodal Bioimaging Using a Rare Earth Doped Gd2O2S:Yb/Er Phosphor with Upconversion Luminescence and Magnetic Resonance Properties. *J. Mater. Chem. B* **2013**, *1* (11), 1561.

(8) Osseni, S. a; Lechevallier, S.; Verelst, M.; Perriat, P.; Dexpert-Ghys, J.; Neumeyer, D.; Garcia, R.; Mayer, F.; Djanashvili, K.; Peters, J. a; et al. Gadolinium Oxysulfide Nanoparticles as Multimodal Imaging Agents for T2-Weighted MR, X-Ray Tomography and Photoluminescence. *Nanoscale* **2014**, *6* (1), 555–564.

(9) Larquet, C.; Klein, Y.; Hrabovsky, D.; Gauzzi, A.; Sanchez, C.; Carenco, S. Tunable Magnetic Properties of (Gd,Ce) 2 O 2 S Oxysulfide Nanoparticles. *Eur. J. Inorg. Chem.* **2019**, *2019* (6), 762–765.

(10) Larquet, C. Nanoparticles of Lanthanide and Transition Metal Oxysulfides: From Colloidal Synthesis to Structure, Surface, Optical and Magnetic Properties, 2018.

(11) Johnson, N. J. J.; Oakden, W.; Stanisz, G. J.; Prosser, R. S.; van Veggel, F. C. J. M. Size-Tunable, Ultrasmall NaGdF 4 Nanoparticles: Insights into Their T 1 MRI Contrast Enhancement. *Chem. Mater.* **2011**, *23* (21), 4877–4877.

(12) Bridot, J. L.; Faure, A. C.; Laurent, S.; Rivière, C.; Billotey, C.; Hiba, B.; Janier, M.; Josserand, V.; Coll, J. L.; Elst, L. Vander; et al. Hybrid Gadolinium Oxide Nanoparticles: Multimodal Contrast Agents for in Vivo Imaging. *J. Am. Chem. Soc.* **2007**, *129* (16), 5076–5084.

(13) Fang, J.; Chandrasekharan, P.; Liu, X.-L.; Yang, Y.; Lv, Y.-B.; Yang, C.-T.; Ding, J. Manipulating the Surface Coating of Ultra-Small Gd2O3 Nanoparticles for Improved T1-Weighted MR Imaging. *Biomaterials* **2014**, *35* (5), 1636–1642.

(14) Smith, A. M.; Mancini, M. C.; Nie, S. Bioimaging: Second Window for in Vivo Imaging. *Nat. Nanotechnol.* **2009**, *4* (11), 710–711.

(15) Teodorescu, M.; Bercea, M. Poly(Vinylpyrrolidone) – A Versatile Polymer for Biomedical and Beyond Medical Applications. *Polym. - Plast. Technol. Eng.* **2015**, *54* (9), 923–943.

(16) Lee, H. Y.; Lim, N. H.; Seo, J. A.; Yuk, S. H.; Kwak, B. K.; Khang, G.; Lee, H. B.; Cho, S. H. Preparation and Magnetic Resonance Imaging Effect of Polyvinylpyrrolidone- Coated Iron Oxide Nanoparticles. *J. Biomed. Mater. Res. - Part B Appl. Biomater.* **2006**, *79* (1), 142–150.

(17) Lin, S. L.; Liu, T. Y.; Lo, C. L.; Wang, B. S.; Lee, Y. J.; Lin, K. Y.; Chang, C. A. Synthesis, Surface Modification, and Photophysical Studies of Ln 2 O 2 S:Ln' 3+ (Ln=Gd, Tb, Eu; Ln'=Tb and/ or Eu) Nanoparticles for Luminescence Bioimaging. *J. Lumin.* **2016**, *175*, 165–175.

(18) Larquet, C.; Hourlier, D.; Nguyen, A.; Torres-Pardo, A.; Gauzzi, A.; Sanchez, C.; Carenco, S. Thermal Stability of Oleate-Stabilized Gd2O2S Nanoplates in Inert and Oxidizing Atmospheres. *ChemNanoMat* **2019**, *5* (4), 539–546.

(19) Wang, Y.; Wang, S.; Wu, Z.; Li, W.; Ruan, Y. Photoluminescence Properties of Ce and Eu Co-Doped YVO 4 Crystals. *J. Alloys Compd.* **2013**, *551*, 262–266.

(20) Kim, G. C.; Mho, S. I.; Park, H. L. Observation of Energy Transfer between Ce3+ and Eu3+ in YAIO3:Ce, Eu. *J. Mater. Sci. Lett.* **1995**, *14* (11), 805–806.

(21) Kumar, A.; Babu, S.; Karakoti, A. S.; Schulte, A.; Seal, S. Luminescence Properties of Europium-Doped Cerium Oxide Nanoparticles: Role of Vacancy and Oxidation States. *Langmuir* **2009**, *25* (18), 10998–11007.

(22) He, X.; Liu, X.; Li, R.; Yang, B.; Yu, K.; Zeng, M.; Yu, R. Effects of Local Structure of Ce3+ Ions on Luminescent Properties of Y3Al5O12:Ce Nanoparticles. *Sci. Rep.* **2016**, *6* (1), 22238.

(23) Bower, D. V.; Richter, J. K.; von Tengg-Kobligk, H.; Heverhagen, J. T.; Runge, V. M. Gadolinium-Based MRI Contrast Agents Induce Mitochondrial Toxicity and Cell Death in Human Neurons, and Toxicity Increases With Reduced Kinetic Stability of the Agent. *Invest. Radiol.* **2019**, *54* (8), 1.

(24) Ajithkumar, G.; Yoo, B.; Goral, D. E.; Hornsby, P. J.; Lin, A.-L.; Ladiwala, U.; Dravid, V. P.; Sardar, D. K. Multimodal Bioimaging Using a Rare Earth Doped Gd2O2S:Yb/Er Phosphor with Upconversion Luminescence and Magnetic Resonance Properties. *J. Mater. Chem. B* **2013**, *1* (11), 1561.

Conclusion and perspectives

In this work, we applied safer-by-design approach for bimetallic gadolinium-cerium oxysulfide nanoplatelets of compositions $Gd_{2(1-x)}Ce_{2x}O_2S$ as model of emerging nanomaterials. The nanoparticles were designed for potential applications in photocatalysis and fluorescent-magnetic biomedical imaging. The objective was to optimize the performance of the material while minimizing its toxicity. By deploying this safer-by-design approach, we expect developing nanomaterials that meet the safe and performance criteria in close relation with the activity sector and its regulations.

1. $Gd_{2(1-x)}Ce_{2x}O_2S$ nanoplatelets

Crystalline $Gd_{2(1-x)}Ce_{2x}O_2S$ nanoplatelets of dimensions 2 × 20 nm were prepared by colloidal synthesis in organic solvents. We were able to precisely control the cerium content of the nanoparticles by adjusting the stoichiometry of the cerium precursor. However, the nanoparticles oxidized in ambient air. As a result, both cerium(III) and cerium(IV) were present. The nanoplatelets terminate by $[Ln_2O_2]^{2+}$ (Ln = Gd, Ce) layers in their basal facets. The resulting charged surfaces are coordinated by oleates, making the nanoparticles hydrophobic. We also demonstrated that the sodium in particular, or alkali-metal in general, were necessary for the formation of $Gd_{2(1-x)}Ce_{2x}O_2S$ nanoplatelets. They likely remained on the surface of the nanoplatelets in the final products and their quantity is irreproducible through experiments.

The non-consistent presence of sodium could be a problem for studies of performance in targeted applications of the nanoparticles and of their toxicity. Therefore, it was necessary to elucidate its role in the synthesis of the $Gd_{2(1-x)}Ce_{2x}O_2S$ nanoplatelets. Small and wide-angle X-ray scattering (SAXS-WAXS) experiments showed that during the synthesis with oleic acid, a lamellar mesophase, consistent with a bilayer of sodium oleate was formed. This mesophase then served as a template for nucleation and growth of the $Gd_{2(1-x)}Ce_{2x}O_2S$ nanoplatelets. Unveiling the formation mechanism of the nanoplatelets would enable the possibility to control their size and shape, which could be of importance for their design for targeted applications.

2. Safer-by-design $Gd_{2(1-x)}Ce_{2x}O_2S$ nanoparticles for photocatalysis

We demonstrated for the first time that the bandgap and the absorption of $Gd_{2(1-x)}Ce_{2x}O_2S$ nanoplatelets were tunable with their cerium content. Higher cerium content of the nanomaterial led to smaller bandgap and absorption in the visible region of the spectrum, making them relevant for photocatalysis under visible light. Indeed, cerium-containing nanoparticles showed catalytic activities with 501 nm irradiation, even though relatively low. While the cerium had positive effects on the functionality of the nanoparticles, its presence seemed to result in higher cytotoxicity of the nanoparticles. The cerium content may need to be compromised to ensure the safety of the material.

The oleates ligands on the surface of the nanoparticles likely hinder their reactivity towards water molecules. In order to improve the photocatalytic activity of $Gd_{2(1-x)}Ce_{2x}O_2S$ nanoplatelets, they need to be removed. Since the nanoplatelets are very thin, complete removal of the ligands may result in drastic modification of the overall object. Nevertheless, preliminary results suggested that thermal treatment might be a promising method. The ligand removal is crucial to obtain a photocatalyst prototype based on oxysulfide nanoplatelets.

We also explored the origin of the cytotoxicity of cerium-containing nanoparticles. Their irreproducible sodium content, Ce^{III}/Ce^{IV} ratio and specific surface area prevented clear conclusion. Nevertheless, results from X-ray hyperspectral imaging of exposed cells hinted at cerium leaching and redox reaction involving this element. Confirmation of this would give important insights to develop strategies to mitigate this cytotoxicity.

3. $Gd_{2(1-x)}Ce_2O_2S$ nanoparticles for biomedical imaging

Lanthanide doping is a suitable strategy to include photoluminescence properties in Gd_2O_2S nanoplatelets. Moreover, we were able to coat Eu-doped Gd_2O_2S nanoplatelets with polyvinylpyrrolidone (PVP) to make them water-dispersible while preserving their emission. This makes them suitable for fluorescent imaging. Their performance is still to be confirmed by observation in living cells. Gd_2O_2S nanoparticles could also be employed for MRI. Magnetic relaxation experiments need to be done to determine their relaxation constants. Then, the coating process might need to be further adjusted for optimized performance in imaging.

Preliminary results on cytotoxicity of PVP-coated nanoparticles showed an absence of adverse effect. However, additional toxicity assays similar to those carried out in the case of $Gd_{2(1-x)}Ce_2O_2S$ nanoparticles for photocatalysis are required to conclude. The effect of the PVP-coating on the nanoparticle toxicity is also to be determined. Coating could be a general strategy to mitigate the toxicity of oxysulfide nanoplatelets.

Finally, we showed that cerium quenched the photoluminescence of europium in nanoplatelets containing both elements. Overall, we believe that gadolinium oxysulfide Gd_2O_2S nanoparticles are a better candidate for biomedical applications.

4. Safer-by-design approach for emerging nanomaterials

Safer-by-design concept was applied for the first time for bimetallic gadolinium-cerium oxysulfide nanoparticles of compositions $Gd_{2(1-x)}Ce_2O_2S$ as a model of emerging nanomaterials. It effectively allowed early detection of toxicity of the nanomaterial. Thus, strategies to mitigate this latter could be envisaged early on. This is especially important for materials whose toxicity is unknown.

Our work highlighted the importance of in-depth characterization of the nanomaterials to identify key physicochemical parameters that influence their performance and toxicity. This could be challenging for emerging systems since they are usually not completely mastered. Nevertheless, the knowledge gain is enormous, in particular for fundamental research.

The safer-by-design approach for emerging nanomaterials emphasizes on the ability to modify the nanomaterial to improve its performance or mitigate its toxicity. Therefore, it could be difficult to apply for systems that are not as flexible.

Overall, the safer-by-design approach is useful to anticipate risks relating to nanomaterials and thus for regulations compliance. It should be systematically applied in the design of nanomaterial-containing products that will go to the market. However, for emerging nanomaterials, at which stage of their research it should be applied to have the maximum impact may depend on the material.

Appendix I

Experimental Section

Table of contents

ES.1. Synthesis and post-synthetic treatment of nanoparticles 185
ES.1.1. Synthesis of $Gd_{2(1-x)}Ce_xO_2S$ nanoparticles 185
ES.1.2. Thermal treatment of Gd_2O_2S nanoparticles 186
ES.1.3. Polymer coating of $Gd_{2(1-x)}Ce_xO_2S$ nanoparticles 186
ES.2. Characterization of nanoparticles 186
ES.2.1. Powder X-ray Diffraction (XRD) 186
ES.2.2. Transmission Electron Microscopy (TEM) 187
ES.2.3. Energy Dispersive X-ray Spectroscopy (EDS) 187
ES.2.4. X-ray Absorption Near Edge Spectroscopy (XANES) 187
ES.2.5. Fourier Transform Infrared Spectroscopy (FTIR) 187
ES.2.6. UV-visible spectroscopy 188
ES.2.7. Photoluminescence spectroscopy 188
ES.2.8. Thermogravimetric analysis (TGA) 188
ES.2.9. Physical adsorption 189
ES.3. Photocatalysis tests 189
ES.3.1. Photodegradation of rhodamine B 189
ES.3.2. Radical production evaluation with dithiothreitol (DTT) 189
ES.4. Toxicity assessment 190
ES.4.1. Cell culture 190
ES.4.2. Nanoparticle dispersion for cellular studies 190
ES.4.3. Cell viability assays 190
ES.4.4. Intracellular ROS activity assessment 191
ES.4.5. Protein expression analysis 191
ES.4.6. Measurement of pro-inflammatory cytokine secretion 192
ES.4.7. X-ray Absorption (XAS) and Fluorescence (XRF) hyperspectral imaging 193
ES.4.8. Non-surgical intratracheal instillation of mice 194

References 194

ES.1. Synthesis and post-synthetic treatment of nanoparticles

ES.1.1. Synthesis of $Gd_{2(1-x)}Ce_xO_2S$ nanoparticles

Oleylamine (OAm; technical grade, 70%), oleic acid (OA; technical grade, 90%), 1-octadecene (ODE; technical grade, 90%), sulfur (S_8; ≥ 99.5%), sodium oleate (Na(oleate); ≥ 99%), cesium carbonate (Cs_2CO_3; 99%) and europium(III) acetylacetonate ($Eu(acac)_3 \cdot xH_2O$) were purchased from Sigma-Aldrich. Potassium acetylacetonate ($K(acac) \cdot xH_2O$, 97%) was purchased from Alfa Aesar. Sodium acetylacetonate ($Na(acac) \cdot xH_2O$, ≥ 98%), lithium acetylacetonate ($Li(acac) \cdot xH_2O$, 98+%), calcium (II) acetylacetonate ($Ca(acac)_2 \cdot xH_2O$), gadolinium (III) acetylacetonate ($Gd(acac)_3 \cdot xH_2O$; 99.9%) and cerium (III) acetylacetonate ($Ce(acac)_3 \cdot xH_2O$; 99.9%) were purchased from Strem Chemicals. The latter was stored in the glovebox. All chemicals described above were used without further purification.

Oxysulfide nanoparticles were prepared via a solvothermal reaction under purified nitrogen atmosphere using standard air-free techniques with Schlenk line. In a typical synthesis using sodium acetylacetonate, $Gd(acac)_3 \cdot xH_2O$ (227 mg, 0.5 mmol, 1 equiv.), S_8 (8 mg, 0.032 mmol, 0.5 equiv. in S), $Na(oleate) \cdot xH_2O$ (152 mg, 0.5 mmol, 1 equiv.) were added to a mixture of OA (0.71 g, 2.5 mmol, 5 equiv.), OAm (4.54 g, 17 mmol, 34 equiv.) and ODE (8.10 g, 32.5 mmol, 65 equiv.) in a 100 mL three-necked flask at room temperature. The yellow mixture was degassed at 120 °C under vacuum for 20 min then heated to 310 °C, giving a pale-yellow solution. The solution was stirred at this temperature for 30 min under nitrogen. After heating, it was left to cool to room temperature.

The nanoparticles were isolated by centrifugation (6000 g, 10 min, 20 °C) using 30 mL of ethanol. They were washed at least three times using 40 mL of a *n*-hexane/ethanol mixture (1/3 in volume) to remove remaining reagents and organic matter. From 100 to 120 mg of dried white powder were obtained, corresponding to a 100% yield of Gd_2O_2S (this calculation neglects the weight of organic ligands).

Syntheses of Gd_2O_2S nanoparticles using other alkali and alkaline earth cation sources such as Li(acac), Na(acac), K(acac), Cs_2CO_3, $Ca(acac)_2$ were carried out in the same fashion and with the same equivalence of alkali and alkaline earth cation (1 equiv.).

Syntheses of $Gd_{2(1-x)}Ce_xO_2S$ nanoparticles and Eu-doped $Gd_{2(1-x)}Ce_xO_2S$ nanoparticles were carried out in the same fashion. Added quantities of gadolinium precursor $Gd(acac)_3{\cdot}xH_2O$, cerium precursor $Ce(acac)_3{\cdot}xH_2O$ and europium precursor $Eu(acac)_3{\cdot}xH_2O$ were adjusted accordingly so that the total amount of lanthanides added was 0.5 mmol. For these syntheses, from 50 mg to 100 mg of dried powder were obtained depending on the cerium content of the nanoparticles.

ES.1.2. Thermal treatment of Gd_2O_2S nanoparticles

As prepared Gd_2O_2S nanoparticles (100 mg) were heated at 500 °C for 2 h under argon flow in a quartz tube with a Carbolite tube furnace. The heating rate was fixed at 10 °C.min^{-1}. After heating, the tube was left in the furnace until the temperature dropped to around 100 °C. It was then removed and was left to cool down to room temperature naturally. The black solid was recovered by centrifugation (6000 g, 10 min, 20 °C) using 50 mL of ethanol.

ES.1.3. Polymer coating of $Gd_{2(1-x)}Ce_xO_2S$ nanoparticles

For the coating process, polyvinylpyrrolidone (PVP) (MW = 55,000) was purchased from Sigma-Aldrich. In a typical experiment, as prepared $Gd_{2(1-x)}Ce_xO_2S$ nanoparticles (ca. 100 mg, 0.25 mmol) were dispersed in 5 mL of *n*-hexane and the resulting suspension was stored in the glovebox. Then, 1 mL of the nanoparticle suspension, 2 mL of dichloromethane and 2 mL of a solution of PVP (100 mg, 1.8 µmol, 0.032 eq. vs. Gd_2O_2S) in dimethylformamide (DMF) were introduced into a Schlenk tube under nitrogen. The clear mixture was heated at reflux at 90 °C with an oil bath under vigorous stirring for 4 h. The reaction medium was left to cool down to room temperature and 25 mL of diethyl ether was added. Precipitate appeared immediately and the product was recovered by centrifugation at 6000 g for 30 min. It was washed with 25 mL of a mixture of toluene/diethyl ether (1/4 in volume) three times.

ES.2. Characterization of nanoparticles

ES.2.1. Powder X-ray Diffraction (XRD)

Powder XRD measurements were performed with a Bruker D8 X-ray diffractometer operating in the reflection mode at Cu Kα radiation with 40 kV beam voltage and 40 mA

beam current. From 10 to 50 mg of powder were deposited on a low-noise Si monocrystal sample holder for the measurements. Typical diffraction patterns were recorded with steps of 0.05° and a scanning speed of 2.5-5 s/point. For easier phase identification, the diffraction patterns were systematically shifted 0.25 ° to correct the extra sample height due to the sample holder. The background was also subtracted using EVA software.

ES.2.2. Transmission Electron Microscopy (TEM)

TEM images were recorded on a FEI TECHNAI G2 Spirit microscope operating at 120 kV equipped with a Gatan CCD camera. Samples were prepared by evaporating a drop of *n*-hexane diluted nanoparticles suspension on a carbon-coated copper grid.

STEM bright-field and HAADF were performed using a spherical aberration corrected JEOL 2100 F operating at 200 kV. EDS mapping was performed using JEOL Silicon Drift Detector (DrySD60GV: sensor size 60 mm ^{2}) with a solid angle of approximately 0.5 srad.

ES.2.3. Energy Dispersive X-ray Spectroscopy (EDS)

A small amount of powder was deposited on carbon adhesive tape on a scanning electron microscope sample holder. EDS analyses were performed on a SEM HITACHI S-3400N instrument at 20 kV. Cobalt was used as calibrator and the analyses were performed on at least three different zones on the samples to calculate an average chemical composition.

ES.2.4. X-ray Absorption Near Edge Spectroscopy (XANES)

The experiments were carried out at the SOLEIL synchrotron facility using an electron energy of 2.7 GeV and an average ring current of 450 mA. X-ray absorption spectra were recorded at beamline SAMBA. From 2 to 3 mg of nanoparticles in the form of dry powder were diluted in ca. 40 mg of graphite. The mixtures were compressed to pellets of diameter 6 mm with a pressure of 2 t. Measurements were performed in transmission mode at the cerium L_{III}-edge (5723 eV). All acquired data were normalized to the edge jump for analysis.

ES.2.5. Fourier Transform Infrared Spectroscopy (FTIR)

Infrared spectra were recorded on a Spectrum 400 (PerkinElmer) spectrometer. From 1 to 3 mg of dry powder were deposited on the attenuated total reflectance (ATR) diamond crystal.

Transmittance was measured from 550 cm^{-1} to 4000 cm^{-1} with steps of 0.5 cm^{-1}. For each sample, at least 4 spectra were collected.

ES.2.6. UV-visible spectroscopy

Measurements in liquid mode were carried out with suspensions of nanoparticles loaded in a 3.5 mL absorption quartz cell with optical path length 10 mm. Absorption spectra were recorded using a Cary-WinUV 5000 spectrophotometer (AGILENT) between 300 nm and 800 nm with steps of 1 nm.

For measurements in diffuse reflectance mode, dry powders of nanoparticles were loaded in the sample holder to make a uniform layer of solid. The UV-visible diffuse reflectance spectra were measured using an integration sphere between 250 nm and 800 nm at 1 $nm.s^{-1}$ and corrected with a sample of $BaSO_4$ as reference. The Kubelka-Munk function F(R) was calculated from obtained apparent absorbance according to the formula:

$$F(R) = \frac{(1-R)^2}{2R}$$

where R is the reflectance. The apparent absorbance given by the spectrometer is related to the reflectance by the following equation:

$$A = \log(1/R)$$

ES.2.7. Photoluminescence spectroscopy

For photoluminescence measurements, suspension of nanoparticles was loaded in a 45 µL fluorescence quartz cell with optical path lengths 3 x 3 mm (Hellma). The spectra were recorded using a FluoroMax-3 spectrofluorometer (HORIBA) between 400 nm and 800 nm with steps of 1 nm. The excitation wavelength was 250 nm. The slits and integration time were fixed at 5 nm and 0.1 s, respectively. No cut-off filter was used for the experiments.

ES.2.8. Thermogravimetric analysis (TGA)

Thermogravimetric analyses were performed on a TA Intruments SDT Q600 TGA-coupled thermoscale. The two thermoscale beams were tarred with a platinum crucible in each. Around 10 mg of sample were placed in one of the crucibles. The other empty crucible serves

as reference. Measurements were conducted under nitrogen with temperature ramp of 5 °C.min^{-1} between 20 °C and 700 °C.

ES.2.9. Physical adsorption

The specific surface area of the nanoparticle powders was determined by N_2 physical adsorption at -196 °C on a BELSORP-max device. The results were analyzed using the Brunauer-Emmett-Teller (BET) theory in the $0.05 \geq P/P_0 \geq 0.20$ range on the BELMaster software. The samples were degassed at 150 °C for 16 h prior to the measurement.

ES.3. Photocatalysis tests

ES.3.1. Photodegradation of rhodamine B

In a closed flask, 25 mg of pristine $Gd_{2(1-x)}Ce_xO_2S$ nanoparticles and 25 mL of a 10^{-5} M solution of rhodamine B were mixed together. The mixture was sonicated for 1 min and was left in the dark under vigorous stirring for 1 h. It was then irradiated with nine LEDs producing cyan light (λ = 501 nm) for up to 7 days. At regular time intervals, 1 mL of the mixture was taken and centrifuged at 13,000 rpm for 2 min to remove the nanoparticles. The process was repeated twice and the final supernatant was analyzed by UV-visible absorption spectroscopy. The background of recorded spectra was subtracted to eliminate the contribution of remaining nanoparticles in the supernatant.

ES.3.2. Radical production evaluation with dithiothreitol (DTT)

For this experiment, dithiothreitol (DTT) and 5.5'-dithiobis-(2-nitrobenzoic acid) (DTNB or Ellman's reagent) were purchased from Sigma-Aldrich. Prior to the experiment, suspensions of $Gd_{2(1-x)}Ce_xO_2S$ nanoparticles in distilled water at concentrations from 50 to 1000 µg.mL^{-1} were prepared and sonicated for 15 min. In a 96-well plate, 160 µL of the nanoparticle suspension and 40 µL of a 1 mM aqueous solution of DTT were added. The plate was either left in the dark or under irradiation by LEDs (λ = 391 or 501 nm) for 4 h. Then, it was centrifuged at 3000 rpm, 4 °C for 15 min to remove the nanoparticles. The supernatant (90 µL) was taken from each well and was added to 90 µL of a 5 mM DTNB solution in Dulbecco's modified Eagle's medium (DMEM). Absorbance at 405 nm of the mixture was measured using a TECAN microplate spectrometer.

ES.4. Toxicity assessment

ES.4.1. Cell culture

Murine macrophages RAW 264.7 (ATCC) were maintained in Dulbecco's modified Eagle's medium (DMEM) containing 4.5 g/mL of glucose, 10% fetal bovine serum (FBS), 100 U/mL penicillin and 100 U/mL streptomycin at 37 °C, 5% CO_2 atmosphere. The cells were cultured in 75 cm^2 flask for 2 – 3 days and harvested by scraping. They were then cultured in 96-well plates for cell viability assays or onto silicon nitride membrane for X-ray hyperspectral imaging. This was carried out between passages 5 and 12.

ES.4.2. Nanoparticle dispersion for cellular studies

Nanoparticle stock suspensions (5 mg/mL) were prepared by dispersing 25 mg of dry powder of nanoparticles in 5 mL of sterile water with the help of sonication. The stock suspension was then divided into aliquots of 1 mL and they were stored at 4 °C. Prior to conducting cellular studies, the suspensions were sonicated for 30 min.

ES.4.3. Cell viability assays

For viability assays, 15,000 cells were seeded in a 96-well plate. The nanoparticle stock suspensions were diluted in DMEM medium without phenol red to avoid interference of the latter with subsequent colorimetric and fluorescent assays. A series of suspensions at different concentrations (1, 10, 50, 100 µg/mL) was prepared. After 24 h of culture at 37 °C, the cells were washed with fresh DMEM medium without phenol red and 100 µL of the previously prepared nanoparticle suspensions were added. Cells exposed to nanoparticles were then incubated for another 24 h. Mitochondrial activity, cellular DNA content and membrane integrity were respectively assessed by WST-1 (Roche), Hoechst (Sigma-Aldrich) and LDH (Roche) assays using a TECAN microplate spectrometer.

For WST-1 assay, the cell culture medium was removed at the end of nanoparticle exposure and the plate was washed twice with fresh medium. Then, 100 µL of the WST-1 solution (concentration not provided by the manufacturer) were added to each well. After 3 h of incubation at 37 °C, the absorbance of the medium was measured at 450 nm.

For Hoechst assay, the cell culture medium was removed at the end of nanoparticle exposure and the plate was washed twice with Dulbecco's phosphate-buffered saline (DPBS) with no calcium nor magnesium. Then, the cells were incubated with 20 µL of sterile water for 45 min at 37 °C. At that time, 200 µL of Hoechst 33,258 solution (2 µg/mL) in fluorescence buffer (provided by the manufacturer) was added. The fluorescence intensity of the medium was measured at 460 nm with excitation at 360 nm.

For LDH assay, supernatants of cells exposed for 24h to the various concentrations of nanoparticles were transferred to a new plate and were mixed with 100 µL of reconstituted substrate solution (containing tetrazolium dye, sodium lactate as reactants and diaphorase, NAD^+ as catalysts for the reaction) for 15 min at room temperature in the dark. The reaction was terminated by the addition of 25 µL of HCl 1 M as stop solution. The absorbance of the medium was measured at 490 nm.

ES.4.4. Intracellular ROS activity assessment

Assessment of intracellular ROS activity was carried out using H_2DCF-DA assay (Molecular Probes by ThermoFisher). In a similar fashion to cell viability assays, 15,000 cells were seeded in a 96-well plate for 24 h. They were washed twice with Hank's Balanced Salt Solution (HBSS) with no calcium nor magnesium. The cells were then incubated with 100 µL of a H_2DCF-DA solution at 10 µM for 1 h at 37 °C. After the incubation, the supernatant was removed and the plate was washed twice with fresh HBSS. The cells were treated with 100 µL of nanoparticle suspensions at different concentrations. The fluorescence intensity of the medium was measured at 530 nm before nanoparticle treatment and at 15 min and 45 min after the treatment. The excitation light was fixed at 485 nm.

ES.4.5. Protein expression analysis

In a 6-well plates, 10^6 cells were seeded and cultured for 24 h. After the incubation, the cells were washed with fresh medium without phenol red and 2 mL of nanoparticle suspension in DMEM medium without phenol red was added. After 24 h of treatment, the cells were collected by scraping with RIPA mammalian protein extraction lysis buffer (Sigma-Aldrich) with 10% of protease inhibitor cocktail (Sigma-Aldrich) and 10% of phosphatase inhibitor cocktails (Sigma-Aldrich) to prevent protein degradation and dephosphorylation by endogenous proteases and phosphatases present in the whole cell extract. The obtained

mixtures were centrifuged to remove cell debris and nanoparticles. The supernatant was stored at -80 °C for protein analysis. The total protein concentration in the supernatant was determined by Bradford assay (Bio-Rad) with bovine serum albumin (BSA) (Sigma-Aldrich) as the standard.

The analysis of protein expression was carried out by western blotting. For this experiment, the HO-1 antibody (rabbit) was purchased from Enzo Life Sciences (concentration not provided by the manufacturer) and was diluted 1000 times in a solution of BSA 1%, while the β-actin antibody (mouse) was purchased from Sigma-Aldrich and was diluted 5000 times in a solution of milk 5%. In a typical experiment, 40 µL of a solution containing 30 µg of protein in Laemmli buffer was loaded on a sodium dodecyl sulfate-polyacrylamide gel electrophoresis (SDS-PAGE) gel (4% and 10% of acrylamide for stacking and resolving parts of the gel, respectively). The gel was run at a constant voltage of 60 V for 1 h then at 120 V for 1.5 h. The proteins were transferred to a nitrocellulose membrane by electroblotting at 20 V, 4 °C for 18 h. Blocking of unreacted sites of the membrane was performed by incubation with a solution of milk 5% for 1 h. The membrane was incubated with primary antibody (HO-1 or β-actin) at 4 °C for 16 h then with secondary antibody coupled to peroxidase ECL or alkaline phosphatase at room temperature for 2 h. It was finally reacted in the dark with peroxidase substrate (ECL, Bio-Rad) or alkaline phosphatase (Bio-Rad) for revelation of HO-1 or β-actin, respectively. Detection of luminescence signals and acquisition of images of the membrane were performed on a G-box (Syngene, UK). Quantification of luminescence intensity was carried out with ImageJ software.

ES.4.6. Measurement of pro-inflammatory cytokine secretion

In a 6-well plates, 10^6 cells were seeded and cultured for 24 h. After the incubation, the cells were washed with fresh medium without phenol red and 2 mL of nanoparticle suspension in DMEM medium without phenol red was added. After 24 h of treatment, the supernatant was taken and stored at -80 °C for assessing cytokine and chemokine levels.

The IL- 6, IL-1β and TNF-α pro-inflammatory cytokines was quantified using the supernatant collected from the treated cells. The analyses were conducted using Quantikine ELISA kits purchased from R&D Systems. The measurement of the secreted cytokine level involved transferring 50 µL of the collected cell culture supernatant into 96-well plates coated with the capture antibody against the targeted cytokine. Then a detection antibody was added and

bound to the captured cytokine. Unbound detection antibody was washed away. The sandwich capture antibody-cytokine-detection antibody was revealed by adding a tetramethylbenzidine (TMB) substrate solution to develop a blue color. A hydrochloric acid solution provided by the manufacturer was added to stop the reaction and the color turned yellow. The detailed protocol was based on the manual provided in the kit purchased. The cytokine levels were quantified by measuring absorbance of the medium at 450 nm using a TECAN microplate spectrometer.

ES.4.7. X-ray Absorption (XAS) and Fluorescence (XRF) hyperspectral imaging

Murine macrophages RAW 264.7 were seeded at concentration of $4{,}10^5$ cells/mL onto 200 nm thick silicon nitride (Si_3N_4) membrane windows (Silson Ltd., United Kingdom) placed in 12-well plates. After 24 h of culture at 37 °C, they were washed with fresh medium and were exposed to suspensions of nanoparticles at 10 µg/mL. RAW 264.7 cells similarly grown onto the windows, but not exposed to nanoparticles (untreated cells), were used as control.

After another 24 h of incubation, the membranes were washed with Dulbecco's phosphate-buffered saline (DPBS) with no calcium nor magnesium, then rapidly with water. The water was removed by blotting on a Kimwipes paper without direct contact to the thin membrane. The windows were then snap-frozen by plunging into isopentane cooled by liquid nitrogen for 30 s. They were stored in 24-well plates cooled at -80 °C in a freezer or with dry ice.

X-ray hyperspectral imaging experiments were carried out at ID21 beamline of ESRF synchrotron (Grenoble, France) in a vacuum chamber passively cooled at *ca.* -130 °C by liquid nitrogen. The silicon nitride (Si_3N_4) membrane windows were mounted onto a pre-cooled copper sample holder immersed in liquid nitrogen and were rapidly inserted into the vacuum chamber. Measurements at Gd L_3-edge were carried out first. µXRF maps were acquired with an incoming energy of 7.4 keV with 0.5 μm^2 steps and an integration time of 100-150 ms. µXAS spectra were recorded at different points in the maps to compare with those of pristine nanoparticles. Energy of the beam was then set to 5.8 keV at Ce L_3-edge. µXRF and µXAS maps were recorded in areas presenting high nanoparticles concentrations near the cells. Reference sample on Si_3N_4 membrane RF8-200-52454-17 purchased from AXO DRESDEN GmbH (Dresden, Germany) was used for quantification of elements.

Analysis of the XRF images and spectra was carried out using the multiplatform program PyMCA.[1] To calculate weight fractions, the thickness of the cells and the density of the medium were estimated at 15 µm and 1 g/mL respectively.

ES.4.8. Non-surgical intratracheal instillation of mice

Twelve-week-old male C57 BL/6 mice were purchased from Janvier Labs (Le Genest-Saint-Isle, France). Under ketamine/xylazine (100/10 mg/kg) anesthesia, the animals were held vertically and the tongue was gently pulled out of the mouth using forceps. Then, 50 µg of nanoparticles dispersed in 15 µL of distilled water was directly instilled to the trachea through a catheter. Animal sacrifice was performed 24 h after instillation. After the mice had been anesthetized, bronchoalveolar lavage (BAL) was performed by cannulating the trachea and gently lavaging the lung three times with 1 mL of sterile phosphate-buffered saline (PBS). Cells in BAL fluids were adhered onto microscopic slides and stained with Diff-Quick (Dade Behring, La Défense, France) for differential cell count. BAL fluids were stored at -80 °C for assessing cytokine and chemokine (IL- 6, IL-1β and TNF-α) levels using ELISA kits (R&D Systems).

References

(1) Solé, V. A.; Papillon, E.; Cotte, M.; Walter, P.; Susini, J. A Multiplatform Code for the Analysis of Energy-Dispersive X-Ray Fluorescence Spectra. *Spectrochim. Acta Part B At. Spectrosc.* **2007**, *62* (1), 63–68.

Appendix II

List of publications

1. Publications

1. Larquet, C.; **Nguyen, A.-M.**; Ávila-Gutiérrez, M.; Tinat, L.; Lassalle-Kaiser, B.; Gallet, J.-J.; Bournel, F.; Gauzzi, A.; Sanchez, C.; Carenco, S.
   Synthesis of Ce_2O_2S and $Gd_{2(1-y)}Ce_{2y}O_2S$ Nanoparticles and Reactivity from in Situ X-Ray Absorption Spectroscopy and X-Ray Photoelectron Spectroscopy.
   Inorg. Chem. **2017**, *56* (22), 14227–14236.
   In this work, I participated in the synthesis and characterization (XRD, TEM, EDS, FTIR) of the bimetallic gadolinium-cerium oxysulfide nanoplatelets. I also contributed to the preparation of the article.

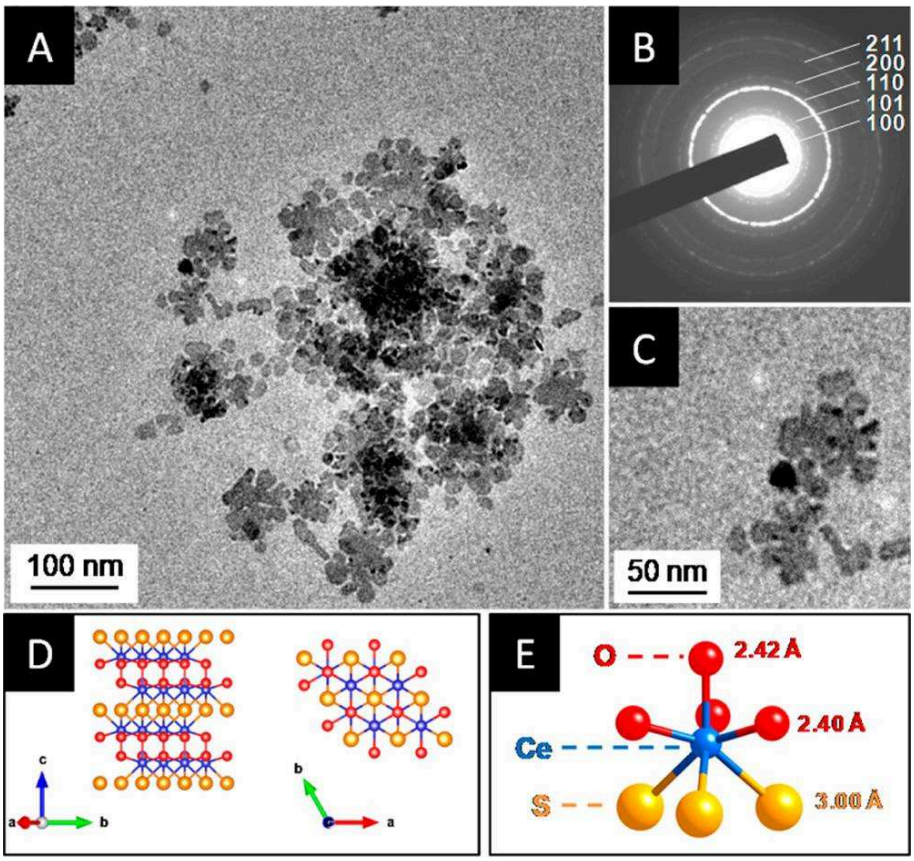

2. Larquet, C.; Hourlier, D.; **Nguyen, A.-M.**; Torres-Pardo, A.; Gauzzi, A.; Sanchez, C.; Carenco, S.

   Thermal Stability of Oleate-Stabilized Gd_2O_2S Nanoplates in Inert and Oxidizing Atmospheres.

   ChemNanoMat **2019**, *5* (4), 539–546.

   In this article, I carried out some experiments regarding thermal treatment of the oxysulfide nanoplates. I also contributed to the FTIR analysis of the products.

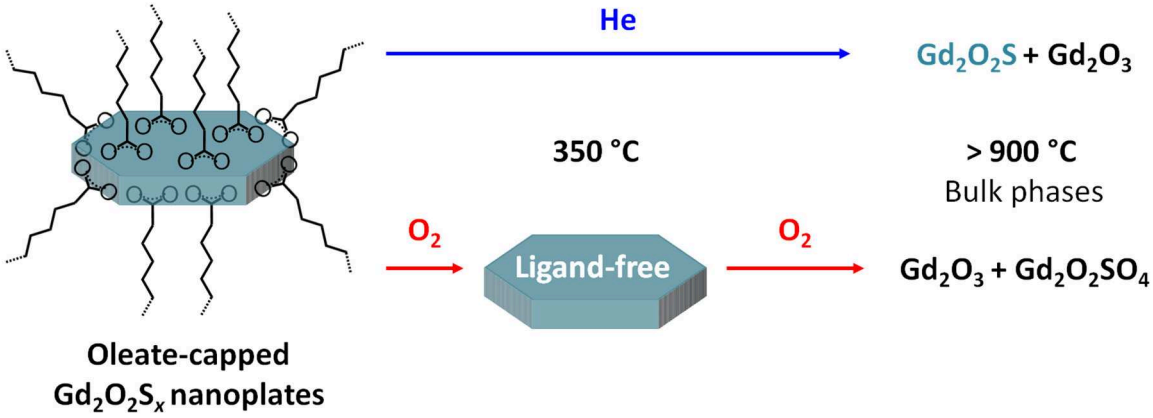

3. Larquet, C.; **Nguyen, A.-M.**; Glais, E.; Paulatto, L.; Sassoye, C.; Selmane, M.; Lecante, P.; Maheu, C.; Geantet, C.; Cardenas, L.; Chanéac, C.; Gauzzi, A.; Sanchez, C.; Carenco, S.

   Band Gap Engineering from Cation Balance: The Case of Lanthanide Oxysulfide Nanoparticles.

   Chem. Mater. **2019**, *31* (14), 5014–5023.

   Alongside the first author, I synthesized and characterized (XRD, TEM, EDS, FTIR, UV-visible absorption) the bimetallic gadolinium-cerium oxysulfide nanoplatelets. I also contributed to the preparation of the article, especially the discussion regarding the structure of the nanoplatelets.

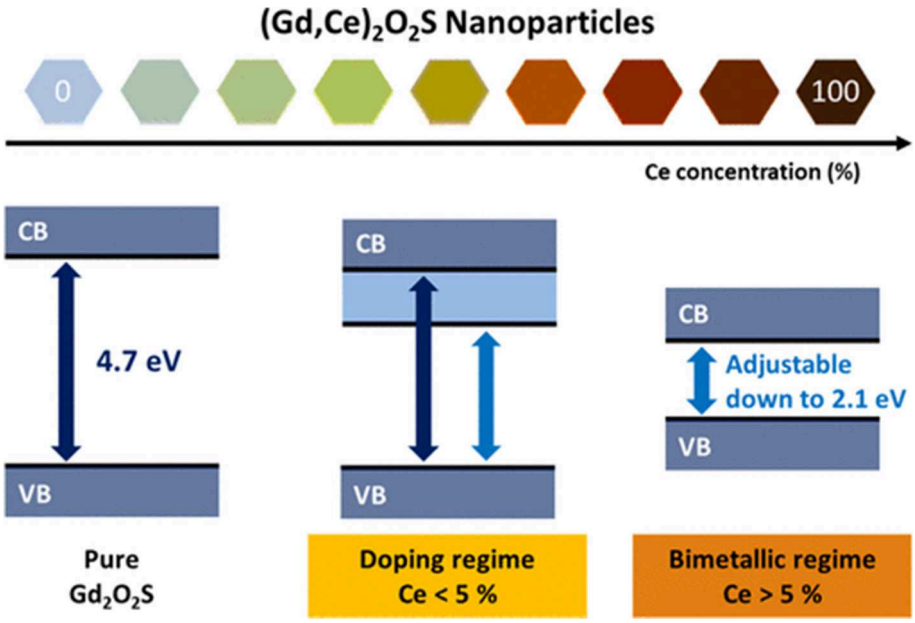

4. **Nguyen, A.-M.**; Bahri, M.; Dreyfuss, S.; Moldovan, S.; Miche, A.; Méthivier, C.; Ersen, O.; Mézailles, N.; Carenco, S.

   Bimetallic Phosphide $(Ni,Cu)_2P$ Nanoparticles by Inward Phosphorus Migration and Outward Copper Migration.

   Chem. Mater. **2019**, acs.chemmater.9b01505.

   I started this work during my Master internship at LCMCP and have continued to work on it during my Ph.D. I studied the reactivity of core-shell Cu-Ni nanoparticles with white phosphorus and elucidated the reaction pathway by a combination of local (*in situ* STEM coupled to EDS) and ensemble (XRD, NMR, EDS, XPS) characterization techniques.

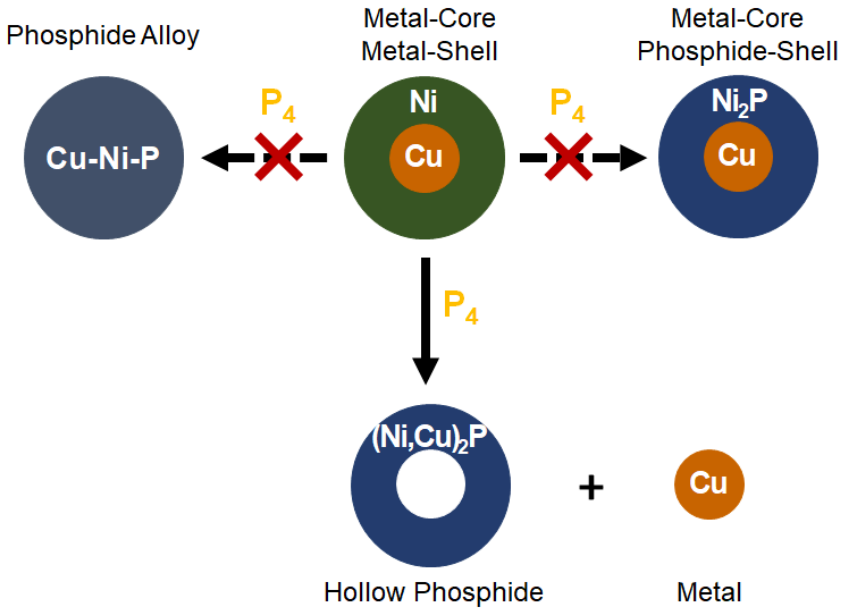

5. Larquet, C.; Carrière, D.; **Nguyen, A.-M.**; Le, T. K.-C.; Frogneux, X.; Génois, I.; Le Griel, P.; Gauzzi, A.; Sanchez, C.; Carenco, S.

   Growth Mechanism of Gd_2O_2S Nanoparticles in Sodium-Stabilized Lamellar Mesophase: Redefining the Role of Alkali Cations in Lanthanide Oxysulfide Crystallization.

   To be submitted.

   In this work, I varied the synthesis conditions to get insights on the role of the alkali-metal in the formation of Gd_2O_2S nanoparticles. I also contributed to the discussion regarding the nanoparticle growth mechanism.

Appendix III

Synthesis of Ce_2O_2S and $Gd_{2(1-y)}Ce_{2y}O_2S$ Nanoparticles and Reactivity from *in situ* X-ray Absorption Spectroscopy and X-ray Photoelectron Spectroscopy

Inorganic Chemistry

Article

Cite This: Inorg. Chem. 2017, 56, 14227-14236

pubs.acs.org/IC

Synthesis of Ce_2O_2S and $Gd_{2(1-y)}Ce_{2y}O_2S$ Nanoparticles and Reactivity from in Situ X-ray Absorption Spectroscopy and X-ray Photoelectron Spectroscopy

Clément Larquet,[†,‡] Anh-Minh Nguyen,[†] Mario Ávila-Gutiérrez,[†] Lionel Tinat,[†] Benedikt Lassalle-Kaiser,[§] Jean-Jacques Gallet,[§,∥] Fabrice Bournel,[§,∥] Andrea Gauzzi,[‡] Clément Sanchez,[†] and Sophie Carenco*[,†]

[†]Sorbonne Universités, UPMC Univ Paris 06, CNRS, Collège de France, Laboratoire de Chimie de la Matière Condensée de Paris, 4 place Jussieu, 75005 Paris, France

[‡]Sorbonne Universités, UPMC Univ Paris 06, CNRS, IRD, MNHN, Institut de Minéralogie, de Physique des Matériaux et de Cosmologie, 4 place Jussieu, 75005 Paris, France

[§]Synchrotron SOLEIL, L'Orme des Merisiers, 91192 Saint-Aubin - BP 48, Gif-sur-Yvette Cedex, France

[∥]Sorbonne Universités, UPMC Univ Paris 06, CNRS, Laboratoire de Chimie Physique Matière et Rayonnement, 4 place Jussieu, 75005 Paris, France

Supporting Information

ABSTRACT: Lanthanide oxysulfide nanoparticles have recently attracted interest in view of their potential applications, such as lighting devices and MRI contrast agents, which requires a good stability in air and a controlled surface. In order to address these issues, in this work, air-sensitive Ce_2O_2S nanoparticles of hexagonal shape were successfully prepared and characterized under inert conditions. Bimetallic $Gd_{2(1-y)}Ce_{2y}O_2S$ nanoparticles of similar shape and size were also synthesized for the whole composition range (y from 0 to 1). X-ray diffraction structural data are found to follow Vegard's law up to $y = 0.4$, which is attributed to the loss of stability in air of Ce-rich nanocrystals beyond this threshold. This picture is supported by X-ray absorption spectra taken at the S K-edge and Ce L_3-edge that show the partial oxidation of sulfide species and of Ce^{III} to Ce^{IV} in the presence of air or water. A complementary near-ambient-pressure X-ray photoelectron spectroscopy study shows that at least two types of oxidized sulfur species form on the nanoparticle surface. Even in Gd_2O_2S nanoparticles that are generally considered to be air-stable, we found that sulfide ions are partially oxidized to sulfate in air. These results unveil the physicochemical mechanisms responsible for the surface reactivity of lanthanide oxysulfides nanoparticles in air.

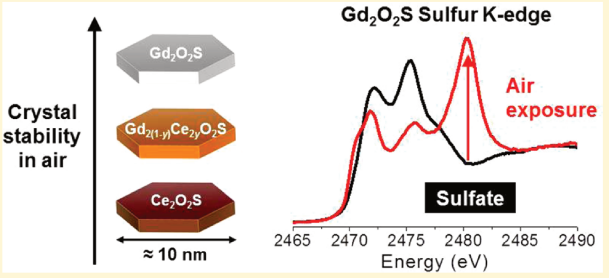

INTRODUCTION

In the past decade, the development of novel methods enabling the synthesis of nanoparticles has resurrected interest in bianionic materials such as oxysulfides M_xO_ySz. These compounds are particularly attractive, as they contain abundant heteroatoms.[1] The combination of lanthanide with oxygen and nonoxidized sulfur has been known for more than 60 years.[2] Since the first report on lanthanide oxysulfides, only a few compositions have been synthesized via solid-state or solid−gas reactions at high temperatures. These synthesis techniques employ various sulfur sources (elemental sulfur, H_2S, or CS_2) as sulfidation agents. Some of them also involve a transition metal, producing not only bimetallic compounds, such as $Ln_2Ti_2S_2O_5$ and $LnCrOS_2$ (Ln = La−Lu),[3−5] but also $LaInOS_2$ and $La_5In_3S_9O_3$.[6]

Ln_2O_2S nanoparticles have been extensively studied and characterized for their promising magnetic,[7−9] photocatalytic,[8] and luminescent properties.[10,11] In the last case, the most studied compounds are La_2O_2S,[12−15] Gd_2O_2S,[16−21] and Y_2O_2S,[22−30] especially with rare-earth doping (Eu^{III}, Tb^{III}, Yb^{III}, etc.). Doped lanthanide oxysulfide Ln_2O_2S:Ln^{III} nanoparticles (with mostly Ln = La, Gd, Y in the Ln_2O_2S phase) are particularly interesting as luminescent materials in biological media because the oxysulfide phase is an efficient matrix enabling the fluorescence of the doping ion. One important research direction aims at the development of efficient luminescent materials characterized by a long lifetime, which would open the field of *in vivo* imaging.

The synthesis of oxysulfide nanoparticles is challenging, as rare-earth metals have a better affinity with O^{2-} than with S^{2-} according to the hard and soft acid and base (HSAB) theory. Moreover, the fairly high temperatures required for the formation of the crystalline phase can cause the sintering of

Received: September 13, 2017
Published: November 1, 2017

DOI: 10.1021/acs.inorgchem.7b02336
Inorg. Chem. 2017, 56, 14227−14236

the nanoparticles. As a matter of fact, well-crystallized Ln_2O_2S nanoparticles have been hitherto obtained only for Ln = La, Pr, Nd, Sm, Eu, Gd, Tb, Y. Ding and co-workers[14] proposed an efficient and versatile synthesis of lanthanide oxysulfide nanoparticles by thermal decomposition of molecular species in solution, yielding Na-doped Ln_2O_2S (Ln = La, Pr, Nd, Sm, Eu, Gd, Tb). In organic solvents, they obtained small and monodisperse oxysulfide nanoplates of diameters in the 10−25 nm range depending on the lanthanide. Moreover, Pasberg et al. reported Ln_2O_2S nanoparticles containing Lu and Gd.[31]

In this context, cerium oxysulfide Ce_2O_2S nanoparticles would display ideal optical properties owing to the much smaller band gap energy (brown material) in comparison to other Ln_2O_2S compounds, where the band gap is larger than 3.5 eV for all other Ln. Such a low band gap permits an absorption in the visible-light range, which is desirable for application in photocatalysis. Moreover, the two possible oxidation states of cerium (Ce^{III} and Ce^{IV}) would make Ce_2O_2S a promising material for catalytic or electrocatalytic reactions. The most suitable material for these applications would be nanoparticles of Ce_2O_2S, in order to get a high surface to volume ratio and to benefit from the numerous available processes to design catalysts with nanoparticles.

To the best of our knowledge, the synthesis of colloidal cerium oxysulfide nanoparticles including Ce_2O_2S has not yet been reported, despite the fact that the bulk phase has been known since the 1950s.[2,32] One difficulty is that the oxidation state of cerium can be either Ce^{III} (the oxidation state in Ce_2O_2S) or Ce^{IV}. As a result, the oxidation of bulk Ce_2O_2S led to mixed-valence crystalline bulk phases, such as $Ce_2O_{2.5}S$,[32−34] $Ce_4O_4S_3$,[35] and $Ce_6O_6S_4$.[36] Systems including nanoscaled Ce_2O_2S supported on graphitized carbon[37] or N- and S-doped carbon[38] were recently developed for applications in Li-ion batteries and the ORR reaction, respectively.

Here, we report on the first synthesis of Ce_2O_2S nanoparticles and on their characterization by transmission electron microscopy (TEM) and X-ray diffraction (XRD). We show that their structure evolves rapidly not only in air but also in the presence of water. In situ X-ray absorption spectroscopy evidences the partial oxidation of Ce^{III} into Ce^{IV} and the formation of oxidized sulfur species. The latter were also found on the surface of Gd_2O_2S nanoparticles, although these nanoparticles are generally considered stable in air. Bimetallic $Gd_{2(1-y)}Ce_{2y}O_2S$ nanoparticles of similar shape and size with y ranging from 1 to 90% were also synthesized. The lattice parameter a was measured and compared to the theoretical value obtained from Vegard's law. We identified three regimes, related to the stability of the nanoparticles in air. Above 40% of cerium, the nanoparticles were not air-stable. Nevertheless, the nanoparticles of $Gd_{2(1-y)}Ce_{2y}O_2S$ keep the Ln_2O_2S structure and morphology up to 80%, making gadolinium an efficient cocation to protect the cerium oxysulfide structure. Thus, cerium-rich nanoparticles could be used even in ambient air, unlike Ce_2O_2S nanoparticles, whose high sensitivity to air would cause the material degradation. Finally, the reactivity of $GdCeO_2S$ (y = 50%) and Gd_2O_2S in water vapor and O_2 was investigated using near-ambient-pressure X-ray photoelectron spectroscopy. This study confirmed the swift and partial oxidation of Ce^{III} to Ce^{IV}. We showed that not only sulfate but also S^{IV} species form on the nanoparticle surface, which was attributed to intermediate sulfite ions. To the best of our knowledge, this study constitutes the first report on Ce_2O_2S nanoparticles, the first example of a bimetallic lanthanide oxysulfide phase with great solubility, and an unprecedented investigation of the surface reactivity of metal oxysulfides.

RESULTS AND DISCUSSION

Synthesis of Ce_2O_2S Nanocrystals. $Ce(acac)_3$ hydrate was reacted at 310 °C for 30 min with a stoichiometric amount of sulfur (0.5 equiv vs Ce) in a mixture of oleylamine, oleic acid, and 1-octadecene, in the presence of Na(oleate) hydrate (see the Experimental Section). The reaction was performed under inert atmosphere. In a first attempt, the particles were isolated and washed under ambient air. The product was dark brown at first but turned greenish after a few hours and light brown after a few weeks (Figure S1 in the Supporting Information), suggesting product decomposition in air. Consistent with this observation, the X-ray diffraction pattern matched the pattern of Ce_2O_2S a few hours after the synthesis and evolved into another pattern similar to that of CeO_2 in a time span of 2 weeks (Figure S2 in the Supporting Information). A similar observation was previously reported in bulk samples as well, but in a time span of months,[32] and the final product was identified by Sourisseau et al.[33,34] to be $Ce_2O_{2.5}S$ with an insertion of oxygen in the layer of cerium oxide owing to a partial oxidation of Ce^{III} in Ce^{IV}. This suggests that washing and handling of the nanoparticles in air was inappropriate, although the synthetic route itself was efficient.

To overcome this issue, we isolated the nanoparticles from the crude product and washed them with anhydrous solvents under the inert atmosphere of a glovebox (H_2O <0.5 ppm, O_2 <0.5 ppm). Transmission electron microscopy (TEM) carried out on these nanoparticles confirmed the formation of nanoplates whose dimensions vary between 10 and 20 nm in length and between 1.5 and 2.5 nm in thickness (Figure 1A). Because of the high amount of remaining ligands on the nanoparticles (washing them in the glovebox is a hard process),

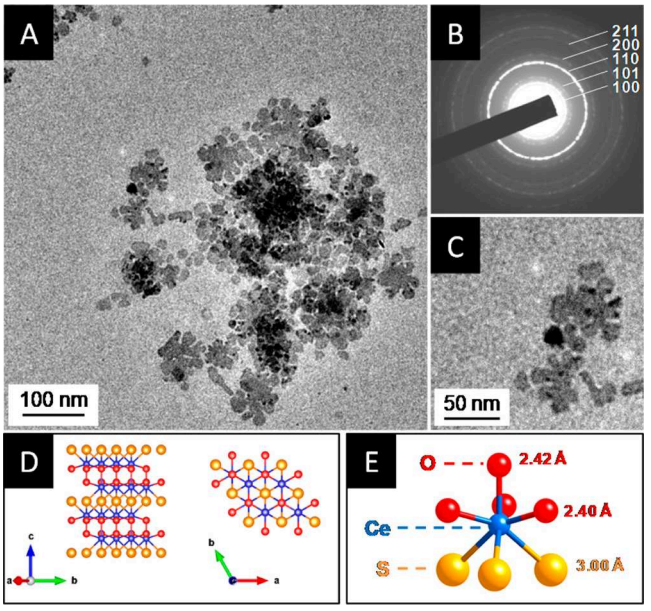

Figure 1. TEM image (A) and the corresponding diffraction pattern (B) of representative Ce_2O_2S nanoparticles. (C) Enlargement of the Ce_2O_2S nanoplates. (D) Representations of the lamellar and hexagonal structure of Ce_2O_2S (JCPDS 02-2554) and (E) the cerium environment in the structure.

DOI: 10.1021/acs.inorgchem.7b02336
Inorg. Chem. 2017, 56, 14227−14236

we were not able to perform high-resolution transmission electron microscopy (HRTEM).

Despite their small size, an X-ray diffraction pattern (XRD) confirmed the crystalline structure of Ce_2O_2S nanoparticles (Figure S3 in the Supporting Information). The pattern matches the reference pattern of hexagonal Ce_2O_2S. Diffraction peaks have different widths, which is related to the anisotropy of the nanoparticle shape. Scherrer's formula applied to the (110) diffraction peak gives an average crystal domain size in the range of 8−14 nm, consistent with the observed width of the nanoplates. Hence, each nanoplate is made of a single nanocrystal. Selected-area electronic diffraction (SAED) performed on a few nanoparticles confirmed their good crystalline properties, as the *d* spacings of the diffraction rings (Figure 1B) match well with those of the Ce_2O_2S reference structure (JCPDS 26-1085).

Energy-dispersive X-ray spectroscopy (EDS) was performed on the nanoparticles. Consistent with previous work by Ding et al.,[14] the data indicate the presence of significant amounts of sodium in the nanoparticle powders. Due to its sensitivity, only a limited washing was performed on the Ce_2O_2S sample. As a result, a high quantity of sodium oleate remained (Na/Ce ≈ 2.7). According to these authors, the role of sodium is critical in the crystallization of all Ln_2O_2S nanoplates prepared by this route, although recently Lei et al. reported a sodium-free synthesis.[21] The study of the role of this cation on the crystallization process goes beyond the scope of the present work and will be the object of a future paper.

The EDS data indicate a S:Ce ratio of 26 ± 4%, which illustrates a sulfur deficiency already observed in previous work on other Ln_2O_2S nanoparticles.[14] We thus propose that the Ce_2O_2S nanoplates are terminated by $[Ce_2O_2]^{2+}$ sheets and stabilized by oleate chains.

Chemical Transformation of the Nanoparticles Exposed to Air. As mentioned above, brown Ce_2O_2S becomes green after exposure to air. Isolation and storage of the nanoparticles under a controlled inert atmosphere is thus critical. As discussed above, the degradation in air, seen by a loss of the Ln_2O_2S crystalline structure, occurs faster for nanoparticles than for bulk samples, which is attributed to the higher surface to volume ratio of the former. Generally, there is a lack of information regarding the surface reactivity of lanthanide oxysulfide nanoparticles that may be responsible for their degradation. In this work, we employed X-ray absorption near edge spectroscopy (XANES) at the sulfur K-edge to evaluate the sulfur oxidation state in the nanoparticles (Figure 2). Our spectra can be directly compared with those previously obtained on various sulfide, sulfite, sulfonate, and sulfate materials which constitute a set of standard spectra.[39−42] From these spectra, one notes that the features of reduced sulfur species are found at low energy while those of oxidized species appear at higher energy. Remarkably, the oxidation state of sulfur is often linearly related to the edge energy.[39,43,44]

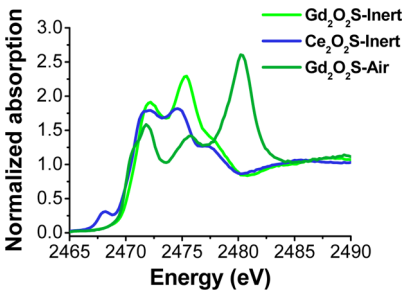

Figure 2. XANES spectra at sulfur K-edge of Gd_2O_2S (*Gd_2O_2S-Inert*) and Ce_2O_2S (*Ce_2O_2S-Inert*) nanoparticles treated and stored under a controlled inert atmosphere and Gd_2O_2S (*Gd_2O_2S-air*) treated and stored for 5 weeks in air.

As a reference material, we first measured Gd_2O_2S nanoparticles (*Gd_2O_2S-air*) synthesized following the same route (described in the Experimental Section). These nanoparticles are stable upon storage in air and during washing steps (see XRD pattern in Figure S4 in the Supporting Information), because Gd only accepts oxidation state III under ambient conditions. Second, we prepared Gd_2O_2S nanoparticles and stored and transferred them to the beamline chamber under controlled inert conditions (*Gd_2O_2S-Inert*). The corresponding XANES spectra are presented in Figure 2.

Gd_2O_2S-Inert (Figure 2, green) does not show the broad peak near 2480 eV characteristic of oxidized sulfur (S^{IV} to S^{VI}). On the other hand, this feature is present in the *Gd_2O_2S-air* spectrum (Figure 2, light green). Accordingly, in the 2470−2475 eV region, the peaks corresponding to reduced sulfur are less pronounced, suggesting that the fully reduced sulfur in as-prepared *Gd_2O_2S-Inert* was partially converted into oxidized sulfur upon exposure to air.

Since the XANES spectra were collected in fluorescence mode, they reflect both the surface and the core of the samples; sulfur oxides could in principle be either on the surface of the nanoparticles or inside the inorganic core. XRD patterns of both samples are, however, identical, which confirms the crystalline structure of Gd_2O_2S (see XRD pattern in the bottom panel of Figure S4 in the Supporting Information). TEM also confirmed that the size and shape of the nanoparticles are preserved (data not shown). Oxidation of sulfur due to exposure in air is then likely a surface phenomenon. In addition, Fourier transform infrared spectra exhibit specific peaks corresponding to sulfate functions (Figure S5 in the Supporting Information). To the best of our knowledge, this is the first observation of surface reactivity of Gd_2O_2S, which is usually considered a stable phase in air. *Ce_2O_2S-Inert* did not show any sign of surface oxidation, as expected from the care taken to avoid air exposure. Its spectrum features an additional contribution at low energy (2468 eV) whose origin is not known at this stage. The small feature at 2468 eV was found to be linked to the presence of cerium and is under investigation.

When the nanoparticles react with air (i.e., with water vapor and/or dioxygen), swift oxidation from Ce^{III} to Ce^{IV} may occur in addition to sulfur oxidation. XANES spectra were then taken at the Ce L_{III}-edge, using an environmental cell in flowing water. The sample was taken out of the glovebox and quickly placed in the cell. Prior to exposure to water, the spectrum presented the characteristic peak of Ce^{III} at 5719.2 eV and two small contributions characteristic of Ce^{IV} at around 5723 and 5729.5 eV (Figure 3, dark blue spectrum). Due to the brief exposure of the sample to air, the S K-edge spectra presented a small peak in the energy region corresponding to oxidized sulfur (inset of Figure 3, purple spectrum), but most of the sulfur was still reduced, as expected from the ex situ spectrum presented above. Following the introduction of water into the cell for a few minutes, the Ce L_{III}-edge spectrum exhibited a strong peak of Ce^{IV} and a small peak of Ce^{III} (Figure 3, light blue spectrum). The S K-edge spectrum also exhibits the characteristic features of more oxidized species: namely, an

DOI: 10.1021/acs.inorgchem.7b02336
Inorg. Chem. 2017, 56, 14227−14236

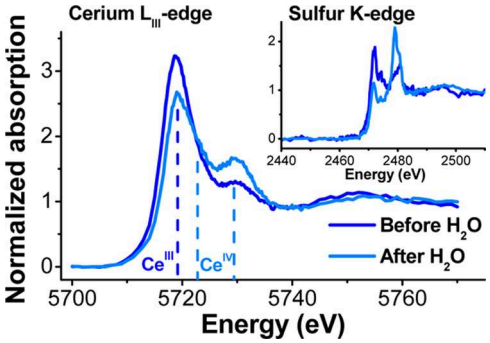

Figure 3. In situ cerium L_{III}-edge and sulfur K-edge XANES spectra of Ce_2O_2S nanoparticles before and after exposure to water. The positions of the peaks attributed to Ce^{III} and Ce^{IV} are consistent with previously published XANES Ce L_{III}-edge spectra.[45,46]

intense peak near 2480 eV and minor peaks in the 2470−2475 eV range (see Figure 3, light blue spectrum).

At this stage, we cannot come to a conclusion on the different roles of H_2O and of O_2 in the surface oxidation of Gd_2O_2S and in the oxidation of Ce_2O_2S in the core of the nanoparticles, because the water used in the cell contained dissolved O_2. Nevertheless, the in situ XANES experiment shows that oxidation is a swift process for the Ce_2O_2S nanoparticles and that both sulfur and cerium are affected.

We presume that the oxidation of sulfur and of cerium may be related to two distinct mechanisms: (i) cerium oxidation leads to the formation of a mixed-valence phase such as $Ce_2O_{2.5}S$; (ii) the oxidation of the sulfides leads to the formation of S^V and of S^{VI} species (e.g., sulfates). We argue that the first mechanism is specific to nanoparticles containing cerium, while the second mechanism should occur in any Ln_2O_2S phase, including Gd_2O_2S.

Experimentally, we have observed that *Ce_2O_2S-Inert* turns from dark brown to dark green after exposure to air. Dark green is the color of $Ce_2O_{2.5}S$, suggesting a fast oxidation of Ce^{III}. The color of the nanoparticles fades only after several days. Oxysulfate phases[47] were not detected by XRD during aging under air (Figure S2 in the Supporting Information). At this stage, in the case of Ce_2O_2S, it is unclear whether the oxidized sulfur species are solely at the surface of the nanoparticles or are present as amorphous phases. In any case, degradation eventually led to CeO_2 and amorphous species. These amorphous compounds may contain oxidized sulfur, as the XANES experiments (Figures 2 and 3) show the formation of S^V and S^{VI} species when the lanthanide oxysulfide nanoparticles are exposed to air and/or water.

In order to take advantage of the phase stability of Gd_2O_2S and of the potential reactivity of Ce_2O_2S, we attempted the synthesis of Gd-Ce bimetallic oxysulfide nanoparticles, described by the general formula $Gd_{2(1-y)}Ce_{2y}O_2S$ with y between 0 and 100%. Cerium loading is defined as $y = n_{Ce}/[n_{Ce} + n_{Gd}]$, where n is the number of moles. To the best of our knowledge, such bicationic nanoparticles of the Ln_2O_2S family without phase separation have never been reported.

A Bridge between Ce_2O_2S and Gd_2O_2S: $Gd_{2(1-y)}Ce_{2y}O_2S$ Nanoparticles. Different strategies may be used to obtain bimetallic nanoparticles. Most of the synthetic routes hitherto reported consist of the reaction between small amounts (usually ≤1%) of a dopant and the lanthanide.[12−21,23,25−29,48−54] This approach is justified by the very similar ionic radii of the lanthanides ranging from $r_{La(III)}$ = 1.03 Å to $r_{Lu(III)}$ = 0.86 Å, which favors the formation of a crystalline phase with randomly distributed ions.

Synthesis and Composition of the Compounds. Following the above considerations, in the present case we simply mixed the precursors of Gd and Ce in an appropriate stoichiometry, since the radii of Gd and Ce were close enough ($r_{Gd(III)}$ = 0.94 Å; $r_{Ce(III)}$ = 1.01 Å). This straightforward route enabled us to obtain bimetallic powders in a wide range of composition from y = 0% to y = 90%. In the nanoparticles, the Gd/Ce ratio measured by energy dispersive X-ray spectroscopy (EDS) was found to be consistent with the nominal composition (Figure S6 and Table S1 in the Supporting Information).

From y = 0% to y = 80%, the color of these nanoparticle samples does not change over time. For y = 90%, the powder was initially deep brown but became light brown within 2 weeks in air at room temperature, suggesting a decomposition of the structure.

Structural Analysis of Compounds Exposed to Air. XRD patterns of nanoparticles isolated in air were systematically obtained (Figure S4 in the Supporting Information). For 90% cerium, the pattern was not consistent with the reference pattern of Ln_2O_2S, in agreement with the observation mentioned above. The XRD pattern shows diffraction peaks of CeO_2 in addition to those of Ln_2O_2S, as observed for Ce_2O_2S nanoparticles (Figure S8 in the Supporting Information). Below 90%, the patterns were consistent with Ln_2O_2S but a small shift of the peaks is observed.

The lattice parameter $a = 2d_{(110)}$ was determined by fitting the position of the (110) and (111) diffraction peaks using pseudo-Voigt curves (Figure 4A). Two regimes are observed. From 0 to 40%, the lattice parameter follows Vegard's law expected using the lattice parameters of Gd_2O_2S and Ce_2O_2S (Figure 4B).[55,56] This indicates that both cerium and gadolinium ions partially occupy the same site in the unit

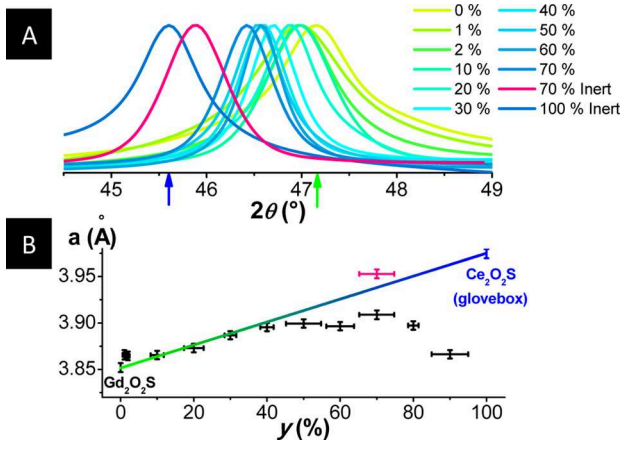

Figure 4. (A) X-ray diffraction normalized (110) peaks fitted using pseudo-Voigt functions for $Gd_{2(1-y)}Ce_{2y}O_2S$ nanoparticles isolated in air and under an inert atmosphere for two $Gd_{0.6}Ce_{1.4}O_2S$ and Ce_2O_2S samples (see Figure S9 in the Supporting Information). Vertical arrows indicate the (110) reflection position of Ce_2O_2S (blue, JCPDS 26-1085) and Gd_2O_2S (green, JCPDS 26-1422). (B) Lattice parameter a as a function of the cerium fraction y. The straight colored line is a linear fit to the data. The data concern bimetallic $Gd_{2(1-y)}Ce_{2y}O_2S$ nanoparticles isolated in air (black dots with error bars) or under an inert atmosphere (pink and blue dots with error bars). The lattice parameters of the samples kept under an inert atmosphere correspond to those expected by Vegard's law.

DOI: 10.1021/acs.inorgchem.7b02336
Inorg. Chem. 2017, 56, 14227−14236

cell. From $y > 40\%$ to $y = 80\%$ the lattice parameter a levels off. To explain this behavior, we envisage the following two scenarios: (i) 40% is the solubility limit of cerium or (ii) there is no solubility limit but the phase is not stable in air.

Structural Analysis of Compound with y = 70% under Inert Atmosphere. In order to clarify the above point, in a complementary experiment, the as-prepared $y = 70\%$ compound ($Gd_{0.6}Ce_{1.4}O_2S$) was isolated and washed under inert conditions. The value of the lattice parameter of this sample is larger than that of the sample isolated in air and nicely follows Vegard's law (Figure 4B, pink dot), which supports scenario ii.

It is interesting to analyze the compounds after air exposure. As discussed above and according to Table S1 in the Supporting Information, the EDS data show that the ratio of lanthanide present in the powder is equal to the nominal ratio. This fact, in addition to the leveling off of the a parameter for $y = 40\%$, suggests that secondary Ce-containing species are formed on the surface of the Ln_2O_2S bimetallic structure as a consequence of air exposure. In order to investigate this question, an additional TEM study was carried out.

Transmission Electron Microscopy on the y = 0, 37.5, 50, 75% Compounds. Similar to the case of the Gd_2O_2S and Ce_2O_2S nanoparticles, bimetallic Gd-Ce oxysulfide nanoparticles crystallize in the form of hexagonal nanoplates (Figure 5). Transmission electron microscopy images typically display

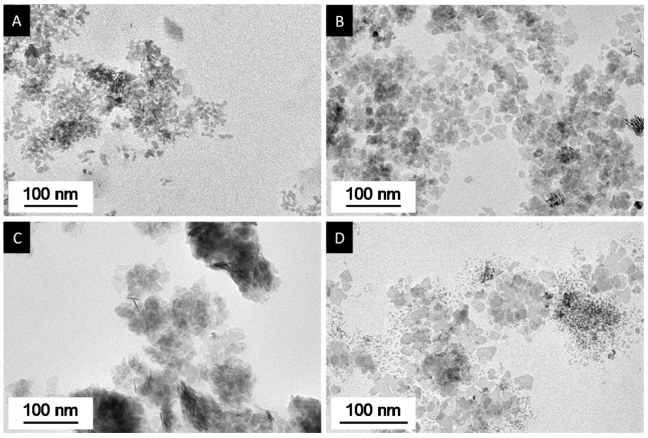

Figure 5. TEM micrographs of $Gd_{2(1-y)}Ce_{2y}O_2S$ nanoparticles containing the following cerium fractions: (A) $y = 0\%$; (B) $y = 37.5\%$; (C) $y = 50\%$; (D) $y = 75\%$.

the {001} or {100} facets of the nanoplates. Their width and thickness are 10−20 and 2 nm, respectively, somewhat larger than the $y = 0$ Gd_2O_2S nanoparticles (7.80 ± 1.28 nm in width and 1.52 ± 0.14 nm in thickness). The width of the nanoparticles is in agreement with Scherrer's crystalline domain size calculated from the (110) reflection peak (Table S2 in the Supporting Information). High-resolution transmission electron microscopy (HRTEM) confirmed that both Gd_2O_2S and bimetallic nanoparticles are single crystals of $Gd_{2(1-y)}Ce_{2y}O_2S$. An analysis of the Fourier transforms of the HRTEM images (Figure S10 in the Supporting Information) agrees with the crystal system and with the lattice parameters obtained by means of XRD.

For $y > 70\%$, we find some smaller and shapeless nanoparticles that may consist of cerium-containing species which nucleate in the solution during the synthesis or of degraded Gd-Ce oxysulfide nanoparticles exposed to air, as indicated by the smaller a lattice parameter, of these particles.

Altogether, the substitution of Gd by Ce in Gd_2O_2S slightly affects the oxysulfide nanoparticle morphology, and nanoplates of dimensions 30 nm or smaller are obtained. For $y < 80\%$, the reactivity of cerium in $Gd_{2(1-y)}Ce_{2y}O_2S$ is found to be lower than that in pure Ce_2O_2S nanoparticles, but it is still sufficient to destabilize the structure for $y > 40\%$.

Reactivity toward O_2 and H_2O: Comparison between Gd_2O_2S and $GdCeO_2S$. So far, we have discussed the effect of air as an oxidizing medium, without differentiating the roles of water and of dioxygen. In order to address this question, a near-ambient-pressure X-ray photoelectron spectroscopy (NAP-XPS) facility of the UPMC installed at the TEMPO beamline of SOLEIL was used as a surface analysis technique. We considered the following two scenarios for the oxidation of sulfur and of cerium: (i) the oxidation of both elements occurs independently; (ii) one of the two ions (Ce^{III} and S^{-II}) delays the oxidation of the other ion. In case i, sulfur in $GdCeO_2S$ and in Gd_2O_2S should oxidize at the same rate. In case ii, the sequential oxidation of cerium and of sulfur, or vice versa, should be observed by XPS. In order to verify these two scenarios, fresh Gd_2O_2S and $GdCeO_2S$ ($y = 50\%$) nanoparticles were synthesized, isolated in air, and drop-casted on gold-covered silicon wafers. Exposure to air was limited, and the samples were stored under an inert atmosphere and introduced in the setup via a glovebag connected to the load lock of the NAP-XPS.

The nanoparticles were analyzed at room temperature under vacuum, under water pressure and under a mixture of water and oxygen, and then back under vacuum. The two samples were deposited on a single sample holder and subsequently exposed to exactly the same atmospheres. Thoroughly degassed water vapor was introduced before introducing the O_2 gas, as the former gas is less oxidizing than the latter. O_2 was then introduced along with water, because obtaining ultrahigh-vacuum conditions after having introduced water would require baking the vacuum chamber for a long time, which is not compatible with the constraints set by synchrotron runs. For the same reason, the last measurements under vacuum conditions were actually carried out under a residual background pressure of water.

Binding energies (BEs) were calibrated using the Au 4f doublet, as described in Table S3 in the Supporting Information. S 2p and Gd 4d photoemission spectra were collected in a single sweep in the 135−175 eV region of BE (Figure 6). The Ce $3d_{3/2}$ and Ce $3d_{5/2}$ BEs were also monitored in the 870−920 eV region for the $GdCeO_2S$ nanoparticles (Figure 7A). As shown in Figure 7C, we successfully determined the Ce^{III} fraction by using a careful fitting procedure of the intensity which takes into account the overlap of the spin−orbit split peak (Figure 7B).

In all spectra, the sulfide species are identified by a S $2p_{3/2}$ doublet at 161.6 ± 0.3 eV (Figure 6A).[58] Oxidized sulfur is also always present and confirms the XANES result that samples whose workup was carried out in air are already partially oxidized. Here, oxidized sulfur is composed of two major oxidation species that we identify as S^{IV} and S^{VI}. Each S $2p_{3/2}$ spectrum was fitted by a double peak; the BE of the lower-energy component was 168.1 ± 0.7 eV for S^{IV} (in pink) and 171.3 ± 0.5 eV for S^{VI} (in purple). The relative area of each contribution allowed us to plot the ratios of the species for different atmospheres (Figure 6C). For both nanoparticle

DOI: 10.1021/acs.inorgchem.7b02336
Inorg. Chem. 2017, 56, 14227−14236

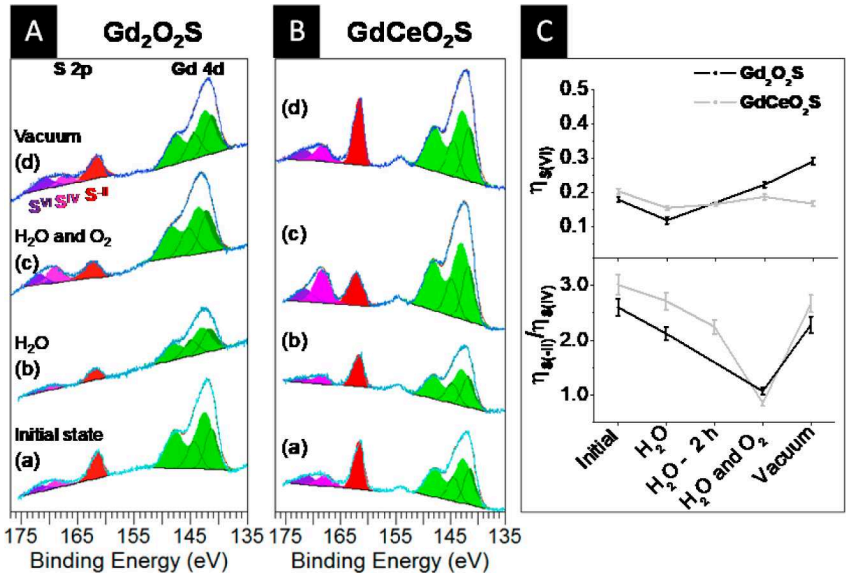

Figure 6. Room-temperature NAP-XPS spectra of air-exposed samples of (A) Gd_2O_2S and (B) $GdCeO_2S$ nanoparticles collected using an incident photon energy of 735 eV under the following conditions: (a) ultrahigh vacuum (10^{-9} mbar); (b) H_2O pressure of 0.2 mbar; (c) mixture of H_2O (0.2 mbar) and O_2 (0.2 mbar) partial pressures; (d) vacuum obtained upon pumping down the chamber after (c). For $GdCeO_2S$ (B), an additional spectrum was also collected after exposing the sample to water vapor for 2 h without beam to avoid radiation damage. Color code: S 2p doublet in red (S^{-II}), pink (S^{IV}) and purple (S^{VI}); Gd 4d doublets in light green and deep green (shake-down satellite peaks).[57] The fitting curves (in brown) are mostly superimposed with the experimental curves. (C) (top) S^{VI} fraction ($\eta_{S(VI)}$) and (bottom) S^{-II}/S^{IV} fraction ratio ($\eta_{S(-II)}/\eta_{S(IV)}$). See Table S3 in the Supporting Information for the details of the fitting procedure.

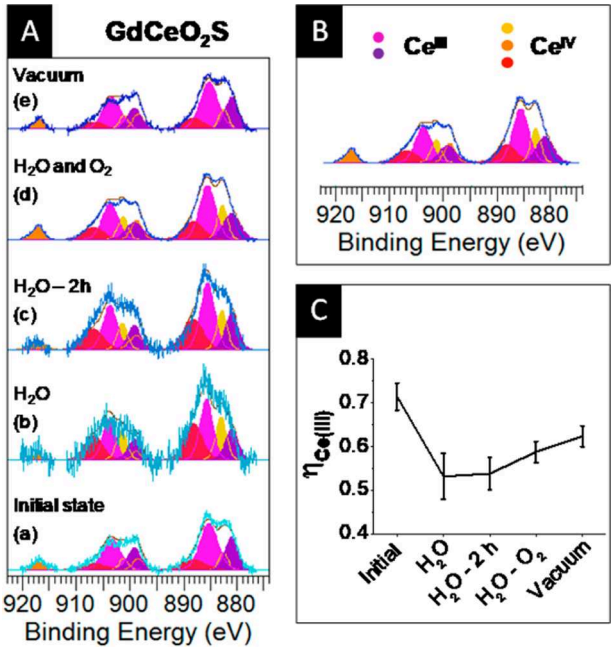

Figure 7. (A) Ce 3d NAP-XPS spectra of $GdCeO_2S$ nanoparticles measured with an incident photon energy of 1100 eV and after background subtraction: (a) ultrahigh vacuum (10^{-9} mbar); (b) H_2O partial pressure of 0.2 mbar; (c) after 2 h of exposure to a H_2O partial pressure of 0.2 mbar; (d) H_2O partial pressure of 0.2 mbar and O_2 partial pressure of 0.2 mbar; (e) back to vacuum. The Ce^{III} species are represented by pink and violet peaks. Yellow, orange, and red peaks are specific to Ce^{IV} species. (B) Typical deconvolution of the Ce^{III} and Ce^{IV} peaks. (C) Evolution of the fraction of Ce^{III} ($\eta_{Ce(III)}$) during the NAP-XPS experiment. See Table S3 in the Supporting Information for the details of the fitting procedure.

samples, the Gd spectrum showed no significant evolution, as expected. The exposure of both Gd_2O_2S and $GdCeO_2S$ samples to water vapor led to a partial S^{-II}–S^{IV} conversion within 2 h (Figure 6C); the S^{-II} species correspond to the oxysulfide, while S^{IV} is attributed to sulfite ions $(SO_3)^{2-}$ formed in a step during the sulfide to sulfate transformation.[59] The addition of O_2 in the chamber led to an increase in S^{IV} concentration within a few minutes, suggesting that O_2 is a stronger oxidizing agent in comparison to water.

The evolution of the S^{VI} fraction is more complex. Initially, the S^{VI} species are attributed to sulfates formed during the short exposure of the nanoparticles to air. For both samples, this fraction does not significantly decrease during subsequent treatments, suggesting that the S^{VI} formed in the room atmosphere prior to the XPS measurement is irreversible. In Gd_2O_2S, the quantity of S^{VI} species increases during the last steps of exposure to O_2 and of pumping. However, in $GdCeO_2S$, this quantity remains almost constant over the course of the further treatments (Figure 6C). It is possible that Ce^{III} was playing a sacrificial role, thus preventing sulfur from further oxidation (Figure 7).

During exposure to water vapor and then to O_2, sulfur oxidation is accompanied by an oxidation of Ce^{III} into Ce^{IV}, especially during the early stage of exposure to air (Figure 7C). However, this oxidation is limited and the Ce^{III}/Ce^{IV} ratio remains significant, consistent with the fact that the bulk crystal structure, which contains Ce^{III}, is preserved, as observed ex situ in the y = 50% samples.

Restoring the high-vacuum conditions almost restored the initial S^{-II} fraction and affected the Ce^{III} fraction. Flahaut et al. previously observed a similar reversibility by heating bulk Ce_2O_2S to 1300 °C under vacuum.[32] Ikeue et al. also reported that oxysulfate sheets can be reduced to oxysulfide sheets under an H_2 atmosphere.[47] Here, the process occurs at room temperature but the ultrahigh-vacuum conditions play a

DOI: 10.1021/acs.inorgchem.7b02336
Inorg. Chem. 2017, 56, 14227–14236

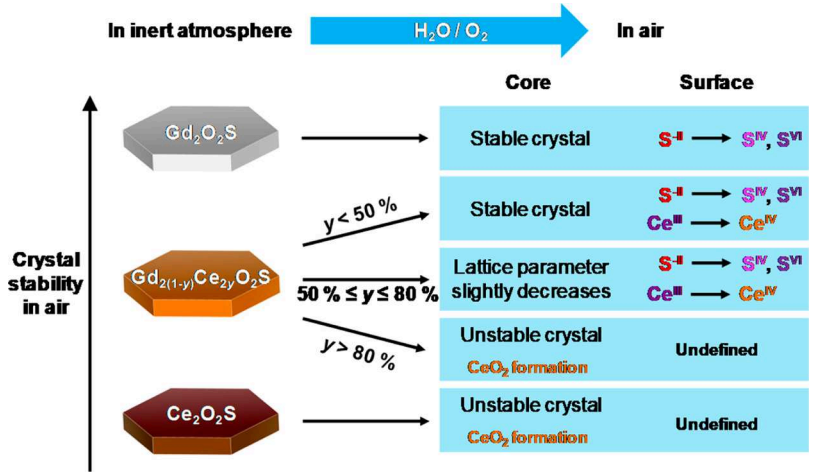

Figure 8. Reactivity of the $Gd_{2(1-y)}Ce_{2y}O_2S$ nanoparticles toward air.

reducing role; furthermore, the effect is enhanced in nanoparticles owing to the high surface/volume ratio. Having said this, the reversibility of the reduction under vacuum conditions is different from the oxysulfide/oxysulfate transition, since the XRD patterns of our samples did not show any structural modification even after several months. This further supports the argument that the oxido reduction process is favored at the surface of the nanoparticles.

CONCLUSION

In this article we showed that cerium oxysulfide Ce_2O_2S nanoparticles can be successfully prepared using colloidal synthesis and that these particles are chemically stable under an inert atmosphere. Their brown color is identical with that of previously reported bulk samples, and the present XANES study shows that they are free of oxidized sulfur species.

We investigated the surface reactivity of related Gd_2O_2S nanoparticles, whose metal cation cannot undergo redox reaction in air. We showed that the formation of oxidized sulfur in air is a swift process, in contrast to previous reports on the stability of these nanoparticles in air.

The synthesis of bimetallic $Gd_{2(1-y)}Ce_{2y}O_2S$ nanoparticles was achieved using the same colloidal route. For all y, we find a linear variation of the lattice parameter a with y according to Vegard's law, thus indicating that confirming the substitution of Gd by Ce in the same site. The exposure of the nanoparticles to air revealed three distinct regimes in terms of structure robustness: (i) for y = 0−0.4, no structural change was observed; (ii) for y = 0.5−0.8, the excess of cerium with respect to the threshold value of 0.4 is ejected from the nanoplates, forming small nanoparticles aside; (iii) for y > 0.9, the nanoparticle structure was not stable in air and evolved into CeO_2, as indicated by a in situ XANES study showing oxidation of Ce^{III} to Ce^{IV}.

A complementary NAP-XPS study provided deeper insights into the reactivity of the nanoparticles with air (Figure 8). We found that water vapor favored the formation of intermediate S^{IV} species, proposed to be sulfite anions and that this process is favored by the addition of O_2. In the case of Ce-containing nanoparticles, the process is accompanied by the partial oxidation of Ce^{III} to Ce^{IV}.

Altogether, the reactivity of cerium in lanthanide oxysulfide was found to be tempered by the presence of gadolinium in the same lattice. Optical and magnetic properties of this series of bimetallic nanoscaled oxysulfides will be described in a forthcoming article. Generally, the substitution strategy seems to be a promising way to reach new families of nanoscaled metal oxysulfides with tailored physical and chemical properties. The surface reactivity of these objects should be taken into account for applications that require long-term air stability (e.g., lighting), colloidal stability (e.g., inks), or controlled interaction with living organisms (e.g., MRI contrast agents).

EXPERIMENTAL SECTION

Synthesis of $Gd_{2(1-y)}Ce_{2y}O_2S$ Nanoparticles. Bimetallic oxysulfides were prepared via a solvothermal reaction including a mixture of organic solvents and metallic complexes. Oleylamine (OM; technical grade, 70%), oleic acid (OA; technical grade, 90%), sulfur (S_8; ≥99.5%), and sodium oleate (Na(oleate); ≥99%) were purchased from Sigma-Aldrich. 1-Octadecene (ODE; technical grade, 90%) was purchased from Acros Organics. Gadolinium acetylacetonate hydrate ($Gd(acac)_3{\cdot}xH_2O$; 99.9%) and cerium acetylacetonate hydrate ($Ce(acac)_3{\cdot}xH_2O$; 99.9%) were purchased from Strem Chemicals. All products were used as received without further purification.

In a typical synthesis of Ce_2O_2S, $Ce(acac)_3{\cdot}xH_2O$ (0.50 mmol), S_8 (0.032 mmol), Na(oleate) (0.50 mmol), OM (17 mmol), OA (2.5 mmol), and ODE (32.5 mmol) were placed in a 100 mL three-neck flask at room temperature. The brown solution was heated to 120 °C under vacuum for 20 min to remove water and other impurities with low boiling points. The mixture was then heated to 310 °C and stirred at this temperature for 30 min under purified N_2. Then it was left to cool under N_2 to room temperature and was directly transferred to an inert-atmosphere glovebox (H_2O, ≤0.5 ppm, O_2, ≤0.5 ppm). The crude product can be dispersed into anhydrous THF. After several centrifugations in anhydrous THF, a brown paste of Ce_2O_2S nanoparticles was obtained.

In a typical synthesis of $GdCeO_2S$, $Gd(acac)_3{\cdot}xH_2O$ (0.25 mmol), $Ce(acac)_3{\cdot}xH_2O$ (0.25 mmol), S_8 (0.032 mmol), Na(oleate) (0.50 mmol), OM (17 mmol), OA (2.5 mmol), and ODE (32.5 mmol) were placed in a 100 mL three-neck flask at room temperature. The brown solution was heated to 120 °C under vacuum for 20 min to remove water and other impurities with low boiling points. The mixture was then heated to 310 °C and stirred at this temperature for 30 min under purified N_2. The transparent solution gradually became turbid starting from 280 °C. Then the mixture was left to cool to room temperature under N_2. The nanoparticles were isolated using ethanol and washed at least three times using a THF/ethanol (1/5) mixture to remove the remaining reagents and organic matter. A 40−90 mg amount of dried $Gd_{2(1-y)}Ce_{2y}O_2S$ particles was thus obtained depending on the initial cerium loading.

It should be noted that a significant decrease in the reaction yield (measured after several washings of the nanoparticles in air) was

DOI: 10.1021/acs.inorgchem.7b02336
Inorg. Chem. 2017, 56, 14227−14236

observed along with the amount of cerium introduced in the nanoparticles: starting from 0.5 mmol of lanthanide precursor, a yield of around 100% vs Gd (95 mg of powder) was obtained for y = 0% (Gd_2O_2S), while a yield of 48% (45 mg) was obtained for y = 70% ($Gd_{0.6}Ce_{1.4}O_2S$).

X-ray Powder Diffraction. The different X-ray diffraction patterns of dry powders were measured on a Bruker D8 diffractometer using Cu Kα radiation at 1.5406 Å. Typical diffractograms were collected with steps of 0.05° and a scanning speed of 5 s/point. The backgrounds of the patterns were subtracted using the EVA software. When low-noise Si monocrystal sample holders were used, the angular position 2θ was corrected by adjusting the sample height (correction around 0.5−1 mm, see Figure S7 in the Supporting Information).

Transmission Electron Microscopy and High-Resolution TEM. A drop of a diluted solution of $Gd_{2(1-y)}Ce_{2y}O_2S$ dispersed in pure THF was allowed to dry on an amorphous carbon coated copper grid. TEM images were collected with a TWIN 120 (TECNAI SPIRIT) instrument at 120 kV and with a JEOL 100CF apparatus. HRTEM was performed on a FEG-TEM JEOL 2100F instrument at 200 kV. For Ce_2O_2S, a drop of a diluted dispersion of the crude nanoparticles in THF was deposited on a copper grid inside the glovebox. The grid was stored under argon and swiftly inserted into the transmission electron microscope.

Energy Dispersive X-ray Spectroscopy. A small amount of powder was deposited on carbon adhesive tape on a scanning electron microscope sample holder. EDX analyses were performed on a SEM HITACHI S-3400N instrument at 10 kV. Titanium was chosen as the reference, and analyses were performed on at least three different zones on the sample.

Near-Ambient-Pressure X-ray Photoelectron Spectroscopy. X-ray photoelectron spectroscopy was performed on the TEMPO B beamline at SOLEIL on the NAP-XPS setup of UPMC. Samples were deposited from a 30 mg·mL^{-1} solution of dispersed nanoparticles in pure THF onto gold-coated (100 nm layer) silica wafers by dip-coating. Spectra were measured under vacuum (10^{-9} mbar), under 0.2 mbar H_2O pressure, or under 0.4 mbar H_2O and O_2 pressure (0.2 mbar each). In order to mitigate beam damage, measurements were performed on several spots on the sample surface.

X-ray Absorption Near-Edge Spectroscopy. Sulfur K-edge and cerium L-edge XANES data were collected on the LUCIA beamline at SOLEIL at an electron energy of 2.7 GeV and an average ring current of 450 mA. The incoming photons were selected with a Si (111) double-crystal monochromator. A 2−3 mg portion of the sample was diluted in ca. 40 mg of graphite and was compressed to form a 6 mm diameter pellet. Up to seven pellets were fixed with carbon adhesive tape on a copper plate placed in a sample holder inside the measurement chamber. During typical analyses, the pressure in the chamber was maintained around 10^{-2} mbar. Measurements were performed in fluorescence mode using a Bruker silicon drift detector, with an outgoing photon angle of 10°. All data were normalized to the edge jump and calibrated to the maximum of the first peak of sodium thiosulfate (2470.8 eV).

Fourier Transform Infrared Spectroscopy. Infrared spectra were collected on a Spectrum 400 (PERKINELMER) spectrometer. The dry sample (1−3 mg) was deposited on an attenuated total reflectance (ATR) crystal. Transmittance was measured between 4000 and 550 cm^{-1} with steps of 0.5 cm^{-1}.

■ ASSOCIATED CONTENT

Supporting Information

The Supporting Information is available free of charge on the ACS Publications website at DOI: 10.1021/acs.inorgchem.7b02336.

Additional figures and tables as described in the text (PDF)

■ AUTHOR INFORMATION

Corresponding Author

*E-mail for S.C.: sophie.carenco@upmc.fr.

ORCID

Benedikt Lassalle-Kaiser: 0000-0003-2141-2496

Sophie Carenco: 0000-0002-6164-2053

Notes

The authors declare no competing financial interest.

■ ACKNOWLEDGMENTS

This work was supported by French state funds managed by the ANR within the Investissements d'Avenir programme under reference ANR-11-IDEX-0004-02, and more specifically within the framework of the Cluster of Excellence MATISSE led by Sorbonne Universités. UPMC, CNRS, and the Collège de France are acknowledged for financial support. We acknowledge the SOLEIL synchrotron for beamtime allocation on the LUCIA and TEMPO beamlines. We thank Patricia Beaunier and Dario Taverna for their help with TEM and HRTEM measurements. We thank Victor Pinty, from the design office of SOLEIL, for the conception of the environmental cell used on LUCIA beamline.

■ REFERENCES

(1) Boyd, D. A. Sulfur and Its Role In Modern Materials Science. *Angew. Chem., Int. Ed.* **2016**, *55*, 15486.

(2) Zachariasen, W. H. Crystal Chemical Studies of the 5f-Series of Elements. VII. The Crystal Structure of Ce2O2S, La2O2S and Pu2O2S. *Acta Crystallogr.* **1949**, *2* (1), 60−62.

(3) Vovan, T.; Dugué, J.; Guittard, M. Oxysulfures Mixtes de Chrome III et de Terres Rares. *Mater. Res. Bull.* **1978**, *13*, 1163−1166.

(4) Dugué, J.; Vovan, T.; Villers, J. Etude Structurale Des Oxysulfures de Chrome(Ill) et de Terres Rares. I. Structure de l'Oxysulfure LaCrOS 2. *Acta Crystallogr., Sect. B: Struct. Crystallogr. Cryst. Chem.* **1980**, *36*, 1291−1294.

(5) Dugué, J.; Vovan, T.; Villers, J. Etude Structurale Des Oxysulfures de Chrome(III) et de Terres Rares. II. Structure de l'Oxysulfure CeCrOS2. *Acta Crystallogr., Sect. B: Struct. Crystallogr. Cryst. Chem.* **1980**, *36*, 1294−1297.

(6) Kabbour, H.; Cario, L.; Moëlo, Y.; Meerschaut, A. Synthesis, X-Ray and Optical Characterizations of Two New Oxysulfides: LaInS2O and La5In3S9O3. *J. Solid State Chem.* **2004**, *177* (4−5), 1053−1059.

(7) Quezel, G.; Ballestracci, R.; Rossat-Mignod, J. Proprietes Magnetiques Des Oxysulfures de Terres Rares. *J. Phys. Chem. Solids* **1970**, *31* (4), 669−684.

(8) He, W.; Osmulski, M. E.; Lin, J.; Koktysh, D. S.; McBride, J. R.; Park, J.-H.; Dickerson, J. H. Remarkable Optical and Magnetic Properties of Ultra-Thin Europium Oxysulfide Nanorods. *J. Mater. Chem.* **2012**, *22* (33), 16728.

(9) Biondo, V.; Sarvezuk, P. W. C.; Ivashita, F. F.; Silva, K. L.; Paesano, A.; Isnard, O. Geometric Magnetic Frustration in RE2O2S Oxysulfides (RE = Sm, Eu and Gd). *Mater. Res. Bull.* **2014**, *54*, 41−47.

(10) Zhao, F.; Yuan, M.; Zhang, W.; Gao, S. Monodisperse Lanthanide Oxysulfide Nanocrystals. *J. Am. Chem. Soc.* **2006**, *128* (36), 11758−11759.

(11) Gai, S.; Li, C.; Yang, P.; Lin, J. Recent Progress in Rare Earth Micro/Nanocrystals: Soft Chemical Synthesis, Luminescent Properties, and Biomedical Applications. *Chem. Rev.* **2014**, *114* (4), 2343−2389.

(12) Huang, Y.-Z.; Chen, L.; Wu, L.-M. Crystalline Nanowires of Ln2O2S, Ln2O2S2, LnS2 (Ln) La, Nd), and La2O2S:Eu3+. Conversions via the Boron-Sulfur Method That Preserve Shape. *Cryst. Growth Des.* **2008**, *8* (2), 739−743.

(13) Liu, Z.; Sun, X.; Xu, S.; Lian, J.; Li, X.; Xiu, Z.; Li, Q.; Huo, D.; Li, J. G. Tb3+- and Eu3+-Doped Lanthanum Oxysulfide Nanocrystals.

DOI: 10.1021/acs.inorgchem.7b02336
Inorg. Chem. 2017, 56, 14227−14236

Gelatin-Templated Synthesis and Luminescence Properties? *J. Phys. Chem. C* **2008**, *112* (7), 2353−2358.
(14) Ding, Y.; Gu, J.; Ke, J.; Zhang, Y. W.; Yan, C. H. Sodium Doping Controlled Synthesis of Monodisperse Lanthanide Oxysulfide Ultrathin Nanoplates Guided by Density Functional Calculations. *Angew. Chem., Int. Ed.* **2011**, *50* (51), 12330−12334.
(15) Hakmeh, N.; Chlique, C.; Merdrignac-Conanec, O.; Fan, B.; Cheviré, F.; Zhang, X.; Fan, X.; Qiao, X. Combustion Synthesis and up-Conversion Luminescence of La2O2S:Er3+,Yb3+ Nanophosphors. *J. Solid State Chem.* **2015**, *226*, 255−261.
(16) Song, Y.; You, H.; Huang, Y.; Yang, M.; Zheng, Y.; Zhang, L.; Guo, N. Highly Uniform and Monodisperse Gd 2 O 2 S:Ln 3+ (Ln = Eu, Tb) Submicrospheres: Solvothermal Synthesis and Luminescence Properties. *Inorg. Chem.* **2010**, *49* (24), 11499−11504.
(17) Thirumalai, J.; Chandramohan, R.; Vijayan, T. a. Synthesis, Characterization and Formation Mechanism of Monodispersed Gd2O2S:Eu3+ Nanocrystals. *J. Mater. Sci.: Mater. Electron.* **2011**, *22* (8), 936−943.
(18) Osseni, S. A.; Lechevallier, S.; Verelst, M.; Dujardin, C.; Dexpert-Ghys, J.; Neumeyer, D.; Leclercq, M.; Baaziz, H.; Cussac, D.; Santran, V.; Mauricot, R. New Nanoplatform Based on Gd2O2S:Eu3+ Core: Synthesis, Characterization and Use for in Vitro Bio-Labelling. *J. Mater. Chem.* **2011**, *21* (45), 18365.
(19) Liu, J.; Luo, H.; Liu, P.; Han, L.; Zheng, X.; Xu, B.; Yu, X. One-Pot Solvothermal Synthesis of Uniform Layer-by-Layer Self-Assembled Ultrathin Hexagonal Gd2O2S Nanoplates and Luminescent Properties from Single Doped Eu3+ and Codoped Er3+, Yb3+. *Dalt. Trans.* **2012**, *41* (45), 13984.
(20) Hernández-Adame, L.; Méndez-Blas, A.; Ruiz-García, J.; Vega-Acosta, J. R.; Medellín-Rodríguez, F. J.; Palestino, G. Synthesis, Characterization, and Photoluminescence Properties of Gd:Tb Oxysulfide Colloidal Particles. *Chem. Eng. J.* **2014**, *258* (6), 136−145.
(21) Lei, L.; Zhang, S.; Xia, H.; Tian, Y.; Zhang, J.; Xu, S. Controlled Synthesis of Lanthanide-Doped Gd 2 O 2 S Nanocrystals with Novel Excitation-Dependent Multicolor Emissions. *Nanoscale* **2017**, *9* (17), 5718−5724.
(22) Hirai, T.; Orikoshi, T. Preparation of Yttrium Oxysulfide Phosphor Nanoparticles with Infrared-to-Green and -Blue Upconversion Emission Using an Emulsion Liquid Membrane System. *J. Colloid Interface Sci.* **2004**, *273* (2), 470−477.
(23) Xing, M.; Cao, W.; Pang, T.; Ling, X. Synthesis of Monodisperse Spherical Y2O2S:Yb,Ho Upconversion Nanoparticles. *Solid State Commun.* **2009**, *149* (23−24), 911−914.
(24) Li, W.; Liu, Y.; Ai, P. Synthesis and Luminescence Properties of Red Long-Lasting Phosphor Y2O2S:Eu3+, Mg2+, Ti4+ Nanoparticles. *Mater. Chem. Phys.* **2010**, *119* (1−2), 52−56.
(25) Fu, Y.; Cao, W.; Peng, Y.; Luo, X.; Xing, M. The Upconversion Luminescence Properties of the Yb3+−Ho3+ System in Nanocrystalline Y2O2S. *J. Mater. Sci.* **2010**, *45* (23), 6556−6561.
(26) Wang, H.; Xing, M.; Luo, X.; Zhou, X.; Fu, Y.; Jiang, T.; Peng, Y.; Ma, Y.; Duan, X. Upconversion Emission Colour Modulation of Y2O2S: Yb, Er under 1.55μm and 980nm Excitation. *J. Alloys Compd.* **2014**, *587*, 344−348.
(27) Han, L.; Hu, Y.; Pan, M.; Xie, Y.; Liu, Y.; Li, D.; Dong, X. A New Tactic to Achieve Y 2 O 2 S:Yb 3+ /Er 3+ up-Conversion Luminescent Hollow Nanofibers. *CrystEngComm* **2015**, *17* (12), 2529−2535.
(28) Lu, X.; Yang, M.; Yang, L.; Ma, Q.; Dong, X.; Tian, J. Y2O2S:Yb3+, Er3+ Nanofibers: Novel Fabrication Technique, Structure and up-Conversion Luminescent Characteristics. *J. Mater. Sci.: Mater. Electron.* **2015**, *26* (6), 4078−4084.
(29) Bakhtiari, H.; Ghasemi, M. R.; Hashemizadeh Aghda, A.; Noorkojouri, H.; Sarabadani, P.; Zeeb, M. Effect of Europium Dopant Concentration on Particle Size and Luminescence of Yttrium Oxysulfide Nanoparticles Prepared by Urea Homogenous Precipitation. *J. Cluster Sci.* **2015**, *26* (5), 1671−1681.
(30) Gu, J.; Ding, Y.; Ke, J.; Zhang, Y.; Yan, C. Controllable Synthesis of Monodispersed Middle and Heavy Rare Earth Oxysulfide Nanoplates Based on the Principles of HSAB Theory. *Huaxue Xuebao* **2013**, *71* (3), 360.
(31) Pasberg, N.; den Engelsen, D.; Fern, G. R.; Harris, P. G.; Ireland, T. G.; Silver, J. Structure and Luminescence Analyses of Simultaneously Synthesised (Lu 1-x Gd X) 2 O 2 S:Tb 3+ and (Lu 1-x Gd X) 2 O 3:Tb 3+. *Dalt. Trans.* **2017**, *46*, 7693.
(32) Flahaut, J.; Guittard, M.; Patrie, M. Les Oxysulfures Me2O2S Des Éléments Du Groupe Des Terres Rares. *Bull. Soc. Chim. Fr.* **1958**, *7*, 990−994.
(33) Sourisseau, C.; Cavagnat, R.; Mauricot, R.; Boucher, F.; Evain, M. Structure and Bondings in Cerium Oxysulfide Compounds I - Electronic, Infrared and Resonance Raman Spectra of Ce2.0O2.5S. *J. Raman Spectrosc.* **1997**, *28* (12), 965−971.
(34) Sourisseau, C.; Fouassier, M.; Mauricot, R.; Boucher, F.; Evain, M. Structure and Bonding in Cerium Oxysulfide Compounds. II—Comparative Lattice Dynamics Calculations on Ce2O2S and Ce2.0O2.5S. *J. Raman Spectrosc.* **1997**, *28* (12), 973−978.
(35) Dugué, J.; Carré, D.; Guittard, M. Etude Structurale Des Oxysulfures de Cérium(III) et Cérium(IV). I. Structure Cristalline de l'Oxysulfure de Cérium Ce4O4S3. *Acta Crystallogr., Sect. B: Struct. Crystallogr. Cryst. Chem.* **1978**, *34*, 3564−3568.
(36) Dugué, J.; Carré, D.; Guittard, M. Etude Structurale Des Oxysulfures de Cérium(III) et Cérium(IV). II. Structure Cristalline de l'Oxysulfure de Cérium Ce6O6S4. *Acta Crystallogr., Sect. B: Struct. Crystallogr. Cryst. Chem.* **1979**, *35*, 1550−1554.
(37) Cheng, J.; Zhu, J.; Wei, X.; Shen, P. K. Ce 2 O 2 S Anchored on Graphitized Carbon with Tunable Architectures as a New Promising Anode for Li-Ion Batteries. *J. Mater. Chem. A* **2015**, *3* (18), 10026−10030.
(38) Yang, L.; Cai, Z.; Hao, L.; Xing, Z.; Dai, Y.; Xu, X.; Pan, S.; Duan, Y.; Zou, J. Nano Ce 2 O 2 S with Highly Enriched Oxygen-Deficient Ce 3+ Sites Supported by N and S Dual-Doped Carbon as an Active Oxygen-Supply Catalyst for the Oxygen Reduction Reaction. *ACS Appl. Mater. Interfaces* **2017**, *9* (27), 22518−22529.
(39) Frank, P.; Hedman, B.; Carlson, R. M. K.; Tyson, T. A.; Roe, A. L.; Hodgson, K. A Large Reservoir of Sulfate and Sulfonate Resides within Plasma Cells from. *Biochemistry* **1987**, *26*, 4975−4979.
(40) Vairavamurthy, A.; Manowitz, B.; Luther, G. W.; Jeon, Y. Oxidation State of Sulfur in Thiosulfate and Implications for Anaerobic Energy Metabolism. *Geochim. Cosmochim. Acta* **1993**, *57* (7), 1619−1623.
(41) Prietzel, J.; Thieme, J.; Tyufekchieva, N.; Paterson, D.; Mcnulty, I.; Kögel-knabner, I. Sulfur Speciation in Well-Aerated and Wetland Soils in a Forested Catchment Assessed by Sulfur K -Edge X-Ray Absorption near-Edge Spectroscopy (XANES). *J. Plant Nutr. Soil Sci.* **2009**, *172*, 393−409.
(42) Morgan, B.; Burton, E. D.; Rate, A. W. Iron Monosulfide Enrichment and the Presence of Organosulfur in Eutrophic Estuarine Sediments. *Chem. Geol.* **2012**, *296−297*, 119−130.
(43) Rodriguez, J. A.; Chaturvedi, S.; Hanson, J. C.; Brito, J. L. Reaction of H2 and H2S with CoMoO4 and NiMoO4: TPR, XANES, Time-Resolved XRD, and Molecular-Orbital Studies. *J. Phys. Chem. B* **1999**, *103*, 770−781.
(44) Rodriguez, J. A.; Jirsak, T.; Freitag, A.; Hanson, J. C.; Larese, J. Z.; Chaturvedi, S. Interaction of SO2 with CeO2 and Cu/CeO2 Catalysts: Photoemission, XANES and TPD Studies. *Catal. Lett.* **1999**, *62* (2), 113−119.
(45) Cui, D.; Zhang, P.; Ma, Y.; He, X.; Li, Y.; Zhang, J.; Zhao, Y.; Zhang, Z. Effect of Cerium Oxide Nanoparticles on Asparagus Lettuce Cultured in an Agar Medium. *Environ. Sci.: Nano* **2014**, *1* (5), 459−465.
(46) Gregson, M.; Lu, E.; Tuna, F.; McInnes, E. J. L.; Hennig, C.; Scheinost, A. C.; McMaster, J.; Lewis, W.; Blake, A. J.; Kerridge, A.; Liddle, S. T. Emergence of Comparable Covalency in Isostructural Cerium(iv)− and Uranium(iv)−carbon Multiple Bonds. *Chem. Sci.* **2016**, *7* (5), 3286−3297.
(47) Ikeue, K.; Kawano, T.; Eto, M.; Zhang, D.; Machida, M. X-Ray Structural Study on the Different Redox Behavior of La and Pr Oxysulfates/oxysulfides. *J. Alloys Compd.* **2008**, *451* (1−2), 338−340.

DOI: 10.1021/acs.inorgchem.7b02336
Inorg. Chem. 2017, 56, 14227−14236

(48) Jiang, G.; Wei, X.; Zhou, S.; Chen, Y.; Duan, C.; Yin, M. Neodymium Doped Lanthanum Oxysulfide as Optical Temperature Sensors. *J. Lumin.* **2014**, *152*, 156−159.
(49) Jiang, G.; Wei, X.; Chen, Y.; Duan, C.; Yin, M.; Yang, B.; Cao, W. Luminescent La2O2S:Eu3+ Nanoparticles as Non-Contact Optical Temperature Sensor in Physiological Temperature Range. *Mater. Lett.* **2015**, *143*, 98−100.
(50) Bagheri, A.; Rezaee Ebrahim Saraee, K.; Shakur, H. R.; Zamani Zeinali, H. Synthesis and Characterization of Physical Properties of Gd2O2S:Pr3+ Semi-Nanoflower Phosphor. *Appl. Phys. A: Mater. Sci. Process.* **2016**, *122* (5), 1−8.
(51) Zhao, Q.; Zheng, Y.; Guo, N.; Jia, Y.; Qiao, H.; Lv, W.; You, H. 3D-Hierarchical Lu2O2S:Eu3+ Micro/nano-Structures: Controlled Synthesis and Luminescence Properties. *CrystEngComm* **2012**, *14* (20), 6659.
(52) Wang, G.; Zou, H.; Zhang, B.; Sun, Y.; Huo, Q.; Xu, X.; Zhou, B. Preparation and Luminescent Properties of 1D Lu2O2S:Eu3+ Nanorods. *Opt. Mater. (Amsterdam, Neth.)* **2015**, *45*, 131−135.
(53) Rosticher, C.; Viana, B.; Fortin, M.-A.; Lagueux, J.; Faucher, L.; Chanéac, C. Gadolinium Oxysulfide Nanoprobes with Both Persistent Luminescent and Magnetic Properties for Multimodal Imaging. *RSC Adv.* **2016**, *6* (60), 55472−55478.
(54) Cichos, J.; Karbowiak, M.; Hreniak, D.; Stręk, W. Synthesis and Characterization of Monodisperse Eu3+ Doped Gadolinium Oxysulfide Nanocrystals. *J. Rare Earths* **2016**, *34* (8), 850−856.
(55) Vegard, L. Die Konstitution Der Mischkristalle Und Die Raumfüllung Der Atome. *Eur. Phys. J. A* **1921**, *5* (1), 17−26.
(56) Denton, A. R.; Ashcroft, N. W. Vegard's Law. *Phys. Rev. A: At., Mol., Opt. Phys.* **1991**, *43* (6), 3161−3164.
(57) Uwamino, Y.; Ishizuka, T.; Yamatera, H. X-Ray Photoelectron Spectroscopy of Rare-Earth Compounds. *J. Electron Spectrosc. Relat. Phenom.* **1984**, *34* (1), 67−78.
(58) Smart, R. S. C.; Skinner, W. M.; Gerson, A. R. XPS of Sulphide Mineral Surfaces: Metal-Deficient, Polysulphides, Defects and Elemental Sulphur. *Surf. Interface Anal.* **1999**, *28* (1), 101−105.
(59) Manocha, A. S.; Park, R. L. Flotation Related ESCA Studies on PbS Surfaces. *Appl. Surf. Sci.* **1977**, *1* (1), 129−141.

DOI: 10.1021/acs.inorgchem.7b02336
Inorg. Chem. 2017, 56, 14227−14236

Appendix IV

Thermal Stability of Oleate-Stabilized Gd_2O_2S Nanoplates in Inert and Oxidizing Atmospheres

ACES Asian Chemical Editorial Society

DOI: 10.1002/cnma.201800578

CHEMNANOMAT
Full Paper

Thermal Stability of Oleate-Stabilized Gd_2O_2S Nanoplates in Inert and Oxidizing Atmospheres

Clément Larquet,[a, b] Djamila Hourlier,[c] Anh-Minh Nguyen,[a] Almudena Torres-Pardo,[d] Andrea Gauzzi,[b] Clément Sanchez,[a] and Sophie Carenco*[a]

Abstract: Capping ligands play an important role in the chemistry of nanoparticles synthesized with organic surfactants. This is relevant to a number of device applications where heating may cause major modifications of crystalline nanoparticles including amorphization, surface rearrangements or sintering. Ultrathin monodisperse $Ln_2O_2S_x$ oxysulfide nanoparticles (Ln = lanthanide) obtained in a mixture of oleylamine, oleic acid and 1-octadecene show promising luminescence and light absorption properties. In view of applications, one open question concerns the thermal behavior and the role of the ligands on the thermal reactivity of the nanoparticles. In this report, we show that the thermal stability of $Gd_2O_2S_x$ nanocrystals is limited because of their non-stoichiometric composition and strongly depends on the annealing atmosphere. The sintering temperature of the nanoparticles is lower in air than in inert atmosphere because of a rapid degradation of the ligands. Annealing the nanoparticles in air enables removing the ligands without altering the nanocrystals structure. The decomposition of the $Gd_2O_2S_x$ nanocrystals in inert atmosphere exhibits a complex multi-step behavior that was precisely modeled. This work gives a comprehensive description of the stability conditions of lanthanide oxysulfide nanoparticles. It establishes the conditions for their practical use and opens the way to major improvements of the surface activity of Ln_2O_2S nanoparticles and related nanocrystals.

1. Introduction

Owing to their tunable optical emission and absorption properties, lanthanide oxysulfides Ln_2O_2S (Ln = lanthanide and yttrium) have found applications in various devices such as phosphors for cathode ray tubes,[1–4] scintillators,[5–7] and lasers (emission [8–10] and absorption[11,12]). Following the first studies carried out in the 60's on the synthesis, morphology and doping of bulk samples, these compounds have been recently obtained also in the form of nanoparticles by means of various synthesis routes. This progress has renewed the hype for lanthanide oxysulfides, because these nanoparticles are promising for bimodal imaging (magnetic and optical), a key technology in nanomedicine.[13]

Ln_2O_2S nanoparticles are synthesized either in an aqueous or organic medium, which requires two different sulfidation methods. In water, sulfidation is performed in a subsequent step by heating the precursors at high temperature (T > 600 °C) using either sulfur vapor,[14–16] CS_2 formed *in situ* (S_8 in carbon) [17,18] or H_2S.[19] In organic medium, sulfidation is achieved at milder temperatures and in a single step. For instance, in a mixture of oleylamine, oleic acid and 1-octadecene, $Ln(acac)_3$ reacts with elemental sulfur at 310 °C in inert atmosphere. Oleylamine helps dissolving the elemental sulfur and forming reactive sulfide species.[20] With the help of an alkaline source, Ln_2O_2S nanoplates surrounded by organic ligands are obtained.[21–24]

One open question concerns the thermal stability of nanoscaled Ln_2O_2S, a factor that may limit the practical use of these nanomaterials. For instance, the absorption of light (X-rays in scintillators, visible light for laser absorption) is often accompanied by strong local heating. Owing to the high-temperature sulfidation process, the nanoparticles obtained in aqueous medium are typically larger than 50 nm and their crystal structure is similar to that of the bulk phase.[25–27] This accounts for a high thermal stability up to 1200 °C observed for most lanthanides (cerium excluded).[28]

On the other hand, the small Ln_2O_2S nanocrystals (below 30 nm) obtained in organic media differ markedly from bulk crystals. Typical feature are the non-stoichiometry,[29] the presence of alkyl-chains at the surface[21] and the capability of self-assembling into wires.[30] For example, gadolinium oxysulfide easily form small non-stoichiometric $Gd_2O_2S_x$ nanoplates (8 nm × 1.5 nm) with $x = 0.4–0.6$, which self-assemble in solution into nanowires.[21,22]

In this report, we studied the thermal stability of gadolinium oxysulfide nanoparticles covered with organic ligands in inert and oxidizing atmospheres. In inert atmosphere, we discovered a multi-step behavior with temperature that leads to the phase

[a] Dr. C. Larquet, Mr. A.-M. Nguyen, Prof. C. Sanchez, Dr. S. Carenco
Sorbonne Université, CNRS UMR 7574, Collège de France, Laboratoire de Chimie de la Matière Condensée de Paris (LCMCP), 4 place Jussieu, 75005 Paris, France
E-mail: sophie.carenco@sorbonne-universite.fr

[b] Dr. C. Larquet, Prof. A. Gauzzi
Institut de Minéralogie de Physique des Matériaux et de Cosmochimie (IMPMC), Sorbonne Université, CNRS UMR 7590, IRD UMR 206, MNHN, 4 place Jussieu 75252 Paris Cedex 05, France

[c] Dr. D. Hourlier
Institut d'Electronique, de Microélectronique et de Nanotechnologie (IEMN), UMR 8520, Avenue Henri Poincaré, BP 60069, F-59652 Villeneuve d'Ascq Cedex, France

[d] Dr. A. Torres-Pardo
Departamento de Química Inorgánica, Facultad de químicas, Universidad Complutense, 28040-Madrid, Spain

Supporting information for this article is available on the WWW under https://doi.org/10.1002/cnma.201800578

segregation of bulk oxysulfide Gd_2O_2S and Gd_2O_3. This is explained by the non-stoichiometry ($x \neq 1$) of the $Gd_2O_2S_x$ nanocrystals. Thanks to Fourier transform infrared spectroscopy (FTIR) and thermogravimetric analysis coupled with mass spectrometry (TGA-MS), we were able to determine the nature of the ligands, their amount on the surfaces of the nanocrystals and their coordination modes on the surface gadolinium atoms.

Under oxidizing atmosphere, a few steps of transformation lead to the formation of both bulk gadolinium oxide and gadolinium oxysulfate. Moreover, we could isolate ligand-free nanoparticles by controlling the thermal decomposition of the ligands in oxidizing atmosphere. This process removes the highly hydrophobic character of the nanocrystals, and makes them suitable for practical use, eg. in water or biological media.

2. Results and Discussion

Gd_2O_2S Nanoparticles Synthesis and Structure

Gd_2O_2S nanoparticles were synthesized following an optimized protocol described in the experimental section and previously reported by our group.[22] Briefly, $Gd(acac)_3{\cdot}xH_2O$ (0.5 mmol) was mixed with elemental sulfur (0.5 equiv. S *vs.* Gd), Na(oleate) (1 equiv. *vs.* Gd) in a mixture of oleylamine, oleic acid and 1-octadecene. The reaction was conducted at 310 °C for 30 minutes and yielded the nanoparticles presented in Figure S1.

The Gd_2O_2S nanoparticles crystallize in the *P-3 m1* hexagonal space group. The anisotropic growth leads to the formation of hexagonal-shaped platelets of 7.8 ± 1.3 nm width and 1.5 ± 0.2 nm thickness, i.e. two to three unit cells thick. The S:Gd ratio is ca 0.25, hence much lower than that in the bulk phase, as reported by Ding *et al.*[21] and by our group[22]. This result is explained by the presence of organic ligands at the surface that stabilize $[Gd_2O_2]^{2+}$ terminal layers on the {001} facets of the lamellar compounds. The sample composition is thus better described by the formula $Gd_2O_2S_{0.5}$. For the sake of clarity and consistency with previous published works (by us and others), we will keep below the notation Gd_2O_2S that best represent the crystal structure.

Thermal Stability of Gd_2O_2S Nanoplates in Inert Atmosphere

The thermal stability of the Gd_2O_2S nanoplates was analyzed by thermogravimetric analysis (TGA) coupled with mass spectrometry in inert atmosphere (He). The results of the TGA in inert atmosphere are presented in Figure 1.

Thermal decomposition of Gd_2O_2S nanoparticles is a complex process that can be divided into at least six steps, as shown in Figure 1B. The total mass loss between 25 °C and 1200 °C is 33.4%. One third of the sample was lost in the form of volatile species during the heating. The mass spectrometer installed in-line with the TG oven allowed us to precisely identify the various gas species emitted during each step (Figure 2).

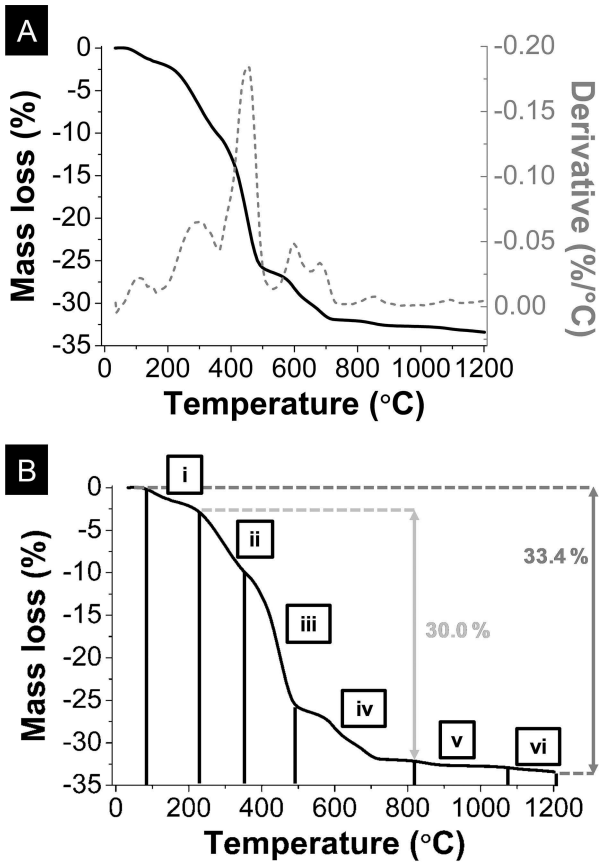

Figure 1. (A) Thermogravimetric analysis of Gd_2O_2S nanoplates performed in inert atmosphere at 2 °C/min and its temperature derivative. The curve is divided into six steps each corresponding to a partial mass loss (B).

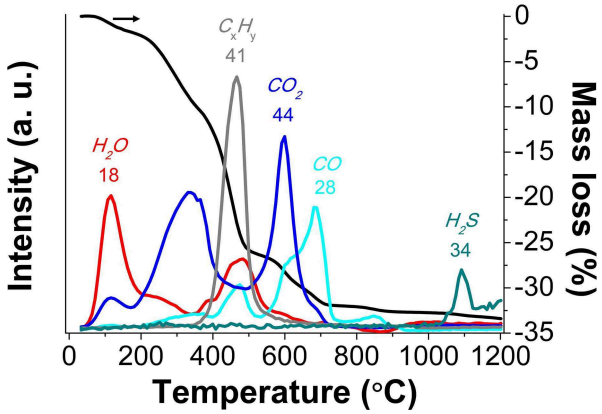

Figure 2. Thermal evolution of the major fragments detected in the gas phase by mass spectrometry: H_2O (*m/z* 18), CO (*m/z* 28), H_2S (*m/z* 34), C_3H_5 (*m/z* 41) and CO_2 (*m/z* 44).

Remarkably, the chemical processes are well separated. For the sake of clarity, only major volatile products detected are shown in Figure 2.

(i) From 40 to 210 °C: **H_2O** (*m/z* 18, 17, 16) + CO_2 (*m/z* 44, 28, 16, 12)

(ii) From 210 to 360 °C: **CO_2** (*m/z* 44, 28, 16, 12)

(iii) From 360 to 490 °C: hydrocarbon species C_xH_y (from alkyl chains of ligands) + CO_2 + CO (*m/z* 28, 16, 12) + H_2O

(iv) From 560 to 710 °C: 2 substeps: **CO_2** + CO first, then only **CO**

(v) From 780 to 900 °C: **CO**

(vi) From 1020 to 1120 °C: **H_2S** mainly (*m/z* 34, 33), and traces of H_2O

The loss of water and CO_2 around 100 °C is attributed to physisorbed molecules. The detection of these species is expected, considering that the condensation of acetylacetonate ligands on oleylamine during the synthesis generates H_2O *in situ* and considering that the samples were isolated and washed in ambient air (Figure 1B step (i)).[31]

In step (ii), the decarboxylation of oleate molecules starts and CO_2 is formed. The sole release of CO_2 must involve oleate groups in which the terminal functionality –(COO–) is rather labile and able to decarboxylate. A number of COO groups are likely farther away from the Gd sites and thus decarboxylated at this step (free oleic acid and weakly bonded oleate), while others oleate molecules remain strongly bonded to the surface of the nanoparticles. Because no C_xH_y are detected at this step, we propose that the alkyl chains of the oleate molecules decarboxylated in step (ii) remain bonded to the oleate groups that are still coordinated to the surface gadolinium. The long alkyl chains may be bonded either by weak interactions between the hydrophobic chains or covalently by reaction *via* the C=C double bonds.

In step (iii), a major decomposition of organic-based ligands occurs, resulting in the detection of numerous fractions related to long alkyl chains. Evidence for this is the release of a set of fragments at *m/z* 41, 55, 43, 69, 81 shown in Figure 3, resulting from the cleavage of the oleate ligands followed by hydrogen radical recombination. The main ion at *m/z* 30 characteristic of oleylamine is absent of the mass spectrum, which indicates that there is no significant amount of oleylamine *vs.* oleates on the surface of the nanoparticles.[32]

It is well known that the decomposition of organic ligands provides not only volatile molecules, but also a carbonized solid residue called free carbon. It results from cracking of the organic chains and recombination of radicals. This degradation step causes the most important mass loss in step (iii), along with the loss of CO_2, CO and H_2O. The decarboxylation goes on and the released CO_2 can react with the free carbon to yield CO according to the Boudouard reaction: $CO_2 + C = 2\ CO$. CO and H_2O can also form by decarbonylation of carboxylate moieties during the ligand decomposition.

There are two crucial points here. First, during steps (ii) and (iii), ligands undergo important modifications: the charge balance can still be ensured by the remaining carboxylates groups. In the meantime, the surface becomes more accessible and thus sintering becomes easier (Figure 4).

Second, as the crystals grow and sinter, the lack of sulfur in the powder makes the formation of larger crystals of stoichiometric Gd_2O_2S impossible. The formation of large crystals of non-stoichiometric $Gd_2O_2S_{\sim 0.5}$ is prohibited as charge balance would not be respected in this case (there are no more ligands to compensate the charge). We could also imagine that the free carbon at the surface of the crystals could limit the sintering process. However, we observe at high temperatures (> 900 °C) the coexistence of large crystals of Gd_2O_2S with allotropes of Gd_2O_3 on the XRD patterns of the annealed powders (Figure S2).

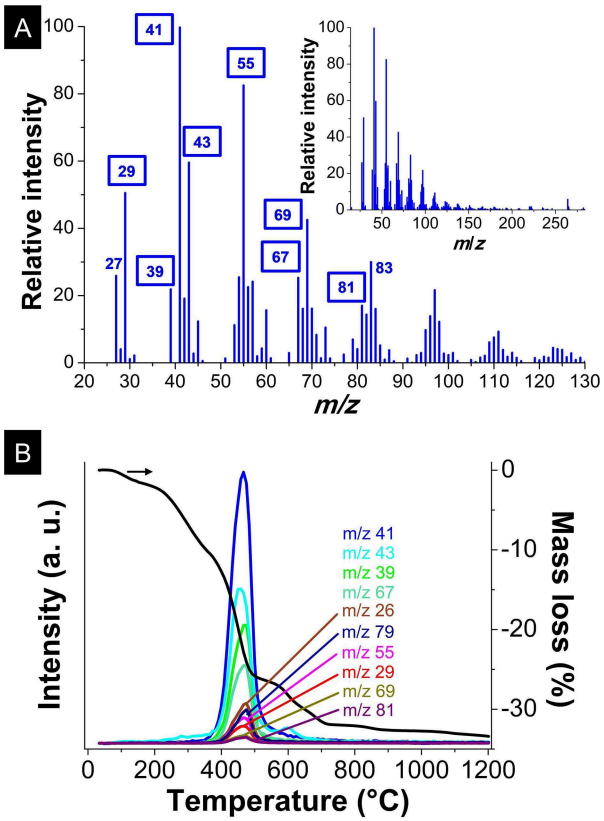

Figure 3. (A) Oleic acid mass spectrum with *m/z* between 20 and 130, from the NIST database.[33] The inset displays the total spectrum. (B) Thermogramm of Gd_2O_2S nanoplates and detected fractions of hydrocarbon species of ligands. Framed numbers in (A) correspond to fractions detected in (B).

Step (iv) can be divided in two sub-steps regarding the evolution of the fragments corresponding to CO_2 and CO (Figure 2). Carbon dioxide comes from the end of the decarboxylation process. Carbon monoxide is likely the product of the reaction between the free carbon (formed by the decomposition of the ligands carbon chains in step (iii)) and CO_2 according to the Boudouard reaction. The equilibrium favors the formation of CO at high temperatures, which could explain that CO becomes the major product in (iv)-*b* (Figure 2B).

At the same time, oxygen from the ligands necessarily feeds the surface of the nanoparticles to maintain charge balance. The carboxylate groups coordinated on the surface form C–O–Gd bonds. Upon heating, a number of the C–O bonds break, leaving excess oxygen on the surface (Figure 4). $[Gd_2O_2]^{2+}$ terminal layers become $[Gd_2O_{2.5}]^{+}$ (red layers in Figure 4) while the ligands decompose. The average formula for the resulting nanoplate turns from $[Gd_2O_2S_{0.67}]^{0.67+}$ to neutral $Gd_2O_{2.33}S_{0.67}$. In parallel, the phase separation and growth lead to large crystals of Gd_2O_2S and Gd_2O_3.

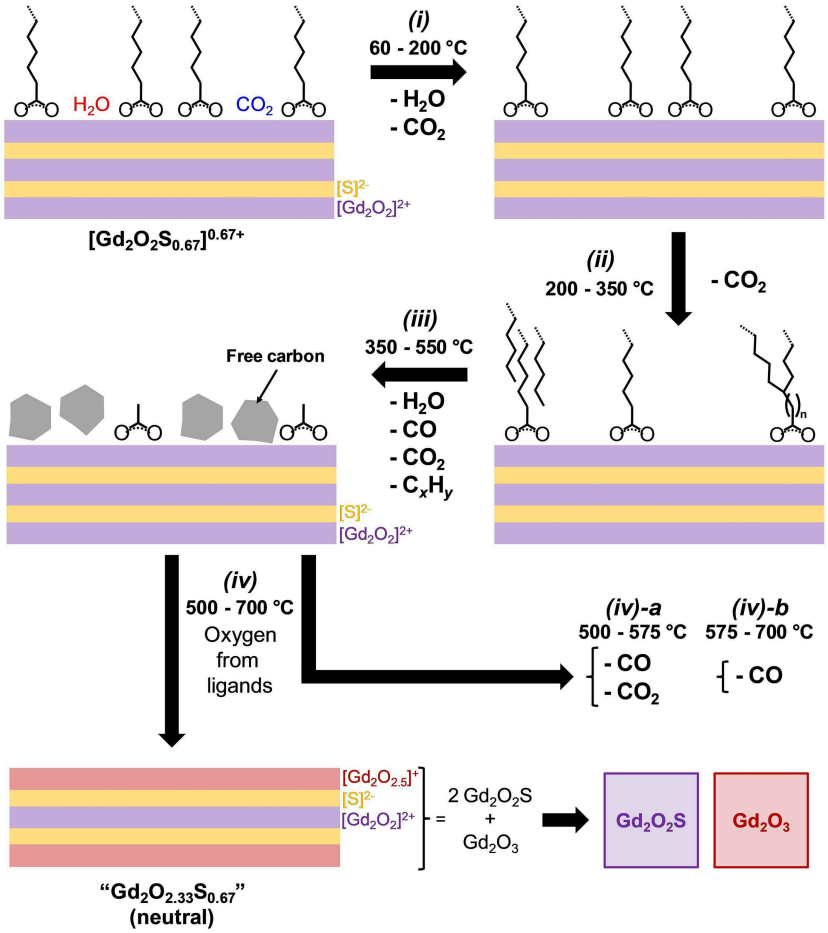

Figure 4. Proposed mechanism of the thermal decomposition during the annealing of Gd_2O_2S nanoplates (steps (i) to (iv)).

Step (v), from 780 to 900 °C, represents a limited mass loss due to CO release. CO was possibly formed at the previous step but adsorbed on Lewis acid sites. Step (vi) corresponds to a loss of a small quantity of H_2S coming from a limited degradation of the oxysulfide phase. The TG analysis and the structural investigations by XRD (Figure S2) indicate that the heat treatment up to 1200 °C did not significantly affect the species present in the crucible (Gd_2O_2S, Gd_2O_3-c and Gd_2O_3-m) between the end of step (v) and that of step (vi).

Ligand Nature, Amount and Coordination

The previous section showed that oleates are the most significant ligands (if not the only ones) around the nanoparticles. Their amount was estimated to be around 30 wt% of the powder of Gd_2O_2S nanoplates. Infrared spectroscopy was then employed to determine the chemical bonds present in the nanopowders. A representative IR spectrum of Gd_2O_2S nanoplates is displayed in Figure 5. The main absorption bands are due to the oleate ligands: 2959 cm^{-1} (CH_3 asymmetric elongation); 2923 cm^{-1} (CH_2 asymmetric elongation); 2853 cm^{-1} (CH_2

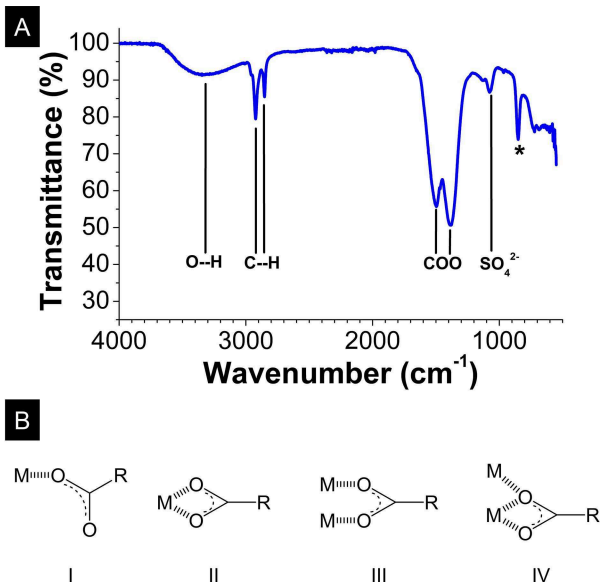

Figure 5. (A) FTIR spectrum of Gd_2O_2S nanoplates collected in ATR mode. The peak at 850 cm^{-1} is under investigation. (B) Four coordination modes between a carboxylate ligand and a metal as references by Deacon and Phillips: monodentate (I), chelating (II), bridging bidentate (III) and monoatomic bridging (IV).[34] Geometric derivatives mixing different bonding types also exist and are not presented.

symmetric elongation); 1497 cm^{-1} (COO asymmetric stretching); 1385 cm^{-1} (COO symmetric stretching).

The frequency difference between the asymmetric and symmetric stretching bands of the COO group is indicative of the bonding type of the carboxylate ligand. In particular, Deacon and Phillips[34] indexed more than eighty acetate or trifluoroacetate compounds whose crystalline structures and infrared spectra were available, according to the acetate coordination type: unidentate ligand, chelating ligand, bridging bidentate ligand and monoatomic bridging ligand (Figure 5B).

For the nanoparticles studied here (Figure 5A), the difference between the two stretching modes of COO group is $\Delta\nu =$ 112 cm^{-1} ($\nu_{asym} = 1497$ cm^{-1} and $\nu_{sym} = 1385$ cm^{-1}). In comparison, the values measured on sodium oleate are $\Delta\nu = 100$, 118 and 139 cm^{-1} (separation of the symmetric band in three contributions, see Figure S3). The low value of $\Delta\nu$ (< 150 cm^{-1}), close to the value of the corresponding sodium carboxylate, is typical of chelating or bridging carboxylate ligands, and rules out the monodentate ligand configuration (Figure 5B, coordination mode I). Moreover, in comparison with the numerous structures presented by Deacon and Philips, this value is one of the lowest, and suggests that chelation is favored in our case (Figure 5B, coordination mode II).

On the basis of thermogravimetric analysis, the calculated amount of ligands is around 30 wt% of the Gd_2O_2S nanoparticles powder. It is thus possible to estimate the ratio between the quantity of oxygen coming from the oleate ligands and the exposed gadolinium of our nanoplates, considering the nanoplate geometry (Figure S1).

We based this estimation on the average mass of powder obtained per synthesis: 100 mg fractioned between 3 mg of lightly adsorbed products (including water, step (i) in Figure 2), 30 mg of oleate ligands and 67 mg of $Gd_2O_2S_x$ nanocrystals. Because only 40% of the gadolinium of the nanoplates is exposed to the surface (both {100} and {001} facets), we calculated that each gadolinium atom monopolized 1.43 oxygen atoms from the oleate ligands (Figure S4). For such a value, a mix between chelation (two oxygen atoms per metallic cation) and bridging (one O per M) can be envisaged. This result is in agreement with the structures of lanthanide carboxylates (from samarium to lutetium[35] and yttrium[36]) for which the IR signals evidenced a ratio of 2 chelating ligands for 1 bridging ligand (total: 1.6 O/Ln).

However, with this ligand quantity, the charge compensation is not reached. If we assume the $Gd_2O_2S_{0.5}$ formula for the nanoparticles (+ 1 total charge), they should be surrounded by 1 equiv. of oleate ligands (−1 charge per molecule) to achieve the charge balance. Here, approximately 0.72 oleate ligand per Gd_2O_2S surrounds the nanocrystals, which is not enough. Nevertheless, one should remember that the oleate ligands are mainly bonded to gadolinium atoms by chelation. It means that there is not much remaining space for an additional ligand to bond a metal. Actually, the number of oleate ions represents a spatial occupation of 4.5 ligands/nm^2, which is already a high value for such ligands (values in the literature are closer to 0.2 nm^2 for each $-COO^-$ group).[37,38] Accordingly, Anderson *et al.* reminded that the steric hindrance between the alkyl chains of the oleate will limit the coverage to the density of crystalline alkyl chains (4.9 chains/nm^2).[39,40]

In this first part, we described the thermal behavior of the nanoparticles annealed under inert atmosphere. This allowed us to identify the nature and to estimate the number of organic ligands surrounding the nanoparticles. However, technological use of such nanoparticles will likely include heating devices under ambient atmosphere. To model these conditions, we performed a second analysis in flowing gas containing a mixture of helium and O_2.

Thermal Behavior Under Oxidizing Atmosphere and Ligand Removal

The thermal behavior of Gd_2O_2S nanoplates was investigated under oxidizing atmospheres with an air-like mixture (O_2/He with 20/80 *v/v*) and at intermediate reaction temperatures, in order to identify the nature of the solid formed at the most relevant steps.

Under O_2/He (20/80 *v/v*), the final mass loss is lower than in inert atmosphere (Figure 6). This is due to the formation of gadolinium oxysulfate $Gd_2O_2SO_4$, detected by XRD (Figure 7). These compounds are known to form from oxysulfides in oxidizing medium (the reverse reaction is possible using H_2) and were shown to be promising for thermally activated oxygen storage.[41]

It is worth noting that the thermal decomposition in oxygen observed in the TGA curve (Figure 6) occurs in three steps. The first mass loss between 40 °C and 200 °C is quite similar to that obtained in inert atmosphere, and corresponds to the loss of physisorbed species H_2O and CO_2. The major mass loss of 25% occurs in the second step between 250 °C and 400 °C. The last step above 500 °C implies a moderate loss of the sample mass (4%).

In order to identify the intermediate compounds, we performed two additional experiments for which we stopped the heating ramp at selected temperatures: 350 °C (within step (ii) in Figure 6A) and 517 °C (after the end of step (ii)). The temperature was kept constant for twenty minutes before cooling down and collecting the powder. When heated around 350 °C for 20 minutes, although the ligands have undergone considerable changes, the resulting product still corresponds to Gd_2O_2S nanocrystals (Figure 7B), as attested by the broadness of the XRD peaks which is similar to these of the starting material. TEM confirmed this by showing the presence of small polycrystalline aggregates as well as nanoparticles still isolated in the sample (see Figure S6). Infrared spectroscopy after this 20 min plateau confirms that the alkyl chains are not detected anymore (Figure S3).

In comparison, the same thermal treatment at 517 °C led to nanoscaled powders majorly consisting of gadolinium oxide. For higher temperatures, XRD indicates that the oxysulfide phase completely disappears as a result of the oxidizing treatment. It may form first an amorphous intermediate, while part of the product crystallizes into cubic gadolinium oxide

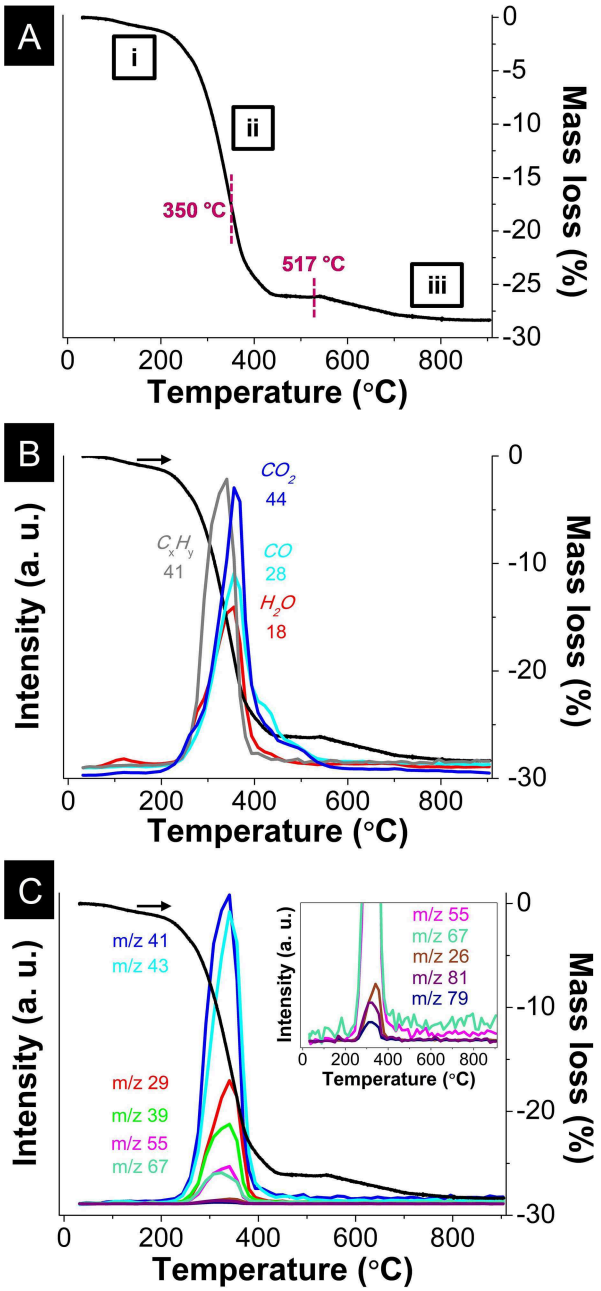

Figure 6. Thermal behavior of Gd_2O_2S nanoplates under oxidizing atmosphere. Evolution of the mass (A) and fragments from mass spectrometry: (B) H_2O (*m/z* 18), CO (*m/z* 28), C_3H_5 (*m/z* 41), CO_2 (*m/z* 44) and (C) various C_xH_y species.

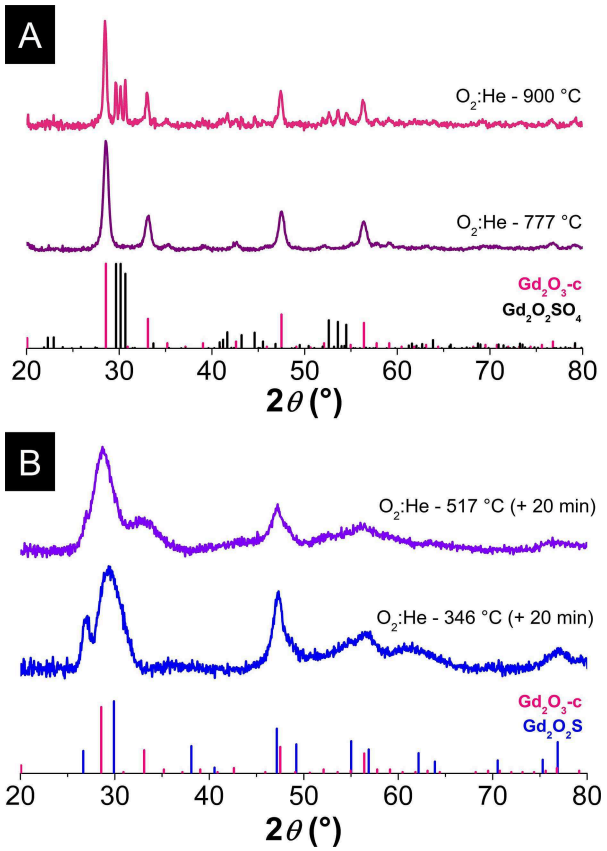

Figure 7. Powder XRD patterns of annealed Gd_2O_2S nanoplates under O_2:He (20/80 *v/v*), (A) at 900 °C (pink) and 777 °C (purple), (B) 517 °C (violet) and 346 °C (blue). In (A) the heating was stopped once the target temperature was reached. In (B), the target temperature was maintained for 20 min before cooling down. XRD pattern references are JCPDS files 26-1422 (Gd_2O_2S, blue), 12-0797 (Gd_2O_3-cubic, pink) and 77-9842 ($Gd_2O_2SO_4$, black).

(Gd_2O_3-cubic). Then the amorphous part crystallizes into gadolinium oxysulfate (Figure 7A).

In this section, we demonstrated that the inorganic crystal of Gd_2O_2S is stable up to around 350 °C under oxidizing atmosphere. The nanoscale of the particles is also preserved at this temperature. It is thus possible to remove the surface ligand at this temperature without degrading the inorganic core of the nanoparticles.

Conclusion

Several analytical techniques w employed to monitor the thermal treatments of Gd_2O_2S nanoplates stabilized by organic ligands. Our results demonstrate that the thermal stability critically depends upon the surrounding atmosphere. In inert atmosphere, the degradation of the nanoplates follows a multi-step process associated with a variety of mechanisms (dehydration, decarboxylation, ligand degradation, decarbonation/decarboxylation and sintering) that lead to distinct mass losses. In oxidizing atmosphere, the various reactions occur simultaneously at lower temperatures. The sulfur-defective structure of the nanocrystals triggers off the formation of gadolinium oxide crystals as well as oxysulfide or oxysulfate species depending on the atmosphere.

This study offers a description of the surface species present on the nanocrystals. Our analysis rules out the possibility of a significant amount of amide ligands derived from oleylamine chains and shows that only oleate groups cover the nanoparticle surface. The oleate groups are coordinated to gadolinium surface atoms in both chelation and bridging modes.We also demonstrated that the hydrophobic oleate chains are

readily removed by a mild treatment at 350 °C in oxygen, which does not alter the nanoplate features. This smooth process may be useful in view of the practical applications of these nanomaterials as thin films for lightening devices or for the post-functionalization with hydrophilic ligands for biomedical applications.

Experimental section

Synthesis of Gd_2O_2S Nanoparticles

Gadolinium oxysulfide nanoparticles were prepared under inert atmosphere in a mixture of organic solvents following a previous report.[22] Oleylamine (OM; technical grade, 70%), oleic acid (OA; technical grade, 90%), sulfur (S_8; $\geq$99.5%) and sodium oleate (Na (oleate); $\geq$99%) were purchased from Sigma-Aldrich. 1-Octadecene (ODE; technical grade, 90%) was purchased from Acros Organics. Gadolinium acetylacetonate hydrate ($Gd(acac)_3{\cdot}xH_2O$; 99.9%) was purchased from Strem Chemicals. All products were used as received without further purification.

In a typical synthesis of Gd_2O_2S, $Gd(acac)_3{\cdot}xH_2O$ (0.50 mmol), S_8 (0.032 mmol), Na(oleate) (0.50 mmol), OM (17 mmol), OA (2.5 mmol) and ODE (32.5 mmol) were placed in a 100 mL three-neck flask at room temperature. The yellow solution was heated to 120 °C under vacuum for 20 min to remove water and other impurities with low boiling points. The mixture was then heated to 310 °C and stirred at this temperature for 30 min under purified N_2. The transparent solution gradually became turbid starting from 280 °C. Then the mixture was left to cool to room temperature under N_2. The nanoparticles were isolated by centrifugation using ethanol and washed at least three times using a THF/ethanol (1/5) mixture to remove the remaining reagents and organic matter.

Thermogravimetric Analysis Coupled with Mass Spectrometry (TGA-MS)

Thermogravimetry analysis (TGA) (Netzsch STA449F3 Jupiter apparatus) coupled with a quadrupole mass spectrometry (MS) (Aëolos QMS403D, 70 eV, electron ionisation) *via* a heated capillary system was used to monitor the decomposition of samples during the annealing process and to analyze the evolved gaseous species. Before each experiment, the TGA system was first evacuated and then flushed with the same ultrahigh purity gas which was used for the thermal treatment. The experiments were carried out under dynamic inert or reactive gas: He (99.999% purity) or 20% O_2 in He (99.999% purity) at a flow rate of 50 cm^3/min. The samples were heated in Al_2O_3 crucibles up to 900 °C or 1200 °C with a heating rate of 2 °C/min.

X-ray Powder Diffraction (XRD)

The X-ray diffraction patterns of dry powders were measured on a Bruker D8 diffractometer using Cu Kα radiation at 1.5406 Å. Diffractograms were collected with steps of 0.05° and a scanning speed of 5 s/point. The backgrounds of the patterns were subtracted using the EVA software.

Fourier Transform Infrared Spectroscopy (FTIR)

Infrared spectra were collected on a Spectrum 400 (PERKINELMER) spectrometer. The dry sample (1 to 3 mg) was deposited on the attenuated total reflectance (ATR) crystal. Transmittance was measured between 4000 cm^{-1} and 550 cm^{-1} with steps of 0.5 cm^{-1}.

Acknowledgements

This work was supported by French state funds managed by the ANR within the Investissements d'Avenir programme under reference ANR-11-IDEX-0004-02, and more specifically within the framework of the Cluster of Excellence MATISSE led by Sorbonne Université. Sorbonne Université, CNRS, and the Collège de France are acknowledged for financial support. We acknowledge the National Center for Electron Microscopy (UCM) for assistance with the generation of electron microscopy data.

Conflict of Interest

The authors declare no conflict of interest.

Keywords: Gadolinium oxysulfide nanoparticles · organic ligands · structural stability · thermogravimetric analysis · mass spectrometry.

[1] M. R. Royce, *U.S. Patent N°3418246*, **1968**.
[2] T. Jüstel, H. Nikol, C. Ronda, *Angew. Chem. Int. Ed.* **1998**, *37*, 3084–3103; *Angew. Chem.* **1998**, *110*, 3250–3271.
[3] C. . Ronda, T. Jüstel, H. Nikol, *J. Alloys Compd.* **1998**, *275–277*, 669–676.
[4] A. V. Strel'tsov, V. P. Dmitrienko, A. O. Dmitrienko, Y. V. Gulyaev, N. I. Sinitsyn, G. V. Torgashov, *J. Commun. Technol. Electron.* **2009**, *54*, 487–492.
[5] L. H. Brixner, *Mater. Chem. Phys.* **1987**, *16*, 253–281.
[6] W. Rossner, B. C. Grabmaier, *J. Lumin.* **1991**, *48–49*, 29–36.
[7] C. M. Michail, G. P. Fountos, P. F. Liaparinos, N. E. Kalyvas, I. Valais, I. S. Kandarakis, G. S. Panayiotakis, *Med. Phys.* **2010**, *37*, 3694–3703.
[8] R. V. Alves, R. A. Buchanan, K. A. Wickersheim, E. A. C. Yates, *J. Appl. Phys.* **1971**, *42*, 3043–3048.
[9] V. M. Markushev, N. É. Ter-Gabriélyan, C. M. Briskina, V. R. Belan, V. F. Zolin, *Sov. J. Quantum Electron.* **1990**, *20*, 773–777.
[10] I. Iparraguirre, J. Azkargorta, O. Merdrignac-Conanec, M. Al-Saleh, C. Chlique, X. Zhang, R. Balda, J. Fernández, *Opt. Express* **2012**, *20*, 23690.
[11] K. Zhu, W. Ding, W. Sun, P. Han, L. Wang, Q. Zhang, *J. Mater. Sci. Mater. Electron.* **2016**, *27*, 2379–2384.
[12] W. Sun, K. Zhu, H. Xu, X. Yang, M. Yu, X. Li, L. Wang, Q. Zhang, *J. Mater. Sci. Mater. Electron.* **2017**, *28*, 697–701.
[13] C. Larquet, Y. Klein, D. Hrabovsky, A. Gauzzi, C. Sanchez, S. Carenco, *Eur. J. Inorg. Chem.* **2019**, DOI 10.1002/ejic.201801466.
[14] L. Hernández-Adame, A. Méndez-Blas, J. Ruiz-García, J. R. Vega-Acosta, F. J. Medellín-Rodríguez, G. Palestino, *Chem. Eng. J.* **2014**, *258*, 136–145.
[15] Y. Tian, F. Lu, M. Xing, J. Ran, Y. Fu, Y. Peng, X. Luo, *Opt. Mater. (Amst).* **2017**, *64*, 58–63.
[16] A. Bagheri, K. Rezaee Ebrahim Saraee, H. R. Shakur, H. Zamani Zeinali, *Appl. Phys. A Mater. Sci. Process.* **2016**, *122*, 1–8.
[17] J. Thirumalai, R. Chandramohan, R. Divakar, E. Mohandas, M. Sekar, P. Parameswaran, *Nanotechnology* **2008**, *19*, 395703.
[18] W. Li, Y. Liu, P. Ai, X. Chen, *J. Rare Earths* **2009**, *27*, 895–899.
[19] S. A. Osseni, S. Lechevallier, M. Verelst, C. Dujardin, J. Dexpert-Ghys, D. Neumeyer, M. Leclercq, H. Baaziz, D. Cussac, V. Santran, *J. Mater. Chem.* **2011**, *21*, 18365.
[20] J. W. Thomson, K. Nagashima, P. M. Macdonald, G. A. Ozin, *J. Am. Chem. Soc.* **2011**, *133*, 5036–41.
[21] Y. Ding, J. Gu, J. Ke, Y.-W. Zhang, C.-H. Yan, *Angew. Chem. Int. Ed.* **2011**, *50*, 12330–12334; *Angew. Chem.* **2011**, *123*, 12538–12542.

[22] C. Larquet, A.-M. Nguyen, M. Ávila-Gutiérrez, L. Tinat, B. Lassalle-Kaiser, J.-J. Gallet, F. Bournel, A. Gauzzi, C. Sanchez, S. Carenco, *Inorg. Chem.* **2017**, *56*, 14227–14236.
[23] L. Lei, S. Zhang, H. Xia, Y. Tian, J. Zhang, S. Xu, *Nanoscale* **2017**, *9*, 5718–5724.
[24] T. Zhang, J. Gu, Y. Ding, Y.-W. Zhang, C.-H. Yan, *ChemPlusChem* **2013**, *78*, 515–521.
[25] M. Xing, W. Cao, T. Pang, X. Ling, *Solid State Commun.* **2009**, *149*, 911–914.
[26] Y. Song, H. You, Y. Huang, M. Yang, Y. Zheng, L. Zhang, N. Guo, *Inorg. Chem.* **2010**, *49*, 11499–11504.
[27] G. Wang, H. Zou, B. Zhang, Y. Sun, Q. Huo, X. Xu, B. Zhou, *Opt. Mater. (Amst).* **2015**, *45*, 131–135.
[28] J. Flahaut, M. Guittard, M. Patrie, *Bull. Soc. Chim. Fr.* **1958**, *7*, 990–994.
[29] W. He, M. E. Osmulski, J. Lin, D. S. Koktysh, J. R. McBride, J.-H. Park, J. H. Dickerson, *J. Mater. Chem.* **2012**, *22*, 16728.
[30] F. Zhao, M. Yuan, W. Zhang, S. Gao, *J. Am. Chem. Soc.* **2006**, *128*, 11758–11759.
[31] S. Carenco, S. Labouille, S. Bouchonnet, C. Boissière, X.-F. Le Goff, C. Sanchez, N. Mézailles, *Chem. Eur. J.* **2012**, *18*, 14165–14173.
[32] J. Sopoušek, J. Pinkas, P. Brož, J. Buršík, V. Vykoukal, D. Škoda, A. Stýskalík, O. Zobač, J. Vřešťál, A. Hrdlička, *J. Nanomater.* **2014**, *2014*, 1–13.
[33] NIST, "Oleic acid mass spectrum (CAS: 112-80-1)," can be found under https://webbook.nist.gov/cgi/cbook.cgi?ID=C112801&Units=SI&-Mask=200#Mass-Spec, **n.d.**
[34] G. B. Deacon, R. J. Phillips, *Coord. Chem. Rev.* **1980**, *33*, 227–250.
[35] R. Vaďura, J. Kvapil, *Mater. Res. Bull.* **1971**, *6*, 865–873.
[36] F. Ribot, P. Toledano, C. Sanchez, *Inorg. Chim. Acta* **1991**, *185*, 239–245.
[37] L. Tong, E. Lu, J. Pichaandi, P. Cao, M. Nitz, M. A. Winnik, *Chem. Mater.* **2015**, *27*, 4899–4910.
[38] H. Hauser, A. Darke, M. C. Phillips, *Eur. J. Biochem.* **1976**, *62*, 335–344.
[39] N. C. Anderson, M. P. Hendricks, J. J. Choi, J. S. Owen, *J. Am. Chem. Soc.* **2013**, *135*, 18536–18548.
[40] H. Lüth, S. C. Nyburg, P. M. Robinson, H. G. Scott, *Mol. Cryst. Liq. Cryst.* **1974**, *27*, 337–357.
[41] K. Ikeue, T. Kawano, M. Eto, D. Zhang, M. Machida, *J. Alloys Compd.* **2008**, *451*, 338–340.

Manuscript received: November 17, 2018
Revised manuscript received: January 18, 2019
Accepted manuscript online: January 18, 2019
Version of record online: February 6, 2019

Abstract:

Nanomaterials possess fascinating properties but are regarded as potentially harmful. This negative image limits the potential for innovation in both research and industry. To maximize the potential of emerging nanomaterials and ensure safety during their life cycle, "safer-by-design" may be employed in the early stage of nanomaterial research. It consists in investigating their properties, functionality and toxicity at the same time. With feedback between each step of the studies, the performance as well as the safety of the materials may be improved.

Bimetallic gadolinium-cerium oxysulfides of compositions $Gd_{2(1-x)}Ce_{2x}O_2S$ are emerging nanomaterials that show potentials in photocatalysis and biomedical imaging. Nanoplatelets of dimension 2 × 20 nm were prepared by colloidal synthesis in organic solvent. In-depth characterization of the products was provided. Then, safer-by-design approach was discussed in relation with oxysulfide nanoplatelets design for photocatalysis (light absorption, photodegradation of dyes, radical production) and biomedical imaging (coating, photoluminescence, magnetic properties). Their potential toxicity was assessed using a combination of *in vitro* (murine macrophage RAW 264.7) and *in vivo* (C57BL/6 mice) models. For both applications, the cerium content and the surface properties of the nanoplatelets appeared to be key parameters that impact their functionality and toxicity. Overall, this work presents the first attempt to develop safer-by-design metal oxysulfide nanoparticles.

Résumé :

Les nanomatériaux possèdent des propriétés fascinantes, mais sont considérés comme potentiellement dangereux. Cette image négative limite les possibilités d'innovation dans la recherche ainsi que dans l'industrie. Afin d'utiliser au mieux le potentiel des nanomatériaux émergents et d'assurer la sureté tout au long de leur cycle de vie, l'approche « safer-by-design » peut être appliquée dès les premières étapes de la recherche. Il s'agit d'étudier simultanément leurs propriétés, leur fonctionnalité et leur toxicité. Avec les informations acquises à chaque étape, la performance et la sureté de ces matériaux pourraient être améliorées.

Les oxysulfures bimétalliques de gadolinium et de cérium de compositions $Gd_{2(1-x)}Ce_{2x}O_2S$ sont des nanomatériaux émergents, prometteurs pour la photocatalyse et l'imagerie biomédicale. Des nanoplaquettes de dimension 2 × 20 nm ont été préparées par synthèse colloïdale en milieu organique. Une caractérisation approfondie des produits a été fournie. Ensuite, l'approche « safer-by-design » a été discutée en relation avec la conception des nanoplaquettes d'oxysulfure pour la photocatalyse (absorption de lumière, photodégradation de colorants, production de radicaux) et l'imagerie biomédicale (revêtement, photoluminescence, propriétés magnétiques). Leur toxicité a été étudiée par une combinaison de modèles *in vitro* (macrophage murin RAW 264.7) ainsi que *in vivo* (souris C57BL/6). Pour les deux applications, le taux de cérium et les propriétés de surface des nanoplaquettes semblaient être les paramètres clés qui influent à la fois sur leur fonctionnalité et leur toxicité. Globalement, ce travail présente la première tentative de développement de nanoparticules d'oxysulfure métallique « safer-by-design ».